

## INFORMATION TO USERS

This manuscript has been reproduced from the microfilm master. UMI films the text directly from the original or copy submitted. Thus, some thesis and dissertation copies are in typewriter face, while others may be from any type of computer printer.

**The quality of this reproduction is dependent upon the quality of the copy submitted.** Broken or indistinct print, colored or poor quality illustrations and photographs, print bleedthrough, substandard margins, and improper alignment can adversely affect reproduction.

In the unlikely event that the author did not send UMI a complete manuscript and there are missing pages, these will be noted. Also, if unauthorized copyright material had to be removed, a note will indicate the deletion.

Oversize materials (e.g., maps, drawings, charts) are reproduced by sectioning the original, beginning at the upper left-hand corner and continuing from left to right in equal sections with small overlaps.

Photographs included in the original manuscript have been reproduced xerographically in this copy. Higher quality 6" x 9" black and white photographic prints are available for any photographs or illustrations appearing in this copy for an additional charge. Contact UMI directly to order.

ProQuest Information and Learning  
300 North Zeeb Road, Ann Arbor, MI 48106-1346 USA  
800-521-0600

UMI<sup>®</sup>



**Mechanisms for Sodium Insertion in  
Carbon Materials**

by

David Andrew Stevens

submitted in partial fulfillment of the requirements  
for the degree of Doctor of Philosophy

in the Department of Chemistry

at

Dalhousie University

Halifax, Nova Scotia, Canada

July, 2000.

© Copyright by David Andrew Stevens, 2000.



National Library  
of Canada

Acquisitions and  
Bibliographic Services

395 Wellington Street  
Ottawa ON K1A 0N4  
Canada

Bibliothèque nationale  
du Canada

Acquisitions et  
services bibliographiques

395, rue Wellington  
Ottawa ON K1A 0N4  
Canada

*Your file* *Votre référence*

*Our file* *Notre référence*

The author has granted a non-exclusive licence allowing the National Library of Canada to reproduce, loan, distribute or sell copies of this thesis in microform, paper or electronic formats.

The author retains ownership of the copyright in this thesis. Neither the thesis nor substantial extracts from it may be printed or otherwise reproduced without the author's permission.

L'auteur a accordé une licence non exclusive permettant à la Bibliothèque nationale du Canada de reproduire, prêter, distribuer ou vendre des copies de cette thèse sous la forme de microfiche/film, de reproduction sur papier ou sur format électronique.

L'auteur conserve la propriété du droit d'auteur qui protège cette thèse. Ni la thèse ni des extraits substantiels de celle-ci ne doivent être imprimés ou autrement reproduits sans son autorisation.

0-612-66682-4

Canada

**DALHOUSIE UNIVERSITY**

**FACULTY OF GRADUATE STUDIES**

The undersigned hereby certify that they have read and recommend to the Faculty of Graduate Studies for acceptance a thesis entitled "Mechanisms for Sodium Insertion in Carbon Materials"

by David Andrew Stevens

in partial fulfillment of the requirements for the degree of Doctor of Philosophy.

Dated: September 1, 2000

External Examiner \_\_\_\_\_  
Research Supervisor \_\_\_\_\_  
Examining Committee \_\_\_\_\_  
\_\_\_\_\_  
\_\_\_\_\_  
\_\_\_\_\_  
\_\_\_\_\_

DALHOUSIE UNIVERSITY

DATE: 6 September, 2000

AUTHOR: David Andrew Stevens

TITLE: Mechanisms for Sodium Insertion in Carbon Materials

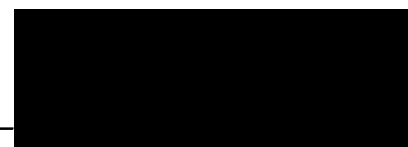
DEPARTMENT OR SCHOOL: Chemistry

DEGREE: PhD

CONVOCATION: October

YEAR: 2000

Permission is herewith granted to Dalhousie University to circulate and to have copied for non-commercial purposes, at its discretion, the above title upon the request of individuals or institutions.

A solid black rectangular box used to redact the author's signature.

Signature of Author

The author reserves other publication rights, and neither the thesis nor extensive extracts from it may be printed or otherwise reproduced without the author's written permission.

The author attests that permission has been attained for the use of any copyrighted material appearing in this thesis (other than brief excerpts requiring only proper acknowledgement in scholarly writing), and that all such use is clearly acknowledged.

## Table of Contents

List of Figures .....	vii
List of Tables .....	xiv
Abstract .....	xv
List of Abbreviations and Symbols.....	xvi
Acknowledgements.....	xix
1. Introduction.....	1
2. Gas Adsorption Porosimetry.....	10
2.1 Analysis of Gas Adsorption Isotherms.....	12
2.2 Gas Adsorption Models.....	15
2.2.1 Langmuir and BET models.....	15
2.2.2 Dubinin approach.....	19
2.2.3 DFT methods .....	23
2.3 Experimental .....	27
3. X-ray Scattering.....	30
3.1 General Theory of Scattering .....	32
3.2 Theoretical Analysis of Small-angle X-Ray Scattering .....	35
3.2.1 Scattering from a sphere .....	38
3.2.2 Scattering from a distribution of pores .....	42
3.3 Wide-angle Scattering .....	50
3.3.1 Layer structure model .....	53
3.3.2 Debye Equation for calculating x-ray powder patterns .....	58
3.4 Experimental .....	59
4. Carbon Structure .....	62
4.1 Introduction to Carbon Terminology .....	62
4.1.1 Structural changes during heat treatment.....	65
4.1.2 Carbon structure analysis.....	67
4.2 Carbon Preparation.....	67
4.2.1 Sample heat treatment.....	68
4.3 Carbon Analysis .....	69

4.3.1	Gas adsorption .....	69
4.3.2	SAXS analysis .....	76
4.3.3	WAXS measurements .....	82
4.4	Carbon Models .....	88
4.4.1	Soft carbon model .....	88
4.4.2	Hard carbon model.....	88
5.	Electrochemical Testing.....	93
5.1	Thermodynamics of Operating Cells.....	95
5.2	Kinetics Within Operating Cells .....	97
5.3	Interpretation of Electrochemical Data .....	98
5.4	Experimental .....	98
5.4.1	Construction of thin film cells .....	98
5.4.2	Construction of <i>in situ</i> x-ray cells.....	100
5.5	Electrochemical Test Results .....	102
5.5.1	Graphitic Carbon.....	102
5.5.2	Soft Carbon .....	103
5.5.3	Electrochemical Performance of Hard Carbons .....	112
6.	In situ X-Ray Scattering.....	121
6.1	<i>In situ</i> WAXS .....	121
6.1.1	Experimental .....	122
6.1.2	Soft Carbon at low scattering angles with Na.....	122
6.1.3	Soft Carbon at low scattering angles with Li.....	125
6.1.4	Soft Carbon at high scattering angles with Na and Li .....	127
6.1.5	Model calculations for Na and Li insertion in soft carbon .....	130
6.1.6	Hard carbon with sodium and lithium at low angles .....	137
6.1.7	Hard carbon with sodium and lithium at high angles .....	140
6.2	SAXS Studies.....	144
6.2.1	<i>In situ</i> SAXS study of soft carbon .....	148
6.2.2	Sodium and lithium SAXS studies of hard carbon .....	152
7.	High Temperature Studies .....	160
7.1	Sodium Expansion Testing.....	160



7.2 Sodium Penetration Test .....	162
7.3 Sodium Vapour Testing.....	162
7.3.1 Experimental.....	163
7.3.2 Interactions of sodium vapour with soft carbon .....	163
7.3.3 Interactions of sodium vapour with hard carbon .....	165
8. Conclusions.....	167
Appendix A. Repeatability.....	170
A1. Gas adsorption .....	170
A2. WAXS measurements .....	171
A3. SAXS measurements .....	172
A4. Electrochemical cell performance .....	172
A5. <i>In situ</i> cell data.....	175
Appendix B. Mathematical Derivations .....	176
B1. Derivation of the Langmuir model .....	176
B2. Derivation of the BET equation.....	178
B3. Evaluation of the integral $\int_V e^{-i \cdot \mathbf{q} \cdot \mathbf{r}} dV$ .....	181
B4. Average value of $e^{i \mathbf{q} \cdot \mathbf{r}_{12}}$ for an isotropic distribution with fixed $r_{12}$ .....	182
Bibliography .....	183

## List of Figures

Figure 1.1: Cross-Section through an aluminium reduction cell. ....	3
Figure 2.1: N <sub>2</sub> gas adsorption isotherms measured at 77K (see section 2.3) for a carbon with significant amount of nanoporosity (solid line – left hand y-axis) and a second carbon containing negligible amounts of nanoporosity - i.e. a meso/macroporous carbon (dashed line – right hand y-axis). ....	14
Figure 2.2: Calculated Langmuir (dotted line – left hand axes) and BET (solid line- right hand axes) plots for the nanoporous (upper graph) and meso/macroporous (lower graph) carbons calculated from the isotherm data (adsorption only) shown in Figure 2.1. The graph for the meso/macroporous carbon also contains a dashed line to show the linearity of the BET model at low relative pressures. ....	20
Figure 2.3: Argon adsorption isotherms for different pore widths calculated through DFT algorithms. Taken from [45]. ....	25
Figure 2.4: DFT fits and calculated pore size distributions obtained for the nanoporous (upper graphs) and mesoporous (lower graphs) carbons. In the isotherm plots, the experimental data are shown with circles, the fit with a solid line. ....	26
Figure 2.5: Schematic diagram of ASAP 2010 Gas Adsorption Porosimeter. ....	28
Figure 3.1: The relationship between scattering angle and inter-atomic spacing for x-ray diffraction derived from the Bragg equation. These data were calculated with a wavelength of 1.5415 Å. The main graph shows d-spacings for small angles whilst the inset presents d-spacings for high (wide) angles. ....	31
Figure 3.2: Atomic scattering factors for lithium, carbon and sodium. ....	34
Figure 3.3: Calculated normalised intensity for different sized spheres. Upper panel – linear plot, lower panel – log-log plot. ....	39
Figure 3.4: Experimental and fitted data for nanoporous carbon (upper graph) and macro/mesoporous carbon (lower graph). The fits are shown as solid lines superimposed on the experimental data. The upper panel in each graph shows the contribution from each term in the scattering equation. ....	49
Figure 3.5: Typical WAXS curve for non-graphitic carbon. ....	51

Figure 3.6: (a) Carbon containing ordered (indicated by squares) and disordered regions. The disordered regions would scatter incoherently with respect to each other, giving a background contribution to the x-ray pattern leaving a series of “isolated” crystallite domains. (b) Model for carbon layer stack with strain. .... 52

Figure 3.7: Upper Panel - calculated intensity for a stack of N carbon layers, with N as indicated on each curve. Lower panel – calculated intensity changes for interlayer insertion, to produce  $\text{Na}_x\text{C}_6$ , with x as indicated on each plot (N = 10). .... 55

Figure 3.8: The effect of increasing strain on a calculated WAXS pattern. .... 57

Figure 3.9: Diagram of the Siemens D5000 Diffractometer geometry for measuring WAXS patterns (upper diagram) and SAXS patterns (lower diagram)..... 60

Figure 4.1: Differences in layer stacking for graphite. Left hand panel shows ABAB... stacking of 2H-graphite. Right hand panel shows ABCABC... stacking of 3R graphite. The hexagonal unit cell for each structure is also shown on each panel. . 64

Figure 4.2:  $\text{N}_2$  Gas adsorption isotherms for PVC samples as a function of heat treatment temperature. For data sets where two curves can be resolved, the lower curve shows the adsorption data whilst the upper curve shows the desorption data. .... 70

Figure 4.3: Pore size distributions for PVC carbon samples as a function of heat treatment temperature. These data were calculated with a carbon slit DFT pore model from the adsorption branch of the  $\text{N}_2$  gas adsorption isotherms presented in Figure 4.2. .... 72

Figure 4.4:  $\text{N}_2$  Gas adsorption isotherms for glucose samples as a function of heat treatment temperature. For data sets where two curves can be resolved, the lower curve shows the adsorption data whilst the upper curve shows the desorption data. Note the different vertical scales for the panels on the right compared to those on the left. .... 73

Figure 4.5: Pore size distributions for glucose derived carbon samples as a function of heat treatment temperature. These data were calculated with a carbon slit DFT pore model from the adsorption branch of the  $\text{N}_2$  gas adsorption isotherms presented in Figure 4.4. The centre panels show an expanded view of the low temperature samples for direct comparison with the results for the high temperature samples on the right. .... 75

Figure 4.6: SAXS curves obtained for PVC carbon as a function of heat treatment temperature. The peak around $q = 0.4 \text{ \AA}^{-1}$ is an artifact of the kapton film used to retain the sample in the holder. ....	77
Figure 4.7: SAXS curves obtained for glucose carbon as a function of heat treatment temperature. ....	80
Figure 4.8: Schematic diagram to show how rotating graphene sheets create larger pores but may also block off pore openings. The left diagram on the left shows a low temperature sample, whilst that on the right shows the same sample after heating to a higher temperature. The rotating sheets are indicated on the left panel by dotted lines. ....	81
Figure 4.9: WAXS patterns measured on carbons derived from PVC as a function of heat treatment temperature. Note the difference in scale between the panels on the left and those on the right. ....	83
Figure 4.10: WAXS patterns measured on carbons derived from glucose as a function of heat treatment temperature. The method used to calculate the layer stacking ratio, $R$ , is indicated on the 1300°C sample. ....	84
Figure 4.11: WAXS patterns measured on carbons derived from PVC as a function of heat treatment temperature after correcting for the effects of the atomic scattering factor and applying the Lorentz-Polarization correction . ....	86
Figure 4.12: WAXS patterns measured on carbons derived from glucose as a function of heat treatment temperature after correcting for the effects of the atomic scattering factor and applying the Lorentz-Polarization correction . ....	87
Figure 4.13: SAXS patterns for resin carbons (left panels) and pitch carbons (right hand panels). As with previous SAXS curves, the peak at around $0.4 \text{ \AA}^{-1}$ comes from the kapton windows in the sample holder. ....	90
Figure 4.14: WAXS patterns for resin carbons (left panels) and pitch carbons (right hand panels). ....	91
Figure 5.1: Schematic diagram of electrochemical cells used in this study. The electrode on the left is the metal whilst that on the right is the test material. The left and right hand panels show the movement of ions and electrons during discharge and charge. ....	93

Figure 5.2: Expanded view of cell components.....	94
Figure 5.3: Measurement of IR drop within operating cells. Upper panel – sodium cell, lower panel – lithium cell. ....	97
Figure 5.4: Interpretation of electrochemical test results. The upper panel is a potential vs capacity curve. The lower panel shows the same data with the charge folded back over the discharge data.....	99
Figure 5.5: Sample holders used for in situ WAXS (left) and SAXS (right) measurements.....	101
Figure 5.6: (a) Lithium and (b) sodium insertion into graphitic carbon. The inset in (b) shows evidence of metal plating at 80 mAh/g during the first discharge and 87 mAh/g during the second discharge.....	103
Figure 5.7: Electrochemical profiles for lithium (left panels) and sodium (right hand panels) insertion into PVC carbons. Note the change of scale for the 800 – 1000°C lithium samples. The vertical lines at the bottom of the curves in some panels indicate the onset of metal plating. ....	104
Figure 5.8: Differential capacity (dQ/dV) curves for carbons prepared from PVC in the range 600-1000°C. The lower curves represent discharge whilst the upper curves represent charge. ....	106
Figure 5.9: Reaction between lithium and hydrogen terminated aromatic carbons. ....	107
Figure 5.10: Lithium and sodium capacities for PVC carbons heat-treated to temperatures between 1100°C and 1700°C. The vertical lines at the bottom of the cycles indicate the start of metal plating.....	108
Figure 5.11: Change in reversible capacity with temperature for PVC carbons. ....	109
Figure 5.12: Electrochemical lithium and sodium insertion into soft carbons prepared from a pitch precursor.....	111
Figure 5.13: Electrochemical profiles for lithium (left hand side) and sodium (right hand side) insertion into glucose derived carbons heat treated in the range 600 – 1000°C. Note that the scale for the lithium cells is different for the 600 and 700°C samples. .....	113

Figure 5.14: Electrochemical profiles for lithium (left hand side) and sodium (right hand side) insertion into glucose derived carbons heat treated in the range 1100 – 1700°C. .....	114
Figure 5.15: Differential capacity (dQ/dV) as a function of heat treatment temperature in the range 600-1000°C for carbon samples derived from glucose.....	116
Figure 5.16: Differential capacity (dQ/dV) as a function of heat treatment temperature in the range 1100-1700°C for carbon samples derived from glucose.....	117
Figure 5.17: Capacity curves for heat-treated resin samples. ....	120
Figure 6.1: In situ WAXS study of sodium insertion into soft carbon. Each scan is offset from the last by 20 counts/s to show changes.....	123
Figure 6.2: Selected scans for sodium insertion into soft carbon. The dashed line is the scan obtained before the current was switched on (as shown in (a)).....	124
Figure 6.3: In situ WAXS study of lithium insertion into soft carbon. Each scan is offset from the last by 20 counts/s to show changes.....	125
Figure 6.4: Selected scans for lithium insertion into soft carbon. The dashed line is the scan obtained before the current was switched on (as shown in (a)).....	126
Figure 6.5: High angle WAXS patterns for sodium insertion into soft carbon. The initial scan has been included as a dashed line on panels (b) to (e) for reference. The sharp peaks are Bragg reflections from cell components. ....	128
Figure 6.6: High angle WAXS patterns for lithium insertion into soft carbon. The initial scan has been included as a dashed line on panels (b) to (e) for reference.....	129
Figure 6.7: In-cell vs out of cell scans (a), together with the results for corrections (b), (c) to the in-cell data.....	132
Figure 6.8: Intensity changes and 002 peak positions for sodium and lithium insertion into pitch-derived soft carbon. ....	133
Figure 6.9: Experimental vs calculated intensity profiles for soft carbon with no change in strain – (a) scan before current was switched on; (b) bottom of discharge for lithium insertion; (c) bottom of discharge for sodium insertion. ....	134
Figure 6.10: Experimental vs calculated intensity profiles for soft carbon after increasing strain – (a) scan before current was switched on; (b) bottom of discharge for lithium insertion; (c) bottom of discharge for sodium insertion.....	136

Figure 6.11: Upper panel - exaggerated schematic of sodium cluster formation between graphene layers that were originally parallel. This would reduce the intensity across the 002 peak. Lower Panel - Calculated Debye pattern for 2 x 2 x 2 unit cells of BCC Na.....	137
Figure 6.12: WAXS measurements of sodium insertion into hard carbon. Each scan has been offset from the last by 10 counts/s for clarity.....	138
Figure 6.13: WAXS measurements of lithium insertion into hard carbon. Each scan has been offset from the last by 10 counts/s for clarity.....	138
Figure 6.14: Selected WAXS scans for sodium insertion into hard carbon. ....	139
Figure 6.15: Selected WAXS scans for lithium insertion into hard carbon.....	141
Figure 6.16: Selected high angle WAXS scans for sodium insertion into hard carbon.	142
Figure 6.17: Selected high angle WAXS scans for lithium insertion into hard carbon.	143
Figure 6.18: A comparison of intensity curves for hard carbon pellets in and out of an electrochemical transmission cell. The scan obtained for graphite showing Porod's law behaviour with a slope of -3.3 is also included, as are fits to each of the scans. .....	147
Figure 6.19: Sample SAXS curves during discharge and charge of a soft carbon cell. The fit obtained for the first scan is shown on subsequent scans for reference.....	150
Figure 6.20: SAXS fit parameters for sodium insertion into and removal from soft carbon.....	151
Figure 6.21: Sample SAXS scans for sodium insertion into glucose-derived hard carbon. The fit obtained for the first scan is included as a dashed line reference on subsequent scans. Each panel also includes the fit obtained. ....	153
Figure 6.22: Fit parameters obtained for sodium insertion into hard carbon. The dashed line in (c) shows the electron density calculated from equation 6.1.....	155
Figure 6.23: Sample SAXS scans for lithium insertion into glucose-derived hard carbon. The fit obtained for the first scan is included as a dashed line reference on subsequent scans. Each panel also includes the fit obtained. ....	157
Figure 6.24: Fit parameters obtained for lithium insertion into hard carbon. The dashed line in (c) shows the electron density calculated from equation 6.1.....	158
Figure 7.1: Schematic diagrams of sodium (a) expansion and (b) penetration tests. ....	161

Figure 7.2: Pitch carbon samples exposed to sodium vapour at 890°C. The equivalent capacity in a room temperature electrochemical cell for each scan is shown in the upper panel. The scan for the unexposed carbon itself is included as the dashed line on all subsequent panels.....	164
Figure 7.3: Glucose carbon samples exposed to sodium vapour at 890°C. The equivalent capacity in a room temperature electrochemical cell for each scan is shown in the upper panel. The scan for the unexposed carbon itself is included as the dashed line on all subsequent panels.....	166
Figure A1: Repeat gas adsorption measurements.....	171
Figure A2: Repeat WAXS measurements completed on a typical hard carbon (upper panel) and a typical soft carbon (lower panel) .....	172
Figure A3: Repeat SAXS measurements completed on a typical nano-porous hard carbon (upper panel) and a typical meso/macro-porous soft carbon (lower panel) .....	173
Figure A4: Repeat sodium and lithium cells for carbon electrodes prepared from samples heat-treated on different days.....	174



## List of Tables

Table 1.1: Operating characteristics of modern aluminium smelters. ....	3
Table 3.1: Atomic scattering factor co-efficients [54]. ....	34
Table 3.2: SAXS model fit parameters for sample carbons. ....	50
Table 3.3: Scan settings used for x-ray measurements. ....	59
Table 4.1: Carbon samples prepared for this study. ....	69
Table 4.2: BET and Langmuir surface areas for carbon samples as a function of heat treatment temperature. The error in these values is estimated to be less than $\pm 10\%$ . ....	76
Table 4.3: SAXS fit parameters for PVC samples modeled using equation 3.41. ....	78
Table 4.4: SAXS fit parameters for glucose carbons as a function of heat treatment temperature. ....	79
Table 4.5: Parameters calculated from WAXS patterns for both PVC and glucose. ....	85
Table 4.6: Calculated SAXS parameters for pitch and resin samples. ....	92
Table 4.7: Calculated WAXS parameters for pitch and resin samples. ....	92
Table 5.1: Capacity changes (mAh/g) for carbons derived from glucose as a function of heat treatment temperature. ....	115
Table 5.2: Average potential of the low voltage plateau (V) for glucose carbons as a function of heat treatment temperature. ....	118
Table 6.1: Comparison of fits for glucose derived hard carbons in air and within an in situ SAXS cell. ....	148
Table 7.1: Sodium expansion values for commercial cathode carbons. ....	161

## **Abstract**

This thesis details the mechanisms for sodium insertion into different carbons using both electrochemical and vapour techniques. Room temperature electrochemical measurements were completed to examine the insertion and removal of sodium from soft (graphitizable) and nanoporous hard (non-graphitizable) carbons prepared by the heat treatment of organic precursors to a range of temperatures. The mechanisms identified from these studies were further investigated through a series of in situ x-ray scattering studies on operating electrochemical cells. The results obtained were then compared with x-ray scattering measurements on carbons after exposure to sodium vapour at 890C.

This work is primarily driven by the aluminium industry's need to understand how sodium insertion causes carbon cathode blocks in aluminium reduction cells to swell. The results obtained are also of relevance to the lithium-ion battery field as they help to verify mechanisms proposed in the literature for lithium insertion into carbon hosts. Some carbons were also identified that could accommodate large amounts of sodium, making them attractive candidates for anodes in rechargeable sodium ion batteries.

For soft carbons, the results showed that both sodium and lithium insert between approximately parallel carbon layers along the sloping voltage region of the electrochemical curves, increasing the average interlayer spacing. The sodium and lithium capacities decreased with increasing carbon heat treatment temperature. For the soft carbons studied, the sodium capacity was found to be consistently lower than the lithium capacity, implying that some lithium-accessible sites were unavailable for sodium insertion.

The electrochemical profiles for the hard carbons also contained capacity along a sloping voltage region and, as with the soft carbons, this was shown to result from the insertion of sodium and lithium between approximately parallel carbon layers. In contrast to the soft carbons, however, the electrochemical profiles for the hard carbons also exhibited significant capacity along low voltage plateaus at chemical potentials close to the chemical potential of the metal. An in situ small angle x-ray scattering experimental method was therefore developed to examine changes in scattering from the nanopores during sodium and lithium insertion/removal. The results from this technique clearly showed that the low voltage plateau capacity resulted from the insertion of sodium and lithium into nanopores in the carbon.

## List of Abbreviations and Symbols

$a; a_1; a_2$	Correlation lengths in x-ray scattering.
A, B, C, D	Constants used to fit small-angle scattering curves.
B	Peak width at half maximum.
$a_i, b_i, c$	A set of coefficients used to generate atomic scattering factor curves.
$A(\mathbf{q})$	Amplitude of a scattered x-ray beam.
BCC	Body centred cubic structure.
BET	Brunnaeur, Emmet and Teller (for BET surface area equation).
$C_j$	A coefficient describing how much of a calculated isotherm to include.
DFT	Density Functional Theory.
$d_{hkl}$	Spacing between the set of planes with Miller Indices hkl.
$dQ/dV$	Derivative of capacity with respect to cell potential.
EC:DEC	Ethylene carbonate:diethyl carbonate.
EPDM	Ethylene propylene diene terpolymer.
F	Faraday's number, 96,487 C/mol.
$f(x); f_e$	The atomic scattering factor for an atom; for an electron.
$F(x)$	The structure factor for a distribution of atoms.
GOF	Goodness of fit parameter.
HMTA	Hexamethylene tetramine.
IR	Internal resistance.
$I_{2\theta}$	Intensity measured at a scattering angle $\theta$
$I(\mathbf{q})$	Intensity measured in the direction $\mathbf{q}$ .
$I_0$	Intensity of an incident x-ray beam.
$k_{ads(n)}, k_{des(n)}$	Rate constants for: adsorption into nth layer; desorption from nth layer.
$K_n$	Ratio of adsorption to desorption rate constants.
$L_c; L_a;$	Average crystallite height; average crystallite width.
LDA	Local Density Approximation.
N	Number of: sites on a surface; scatterers in a material; C layers in a stack.
NMP	N-methyl pyrrolidinone.
$n(\text{Na})$	Amount of sodium in pores.

P	Pressure, equilibrium gas pressure, surface vapour pressure.
$P_0$	Saturation gas pressure.
$P_s$	Probability that one point at the end of a line is in the s phase.
$P_{ss}$	Probability that both points at the end of a line are in the s phase.
PVC	Polyvinyl chloride.
PVDF	Poly(vinylidene fluoride).
$\mathbf{q}, q$	Scattering vector in x-ray scattering; magnitude of scattering vector.
$Q(P)$	Calculated volume adsorbed at equilibrium pressure P.
r	Pore radius, pore width.
$\mathbf{r}; r_{xy}$	A position vector; a vector between two points x and y.
$R_m$	Mean radius of curvature of a surface.
$R; R_g; R_s$	Sphere radius; radius of gyration; equivalent spherical radius of a pore.
$\mathbf{s}_0, \mathbf{s}_1$	Vectors describing incident and scattered x-ray beams respectively.
S	Surface area of an object.
T	Temperature; count time for x-ray measurements.
SANS	Small-angle neutron scattering.
SAXS	Small-angle x-ray scattering.
$V_G; V_M$	Effective volume of a gas molecule.
$V_G; V_M$	Gas volume required to form a monolayer.
$V_P, V(P)$	Volume of gas adsorbed at equilibrium pressure P.
$V(r)$	Potential energy between a surface and gas molecules.
W	Amount of electrical work.
$W; W_0$	Volume adsorbed; micropore volume (Dubinin equation).
WAXS	Wide-angle x-ray scattering.
$\beta$	Affinity coefficient relating the adsorption potentials of two adsorbates.
$\delta; P(\delta)$	Layer strain factor; Probability of having a particular layer strain, $\delta$ .
$\epsilon; \epsilon_c$	Potential difference; adsorption potential.
$\gamma; \gamma(r)$	Surface tension; the auto-correlation function in x-ray scattering.
$\eta_r; \eta_p; \eta_m$	Electron density contrast: at a point r; of a pore; of a matrix.
$\lambda$	Wavelength of x-rays.

$\mu$	Chemical potential.
$\phi$	The volume fraction of void space in an object.
$\theta$	Contact angle between surface and a fluid.
$\theta$	Scattering angle in x-ray studies.
$\theta_m$	Bragg angle for a monochromator.
$\theta_n$	Fraction of sites covered with an n layer stack.
$\rho(r); \rho(\mathbf{r})$	Gas density at r; electron density: at the end of the vector r.
$\Delta\rho$	Electron density contrast between pores and the carbon matrix.
$\rho_{avg}; \rho_p; \rho_m$	Electron density: average; in a pore; of a matrix.
$\Omega_v$	Grand potential function.

## Acknowledgements

First and foremost I wish to acknowledge the support, guidance and encouragement provided by my supervisor, Dr. Jeff Dahn, during my time as a graduate student. It has been an honour to work in his research group.

I would like to thank Dr. M. H. Jericho, Dr. P. D. Wentzell and Dr. M. A. White for serving on my supervisory committee and for their useful comments and suggestions during committee meetings. I would also like to thank Dr. D. D. L. Chung for serving as my External Examiner.

I would like to thank former lab members Weibing Xing who showed me the ropes when I arrived, Edward Buiel for many helpful discussions on carbon, and Ian Courtney and Jason Mueller-Neuhaus for useful discussions on a range of topics. I would also like to thank current lab members Luc Beaulieu, Aaron Davis, Tim Hatchard, Shane Beattie, Dean MacNeil, Jennifer Seel, Mark Obravac, Kevin Hewitt and Zhonghua Lu for help with various aspects of my work and for making the lab such a vibrant and interesting place to work. I would like to thank Andy George for preparing the high temperature samples, Alex Feargrieve and Simon Trussler for machine shop support, Bridget Trim, Judy Hollet and Barabara Gauvin for administrative support and Giselle Andrews for helping with Chemistry Department issues.

I wish to acknowledge the generous financial support for my project received from Comalco Aluminium Ltd. I would like to thank Mr. Les Edwards for his efforts to establish the project, Mr. Geoff Bearne for supporting my work after I moved into the Reduction group and Dr. Ray Shaw for his helpful comments during project reviews and for finding the time to approve articles and the thesis for publication.

Finally I would like to express my deep gratitude to Amanda for her unwavering support and encouragement during my time here. I am very happy to have been able to share this experience with such a wonderful person.

# Chapter 1

## Introduction

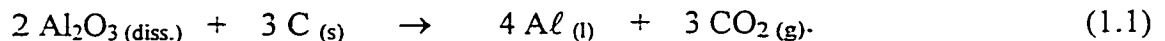
Although this is a thesis about carbon and its interactions with sodium, it has its origins in the aluminium industry, even though the two areas may appear to be unrelated to those who are not familiar with aluminium smelting. In order to understand the motivation for this work, it is therefore necessary to understand the aluminium production process, and, in particular, to understand the basics of operation of an aluminium reduction cell.

Aluminium is the most abundant metal in the earth's crust and is one of the most useful materials in industrialized societies [1]. It is one of the most electropositive metals and, as a result, is highly reactive in its elemental form. It is therefore found in nature in the +3 valence state. Although aluminium-containing ores such as bauxite can be relatively easily purified through caustic digestion to extract the hydroxide followed by calcination to the oxide,  $\text{Al}_2\text{O}_3$  (alumina) [2], reducing the oxide to the metal requires large amounts of energy. Alumina has a very high melting point ( $2045^\circ\text{C}$ ) making direct reduction from solution prohibitively expensive and technically difficult. A practical process for extracting aluminium metal from alumina at low temperatures ( $< 1000^\circ\text{C}$ ) was discovered independently by Hall and Heroult in 1886. The Hall-Heroult process has been the standard industrial method for aluminium smelting for over 100 years and is used to produce more than 20,000,000 tonnes of aluminium metal annually. In 1999 the average metal price was approximately US\$1350 per tonne.

Figure 1.1, adapted from Haupin [3], presents a schematic diagram of the cross-section through a Hall-Heroult aluminium reduction cell. In order to give an idea of the scale of smelting operations, Table 1.1 presents typical operational statistics for a modern aluminium smelter [4].

In a Hall-Heroult reduction cell, a small amount of alumina is dissolved in molten bath (a NaF/AlF<sub>3</sub>/CaF<sub>2</sub> molten salt solution) maintained at ~ 960°C. Large currents passing through the cell reduce the Al<sup>3+</sup> containing species to aluminium, whilst carbonaceous anodes in the cell are oxidised to CO<sub>2</sub>. Approximately 0.4 kg of carbon is consumed for every kilogram of metal produced. Despite having a significantly lower operating temperature than that required for direct reduction from the molten salt, the Hall-Heroult process is still a highly energy intensive process. Each kilogram of metal produced requires ~ 14 kWh of electricity for the reduction step alone [4].

Although the in-cell reaction chemistry is complex, the primary process can be represented by [5]:



Aluminium is periodically removed from the cell by vacuum, whilst alumina is periodically fed into the cell from the top, essentially giving a continuous process. The aluminium forms as a pool of molten metal (aluminium has a melting point of 660°C, well below the bath temperature) that acts as the effective cathode surface where further aluminium deposition occurs. As the metal has a slightly higher density than bath, it remains under the bath layer, pooling on top of the carbonaceous cathode blocks. These cathode blocks act as both current conductors and as the container for holding the metal and the bath. Carbon is used because it is one of the few practical, low-cost materials that is chemically resistant to the highly corrosive molten bath, dissolves only slowly in the metal and has the desired electrical and thermal properties for effective cell operation.

During the reduction process, some sodium metal is also produced from the NaF in the bath, as evidenced by the presence of ~ 0.02 wt% sodium metal in the aluminium removed from the cell [6]. The actual concentration depends on factors such as the ratio of NaF to AlF<sub>3</sub>, the cell temperature and the extent of mixing in the bath. It is believed



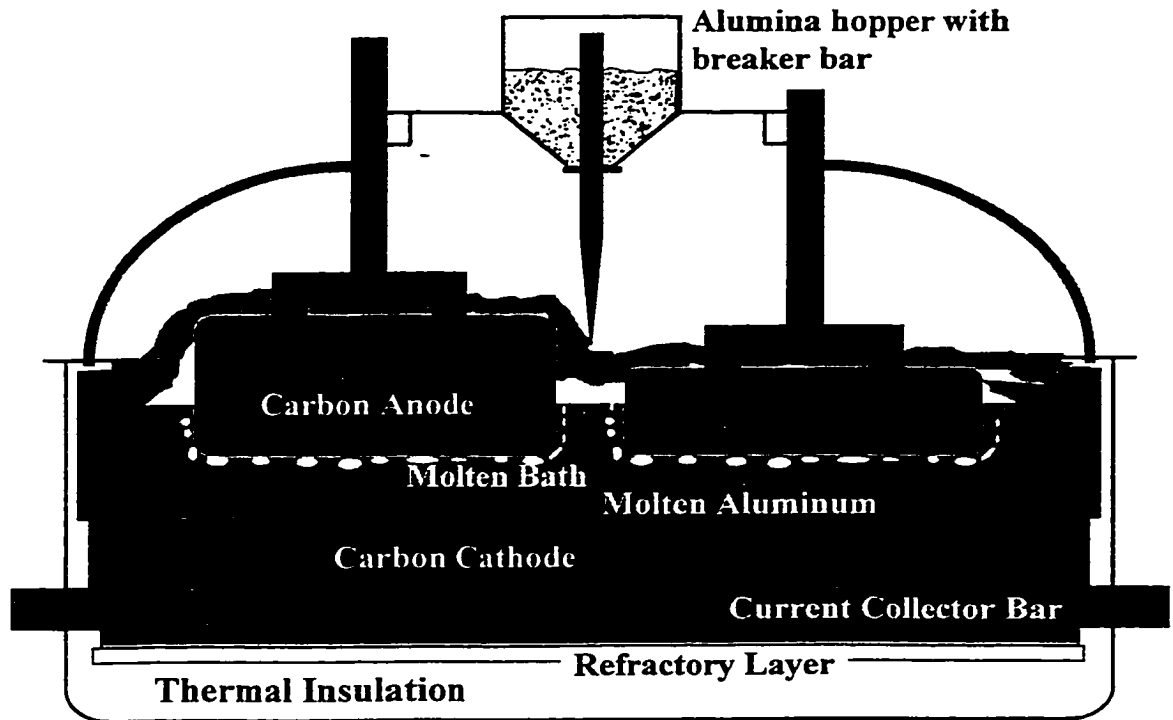
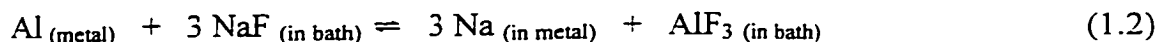


*Figure 1.1: Cross-Section through an aluminium reduction cell.*

*Table 1.1: Operating characteristics of modern aluminium smelters.*

<b>Number of cells operating:</b>	300-500 per smelter, connected in series
<b>Approximate metal output:</b>	1 - 1.5 tonnes per cell per day
<b>Average alumina concentration:</b>	2 - 7 wt%
<b>Cell voltage:</b>	~ 4.5 V
<b>Cell current:</b>	~ 300 kA (can be up to 800 kA)
<b>Approximate cell life:</b>	5 years
<b>Carbon cathode block dimensions:</b>	4 m long x 1m wide x 1m high (10 per cell)
<b>Metal pool depth:</b>	20 cm
<b>Distance from anode to metal surface:</b>	4 cm

that the sodium forms either through direct reduction or, more likely, through back reaction of bath components at the metal-bath interface according to [7]:



Thermodynamic studies suggest that the equilibrium position at cell operating temperatures lies to the left [8]. Despite this, however, the conditions in an operating reduction cell are such that this reaction (or something similar) does occur to a reasonable extent. The important point is that there is always some sodium present in the metal that is in direct contact with the cathode carbon.

Sodium in the metal can move through the matrix of the cathode carbon [9], primarily through a diffusion process, where the Na diffusion constant has been estimated at  $2\text{-}5 \times 10^{-5} \text{ cm}^2\text{s}^{-1}$  at cell operating temperatures [8]. As it moves through the carbon, the sodium can cause swelling [10], with the maximum extent of swelling being dependent primarily on the type of cathode carbon used. Although the swelling has some operational benefits such as sealing cracks in the cell, it can result in loss of cathode integrity through increased erosive wear. In extreme cases it can cause the cathode block itself to crack, providing a pathway for molten aluminium to leak out, eating through the refractory layers and ultimately the steel shell, after which it can pour freely from the cell. This process, known as a tap-out, is one of the major safety concerns for operators of reduction cells. It also results in the need for a complete reline of the cell, leading to a loss in production and significant materials costs.

Numerous researchers have studied the interactions between carbon materials and sodium, primarily through work completed in support of either cathode carbon manufacturers or aluminium smelters. As a result of this work, the correlation between carbon type and the resultant sodium expansion characteristics is reasonably well understood. However, the mechanisms through which sodium is able to enter the carbon matrix are still the subject of some debate, with different researchers proposing different mechanisms based on the analysis tools used and the nature of the data collected.

In 1959, Asher described the formation and structure of a sodium-graphite compound with the formula  $\text{NaC}_{64}$ . This compound was described as an 8<sup>th</sup> stage

compound, meaning that sodium atoms were located between aromatic sheets, with 8 aromatic layers between each sodium layer [11]. This appears to be one of the earliest reports of the preparation of a sodium-containing carbon. Shortly after this work, in 1962, Berger et al. [12] presented the first major study of the interactions between sodium and different types of carbon. In this excellent study, the authors exposed a variety of carbon samples to sodium vapour at a range of vapour pressures using a two-zone reactor. The amount of sodium absorbed by the samples was measured with a thermo-balance. In addition, the structural changes occurring within the carbons were determined through measurement of x-ray diffraction patterns of the materials before and after exposure to the sodium vapour. The information obtained from this comprehensive study allowed the authors to propose that sodium can be inserted between carbon layers and/or condense within porosity depending on the nature of the carbon structure.

In the last 20 years, the majority of research completed worldwide on the interactions of sodium with carbon hosts has been driven by the needs of the aluminium industry. The development of larger cells with lower tolerances in construction has resulted in strong demand for sodium-resistant carbons. The sodium expansion characteristics of cathode carbons have now become critical, especially as inputs to different finite element models for predicting cell performance and optimising cell design. Thus, in order to provide reliable sodium expansion data, many of the papers published during the last 2 decades have concentrated on measuring sodium uptake and sodium expansion of “real” cathode materials (see for example [13], [14], [15]). The experimental methods used for these studies were designed to provide a controlled test environment as close to that in an operating reduction cell as possible. These studies have given some valuable information on some of the sodium capacities and expansion properties of different carbon types. It is now assumed that cathode carbon suppliers will provide sodium expansion data for their cathode blocks, along with other traditional properties such as density, ash content and thermal expansion data. Unfortunately, the mechanisms through which sodium becomes incorporated in carbonaceous hosts cannot be readily deduced from these “industrial” test methods.

Researchers have recently started utilizing alternative approaches. Some have used experimental techniques closely aligned to the methods originally used by Berger et

al.[12], whilst others have tried using room-temperature electrochemical methods used in battery research. Some examples of those using similar methods to Berger et al. include Mikhalev and Oye [16], who have developed a sodium vapour porosimeter capable of generating sodium adsorption isotherms for commercial cathode carbons, and Sechet et al. [17], who used sodium vapour exposure followed by x-ray diffraction studies to show how carbon structure changes with sodium incorporation.

Researchers completing room temperature electrochemical measurements have been inspired in part by the success of such methods for understanding lithium insertion behaviour in carbon materials. Lithium insertion into carbon has been the subject of extensive research because many carbons can be used as anode materials in rechargeable lithium-ion batteries (see for example [18], [19]). For such studies, room temperature electrochemical measurements in non-aqueous solvents are used to determine the nature of the sites available for lithium incorporation.

As a result of the behavioural similarities between sodium and lithium in many situations, it is reasonable to assume that the techniques used to study lithium insertion in carbons can also be used to complete similar studies of sodium insertion in carbon materials. Some researchers have therefore tried using similar methods to examine sodium uptake in carbon materials, with varying levels of success. Studies have been completed on polyacetylene [20], petroleum coke [21], carbon black [22], pitch coke [23] and meso-carbon microbead (MCMB) precursors [24]. Some of these studies suffered from problems related to effective removal of sodium from the carbons after insertion. The removal step is required in order to determine the true capacity of the materials as some reactions occur when current flows that are not related to insertion of sodium into the carbon. This will be discussed in more detail in chapter 5. The paper on MCMB carbons, published at the time this thesis was being written, is one of the few papers to present both sodium insertion and removal data. This shows that people are only now starting to develop reliable methods for determining sodium insertion mechanisms through room temperature electrochemical studies.

In keeping with these recent developments, the research project reported in this thesis was established to further the understanding of the interactions between sodium and carbon hosts primarily through the use of room temperature electrochemical studies.

The goals of this research were to determine the mechanisms through which sodium is incorporated into carbonaceous hosts and to understand how sodium uptake is affected by changes in carbon structure.

A number of experimental methods were used to obtain the information necessary for understanding these sodium/carbon interactions. The repeatability of the experimental methods used was good, as shown in Appendix A.

Gas adsorption porosimetry can be used to determine the size(s) and amount of open porosity in solids, where open porosity can be defined as void space accessible to a probe gas molecule. It is one of the few techniques capable of quantifying porosity with nanometre size dimensions. Many carbon materials contain large amounts of such porosity, thus gas adsorption porosimetry was used to determine the distribution of open porosity and the total surface area of the carbons prepared in this work. The standard gas adsorption technique involves measuring the volume of gas adsorbed as a function of gas pressure at fixed temperature. The data obtained are generally presented as a gas adsorption isotherm, with the gas volume adsorbed per gram of sample on the vertical axis and pressure on the horizontal axis. A number of theories have evolved over the last 90 years to explain the gas adsorption isotherms obtained for solids in general and carbons in particular. The theories relevant to carbon structures will be summarised in Chapter 2. This chapter also contains a description of the experimental method used to generate the gas adsorption isotherms.

Another important tool for understanding carbon structure is x-ray scattering. There are two types of measurements that can be made. Small-angle measurements probe the pore structure of the carbon (they can also be used to assess particle sizes with nanometre sized dimensions). This technique differs from gas adsorption in two fundamental ways: it measures both closed and open porosity (as opposed to just open porosity for gas adsorption) and it does not involve a direct physical interaction between the material of interest and probe molecules. This gives this technique certain advantages over gas adsorption that are utilised for the *in situ* studies presented in Chapter 6. Probably the major disadvantage of this technique is that data analysis can be difficult. Wide-angle scattering measurements can be used to obtain information on the arrangement of carbon atoms within the host structure. For instance, wide-angle

measurements have been used to show that many carbons contain aromatic layers stacked more or less parallel to each other in small domains. Both small and wide-angle x-ray scattering measurements were completed on the heat-treated carbon samples. The small-angle measurements were used to complement the gas adsorption measurements, whilst the wide-angle measurements were used to understand the changes in atomic structure with changes in heat-treatment temperature and carbon precursor. Chapter 3 presents the relevant theory for both small and wide-angle scattering.

The combination of gas adsorption and x-ray scattering studies can be used to develop models of carbon structure both on the atomic scale and on a larger scale as a function of heat-treatment temperature and carbon type. A number of such models have been proposed by different authors. The most useful of these models are reviewed at the start of Chapter 4. This chapter then goes on to explain how the carbons were produced for subsequent electrochemical testing and presents gas adsorption and x-ray scattering data on these carbons. With this information, together with the models proposed by other authors, Chapter 4 concludes with a summary of the carbon structural model to be used for interpreting the results from electrochemical testing.

The primary research tool used for this thesis was electrochemical analysis. Electrochemical measurements were completed on electrode materials prepared from the carbon samples. The theory behind the electrochemical techniques used will be presented in Chapter 5, together with a discussion of lithium-ion battery technology (in particular carbon anode materials for lithium-ion batteries) to show how the methodology used provides an excellent framework for sodium insertion studies. Chapter 5 also contains a detailed discussion of the results obtained for the electrochemical insertion of sodium into carbon materials and compares these results with those obtained for lithium insertion into the same materials. These results provided strong evidence for the nature of the interactions between sodium species and the carbon hosts and led to the identification of three predominant mechanisms through which sodium can be incorporated into a carbon host.

To prove the validity of the mechanisms proposed, x-ray scattering methods were combined with electrochemical measurements through a powerful technique known as *in situ* x-ray scattering. In this technique, x-ray scattering curves are measured on operating

electrodes. These measurements allow the researcher to observe the structural changes that occur in the carbon hosts as sodium (or lithium) is inserted into and removed from the carbon matrix. The results obtained from this work in particular (presented in Chapter 6) provide very strong evidence for two of the three mechanisms proposed in Chapter 5.

Most of the experimental measurements completed for this thesis were made on samples at or close to room temperature. In order to demonstrate the validity of the mechanisms proposed for cathode carbon materials held at  $\sim 1000^{\circ}\text{C}$ , a simple sodium vapour test was developed. In this test, carbon samples were exposed to sodium vapour at  $890^{\circ}\text{C}$  under inert atmosphere. After cooling, the sodium-filled carbons were analysed using x-ray scattering techniques. It will be shown in Chapter 7 that the results obtained were essentially the same as those obtained on the same materials prepared in room temperature syntheses. These results imply that the primary sodium insertion mechanisms for carbons in operating aluminium reduction cells are the same as those seen at room temperature.

Although this work was primarily completed for the aluminium industry, it is also of relevance to the rechargeable battery industry, where it will help any potential development of rechargeable sodium-ion battery technology, a lower-cost alternative to rechargeable lithium-ion batteries. In fact, the experimental work completed during this project has identified anode materials that have almost the same gravimetric capacity for sodium as current commercial lithium-ion battery anode materials (MCMB) have for lithium. It appears that this is the first time such high capacity anode materials for rechargeable sodium-ion batteries have been identified.

## Chapter 2

### Gas Adsorption Porosimetry

One of the simplest physical properties of a material to visualise is its density - the volume occupied by a given mass of the material. Measuring the density of something like a metal is a relatively straightforward process – it can be easily machined into a regular shape and then weighed or simply placed in a fluid such as water and the volume of fluid displaced can then be measured (Archimedes density). For something that contains holes or for fine powders, the concept of density becomes somewhat more nebulous. Should the volume within the holes be included? What about the space between particles? At what point does a hole become part of the material itself? How do you measure holes that are not much bigger than atomic dimensions? Parts of these questions can be answered by being more specific with terminology and completing a range of density measurements, as outlined in the next paragraph. Normally however, for complicated distributions of particles and/or pores, it is necessary to turn to more complex analysis techniques that are able to measure pore size distributions.

The term bulk density is often used to describe the density obtained by measuring the outer dimensions of an object and thus includes inter- and intra-particle porosity. Fractional packing density is used to represent a powder when all the particles are well packed together [25]. This is often measured as the tapped density, where the sample is loaded into a cylinder that is raised and dropped a small distance repeatedly until the powder volume stops decreasing. Real density describes the density obtained by filling the inter-particle and macroporosity with a suitable solvent, whilst the true density can be measured by helium pycnometry [26], where the majority of the open fine porosity



in a solid can be measured by filling with helium gas. All these different density numbers provide different information about the nature of the solid/powder. By measuring a range of different densities, information can be obtained on the volume of the object that falls into different classifications, eg inter-particle porosity, macroporosity, microporosity etc. Although this division of volume can be very useful for comparing solid materials, it provides only limited information about the size and distribution of pore sizes in the material. This is where more specialised techniques such as mercury porosimetry and gas adsorption porosimetry can be used.

The next level of detail on carbon structure can be obtained with mercury porosimetry. In this technique, mercury is forced into an evacuated sample under high pressures and the volume of mercury intruded into the sample is measured as a function of pressure [27]. As mercury does not wet most materials, pressure is required to force it into the pores. The pore size being examined can be related to the applied pressure by the Washburn equation (which assumes cylindrical pores) [27]:

$$r = \frac{2\gamma \cos \theta}{\Delta P}. \quad (2.1)$$

In this equation,  $r$  is the pore radius,  $\gamma$  is the surface tension of the mercury,  $\theta$  is the contact angle between the mercury and the surface of the material being examined and  $\Delta P$  is the pressure difference between the interior of the pore and the pressure applied to the external fluid. As the samples are normally evacuated prior to analysis, it is appropriate to replace  $\Delta P$  with  $P$ , the external pressure for most of the analysis.

Modern instruments are capable of applying pressures from sub-atmospheric up to 414 MPa ( $60.0 \times 10^3$  psi), which corresponds to pore diameters that range from  $\sim 0.3$  mm down to  $\sim 3$  nm. Although this technique covers a large range of pore sizes, its effectiveness in measuring very fine porosity, is quite restricted, both because the Washburn equation is less reliable in small pores and because the high pressures can easily change the structure of the material (eg by causing pore walls to collapse). An alternative approach is therefore required to effectively analyse nanometre-sized porosity. The standard technique used is gas adsorption porosimetry. Other techniques that can be

used include small-angle scattering of x-rays (discussed in Chapter 3) and neutrons as well as electron microscopy studies.

The principle of operation of a typical gas adsorption porosimeter is relatively straightforward. The sample (called the adsorbent) is evacuated, normally at elevated temperatures, to remove most adsorbed contaminants. The probe gas (the adsorbate) is then introduced into the sample tube and the amount taken up by the adsorbent is recorded after the gas reaches an equilibrium or near-equilibrium pressure. Equilibrium is deemed to have been reached when the rate of change of volume adsorbed falls below a threshold value. The rate of change of volume adsorbed is measured either gravimetrically or, more commonly, by monitoring gas pressure changes. These measurements are generally completed at constant temperature giving an adsorption isotherm, which relates the amount adsorbed to the partial pressure of the adsorbate gas. A pore size distribution can be calculated from a range of models, however care must be taken to ensure that the model being used is relevant and that the assumptions made in generating the model are reasonable for the material being studied.

The shape and scale of the adsorption isotherm depend on the nature of the adsorbate and its interactions with the host solid. Thus there can be no absolute porosity value or pore size distribution for a material. A wide range of adsorbate molecules such as  $N_2$ ,  $CO_2$ , Kr,  $H_2O$ ,  $C_6H_6$ , alkanes and  $CCl_4$  has been used to quantify porosity [28], [29], [30], [31], with each adsorbate giving different information. When completing gas adsorption measurements it is therefore important to select an adsorbate that is relevant to the property of interest. For example, it is more logical to measure a butane adsorption isotherm than an  $N_2$  adsorption isotherm for an activated carbon designed to trap petroleum vapours.

## 2.1 Analysis of Gas Adsorption Isotherms

Although it is tempting to analyse gas adsorption data using sophisticated models, it is worth considering the amount of information that can be obtained from the shape of the isotherm. Although the isotherm presents volume adsorbed as a function of gas

pressure, there is a strong correlation between gas pressure and pore size – the smaller the pore being considered, the smaller is the external pressure required to fill that pore. This occurs because the attractive potentials from the walls of narrow pores overlap, enhancing the overall adsorption potential in these pores. This enhanced potential makes condensation of the gas within pores energetically favourable, allowing it to occur at pressures much lower than the saturation pressure of the gas. Thus, just by looking at the shape of the adsorption isotherm or comparing isotherms for different materials measured under the same conditions, it is easy to get a feel for the amount and size of porosity in the materials measured.

IUPAC has introduced a classification scheme to describe pores of different sizes [32]. The terminology recommended is listed below. Although this scheme exists, in this thesis the term nanopore will be used in place of micropore as nanopore is a more logical description for the pores being examined. The terms mesopore and macropore will be retained.

#### IUPAC Pore Size Classification Scheme

Pore width > 50 nm:	Macropores
Pore width between 2 and 50 nm:	Mesopores
Pore width less than 2 nm:	Micropores

Examples of the two types of isotherms of relevance to this thesis are presented in Figure 2.1. The nanoporous carbon adsorbs a large volume of gas at low pressures and then essentially adsorbs no more after the pores are filled. This is known as a Type I isotherm [32]. The mesoporous carbon on the other hand adsorbs at all pressures. The initial volume adsorbed in this carbon is generally attributed to the development of a monolayer on the walls of the mesopores. In the intermediate pressure region, the volume adsorbed increases continuously. This can be envisaged as the development of multi-layer adsorption within the pores. Finally, at pressures close to gas saturation pressure (i.e. relative pressure of 1), the volume adsorbed increases rapidly with only a small change in pressure - this can be attributed to condensation of the gas within the pores. This type of isotherm is classified as a Type II isotherm [32].

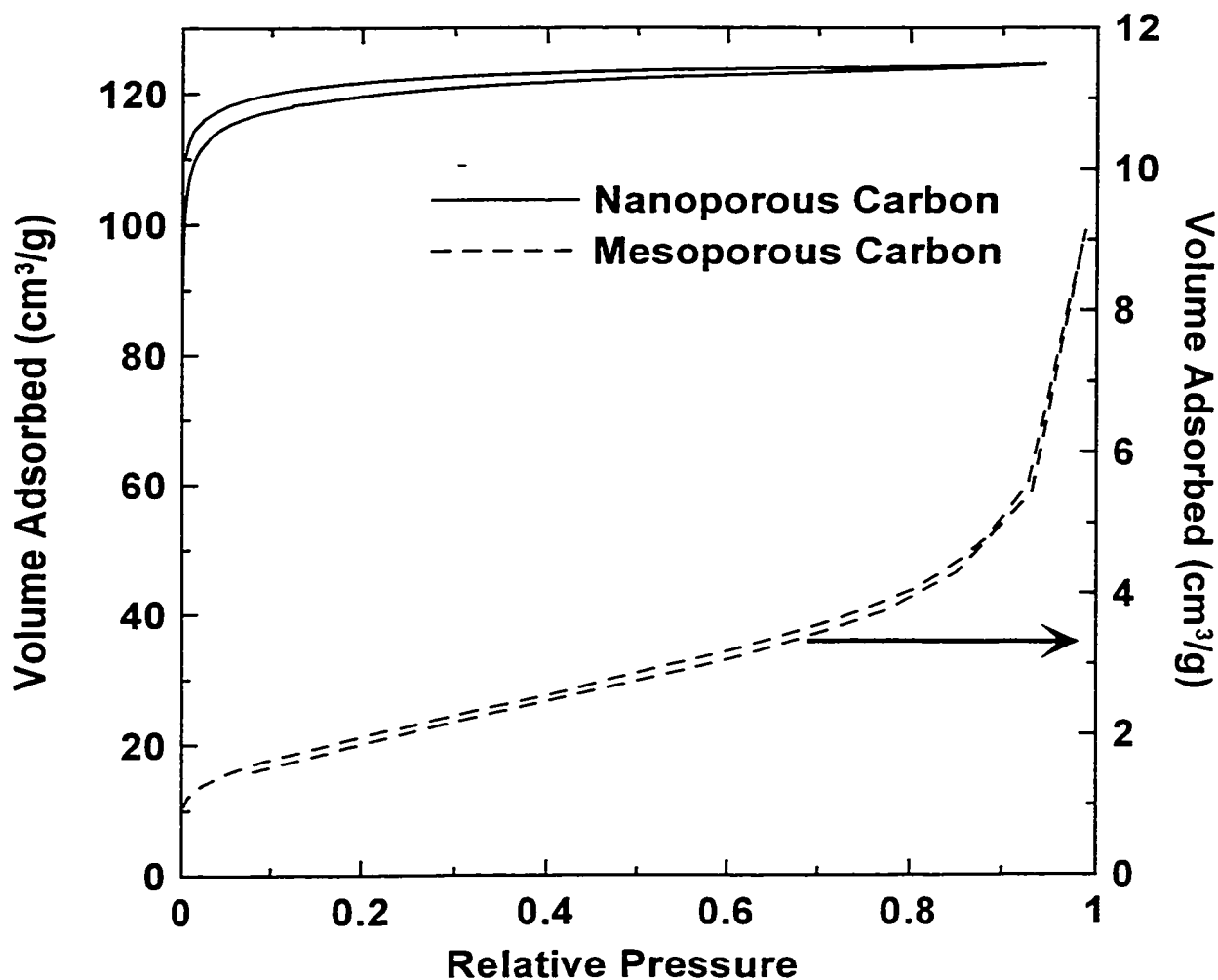


*Figure 2.1:  $N_2$  gas adsorption isotherms measured at 77K (see section 2.3) for a carbon with significant amount of nanoporosity (solid line – left hand y-axis) and a second carbon containing negligible amounts of nanoporosity - i.e. a meso/macroporous carbon (dashed line – right hand y-axis).*

In order to quantify the differences between isotherms measured on different carbons, there are a number of models available for extracting surface areas and pore size distributions from adsorption isotherms. The most useful and widely used models for carbon materials are discussed below.

## 2.2 Gas Adsorption Models

### 2.2.1 Langmuir and BET Models

One of the simplest approaches to model the adsorption of gas molecules on a surface is to assume the surface can be represented by a regular array of surface sites onto which gas molecules can adsorb. This is the approach used by Langmuir in 1915 [33]. Brunnaeur, Emmet and Teller extended Langmuir's model to include the adsorption of gas molecules onto already adsorbed molecules (multi-layer adsorption) by use of what is now known as the BET equation [34]. The Langmuir equation and its extension to the BET model can be derived as shown below.

The fundamental assumptions in the Langmuir model are:

- The surface is homogeneous and can be divided into a regular array of sites.
- Each site can accommodate one gas molecule.
- Interactions between gas molecules (adsorbate-adsorbate interactions) are negligible so that the probability that a particular site is filled is independent of whether surrounding sites are filled.

To derive the BET model, the following additional assumptions are required:

- Multi-layer adsorption can occur, so that each site can be filled with a stack of  $n$  molecules.
- The number of layers that can form is large.
- The enthalpy of adsorption into the second and subsequent layers is constant and is just the enthalpy of condensation of the gas.
- Similarly, the enthalpy of desorption from the second and subsequent layers is constant and is just the enthalpy of vaporisation of the gas.

For the derivations presented below, the following definitions apply:

- There are a total of  $N$  sites for adsorption on the surface.
- $\theta_n$  represents the fraction of sites covered with a stack of  $n$  molecules.
- $P$  is the measured pressure at equilibrium.
- $P_0$  is the saturation pressure for the gas.

- $k_{\text{ads}(n)}$  is the rate constant for adsorption of gas molecules into the  $n$ th layer.
- $k_{\text{des}(n)}$  is the rate constant for desorption of gas molecules from the  $n$ th layer.
- $K_n$  is the ratio of these two rate constants:  $K_n = k_{\text{ads}(n)} / k_{\text{des}(n)}$ . For the BET model,  $K_2$  and higher are all the same and hence can be represented by a single value,  $K$ .
- $V_M$  is the volume of gas required to form complete mono-layer coverage of the surface with gas molecules.
- $V_P$  is the volume of gas adsorbed by the adsorbent at equilibrium pressure  $P$ .

If  $V_G$  is the effective volume occupied by each gas molecule (i.e. the volume of an adsorption site) then the volume of gas required to fill all surface sites (i.e. form a mono-layer on the surface) is:

$$V_M = V_G N \sum_{n=0}^{n=L} \theta_n, \quad (2.2)$$

where  $\sum_{n=0}^{n=L} \theta_n = 1$  and  $L$  is the maximum number of adsorbed layers. Extending this to multi-layers gives the total volume of gas adsorbed onto the adsorbent at equilibrium as:

$$V_P = V_G N \sum_{n=0}^{n=L} n \theta_n. \quad (2.3)$$

Taking a ratio of the two volumes gives:

$$\frac{V_P}{V_M} = \frac{\sum_{n=0}^{n=L} n \theta_n}{\sum_{n=0}^{n=L} \theta_n}. \quad (2.4)$$

The rate of adsorption of gas molecules into the  $n$ th layer depends on both the pressure of the gas and the fraction of sites available (i.e. the fraction of sites filled with  $(n-1)$  gas molecules,  $\theta_{n-1}$ ). The rate of desorption of gas molecules from the  $n$ th layer

depends only on the fraction of sites filled with  $n$  layers,  $\theta_n$ . At equilibrium, the rates of adsorption and desorption are equal, giving:

$$k_{a(n)} P \theta_{n-1} = k_{d(n)} \theta_n \quad (2.5)$$

This rearranges to give a set of equations:

$$\theta_1 = K_1 P \theta_0 \quad (2.6)$$

$$\theta_2 = K P \theta_1 \quad (2.7)$$

$$\theta_3 = K P \theta_2 \quad (2.8)$$

$$\theta_4 = K P \theta_3 \quad \text{etc.} \quad (2.9)$$

If only mono-layer adsorption occurs (Langmuir model), then only the first expression applies. Under these conditions it can be shown (see Appendix B1) that the first expression gives the Langmuir model:

$$\frac{1}{V_p (P_0 / P)} = \frac{1}{V_M} \left( \frac{P}{P_0} \right) + \frac{1}{c V_M} \quad (2.10)$$

This equation says that for a solid that meets the assumptions used in the Langmuir model, a plot of  $[V_p (P_0 / P)]^{-1}$  vs relative pressure should be linear with a slope of  $(V_M)^{-1}$  and an intercept of  $(c V_M)^{-1}$ , where  $c = K_1 P_0$ .

If however multi-layer adsorption occurs (BET model), then the set of equations above give the BET equation (see Appendix B2):

$$\frac{1}{(P_0/P - 1) V_p} = \frac{1}{V_m c} + \frac{(c-1)}{V_m c} \left( \frac{P}{P_0} \right) \quad (2.11)$$

This equation implies that for a solid where the BET assumptions are valid, a graph of  $((P_0/P - 1)V_p)^{-1}$  vs  $(P/P_0)$  should be linear, and the slope and intercept can be used to determine the volume required for mono-layer coverage.

The Langmuir or BET surface areas of the solid can then be calculated from the mono-layer volumes obtained from the Langmuir and BET plots respectively, by assuming a fixed value for the cross-sectional area of the gas. Normally this cross-sectional area is obtained from the density of the liquid phase of the gas [27]. For  $N_2$ , the molecules are assumed to pack as spheres in a hexagonal close packed array. This gives a molecular cross-sectional area of  $0.16 \text{ nm}^2$  [35].

Both the Langmuir and BET models have limitations. If multi-layer adsorption occurs, then the Langmuir model should not be used. Conversely if there are restrictions on how many layers of gas molecules can be adsorbed (for example within pores of similar size to that of the gas molecules themselves) then the BET model breaks down. To overcome this limitation, some authors have derived modified BET equations for fixed numbers of layers [36]. The validity of this approach is questionable, both because the actual number of layers has to be arbitrarily selected and because interlayer interactions in small pores cannot be assumed to be constant. Both models also assume that interactions between adsorbate molecules within each layer are negligible. Thus both models are most appropriately applied when the relative pressure is low and hence the fraction of sites covered is also low. As the adsorbed sites are on average far apart under these conditions, they can be effectively treated independently. At higher relative pressures, particularly with the BET model, deviations from linearity are often seen. These deviations most likely result from increased adsorbate-adsorbate interactions. As a result, the BET model is generally used over a restricted range of partial pressures. For low surface area materials, it is often used up to a maximum relative pressure of  $\sim 0.35$ . For some nano-porous carbons, deviations from linearity occur at much lower relative pressures and hence some authors use only the data up to a relative pressure of 0.1 [37].



Recognizing these limitations, the two models can still be used to provide some useful information on different materials. In this thesis, the carbon materials can have significant quantities of nanoporosity. Where this occurs, multi-layer adsorption is severely restricted and, in the limit when the pore size is close to the size of the adsorbate molecule, it can be assumed that primarily mono-layer adsorption occurs. Thus for nanoporous carbons, the Langmuir surface area is more appropriate for analyzing adsorption.

The use of the two models to analyse two types of carbons prepared in this thesis is shown in Figure 2.2, where the isotherm data presented earlier in Figure 2.1, have been converted into Langmuir and BET co-ordinates. It is clear from this figure that the Langmuir model is linear for the nanoporous carbon, whereas for the mesoporous carbon, the BET model remains linear over a larger range than the Langmuir model. This figure also shows the BET model deviation from linearity above a relative pressure of  $\sim 0.35$ .

### 2.2.2 Dubinin Approach

The BET and Langmuir models rely on quite restrictive assumptions about the nature of the surface and the interactions between adsorbate molecules. A number of authors have tried alternative approaches. Of these, probably the most widely used in the analysis of porosity in carbon are those by Dubinin [38] and co-workers and, more recently, methods based on the results from density functional theory (DFT) modeling (which will be discussed in the next section).

The BET and Langmuir models were derived for solids where gas molecules interact with a homogeneous surface. Although this is a reasonable model for the external surface of a particle and the internal surface of a pore whose dimensions are large relative to the size of an adsorbate molecule, its validity in smaller pores is easily disputed.

A range of models has been developed to extract pore size distributions from adsorption isotherms by explicitly including the effects of pore walls. The simplest of these models are based on the Kelvin equation, which relates the reduced vapour pressure,  $P$ , of the curved surface of liquid condensed within a narrow pore to the radius

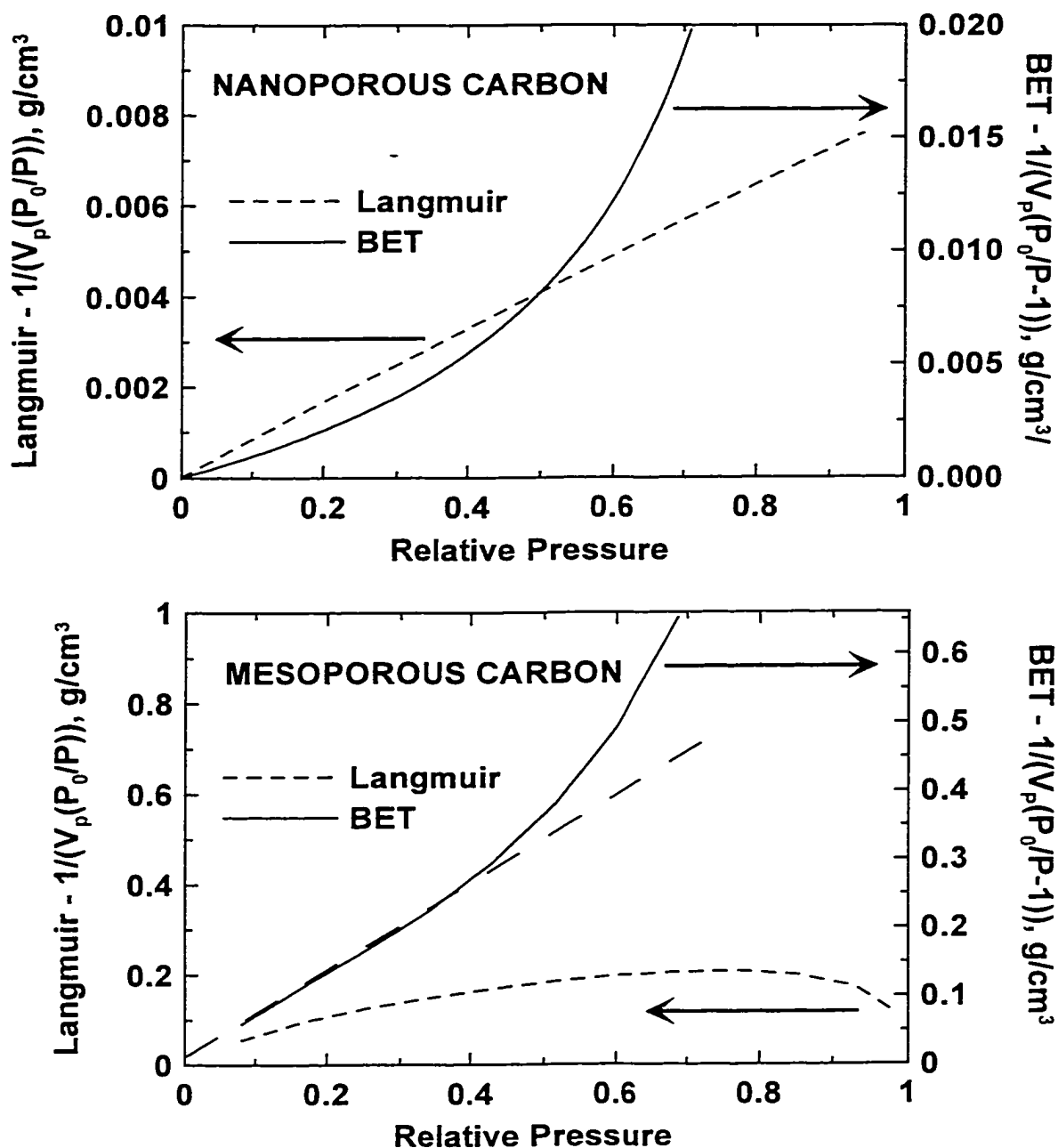


Figure 2.2: Calculated Langmuir (dotted line – left hand axes) and BET (solid line- right hand axes) plots for the nanoporous (upper graph) and meso/macroporous (lower graph) carbons calculated from the isotherm data (adsorption only) shown in Figure 2.1. The graph for the meso/macroporous carbon also contains a dashed line to show the linearity of the BET model at low relative pressures.

of curvature of the surface according to [39]:

$$RT \ln\left(\frac{P}{P_0}\right) = \frac{\gamma V}{R_m}, \quad - \quad (2.12)$$

where  $\gamma$  is the surface tension,  $V$  is the molar volume of the condensed vapour and  $R_m$  is the mean radius of curvature of the surface. This equation basically states that a vapour can condense in a narrow pore at a pressure much lower than the saturation pressure of the gas. This equation breaks down at low pressures – for example with a relative pressure of 0.001, at the boiling point of nitrogen, the predicted pore radius being examined is  $\sim 0.7 \text{ \AA}$ . This is too small for pores and yet in  $N_2$  gas adsorption measurements, significant quantities of gas are adsorbed at and below this pressure. Thus models based on the Kelvin equation are not reliable for measuring nanometre-sized porosity. The equation breaks down because the fluid inside the pore can no longer be considered to be homogeneous and because the interactions between the gas molecules and the pore walls become the most important parameters.

To overcome these limitations, models need to incorporate expressions to describe the adsorption potential induced by the pore walls. Probably the most widely used models are those derived by Dubinin and co-workers [40], [41]. These are based on Polanyi's adsorption theory. In this theory, the interaction between a surface and a gas phase is modeled by allowing gas molecules to fall into a potential well over the surface. As the gas molecules get closer to the surface, the fluid density increases as a result of the adsorption potential. If the gas is at a low temperature, it is likely that condensation will occur on the surface, and hence the adsorbate at equilibrium can be approximated by two phases – a condensed phase with vapour pressure  $P$  in equilibrium with a bulk gas phase of pressure  $P$  with a saturation pressure of  $P_0$ .

The net free energy change for moving a small amount of the adsorbate from the gas phase into the condensed phase must be zero when the adsorbate is at equilibrium. The molar free energy change to go from a gas of saturation pressure  $P_0$  to a condensed liquid with vapour pressure  $P$  is given by:

$$\Delta G = RT \ln \frac{P}{P_0}. \quad (2.13)$$

The adsorption potential,  $\bar{\varepsilon}_c$ , represents the work done by the adsorbate surface to move the gas molecules towards the surface. These two processes balance out, giving:

$$\varepsilon_c = -\Delta G = -RT \ln \frac{P}{P_0}. \quad (2.14)$$

Dubinin examined the relationship between the adsorption potential,  $\varepsilon_c$ , and the volume adsorbed at a given pressure for a range of materials and suggested that the isotherms for microporous carbons could be modeled by a Gaussian distribution of adsorption potentials. One form of the Dubinin equation is given by:

$$\frac{W}{W_0} = \exp(-k\Delta G^2/\beta^2) \quad (2.15)$$

where  $W$  is the volume adsorbed,  $W_0$  is the total micropore volume,  $\beta$  is the affinity constant that allows the curve for one adsorbate to be superimposed on another and  $\Delta G$  is called the differential molar free energy of adsorption. It has been shown [42] that the Dubinin equation actually corresponds to a Rayleigh distribution of adsorption potentials.

The Dubinin equation can be rewritten as:

$$\log W = \log W_0 - D \log^2(P/P_0), \quad (2.16)$$

and thus an appropriate plot of volume adsorbed vs relative pressure can be used to determine the total micropore volume. This still does not provide any information on the distribution of pore sizes. In order to extract pore size distributions, there is a need to perform a data transform based on an assumption of the shape of the distribution of micropore sizes [43]. DFT methods provide an alternative method for extracting pore size distributions by calculating the adsorption isotherms expected for a set of pore sizes

and then combining these isotherms through least squares minimisation to generate an overall isotherm that fits the experimental curve. This seems to be a logical approach but it is only recently that the calculation methods and computing power have been developed to make this possible. In this thesis the DFT approach has been chosen in preference to the Dubinin approach for calculating pore size distributions.

### 2.2.3 DFT Methods

The basic problem in gas adsorption analysis is to determine how gas molecules interact with solid surfaces, either at an external surface or in a partly enclosed space such as a pore. The density functional approach to this problem involves establishing an expression for the potential energy of the gas as a function of position (the grand potential function). Through an iterative approach, this grand potential is then minimised in order to obtain the equilibrium gas density profile for a given gas reservoir chemical potential. The grand potential function can be written as [44], [45], [46]:

$$\Omega_v[\rho(\mathbf{r})] = A[\rho(\mathbf{r})]_{hs} + A[\rho(\mathbf{r})]_{gg} + \int (V(\mathbf{r}) - \mu) \rho(\mathbf{r}) d\mathbf{r}. \quad (2.17)$$

In this expression,  $A$  is the Helmholtz free energy of the gas, which depends only on the density of the gas,  $\rho(\mathbf{r})$ , at the position specified by the vector  $\mathbf{r}$ . The Helmholtz free energy is used because gas adsorption is normally measured in a fixed volume. The mean-field theory used in the calculations divides the interactions between gas molecules into the first two terms. The first term represents the repulsive forces between gas molecules and is approximated by a hard spheres model. The second term is the summation of the long-range attractive forces between pairs of gas molecules. The third term corresponds to the potential energy due to attractive forces between the solid surface and the gas molecules,  $V(\mathbf{r})$ . The chemical potential,  $\mu$ , of the gas reservoir is included in this term as a reference point.

The first term can be handled by use of a local density approximation (LDA). This approximation says that the free energy density of a given location is simply the

product of the density at that point and the average free energy for a homogenous reference state represented by the gas reservoir. This removes short-range correlations, which can lead to smoothing of the details close to the surface where layers of gas molecules can form. It is therefore necessary to reintroduce some short-range correlation in order to accurately model adsorption close to the surface. This introduces another term that will not be discussed here.

The second term can be modeled by a summation of Lennard-Jones 6-12 potentials. This term is included as a perturbation to the hard spheres model used to calculate the repulsive forces between gas molecules. Although the Lennard-Jones potential of the second term includes a repulsive component at small separations, this feature is not used. It appears that this methodology is used to simplify the model and presumably reduce computation time. The potential energy interaction between the gas molecules and the surface in the third term can also be modeled with a Lennard-Jones potential.

Through an iterative process, the calculated grand potential equation can be minimised using an appropriate algorithm. This then gives an equilibrium distribution for gas density. For a pore structure represented by two walls, the resultant density distribution can be converted to a volume adsorbed by integrating from one wall to the other. Repeating this process for different gas pressures (by changing the chemical potential of the reservoir) allows the volume of gas adsorbed in a model slit shaped pore of width  $r$  to be calculated as a function of gas pressure. This is in effect a gas adsorption isotherm for a model pore size. Repeating the process again for a range of pore widths generates a series of model adsorption curves.

Figure 2.3 shows the results of a DFT calculation for argon adsorption into pores of different widths where short-range correlations have been explicitly included. Nitrogen adsorption isotherms calculated without the short-range correlations [46] show similar trends.

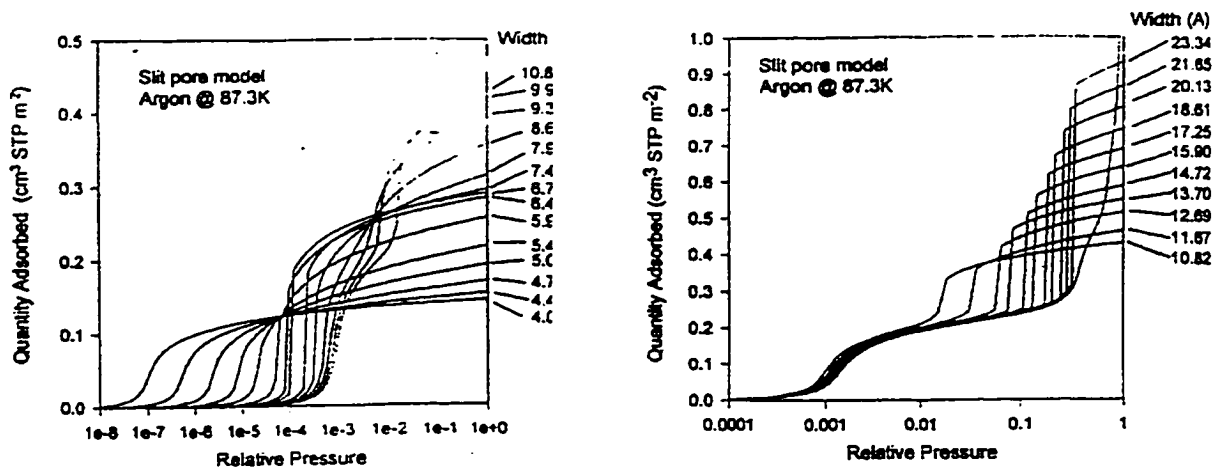


Figure 2.3: Argon adsorption isotherms for different pore widths calculated through DFT algorithms. Taken from [45].

The manufacturers of gas adsorption porosimeters have completed all of this modeling work and include the model isotherms with the DFT software. Thus, when the user performs a DFT analysis, all that occurs is that the following function is minimised using a least squares algorithm:

$$\sum_p \left( V(P) - \sum_j C_j Q(P)_j \right)^2, \quad (2.18)$$

where  $V(P)$  is the experimental volume adsorbed at pressure  $P$ ,  $Q(P)_j$  is the calculated volume adsorbed at pressure  $P$  for the  $j$ th model isotherm, and  $C_j$  is a coefficient effectively describing how much of the contribution from the  $j$ th model isotherm should be included. Once the best fit has been obtained, the pore size distribution can be calculated by summing the volume adsorbed at each pressure for each of the model isotherms multiplied by the appropriate coefficient.

Figure 2.4 shows the results of such a DFT optimisation performed on the two carbon isotherms from Figure 2.1. It can be seen the agreement between the experimental and fitted isotherms is excellent. Also, the pore size distributions extracted from the data clearly show the presence of a narrow distribution of nanopores in the nanoporous carbon and the presence of meso and macropores in the mesoporous carbon.

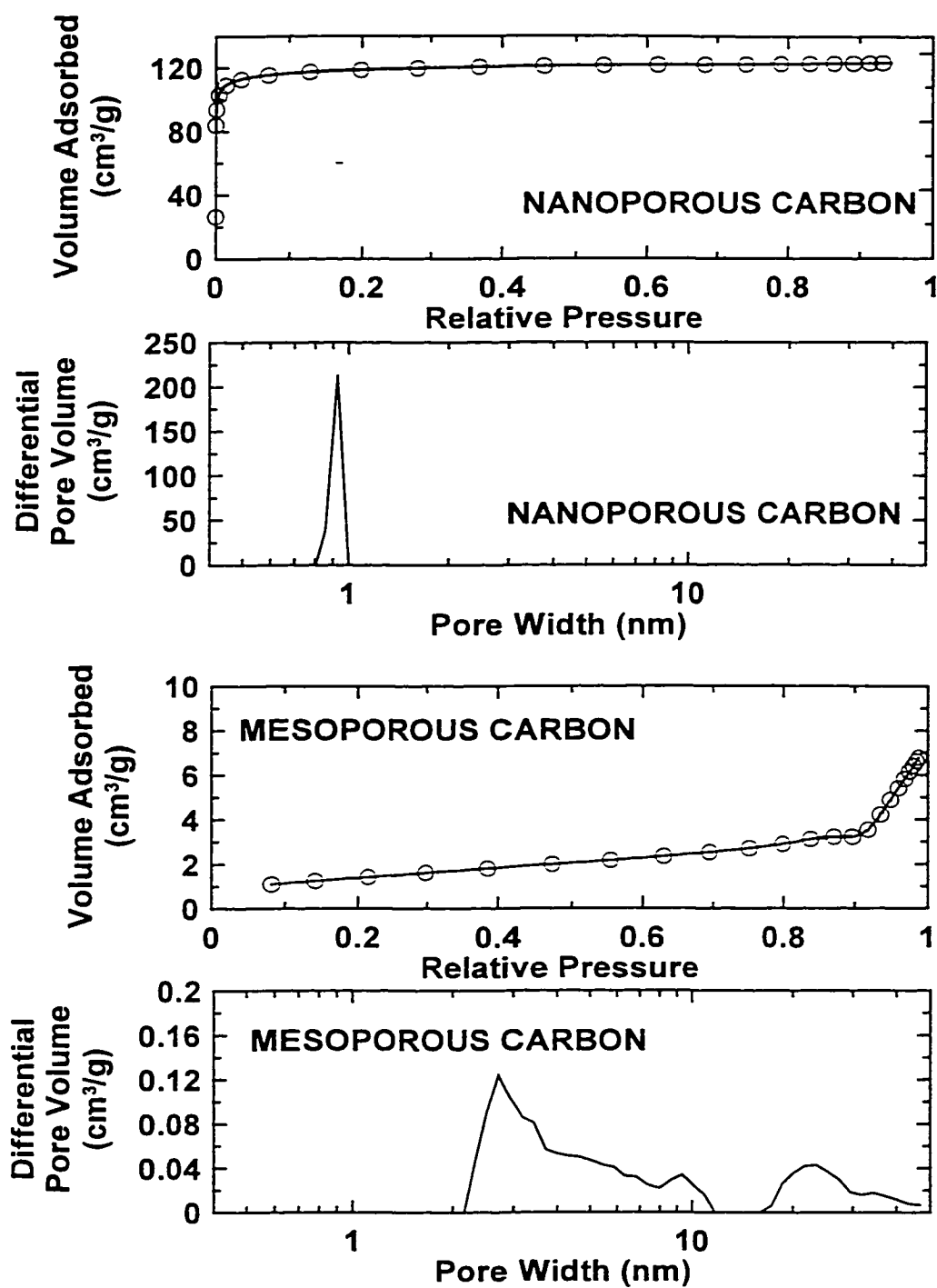


Figure 2.4: DFT fits and calculated pore size distributions obtained for the nanoporous (upper graphs) and mesoporous (lower graphs) carbons. In the isotherm plots, the experimental data are shown with circles, the fit with a solid line.



Based on the information presented in this chapter, the DFT method was selected for analysing the gas adsorption isotherms measured for this thesis, particularly as the slit shaped pore model, based on an infinite carbon sheet, was developed specifically for analysing carbon structures. In addition to the DFT model, Langmuir (for nano-porous carbons) and BET surface area values will be quoted in order to allow for rapid comparison of a range of samples. The higher the calculated surface area, the more porosity is present in the material being measured.

### 2.3 Experimental

All gas adsorption measurements were completed with a Micromeritics ASAP 2010 gas adsorption porosimeter equipped with a turbo pump. The ASAP 2010 is a volumetric porosimeter that measures initial and equilibrium pressures for each point on the isotherm. Essentially the ideal gas law is then used to determine the volume of gas adsorbed for a given equilibrium pressure. Figure 2.5 presents a schematic diagram of the main parts of the porosimeter. It comprises a sample tube of volume  $V_T$  containing a known mass of sample and connected to a manifold of volume  $V_M$  (calibrated with a machined and polished steel sphere) through a solenoid valve. The volume of the tube was determined by dosing the manifold with a known pressure of helium gas and then measuring the pressure in the manifold before and after the solenoid valve was opened to the empty tube. After the sample was degassed under vacuum and elevated temperature, it was immersed in a bath of constant temperature (in this case 77 K, the boiling point of nitrogen). With the solenoid valve closed, the manifold was dosed with adsorbate ( $N_2$ ) to a user-defined pressure. The valve to the sample was then opened and the pressure in the manifold/tube was recorded as a function of time. When the rate of change of pressure dropped below a user selected value (in this case  $< 0.01$  %/min over 20 s time intervals), the pressure was recorded and the process was then repeated with a higher manifold pressure.

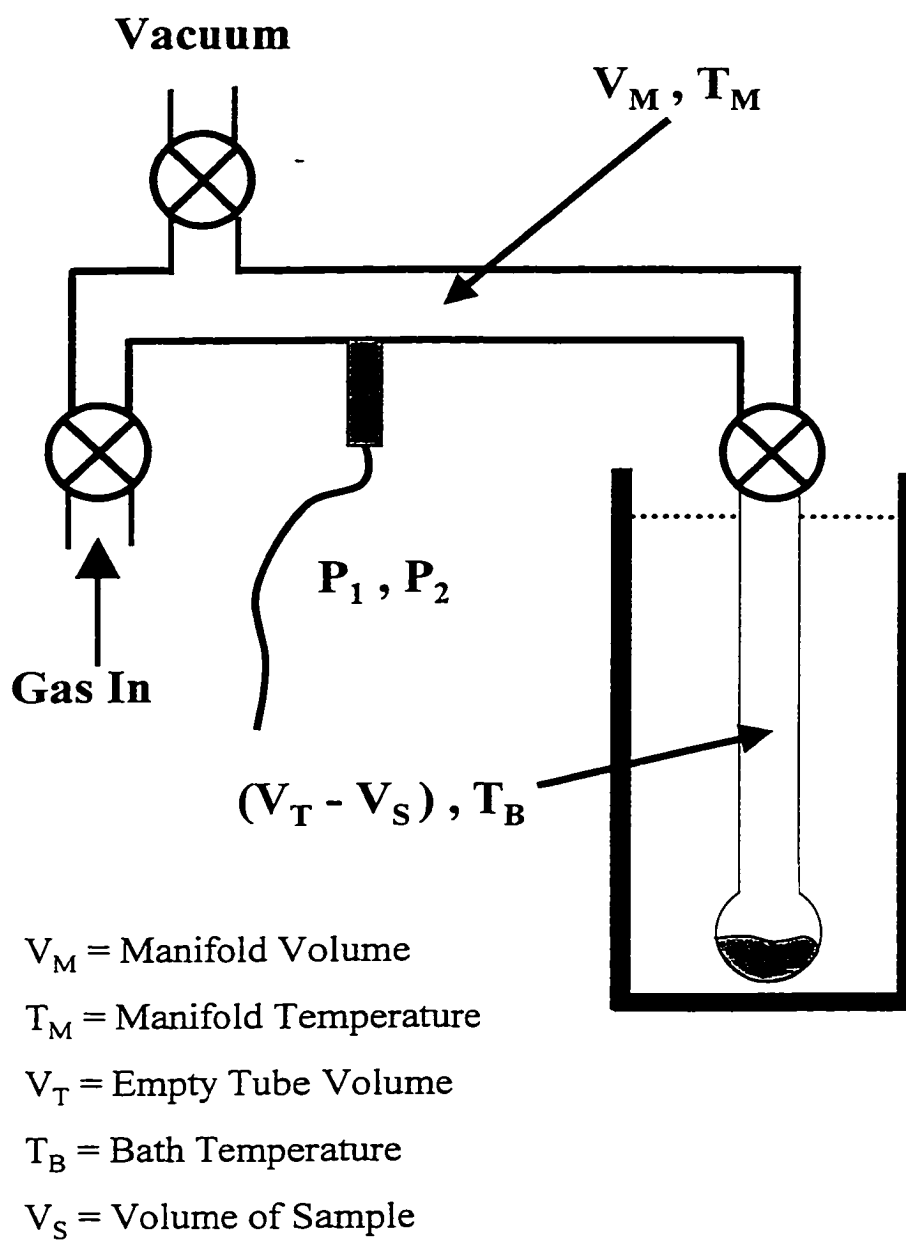


Figure 2.5: Schematic diagram of ASAP 2010 Gas Adsorption Porosimeter.

The following experimental procedure was used for all samples:

A clean, dry glass sample tube was evacuated at 250°C to remove any adsorbed gases then backfilled with helium (UHP grade, Air Liquide) before being weighed and then filled with approximately 1 g of powdered sample. It was placed back on the degassing station and evacuated, again at 250°C to remove any adsorbed species such as moisture from the carbon. Evacuation was continued until the outgas rate from the sample was indistinguishable from that of the empty tube. This required at least 24 hours per sample. The tube was again backfilled with helium and re-weighed, to determine the mass of clean sample in the tube. It was then placed on the analysis station (which was connected to the turbo pump) and re-evacuated at elevated temperature until the outgas rate was the same as that from the manifold of the porosimeter (generally < 60µm Hg/min).

After degassing, the sample tube was immersed in a constant temperature bath and allowed to equilibrate whilst under vacuum. Liquid nitrogen was used to maintain the sample at the boiling point of nitrogen during analysis. UHP nitrogen from Air Liquide was used as the analysis gas.

Adsorption analysis was completed up to a relative pressure of 0.95. After this, desorption data were measured by evacuating the manifold to a pressure lower than the equilibrium pressure of the previous point then allowing the gas to re-equilibrate with the sample valve open. The volume adsorbed/desorbed for a given equilibrium partial pressure was determined with the ideal gas law after correcting the data for the freespace in the tube and the non-ideal gas behaviour of the adsorbate.

## Chapter 3

### X-ray Scattering

The previous chapter summarised the use of gas adsorption techniques for the analysis of the physical structure of solids. In this chapter it will be shown that the results from such studies can be complemented by small-angle x-ray scattering studies. In addition it will be shown how wide-angle x-ray scattering can be used to partially understand the atomic structure of non-crystalline materials.

It is useful to begin discussions of x-ray scattering from solids by discussing how x-rays interact with matter. The fundamental principle involved is that x-rays are scattered in all directions when they interact with electrons, with the scattered radiation having the same wavelength as the incident radiation (some fraction of the incident beam is also inelastically scattered giving rise to Compton modified scattering of longer wavelengths) [47]. If a beam of x-rays is directed towards a sample and the intensity of the scattered beam is measured, then it is found that, for certain angles, the scattered intensity is higher than the background because constructive interference occurs between the waves scattered from different locations within the sample. Constructive and destructive interference effects can occur because the wavelengths of x-rays are of the same order of magnitude as the scale of fluctuations in electron density in a material. When highly crystalline materials are studied, the scattering pattern usually contains a number of sharp peaks of varying intensity. These peaks can be used to identify the content and dimensions of the unit cell - the basic repeating structure of the crystal. This is referred to as x-ray diffraction. In disordered materials such as most carbons, the scattering pattern contains broad peaks superimposed on a background. These data can

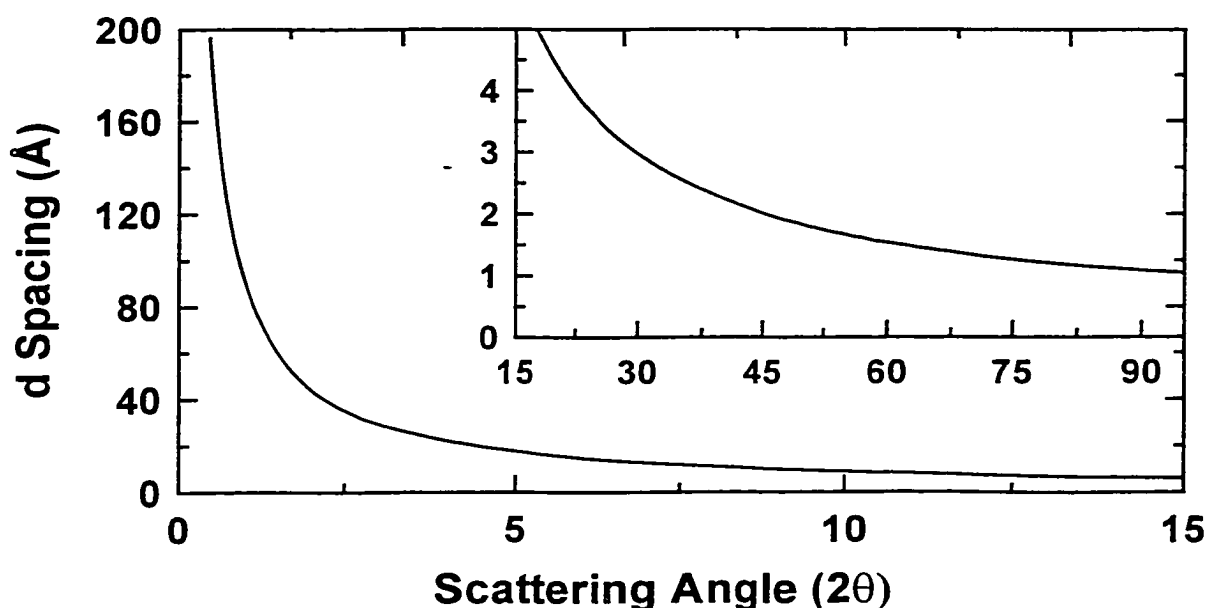


*Figure 3.1: The relationship between scattering angle and inter-atomic spacing for x-ray diffraction derived from the Bragg equation. These data were calculated with a wavelength of 1.5415 Å. The main graph shows d-spacings for small angles whilst the inset presents d-spacings for high (wide) angles.*

be used to determine the approximate size and average structure of partially ordered domains in the solid.

The Bragg equation for x-ray diffraction,

$$\lambda = 2d_{hkl} \sin \theta, \quad (3.1)$$

relates the spacing,  $d_{hkl}$ , between atomic planes, to the angle ( $2\theta$ ) at which constructive interference occurs between the waves scattered by those planes, for a given wavelength of incident radiation,  $\lambda$ . As the scattering angle increases, the inter-atomic distances being examined decrease, as shown in Figure 3.1. The Bragg equation was derived for crystals where the atom locations are well-defined and can be represented by theoretical planes of fixed spacing. It can, however, be used to give an indication of the approximate

length scale of electron density fluctuations that would be required to generate constructive interference in a beam scattered through a given angle.

Normally measurements made at small angles are analysed separately from those made at large angles because the length scales involved provide different information. It can be seen that, at low angles, the length scales are large relative to atomic dimensions (eg 10 - 1000 Å). This is the realm of small-angle x-ray scattering (SAXS) – one of the few experimental techniques capable of resolving structure on this scale. Thus SAXS (and small-angle neutron scattering - SANS) techniques can be used to measure dimensions that are not easily studied by other techniques. For example, SAXS techniques have been used to study the dimensions of micelles [48] and proteins [49] in solution, grain sizes of catalysts [50], and particle sizes [51] and pore structures in carbon materials [52], [53].

Figure 3.1 also shows that wide-angle x-ray scattering (WAXS) measurements provide information on inter-atomic electron density fluctuations. Wide-angle measurements are therefore used to understand the local arrangement of atoms (the average local arrangement for amorphous materials).

### 3.1 General Theory of Scattering

The theory behind x-ray scattering measurements starts with scattering from individual electrons and atoms. According to classical electromagnetic theory, when an x-ray beam encounters an electron, the oscillating electric field of the beam causes the electron to oscillate with the same frequency as the incident beam. During this oscillatory motion, the electron accelerates and decelerates rapidly, emitting radiation with the same wavelength and frequency as the incident beam. The electric field vector of an unpolarized incident beam takes all orientations in a plane perpendicular to the direction of travel with equal probability. The electron therefore sees the electric field restricted to a plane and hence oscillates within the same plane. As the amplitude of the scattered beam depends on the magnitude of the acceleration vector impinging on the electron, the scattered intensity (which is just the square of the amplitude) depends on the

angle at which it is measured. This angular dependence of the intensity of radiation scattered by an electron at an angle of  $2\theta$  to the incident beam was first worked out by J.J. Thompson and can be expressed as [47]:

$$I_{2\theta} \propto \frac{I_0}{r^2} \left( \frac{1 + \cos^2 2\theta}{2} \right), \quad (3.2)$$

where  $I_0$  is the intensity of the incident beam,  $r$  is the distance from the electron to the point of observation and the angular term is known as the polarization factor.

Scattering from an atom can be viewed as the sum of scattering from a distribution of electrons. In addition to the effect of polarization on scattered intensity, the amplitude of the resultant scattered beam from an atom changes with scattering angle because of interference effects between the waves scattered from different electrons in the atom. The atomic scattering factor,  $f(\sin\theta/\lambda)$  allows an atom to be treated as a point source. This factor relates the scattering amplitude at a given angle,  $\theta$ , to the magnitude of scattering from a single electron when the scattering angle is  $0^\circ$ . Empirical equations have been generated to fit atomic scattering factors calculated with Hartree-Fock methods for most elements and ions. In this work, the atomic scattering factor equation derived in reference [54] will be used. For x-rays of wavelength  $\lambda$ , this equation is:

$$f(\sin\theta/\lambda) = \sum_{i=1}^{i=4} a_i e^{-b_i (\sin\theta/\lambda)^2} + c \quad (3.3)$$

The coefficients for the elements of interest in this thesis are shown in Table 3.1. These coefficients produce the curves shown in Figure 3.2 for the three elements. It can be seen that, at low angles, the magnitude of the scattering factor is close to the number of electrons in the element and that it decreases gradually with angle. This decrease occurs because of increasing destructive interference of waves scattered by electrons in different positions around the nucleus as the angle increases. For SAXS measurements, the error introduced by assuming the scattering factor remains constant as a function of

scattering angle is small, simplifying the calculation process. For WAXS calculations however, this factor needs to be explicitly included.

*Table 3.1: Atomic Scattering Factor Co-efficients [54].*

	Lithium	Carbon	Sodium
$a_1$	1.12820	2.31	4.7626
$a_2$	0.750800	1.02	3.1736
$a_3$	0.617500	1.5886	1.2674
$a_4$	0.465300	0.865	1.1128
$b_1$	3.95460	20.8439	3.285
$b_2$	1.05240	10.2075	8.8422
$b_3$	85.3905	0.5687	0.3136
$b_4$	168.261	51.6512	129.424
$c$	0.037700	0.2156	0.0676

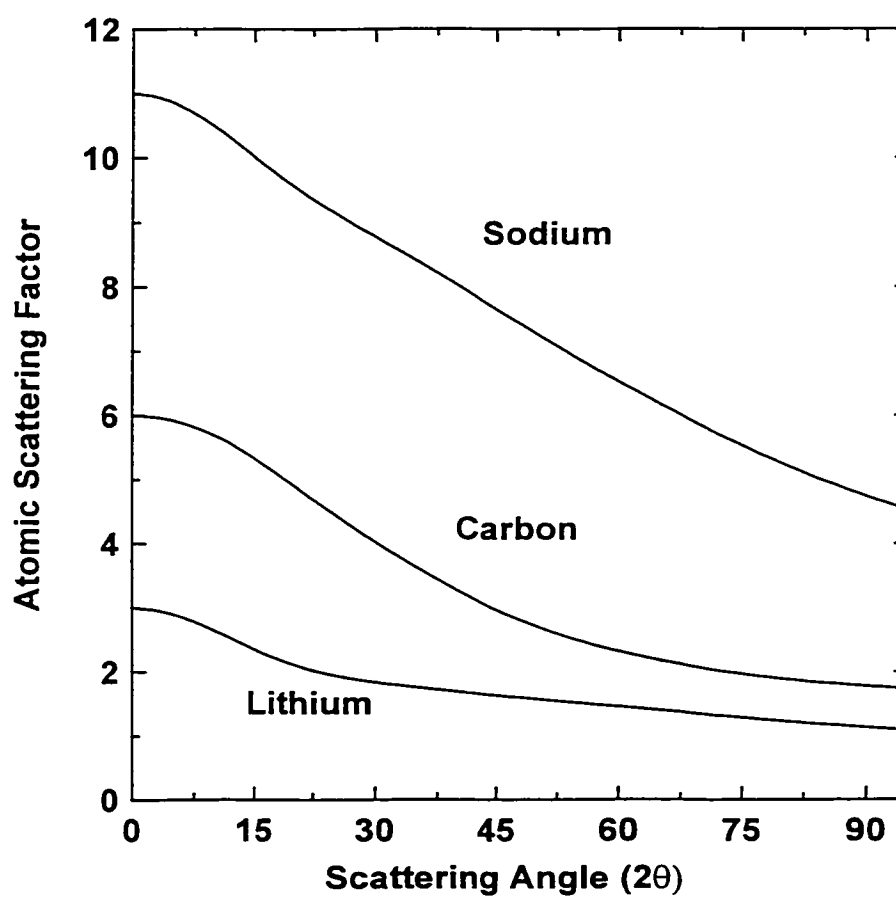


*Figure 3.2: Atomic scattering factors for lithium, carbon and sodium.*



In x-ray scattering measurements, the beam intensity is measured as a function of angle to the incident beam. The intensity is the product of the amplitude of the scattered beam and its complex conjugate. With the scattering vector,  $\mathbf{q}$ , defined by  $\mathbf{q} = 2\pi(\mathbf{s}_1 - \mathbf{s}_0)$ , where  $\mathbf{s}_0$  and  $\mathbf{s}_1$  are vectors describing the incident and scattered beams respectively, the amplitude of the scattered beam is:

$$A(\mathbf{q}) = f_e \sum_{\mathbf{r}} f_r e^{-i \mathbf{q} \cdot \mathbf{r}}, \quad (3.4)$$

where  $\mathbf{r}$  is the vector between a given point and an arbitrary origin,  $f_r$  is the angularly dependent atomic scattering factor for the atom located at  $\mathbf{r}$ ,  $f_e$  represents the scattered amplitude from a single electron and the sum extends over all of the sample. The magnitude of the scattering vector is given by  $q = 4\pi \sin \theta / \lambda$ . An alternative form for equation 3.4 can be generated by replacing the sum with an integral and the scattering factor by a continuous electron density function,  $\rho(\mathbf{r})$ :

$$A(\mathbf{q}) = f_e \int \rho(\mathbf{r}) e^{-i \mathbf{q} \cdot \mathbf{r}} dV. \quad (3.5)$$

In this thesis, the first expression will be used to develop the WAXS theory, whilst both terms will be used to derive the theory behind SAXS data analysis.

## 3.2 Theoretical Analysis of Small-angle X-Ray Scattering

For this thesis, SAXS was used to study nano-scale porosity in the carbons produced and to show that these pores provide sites for the electrochemical insertion of sodium (and lithium) atoms. The theory presented below is designed to provide the reader with an introduction to some of the principles of small-angle scattering and to show how information on porosity in solids can be extracted from experimental curves using a standard function. This function will then be used in later chapters to analyse the

nano-structure of carbon materials. The excellent text by Guinier and Fournet [50] provides a more comprehensive and detailed (although highly mathematical) treatment of the small-angle scattering behaviour of a range of structures. For this derivation it will be assumed that the scattering centres are isotropically distributed about a centre of symmetry. In a large sample illuminated by a typical x-ray beam of mm dimensions this assumption is reasonable.

The amplitude of scattering from a single scatterer (equation 3.4) can be rewritten as:

$$A(\mathbf{q}) = \sum_{\mathbf{p}} f_{\mathbf{p}} e^{-i\mathbf{q} \cdot \mathbf{r}_{\mathbf{op}}} , \quad (3.6)$$

where  $\mathbf{q}$  is the scattering vector and  $\mathbf{r}_{\mathbf{op}}$  is a vector between an arbitrary origin, O, and a point, P, in the scatterer. To simplify later steps, this origin will be located at the centre of the scatterer. Equation 3.6 therefore represents the resultant amplitude emerging from the centre of the scatterer, or in x-ray terms, as the form factor  $F(\mathbf{q})$  of the scatterer (if it is assumed that the scatterer has a centre of symmetry, then this simplifies to  $F(\mathbf{q}) = \sum_{\mathbf{p}} f_{\mathbf{p}} \cos(\mathbf{q} \cdot \mathbf{r}_{\mathbf{op}})$ , which would give an intensity of  $F(\mathbf{q})^2$  from a single scatterer).

Using equation 3.6 for the form factor of a given scatterer and selecting the origin, O, as the origin for an ensemble of scatterers, the resultant amplitude from this ensemble of scatterers is the sum over all scatterers:

$$A(\mathbf{q}) = \sum_{\mathbf{j}} F(\mathbf{q})_{\mathbf{j}} e^{-i\mathbf{q} \cdot \mathbf{r}_{\mathbf{oj}}} , \quad (3.7)$$

where  $F(\mathbf{q})_{\mathbf{j}}$  is the form factor (resultant amplitude) of the Jth scatterer and  $\mathbf{r}_{\mathbf{oj}}$  is the vector between the centre of the scatterer selected to hold the origin for the ensemble, and the centre of the Jth scatterer. The scattered intensity from an ensemble of scatterers is then:

$$I(\mathbf{q}) = A(\mathbf{q})A(\mathbf{q})^* = \sum_{\mathbf{j}} F(\mathbf{q})_{\mathbf{j}} e^{-i\mathbf{q} \cdot \mathbf{r}_{\mathbf{oj}}} \sum_{\mathbf{k}} F(\mathbf{q})_{\mathbf{k}} e^{i\mathbf{q} \cdot \mathbf{r}_{\mathbf{ok}}} \quad (3.8)$$

If the scatterers are assumed to be distributed centrosymmetrically, this intensity expression simplifies to:

$$I(\mathbf{q}) = \sum_K \sum_J F(\mathbf{q})_K F(\mathbf{q})_J \cos \mathbf{q} \cdot (\mathbf{r}_{OJ} - \mathbf{r}_{OK}) \quad (3.9)$$

The vector  $\mathbf{r}_{OJ} - \mathbf{r}_{OK}$  is the same as the vector between the two scattering centres,  $\mathbf{r}_{JK}$ . Substituting this vector into 3.9 and separating out the terms where the summation indices are equal gives:

$$I(\mathbf{q}) = \sum_K F(\mathbf{q})_K^2 + \sum_K \sum_{J \neq K} F(\mathbf{q})_K F(\mathbf{q})_J \cos(\mathbf{q} \cdot \mathbf{r}_{JK}). \quad (3.10)$$

The first term is simply the sum of the intensities of each of the scatterers, whilst the second is the intensity resulting from interactions between the scatterers. If the scatterers are randomly distributed and both  $r$ , the average spacing between the scatterers, and the number of scatterers are relatively large then, for all experimentally observable angles (i.e.  $q > 0$ ), there will be approximately the same number of positive and negative cosine terms. This causes the second term to average to zero, which leads to an important principle for small-angle scattering that greatly simplifies the mathematics involved in treating such an arrangement of scatterers:

*For widely separated, randomly distributed scatterers the observed intensity is simply the sum of the scattered intensity from each scatterer.*

This principle will be used later, but first it is worth considering how the scattered intensity varies with the size of the scatterer. This is best done by analysing the scattering from a sphere of uniform electron density, where exact solutions can be readily derived. Even though the analysis below is for spheres, the general trends identified also apply to objects with different shapes.

### 3.2.1 Scattering from a sphere

Switching to the integral equation (3.5) of the scattered amplitude (as this can be solved exactly for a sphere), the amplitude of scattering from a sphere of radius  $R$ , with constant electron density,  $\rho_{\text{avg}}$ , is:

$$A(\mathbf{q}) = \rho_{\text{avg}} \int_{r=0}^{r=R} e^{-i\mathbf{q}\cdot\mathbf{r}} dV, \quad (3.11)$$

where the dependence of the form factor on scattering angle has been ignored as it is negligible over the small-angle region. The solution to this equation is (see derivation in appendix B3):

$$I(\mathbf{q}) = (3\rho_{\text{avg}}V)^2 \left[ \frac{(\sin(qR) - qR \cos(qR))}{(qR)^3} \right]^2, \quad (3.12)$$

where  $V$  is the volume of the sphere. Writing the equation this way separates it into two terms; the first accounts for the size of the sphere through its volume dependence whilst the second describes scattering normalised so all spheres give the same value at  $q = 0$ . This second term will be referred to as the normalised intensity. Figure 3.3 shows how this normalised intensity varies with sphere radius. The calculated intensities represent a moving average over 5 points, where the increment in  $q$  was  $0.001 \text{ \AA}^{-1}$ . This averaging was performed to smooth out rapid oscillations in the data and to provide calculated curves similar to those expected from the resolution of experimental diffractometers.

There are a number of useful concepts that can be extracted from this set of curves and the associated equation. Firstly, the normalised intensity for all sphere sizes approaches  $\sim 0.11$  at a scattering angle of zero ( $q = 0$ ). This is to be expected as, at  $q = 0$ , all scattered radiation is in phase and hence no destructive interference takes place. Thus, for the limit when  $q = 0$ , the total scattered intensity would be a direct measure of the particle volume (although it is not experimentally observable). The value of  $\sim 0.11$

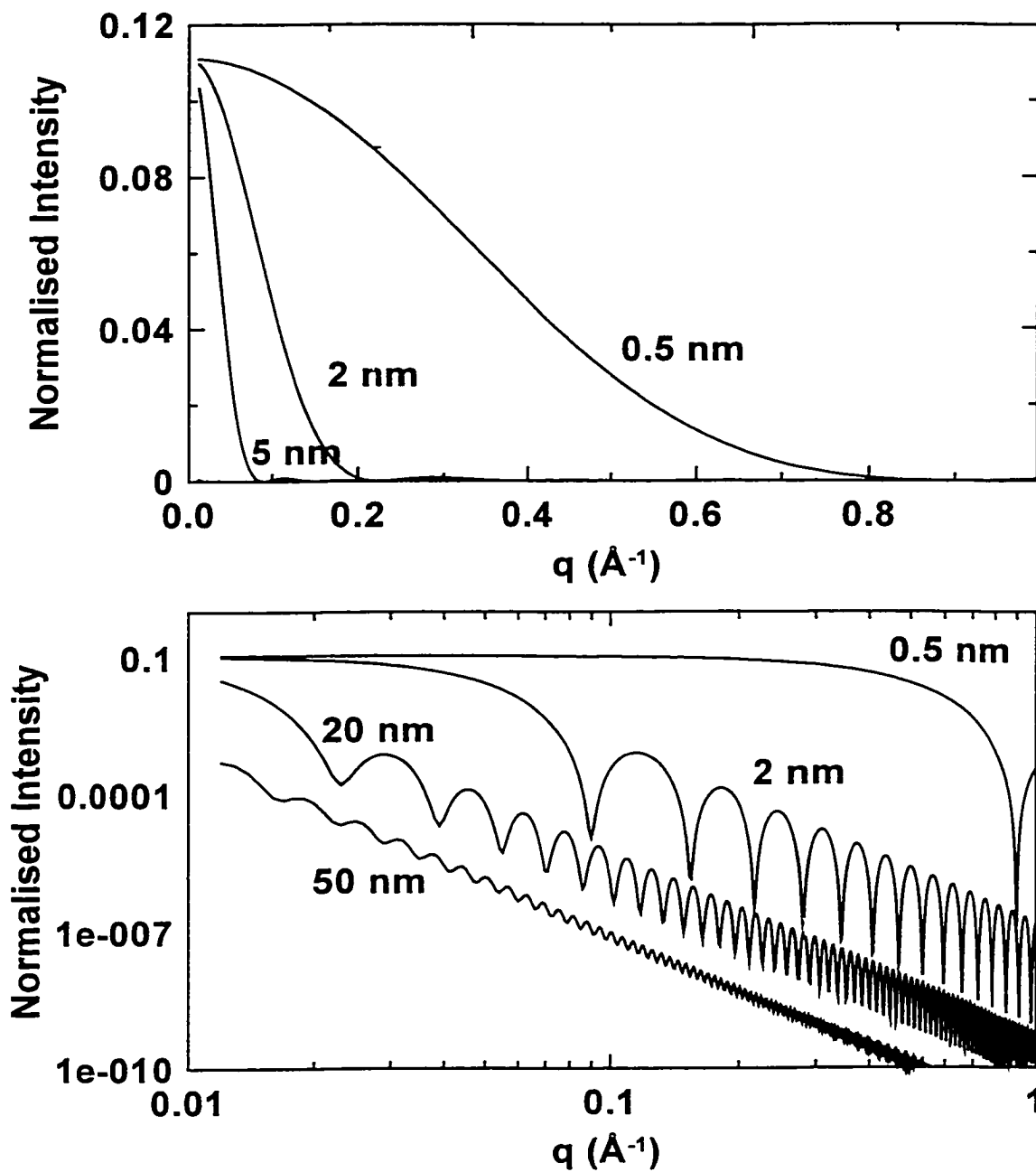


Figure 3.3: Calculated normalised intensity for different sized spheres. Upper panel – linear plot, lower panel – log-log plot.

actually corresponds to 1/9 and can be determined by expanding the trigonometric terms in equation 3.12 as Taylor series (taking only the first two terms of the expansions):

$$\left[ \frac{(\sin(qR) - qR \cos(qR))}{(qR)^3} \right]^2 = \frac{1}{(qR^3)^2} \left[ qR - \frac{(qR)^3}{3!} - qR \left( 1 - \frac{(qR)^2}{2!} \right) \right]^2 \quad (3.13)$$

$$\left[ \frac{(\sin(qR) - qR \cos(qR))}{(qR)^3} \right]^2 = \frac{1}{(qR^3)^2} \left[ \frac{(qR)^3 - 3(qR)^3}{6} \right]^2. \quad (3.14)$$

Thus:

$$\lim_{q \rightarrow 0} \left( \frac{(\sin(qR) - qR \cos(qR))}{(qR)^3} \right)^2 = \frac{1}{9}. \quad (3.15)$$

The curves also show that, for  $q$  values greater than  $0.02 \text{ \AA}^{-1}$  ( $2\theta$  scattering angle  $\sim 0.3^\circ$ ), the normalised intensity decreases dramatically as the size of the sphere increases. This means that for equal volumes of small and large scatterers, the scattered intensity from the small scatterers at experimentally measurable angles will be orders of magnitude higher than that from the large scatterers. Even if there is only a low volume fraction of small scatterers (for example a particle of  $\sim \mu\text{m}$  size containing  $\sim 1 \text{ vol\%}$  of nanometre sized void space), the scattering from the large object can effectively be ignored.

Another feature apparent in the log-log plot of Figure 3.3 is that, (recognising that the oscillations may not be resolved experimentally), the scattered intensity from the larger centres decreases in a linear fashion with increasing scattering angle, with the linear portion of the curve extending to lower angles as the sphere size increases. This behaviour is known as Porod's law behaviour and results from the limiting behaviour of equation 3.12 when  $qR \gg 1$ . In this region, the sine term is negligible and the remaining squared cosine term oscillates so rapidly that it is reasonable to approximate it by an average value of 0.5. These oscillations would not be easily resolved in an experiment

because they would occur over an angular range that is smaller than the resolution of the equipment and because real objects contain a distribution of scattering sizes that would smooth out the curve.

Equation 3.16 shows the form of the scattered intensity when  $qR \gg 1$ .

$$I(q) = \frac{9(f(q)\rho_{\text{avg}}V)^2}{2(qR)^4}, \quad (3.16)$$

which can also be written as:

$$I(q) = \frac{2\pi f(q)^2 \rho_{\text{avg}}^2 S}{q^4}, \quad (3.17)$$

where  $S$  is the surface area of the scatterer. Taking logs of both sides gives:  $\log(I(q)) = \log(2\pi f(q)^2 \rho_{\text{avg}}^2 S) - 4 \log q$ , a linear expression in  $q$  with slope of  $-4$  and an intercept related to the surface area of the scatterer. This is the observed Porod's law behaviour. From this derivation, it can be seen that if a plot of  $\log(\text{intensity})$  vs  $\log(q)$  contains a linear region, with a slope of  $\sim -4$ , then it can be assumed that the size of the scattering object is large relative to the magnitude of  $q^{-1}$ . In other words,

*As the size of an object increases, the normalised intensity decreases rapidly and starts showing Porod's law limiting behaviour at high  $q$ .*

Combining this feature with the concept of independent scattering from widely separated scatterers, allows us to examine the theoretical scattering from a useful arrangement of scatterers: a large number of small pores (widely separated, with electron density  $\rho_p$ ) embedded in a large matrix (electron density  $\rho_m$ ).

### 3.2.2 Scattering from a distribution of pores

Defining the electron density contrast,  $\eta_r$ , as:

$$\eta_r = \rho_r - \rho_m, \quad (3.18)$$

gives the electron density contrast in pores,  $\eta_p$ , and the matrix,  $\eta_m$ , as  $\eta_p = -\rho_m$  and  $\eta_m = 0$  respectively. This allows the scattering amplitude to be written as:

$$A(\mathbf{q}) = \int (\rho_m + \eta_r) e^{i\mathbf{q}\cdot\mathbf{r}} dV = \int \rho_m e^{i\mathbf{q}\cdot\mathbf{r}} dV + \int \eta_r e^{i\mathbf{q}\cdot\mathbf{r}} dV. \quad (3.19)$$

This shows that the amplitude can be separated into two independent terms. The first term involves scattering from a continuous matrix phase whilst the second term is just the amplitude expected for a group of widely separated small particles (as the term disappears when the point  $\mathbf{r}$  is in the matrix phase). The scattered intensity can be obtained by multiplying the amplitude expression by its complex conjugate. This generates four terms:

$$I(\mathbf{q})_1 = \int_{V_1} \rho_m e^{-i\mathbf{q}\cdot\mathbf{r}_1} dV_1 \int_{V_2} \rho_m e^{i\mathbf{q}\cdot\mathbf{r}_2} dV_2, \quad (3.20)$$

$$I(\mathbf{q})_2 = \int_{V_1} \rho_m e^{-i\mathbf{q}\cdot\mathbf{r}_1} dV_1 \int_{V_2} \eta(\mathbf{r}_2) e^{i\mathbf{q}\cdot\mathbf{r}_2} dV_2, \quad (3.21)$$

$$I(\mathbf{q})_3 = \int_{V_1} \eta(\mathbf{r}_1) e^{-i\mathbf{q}\cdot\mathbf{r}_1} dV_1 \int_{V_2} \rho_m e^{i\mathbf{q}\cdot\mathbf{r}_2} dV_2, \quad (3.22)$$

$$I(\mathbf{q})_4 = \int_{V_1} \eta(\mathbf{r}_1) e^{-i\mathbf{q}\cdot\mathbf{r}_1} dV_1 \int_{V_2} \eta(\mathbf{r}_2) e^{i\mathbf{q}\cdot\mathbf{r}_2} dV_2. \quad (3.23)$$

The first term represents scattering from a particle of constant electron density with dimensions of  $\sim$  mm. The calculations of scattered intensity vs object size completed earlier showed that the scattering from a large object is negligible compared to



that from a large number of small widely separated scatterers. Hence the first term can be ignored as it is negligible compared to the fourth term which describes scattering from a large number of small objects. The second and third terms can also be ignored for similar reasons – they are the product of the amplitude from the large scatterer (negligible compared to a group of large scatterers) and the amplitude from the small objects (also small compared to the square of this amplitude). Thus the problem simplifies to analysis of the last term only, which is equivalent to scattering from a group of small particles of theoretical electron density  $-\rho_m$ , in air (ideally in vacuum). The idea that a collection of pores in a solid phase gives the same scattering as a distribution of particles of the same dimensions in air is known as the Babinet Principle of Reciprocity [50]. It can only be used when the dimensions of the continuous phase are large relative to the dimensions of the scatterer phase.

The fourth term rearranges to (dropping the subscript 4):

$$I(\mathbf{q}) = \int_{V_1} \int_{V_2} \eta(\mathbf{r}_1) \eta(\mathbf{r}_2) e^{-i \mathbf{q} \cdot (\mathbf{r}_1 - \mathbf{r}_2)} dV_1 dV_2 . \quad (3.24)$$

As the vectors  $\mathbf{r}_1$  and  $\mathbf{r}_2$  start from the same origin, subtracting one vector from the other generates another vector,  $\mathbf{r}_{12}$  parallel to the vector,  $\mathbf{r}$ , between the two points. Making the appropriate substitutions for  $\mathbf{r}_2$  (with  $\mathbf{r}_1 - \mathbf{r}_2 = \mathbf{r}$ ) and replacing the integration over  $V_2$  with integration over  $r$  (as they represent the same space) gives:

$$I(\mathbf{q}) = \int_r \int_{V_1} \eta(\mathbf{r}_1) \eta(\mathbf{r}_1 - \mathbf{r}) e^{-i \mathbf{q} \cdot \mathbf{r}} dV_1 d\mathbf{r} . \quad (3.25)$$

The average value of the product of the electron density contrasts is given by:

$$\overline{\eta(\mathbf{r}_1) \eta(\mathbf{r}_1 - \mathbf{r})} = \frac{\int_{V_1} \eta(\mathbf{r}_1) \eta(\mathbf{r}_1 - \mathbf{r}) dV_1}{V} , \quad (3.26)$$

where  $V$  is the total volume required to contain all the scatterers. This rearranges to:

$$\int_{V_1} \eta(\mathbf{r}_1) \eta(\mathbf{r}_1 - \mathbf{r}) dV_1 = V \overline{\eta(\mathbf{r}_1) \eta(\mathbf{r}_1 - \mathbf{r})} \quad (3.27)$$

As the electron density contrast was defined as  $\eta_r = \rho_r - \rho_m$ , the product of the contrasts at two different points in the sample separated by a distance  $r$  can be either zero (when either one of the points is in the matrix) or  $\rho_m^2$  if both points are in small scatterers. This second option is the only one that “generates” intensity. For an isotropic distribution of scatterers, the probability that a point will be in the small scatterer phase is simply the volume fraction of this phase,  $\phi_s$ . The probability that the second point is also in the small scatterer phase depends on the distance between the two points – in the limit that  $r = 0$ , the probability is 1, whereas at large  $r$ , the probability is simply  $\phi_s$  again. In between these limits, the probability decreases continuously. This decreasing behaviour can be represented by the function  $\gamma(r)$  where  $P_s$ , the probability that the second point is in the small object phase when the first point is in the same phase is:

$$P_s = \phi + \gamma(r)(1 - \phi), \quad (3.28)$$

which gives the probability,  $P_{ss}$ , that both points are in the small object phase:

$$P_{ss} = \phi [\phi + \gamma(r)(1 - \phi)]. \quad (3.29)$$

Thus the average product of two electron densities is:

$$\overline{\eta(\mathbf{r}_1) \eta(\mathbf{r}_1 - \mathbf{r})} = P_{ss} \eta_p^2 + (1 - P_{ss}) \eta_m^2 = P_{ss} \eta_p^2. \quad (3.30)$$

Combining equation 3.27 with equations 3.29 and 3.30 gives:

$$\int_{V_1} \eta(\mathbf{r}_1) \eta(\mathbf{r}_1 - \mathbf{r}) dV_1 = V \eta_p^2 \phi [\phi + \gamma(r)(1 - \phi)]. \quad (3.31)$$

This allows the scattered intensity to be simplified as follows:

$$I(\mathbf{q}) = \int_V \eta_p^2 \phi [\phi + \gamma(r)(1 - \phi)] e^{-i\mathbf{q}\cdot\mathbf{r}} d\mathbf{r} \quad (3.32)$$

$$= V \eta_p^2 \phi^2 \int_V e^{-i\mathbf{q}\cdot\mathbf{r}} d\mathbf{r} + V \eta_p^2 \phi(1 - \phi) \int_V \gamma(r) e^{-i\mathbf{q}\cdot\mathbf{r}} d\mathbf{r}. \quad (3.33)$$

Although the volume now has an arbitrary shape and hence the first integral cannot be solved analytically, it will evaluate to a real number for an isotropic distribution of scattering centres containing a centre of symmetry. The value of the first integral will therefore be somewhere between zero and  $(q)^{-1}$ . As there are a large number of scatterers, the magnitude of the integral of the second term will be much larger than the magnitude of the first integral, because of the inclusion of the auto-correlation function. Thus the first term can be ignored. As  $r$  increases, the electron density at one point becomes un-correlated to the electron density at the second point. The auto-correlation function therefore tends to zero as  $r$  increases. This allows the integral over fixed volume to be replaced with an integral over an infinite volume. After substituting for the electron density contrast,  $\eta_p$ , this leaves:

$$I(\mathbf{q}) = V (\rho_p - \rho_m)^2 \phi(1 - \phi) \int_0^\infty \gamma(r) e^{-i\mathbf{q}\cdot\mathbf{r}} d\mathbf{r}. \quad (3.34)$$

As it is assumed that the pores are distributed isotropically, the integral over the volume covered by  $r$  can be simplified to (see Appendix B4 for details):

$$I(\mathbf{q}) = V (\rho_p - \rho_m)^2 \phi(1 - \phi) 4\pi \int_0^\infty \gamma(r) r^2 \frac{\sin(qr)}{qr} dr \quad (3.35)$$

Using a probabilistic approach, Debye et al. [55] have shown that the auto-correlation function for a randomly distributed two phase distribution is:

$$\gamma(r) = e^{-r/a}, \quad (3.36)$$

where  $a$  is the correlation length, related to the length scale of the scatterers. Substituting this into the intensity expression gives:

$$I(q) = \frac{V(\rho_p - \rho_m)^2 \phi(1 - \phi)4\pi}{q} \int_0^\infty e^{-r/a} r \sin(qr) dr. \quad (3.37)$$

This expression evaluates to [1]:

$$I(q) = \frac{V(\rho_p - \rho_m)^2 \phi(1 - \phi)4\pi}{q} \frac{2q}{a((a^{-1})^2 + q^2)^2}. \quad (3.38)$$

The volume,  $V$ , is proportional to the number of scatterers,  $N$ , and the volume of each scatterer (i.e.  $V \propto Na^3$ ). This simplifies the intensity expression to:

$$I(q) = \frac{B a^6 (\rho_p - \rho_m)^2}{(1 + a^2 q^2)^2}, \quad (3.39)$$

where the constants, such as  $N$ , have been included in  $B$ .

For pores in the sample that are orders of magnitude larger (but still small relative to the volume illuminated by the sample beam) than the nanopores of interest,  $a^2 q^2 \gg 1$ . This reduces the expression to:

$$I(q) = \frac{A}{q^4}. \quad (3.40)$$

When a material contains both macro and nanopores, Kelliat et al [56] showed that the scattering could be described well by independent contributions from each of the pore sizes. This can be further extended to include two nanopore sizes, one of which is significantly larger than the other, together with a mesopore contribution. Including a constant background term and introducing a variable,  $n$ , to allow for corrections to be made for smearing effects from having a finite slit height in experimental equipment [50] gives the following expression:

$$I(q) = \frac{A}{q^n} + \frac{B a_1^6 (\eta_{\text{nanopore}})^2}{(1 + a_1^6 q^2)^2} + \frac{C a_2^6}{(1 + a_2^6 q^2)^2} + D, \quad (3.41)$$

where  $A$  and  $B$  and  $C$  are parameters related to the number of macropores, small nanopores and larger nanopores respectively. For this equation, it is assumed that the electron density contrast of the larger nanopores remains constant. The Debye autocorrelation length,  $a$ , can be related to the average radius of gyration (defined by Porod [57] as the mean square distance of electrons from the centre of gravity) of the pores by  $R_g = \sqrt{6} a$ . For a spherical pore of radius  $R_s$ , the radius of gyration can be shown to be:  $R_g = \sqrt{3/5} R_s$ , thus the autocorrelation length can be related to an equivalent spherical pore radius by  $R_s = \sqrt{10} a$ , in order to gain an indication of the size of the pores in the carbon.

When comparing an experimental scattering profile with one calculated from a model, there is a need to account for the Lorentz and polarization factors. The Lorentz factor deals with the fact that as the  $2\theta$  scattering angle increases (up to  $90^\circ$ ), the total scattered intensity spreads over a larger area at the distance to the detector. Thus the intensity per unit area (which is measured by the detector) decreases as the scattering angle increases in an experimental. For the derivation presented above, the Lorentz factor was effectively included in the averaging process, as the average value of  $e^{i\mathbf{q}\cdot\mathbf{r}_2}$  was determined by calculating the total scattered intensity for a given  $r$  value and dividing by the area over which that intensity was distributed (giving equation 3.35). Thus there is no need to apply a Lorentz correction to the data. The polarization factor

accounts for changes in the scattered beam intensity resulting from the 2-dimensional plane of rotation of the electric field vector of the incident beam. The polarization factor is essentially constant over the angular range of interest in small-angle measurements and thus can be ignored. It will be more important for the analysis of WAXS data.

Equation 3.41 was used to model all SAXS patterns including those from *in situ* studies. The quality of the fit was determined by a modified chi-squared goodness of fit parameter, GOF:

$$\text{GOF} = \frac{\text{GOF}_{\text{actual}}}{T} = \frac{1}{N-P} \sum_i \frac{(I_{\text{calc}}(i) - I_{\text{exp}}(i))^2}{I_{\text{exp}}(i)}, \quad (3.42)$$

where N is the number of data points, P is the number of parameters varied and T is the count time (s) for each data point. This factor was included as different count times were used for different SAXS measurements. To compare GOF values quoted in later chapters for different experiments, they should be multiplied by the count time for the experiment.

Figure 3.4 shows the results of applying this equation to model experimental data. It can be seen the fits obtained are excellent – the fit lines are difficult to resolve from the experimental data. This figure also shows the contribution of each term in the equation to the resultant fit. The fit parameters obtained are shown in Table 3.2.

Both carbons required nanopores with an equivalent spherical radius of  $\sim 6 \text{ \AA}$ . The difference between the two samples is that the nanoporous carbon required  $\sim 6$  times more of this nanopore contribution than was required for the macro/mesoporous carbon. In addition to a small amount of nanopore contribution, the macroporous carbon also required a contribution from a larger pore size in order to achieve an optimum fit. It is encouraging to note that the pore sizes generated by SAXS analysis are of the same order of magnitude as those found through gas adsorption. Thus, the limited pore size distribution information obtained by SAXS analysis is in reasonable agreement with that generated from those gas adsorption isotherms.

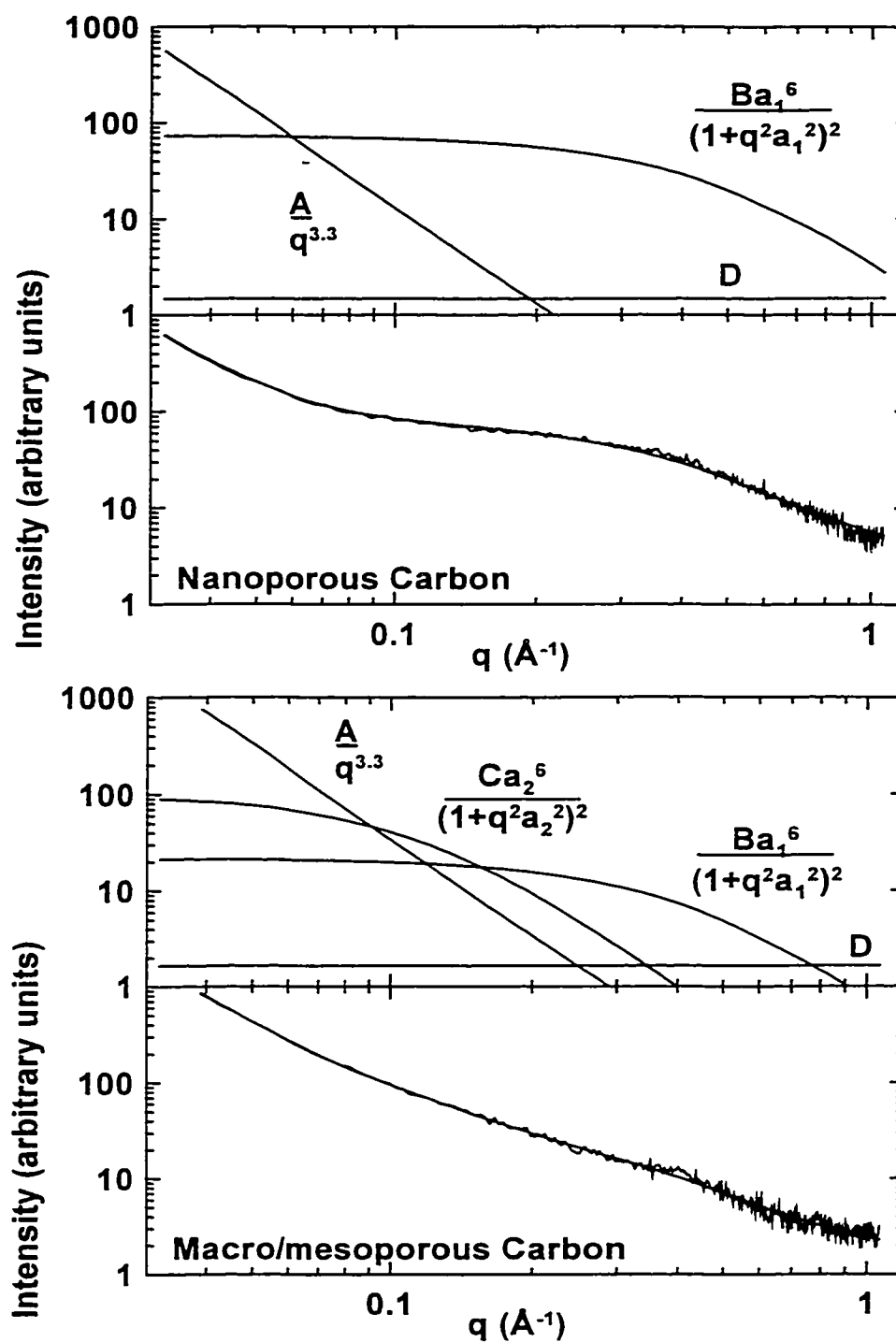


Figure 3.4: Experimental and fitted data for nanoporous carbon (upper graph) and macro/mesoporous carbon (lower graph). The fits are shown as solid lines superimposed on the experimental data. The upper panel in each graph shows the contribution from each term in the scattering equation.

*Table 3.2: SAXS model fit parameters for sample carbons*

	Nanoporous Carbon	Macro/mesoporous Carbon
A	0.0065	0.0170
B	1.47	0.25
$a_1$	1.92	2.10
$R_{s(1)}$	6.1	6.6
C	0	0.0006
$a_2$	N/A	7.54
$R_{s(2)}$	N/A	23.8
D	1.5	1.7
$\chi^2$	0.115	0.095

### 3.3 Wide-angle Scattering

Most diffraction calculations are performed for crystalline materials containing a unit cell that is repeated continuously in three dimensions. When dealing with these structures, concepts such as Bravais lattices, Miller indices and the reciprocal lattice are critical for extracting structural information.

In the case of amorphous materials, such concepts have only limited usefulness because there is no representative unit cell that is repeated throughout the structure (alternatively, the unit cell can be considered to be extremely large incorporating the whole of the sample). With no definable unit cell, there is no need to select the appropriate Bravais lattice to represent that unit cell, nor is the reciprocal lattice of much use because the repeat nature of the reciprocal lattice is not present.

For disordered materials showing some evidence of crystallinity, one approach that can be taken is to assume that the material can be described by a set of small crystallite domains. If it is further assumed that these domains contain the same structure on a small scale as a known crystalline material, then some methods used to analyse crystalline materials can be used. This approach will be taken in this thesis where it will



be assumed that disordered carbons can be constructed from a set of small graphitic domains. These domains can be represented by small layer stacks of finite dimension.

The x-ray scattering patterns of disordered carbons such as those produced for this thesis normally contain a series of broad peaks. An example of a powder diffraction pattern for such a carbon (measured with a diffractometer equipped with a copper source emitting x-rays of average wavelength 1.5415 Å) is shown in Figure 3.5. The main peaks of interest in this thesis have been identified on the figure by the Miller indices corresponding to the equivalent peaks in crystalline 2H graphite (see Chapter 4). The 002 and 004 peaks can be thought of as arising from constructive interference effects from approximately parallel aromatic layers. The 100 and 110 peaks arise from planes of atoms within the layers (i.e. perpendicular to the planes of atoms generating the 002 and 004 peaks).

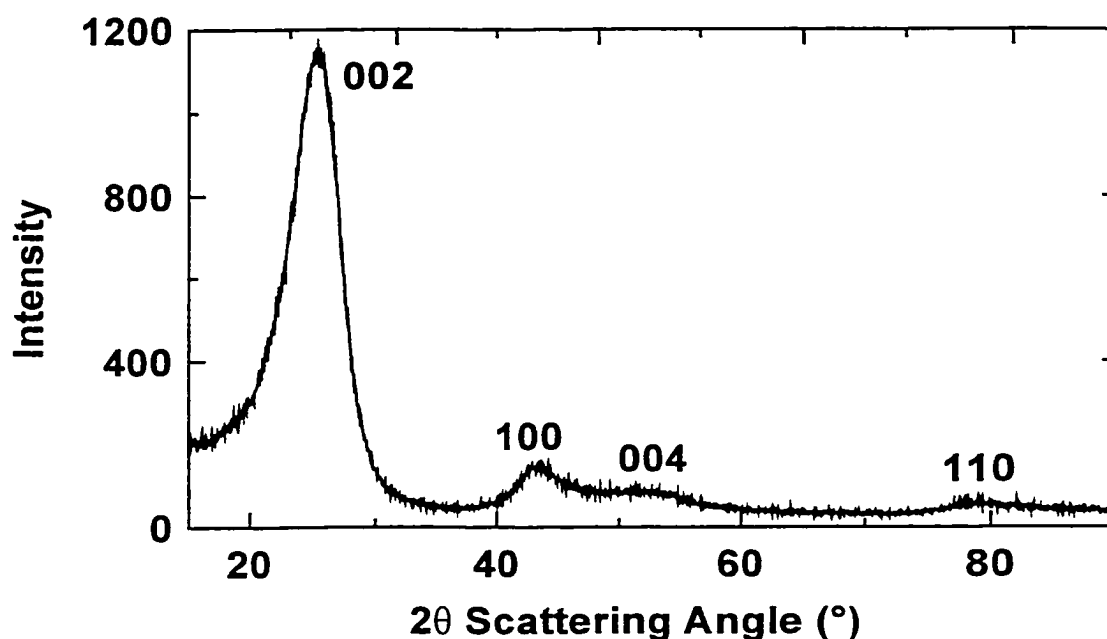


*Figure 3.5: Typical WAXS curve for non-graphitic carbon.*

In later chapters it will be proposed that sodium and lithium atoms can insert between the aromatic layers. In order to model such a process, only the 002 and 004 peaks need to be examined. As these peaks occur at different angles to those that

The inclusion of interlayer atoms increases the complexity of the model dramatically, particularly as the position of both the layer and interlayer atoms varies with the strain. This removes many of the simplifications that Shi was able to use during the derivation of his model equation. A more computationally intensive model was therefore developed as detailed below to include interlayer atoms.

### 3.3.1 Layer structure model

If a stack of  $N$  parallel layers with arbitrary spacing is orientated so that it is perpendicular to the scattering vector of the x-ray beam ( $\mathbf{q}$ ), then the effective structure factor for each layer,  $F(\mathbf{q})$ , will be directly proportional to the product of the atomic scattering factor of the atoms in the layer and the number of atoms in the layer. The layer can then be represented by a point on a line parallel to the scattering vector. The scattered amplitude from the stack is then given by:

$$A(\mathbf{q}) = \sum_{m=1}^{m=N} F_m(\mathbf{q}) e^{i\mathbf{q} \cdot \mathbf{r}_m}, \quad (3.43)$$

where the sum extends over all layers and  $\mathbf{r}_m$  is the vector from an arbitrary origin to the point representing the layer. It is logical to place the origin at the centre of the first layer. The scattered intensity from this set of layers will then be proportional to the product of equation 3.43 and its complex conjugate:

$$I(\mathbf{q}) \propto \sum_{m=1}^{m=N} F_m(\mathbf{q}) e^{i\mathbf{q} \cdot \mathbf{r}_m} \sum_{n=1}^{n=N} F_n(\mathbf{q}) e^{-i\mathbf{q} \cdot \mathbf{r}_n}. \quad (3.44)$$

This expression simplifies to:

The inclusion of interlayer atoms increases the complexity of the model dramatically, particularly as the position of both the layer and interlayer atoms varies with the strain. This removes many of the simplifications that Shi was able to use during the derivation of his model equation. A more computationally intensive model was therefore developed as detailed below to include interlayer atoms.

### 3.3.1 Layer structure model

If a stack of  $N$  parallel layers with arbitrary spacing is orientated so that it is perpendicular to the scattering vector of the x-ray beam ( $\mathbf{q}$ ), then the effective structure factor for each layer,  $F(\mathbf{q})$ , will be directly proportional to the product of the atomic scattering factor of the atoms in the layer and the number of atoms in the layer. The layer can then be represented by a point on a line parallel to the scattering vector. The scattered amplitude from the stack is then given by:

$$A(\mathbf{q}) = \sum_{m=1}^{m=N} F_m(\mathbf{q}) e^{i\mathbf{q} \cdot \mathbf{r}_m}, \quad (3.43)$$

where the sum extends over all layers and  $\mathbf{r}_m$  is the vector from an arbitrary origin to the point representing the layer. It is logical to place the origin at the centre of the first layer. The scattered intensity from this set of layers will then be proportional to the product of equation 3.43 and its complex conjugate:

$$I(\mathbf{q}) \propto \sum_{m=1}^{m=N} F_m(\mathbf{q}) e^{i\mathbf{q} \cdot \mathbf{r}_m} \sum_{n=1}^{n=N} F_n(\mathbf{q}) e^{-i\mathbf{q} \cdot \mathbf{r}_n}. \quad (3.44)$$

This expression simplifies to:

$$I(\mathbf{q}) \propto \sum_{m=1}^{m=N} \sum_{n=1}^{n=N} F_m(\mathbf{q}) F_n(\mathbf{q}) e^{i\mathbf{q} \cdot \mathbf{r}} , \quad (3.45)$$

(where  $\mathbf{r}$  is the vector between the points  $m$  and  $n$ ) which can be rewritten as:

$$I(\mathbf{q}) \propto \sum_{m=1}^{m=N} F_m^2(\mathbf{q}) + 2 \sum_{m=1}^{m=N-1} \sum_{n=m+1}^{n=N} F_m(\mathbf{q}) F_n(\mathbf{q}) \cos(\mathbf{q} \cdot \mathbf{r}) . \quad (3.46)$$

This equation can be used to calculate the intensity expected from a finite layer stack provided the position and atom type of each of the layers is known. The results of this calculation for a series of carbon stacks with increasing  $N$  (with the distance between adjacent layers = 3.4 Å) and no interlayer atoms are shown in Figure 3.7. In this figure, the calculated intensity has been divided by the number of layers in the stack in order to show the intensity per layer. It can be seen that for only one layer, the intensity curve resembles the atomic scattering factor curve – this is not surprising, as there are no interference effects from having only one layer. As the number of layers increases, the heights of both the 002 and 004 peaks increase. This occurs because of constructive interference between the layers. It can also be seen that the 002 peak height increases essentially linearly with the number of layers. This implies that the height of the 002 peak in an experimental scan can be used to obtain an indication of the number of layers in an average stack. The layer stacking ratio,  $R$ , can be used to compare different samples. This parameter is calculated from [60]:

$$R = \frac{B}{A} , \quad (3.47)$$

where  $B$  is the height of the peak and  $A$  is the height of the background.

The second panel in Figure 3.7 shows the effect of increasing the number of atoms in the interlayer space. This uses  $\text{Na}_x\text{C}_6$  as a model stoichiometry. The intensity of the 002 peak drops as  $x$  increases because the interlayer atoms scatter out of phase with the carbon atoms. It is important to note however that the 004 peak shows the opposite

trend – an increase in intensity with increasing interlayer atom concentration. This occurs because the 004 peak is the second order reflection from the carbon layers and hence the interlayer atoms scatter in phase with the carbon layers over this angular range.

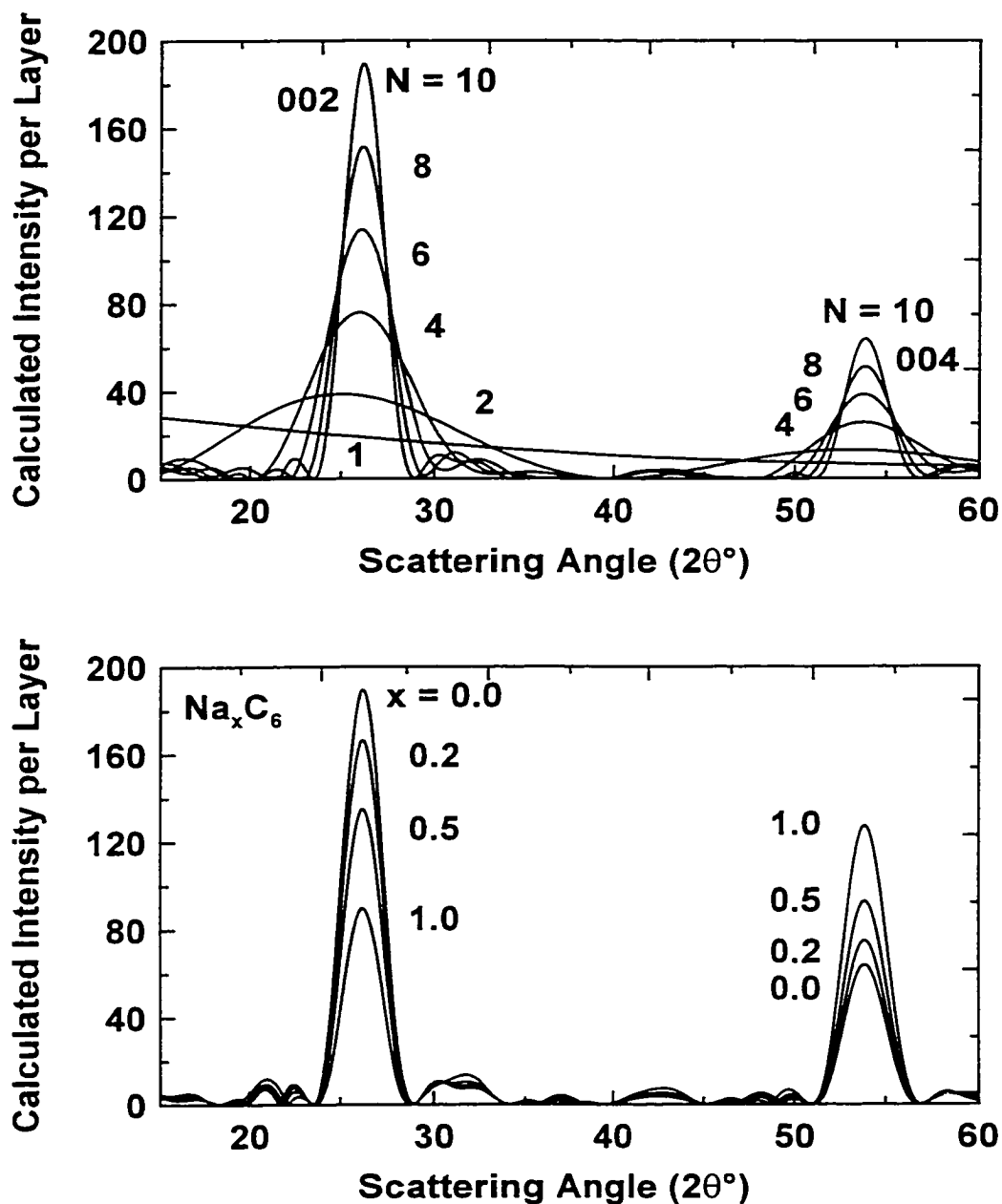


Figure 3.7: Upper Panel - calculated intensity for a stack of  $N$  carbon layers, with  $N$  as indicated on each curve. Lower panel – calculated intensity changes for interlayer insertion, to produce  $\text{Na}_x\text{C}_6$ , with  $x$  as indicated on each plot ( $N = 10$ ).

Figure 3.7 was prepared from data generated with no strain, i.e. a constant interlayer spacing. In order to include strain, equation 3.46 was used to calculate the intensity curves for a large number of crystallites (10,000) where the distances between adjacent layers in each stack were varied. The intensity curves for each stack were then combined to extract an average intensity distribution for layer stacks with strain. The following procedure was used to generate the layer positions for each stack:

- for a stack of  $N$  carbon layers,  $(N-1)$  interlayer strain values,  $\delta$ , were generated using a Gaussian probability distribution,  $P(\delta)$ :

$$P(\delta) = \frac{1}{\sqrt{2\pi\langle\delta^2\rangle}} e^{-\frac{\delta^2}{2\langle\delta^2\rangle}}, \quad (3.48)$$

where  $\langle\delta^2\rangle$  represents the average of the square of  $\delta$  (user specified) and  $\delta$  could be either positive or negative.

- the first carbon layer position,  $d_1$  was set to zero. The position of the second carbon layer,  $d_2$ , was then set to  $(d_{002} + \delta_1)$ , (where  $d_{002}$  was a user specified mean carbon layer spacing), the position of the third carbon layer,  $d_3$ , was set at  $(d_2 + d_{002} + \delta_2)$  and so on.
- the  $(N-1)$  alkali interlayers were then located at the midpoint between each of the carbon layer pairs.

Once these layer positions were allocated, the intensity was determined from equation 3.46. The averaging process was required to smooth out the intensity curve as the number of layers in each stack was small and hence the calculated intensity for a single stack contained a series of sharp peaks across the 002 and 004 peaks. In order to eliminate the harmonics between the main peaks resulting from the finite stack size, the number of layers in each stack was also varied, again according to a Gaussian distribution about a user selected mean value.

Figure 3.8 shows how the calculated pattern changes with increasing strain. It can be seen that increasing the amount of strain in the model causes the intensities of the 002 and 004 peaks to drop and increases the peak widths.

As explained in the SAXS theory section, in order to compare calculated intensities with experimental data when peak shifts occur, there is a need to account for the Lorentz and polarization factors. The Lorentz factor can be included by multiplying the measured intensity by  $q^2$ . For a diffractometer equipped with a monochromator, the polarization factor is [61]:

$$I_{\text{measured}} = \frac{1 + \cos^2 2\theta \cos^2 2\theta_m}{1 + \cos^2 2\theta_m} I_{\text{calc}} \quad (3.49)$$

where  $\theta_m$  is the Bragg angle for the crystal used in the monochromator. In the case of a graphite crystal monochromator,  $\theta_m = 13.3^\circ$ . When the interlayer model is used in Chapter 6, these two corrections will be applied to the experimental data.

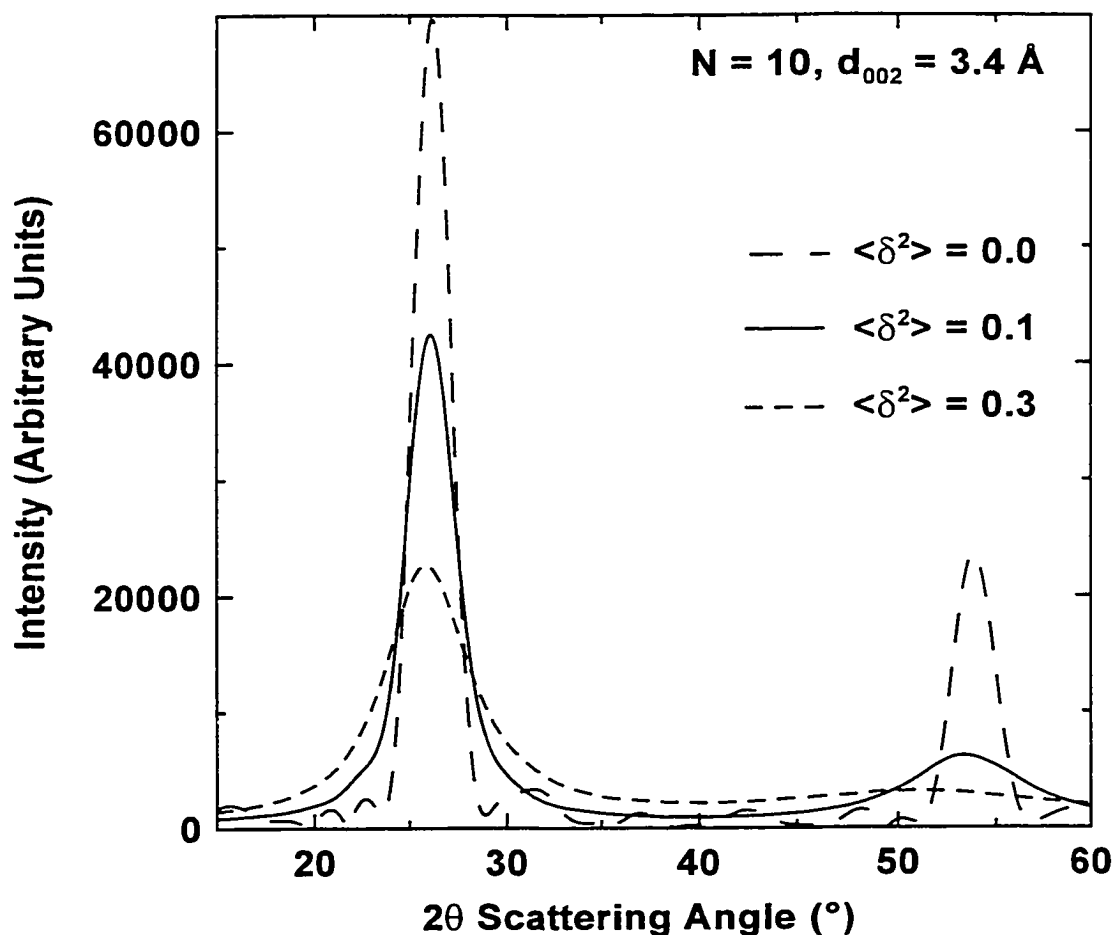


Figure 3.8: The effect of increasing strain on a calculated WAXS pattern.

### 3.3.2 Debye Equation for calculating x-ray powder patterns

The powder pattern expected for a small distribution of atoms where the atomic positions are known can be calculated exactly using what is normally referred to as the Debye formula for powder patterns [62]. For a centrosymmetric distribution of atoms, the scattered intensity can be represented by:

$$I(\mathbf{q}) = \sum_{\mathbf{K}} f(\mathbf{q})_{\mathbf{K}}^2 + \sum_{\mathbf{K}} \sum_{\mathbf{J} \neq \mathbf{K}} f(\mathbf{q})_{\mathbf{K}} f(\mathbf{q})_{\mathbf{J}} \cos(\mathbf{q} \cdot \mathbf{r}_{\mathbf{JK}}). \quad (3.50)$$

This equation is the atomic analogue of equation 3.10, the scattered intensity from a distribution of scattering centres. The particle form factor has just been replaced by the atomic scattering factor. In order to determine the powder averaged scattered intensity, the atomic distribution is assumed to be rigid but is allowed to take all orientations in space. Thus equation 3.50 needs to be averaged over all space, giving:

$$\overline{I(\mathbf{q})} = \sum_{\mathbf{K}} f(\mathbf{q})_{\mathbf{K}}^2 + \sum_{\mathbf{K}} \sum_{\mathbf{J} \neq \mathbf{K}} f(\mathbf{q})_{\mathbf{K}} f(\mathbf{q})_{\mathbf{J}} \overline{\cos(\mathbf{q} \cdot \mathbf{r}_{\mathbf{JK}})}. \quad (3.51)$$

To calculate the average of the cosine term, it is useful to convert it back to the complex notation:

$$\overline{\cos(\mathbf{q} \cdot \mathbf{r}_{\mathbf{JK}})} = \overline{e^{-i\mathbf{q} \cdot \mathbf{r}_{\mathbf{JK}}}}. \quad (3.52)$$

This average has already been calculated in Appendix A4 as:

$$\overline{e^{i\mathbf{q} \cdot \mathbf{r}_{12}}} = \frac{\sin(\mathbf{q} \cdot \mathbf{r}_{12})}{\mathbf{q} \cdot \mathbf{r}_{12}}, \quad (3.53)$$

which simplifies equation 3.50 to the Debye formula for powder patterns:



$$I(q) = \sum_K f(q)_K^2 + \sum_K \sum_{J \neq K} f(q)_K f(q)_J \frac{\sin(q \cdot r_{JK})}{q \cdot r_{JK}} \quad (3.54)$$

Equation 3.54 shows that the powder diffraction pattern for a distribution of atoms can be calculated directly provided the distances between all atoms are known. Thus the expected powder pattern can be calculated exactly if the atomic co-ordinates are known. The main problem with this equation is that the number of calculations required scales as  $N^2$ , where  $N$  is the number of atoms, and hence it is not practical to use it for calculating the powder pattern for a large number of atoms.

### 3.4 Experimental

All x-ray scattering measurements were completed on a Siemens D5000 diffractometer equipped with a Cu source tube. The tube was run at 35mA and 45kV. Figure 3.9 shows a schematic diagram of the diffractometer set-up. A set of collimating slits is used to produce a parallel beam. The divergence slit sets the width of the beam falling on the sample. The anti-scatter slit minimises the amount of secondary radiation entering the detector. The receiving slit determines the width of the beam directed to the detector, whilst the graphite monochromator was used to ensure that no fluorescence radiation impinged on the detector. The detector recorded total counts received for a given angle over the time the diffractometer was held at that angle. Five different classes of experiment were completed, as described below. The scan settings used for each type of experiment are summarised in table 3.3.

*Table 3.3: Scan settings used for x-ray measurements*

	Divergence Slit	AntiScatter Slit	Receiving Slit	First Angle ( $2\theta$ )	Last Angle ( $2\theta$ )	Angle Step	Count Time
Standard SAXS	0.1 °	0.1 °	0.1 mm	0.3 °	15 °	0.05 °	15 s
<i>In situ</i> SAXS	0.1 °	0.1 °	0.1 mm	0.3 °	15 °	0.05 °	30 s
Standard WAXS	0.6 °	0.6 °	0.6 mm	5 °	90 °	0.1°	10 s
<i>In situ</i> WAXS	0.6 °	0.6 °	0.6 mm	15 °	60 °	0.1°	30 s
<i>Ex situ</i> WAXS	0.6 °	0.6 °	0.6 mm	15°	60°	0.1°	30s

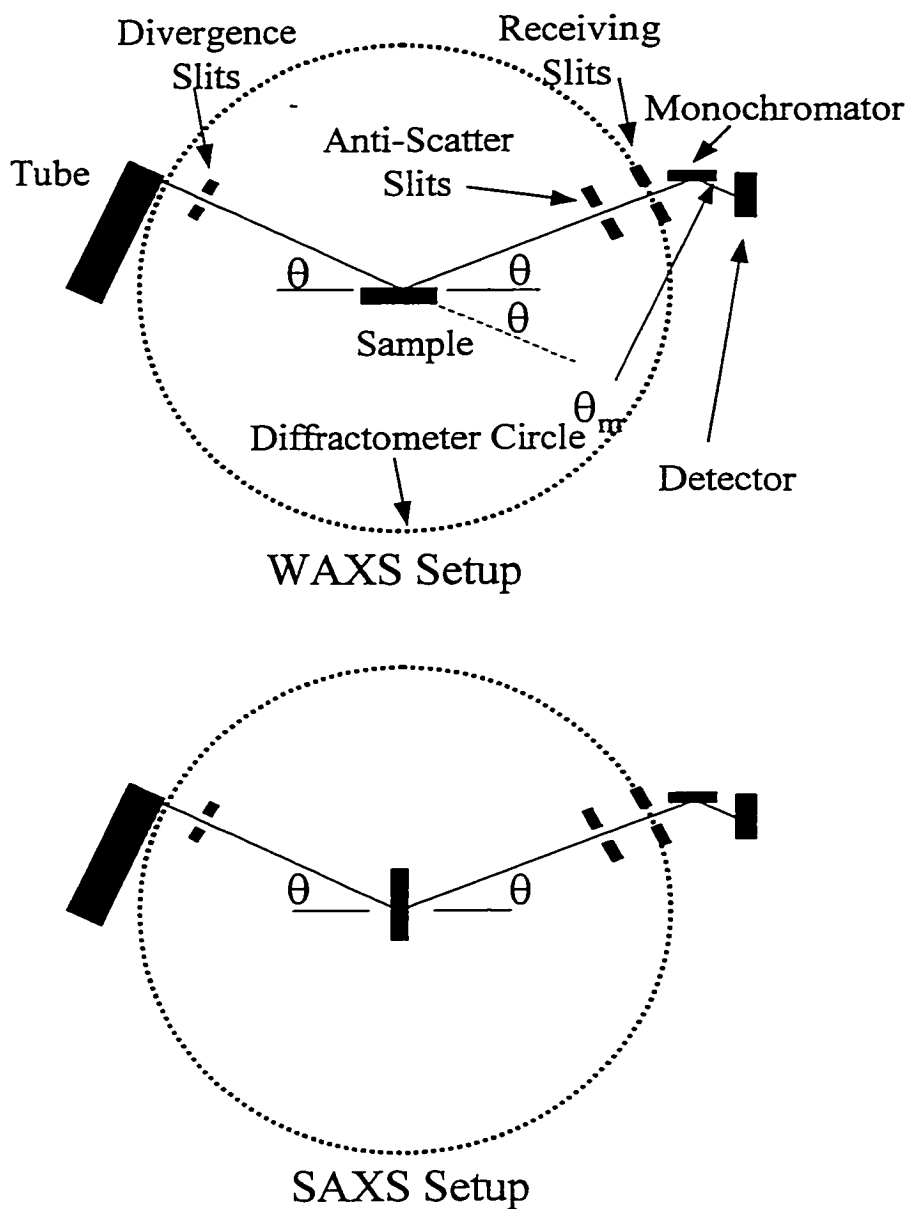


*Figure 3.9: Diagram of the Siemens D5000 Diffractometer geometry for measuring WAXS patterns (upper diagram) and SAXS patterns (lower diagram)*

### Standard SAXS

A known mass of carbon powder was placed in a vertical sample holder, giving a sample thickness of  $\sim 2$  mm. The sample was held in place with kapton film (a

fluorinated polyamide). The sample holder was installed vertically in the diffractometer, allowing for measurements to be made at low angles by running in transmission mode.

### ***In situ* SAXS**

An electrochemical cell was constructed with the carbon electrode/separator/metal foil clamped between two beryllium windows. The cell was held vertically in a delrin holder that also provided electrical contact to the current supply. The scan conditions listed in Table 3.3 were used repeatedly to obtain scans as a function of time.

### **Standard WAXS**

A rectangular well with dimensions 25 x 20 x 2 mm was packed with the powder of interest and a flat surface was obtained by careful compaction with a glass slide. The holder was installed in the diffractometer horizontally.

### ***Ex situ* WAXS**

Air-sensitive samples (i.e. carbons loaded with sodium vapour at high temperature and then cooled) were placed in a shallow well in a holder that was covered by a semi-circular mylar coated dome. The dome was screwed down to seal against an o-ring and the mylar was glued around the top with torr-seal resin. The dome was designed to prevent air exposure whilst not interfering with the scattering measurements. Because of its semi-circular design, the beam was always at right angles to the mylar, minimising both the amount of beam absorption and the amount of radiation scattered from the film hitting the detector. The dome also provided an additional benefit – as it was loaded in a helium filled glove box, the intensity of the beam incident on the sample was actually higher than if the sample had been in air.

### ***In situ* WAXS**

An electrochemical cell was prepared with only one beryllium window over the carbon pellet electrode. This cell was placed in a holder that was designed to keep the cell level, whilst also minimising off-axis shift of the carbon electrode. It was also connected to the current supply.

## **Chapter 4**

### **Carbon Structure**

This project examined the electrochemical performance of solids containing predominantly carbon (> 95 wt%), possibly with minor levels of hydrogen and hetero-atoms such as oxygen or sulphur. Such materials can occur naturally as, for example, coals, but can also be produced from an amazing range of precursors by inert atmosphere heat treatment - for example, researchers have produced carbons from materials as diverse as: olive stones [63], phenolic resin [64], coconut shell [65], wood [66] and saccharose [67]. The structure of the majority of carbons cannot be easily described by standard crystallographic terminology – there is no regularly repeating unit cell or set of crystallographic axes. Nor can they be considered to be truly amorphous like the glasses. The carbon atoms form structural units loosely based on that of graphite – a series of aromatic layers (usually highly defective) stacked somewhat parallel to each other [27]. In this chapter, a rudimentary structural model for carbons based on gas adsorption and x-ray scattering data will be presented that will be used in subsequent chapters to explain sodium and lithium electrochemical performance.

#### **4.1 Introduction to Carbon Terminology**

As they are heated to higher temperatures, some carbons become more and more graphitic in nature, with aromatic layers becoming more ordered and growing in size. These carbons are generally called the soft or graphitizable carbons [58]. Other carbons show very little graphitic structure development even after heat treatment to temperatures

in excess of 3000K. These carbons are called the hard, glassy or non-graphitizable carbons [68]. Work from this thesis and other authors [19] has shown that classifying carbons into these two groups also provides a method for describing sodium and lithium electrochemical performance. Thus, this thesis describes the electrochemical performance of both hard and soft carbons as a function of heat treatment temperature.

Much of the discussion on carbon structure will refer to graphene sheets. As a first approximation, these sheets are based on the aromatic layers in graphite. Thus, a graphene sheet can be thought of as containing  $sp^2$  hybridized carbon atoms arranged in a planar hexagonal network of limited lateral extent. This was the model developed by Franklin in 1951 [69]. Defects such as strained carbon centres,  $sp^3$  hybridized carbons, hetero-atoms and vacancies can result in buckling and distortion of the graphene sheets. The extent of these defects and the nature and position of crosslinks between the layers controls the overall microstructure of the carbon. Maire and Mering first incorporated these defects into a carbon model [58], extending Franklin's model. Large amounts of such defects can result in the graphene sheets being arranged somewhat like a house of cards [70]. In this situation, voids are present between the layers that are potentially able to accommodate atomic species and small molecules. These voids (nano-scale porosity) explain for example the high sorption capabilities of activated carbons used in areas such as water purification and gas masks [27].

Based on this description of carbon structure, it could be said that graphite is the pure, crystalline form of most of these carbons. In fact, it is often useful to describe the carbon structure in terms of a model graphite structure. Pure graphite contains  $sp^2$  hybridised carbons arranged as defect free graphene sheets, essentially of infinite lateral extent. The sheets stack parallel to each other 3.35 Å apart. This distance is large relative to typical carbon – carbon bond lengths, giving weak interlayer bonds and thus the layers are reasonably free to slide relative to each other. Overlap of the  $\pi$  clouds from neighboring atoms within a layer results in delocalisation of electrons, allowing them to move within the layers under the influence of an external electric field. This charge delocalisation gives graphite-based structures excellent electrical properties. It is the combination of these electrical properties with the low cost and high chemical resistance of carbons that explains why they are used so widely as electrodes in metallurgical

processes. The two main crystalline forms of graphite, 2H and 3R, differ only in the layer stacking sequence of the aromatic sheets. For the 2H form, the layer sequence is ABAB... whereas for the 3R form, the layers stack in the sequence ABCABC....[71]. Most commercially available graphites contain predominantly the 2H form. These two different stacking sequences are shown schematically in Figure 4.1.

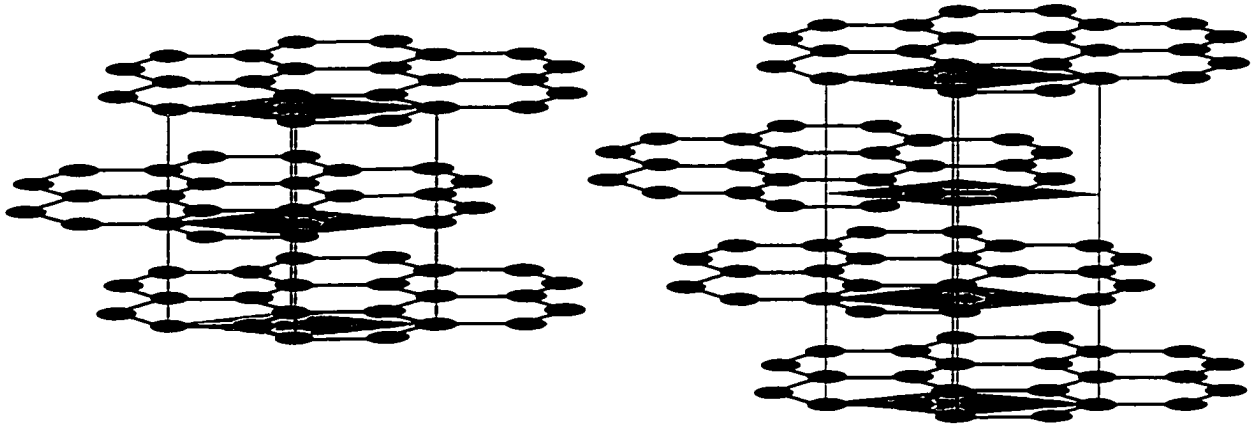


*Figure 4.1: Differences in layer stacking for graphite. Left hand panel shows ABAB... stacking of 2H-graphite. Right hand panel shows ABCABC... stacking of 3R graphite. The hexagonal unit cell for each structure is also shown on each panel.*

When describing carbon structures, the crystallographic properties of graphite are often used as a reference. For instance, x-ray scattering patterns of most carbons show that some constructive interference occurs around a scattering angle of  $20\text{-}26^\circ 2\theta$ . After correcting for polarization and atomic scattering factor effects, this interference corresponds to inter-atomic distances of  $\sim 3.3 - 3.5 \text{ \AA}$ . Thus this peak is related to the distance between graphene sheets, and is normally referred to as the 002 peak, in reference to the 002 interlayer spacing peak of 2H-graphite. The 100 peak is also used to estimate the lateral extent of the graphene sheets. Unless carbon materials are highly graphitic in nature, the 100 peak (around  $44^\circ 2\theta$  scattering angle) is quite broad. In addition, the peak is asymmetric, because it is generated by atoms in 2 dimensional sheets [72]. The peak broadening is generally attributed to crystallite size – the sharper the

peak, the larger the crystallite domains. It also includes contributions from strain within the graphene layers (which effectively manifests itself as a distribution of in-plane interatomic bond lengths), although the strain cannot be separated from the grain size effects for a single peak. Many authors quote  $L_c$  and  $L_a$  values to represent the crystallite height and the lateral extent of the average graphene sheet respectively. These values are calculated from the Scherrer equation [73]:

$$L_c = \frac{0.9 \lambda}{B \cos \theta_{002}}, \quad (4.1)$$

$$L_a = \frac{1.84 \lambda}{B \cos \theta_{100}} \quad (4.2)$$

where  $\lambda$  is the x-ray wavelength,  $\theta$  is the scattering angle of the peak maximum and  $B$  is the full width of the peak at half maximum (in radians).  $L_c$  and  $L_a$  values are considered to be reliable for comparative purposes although the actual values may be much larger [72].

#### 4.1.1 Structural Changes During Heat Treatment

As a result of the complex range of structures formed during heat treatment of most carbonaceous precursors, structural evolution is usually described in rather general terms. It is useful to separate the changes into two regions – those occurring at temperatures below  $\sim 700^\circ\text{C}$ , when significant changes in chemical composition occur and those occurring above  $\sim 700^\circ\text{C}$  when the chemical composition only varies slightly (primarily because the materials have a very high carbon content) and the microstructure changes slowly with temperature. These two regions have been classified by Byrne and Marsh [27] as pyrolysis and carbonization respectively. During pyrolysis, the chemical composition changes through release of small volatile molecules such as  $\text{CH}_4$ ,  $\text{H}_2\text{O}$ ,  $\text{CO}$ ,  $\text{CO}_2$  and  $\text{H}_2$ . These molecules are lost through a series of condensation and elimination

reactions that help establish the basic carbon microstructure in terms of porosity and external size and shape, whilst at the same time decreasing the mole fractions of primarily hydrogen and oxygen in the carbon matrix [74].

Both the soft and hard carbons undergo this structural establishment process, however the nature of the resultant structures is significantly different. The soft carbons develop a reasonably lamellar structure, because they usually have a relatively high aromatic content to start with. The layers therefore are relatively free to move and in fact soft carbons go through a fluid phase during pyrolysis. This fluid phase allows layers to move, where they tend to align themselves into small liquid crystal-like spheres known as mesophase. The mesophase can coalesce forming larger spheres and eventually solidify, as they get too large to remain suspended in solution, forming a structure with the beginnings of graphitic order [75].

The hard carbons on the other hand, do not go through this fluid phase. Rather, the chemical nature of hard carbon precursors encourages crosslinking. This sets the structure into a rigid three-dimensional network that resists rearrangement. This crosslinking also establishes the random layer stacking that leads to nanopore formation.

During carbonization, the soft carbons tend to become more highly lamellar and the graphene sheets coalesce to form larger sheets. There is usually some residual weak crosslinking between layers that pins the structure, and thus, although the layers may be reasonably parallel, there are random rotations and translations of adjacent layers. This is known as turbostratic disorder and is generally not relieved until there is sufficient thermal energy to break the bonds. This does not occur to any significant extent until the temperature exceeds  $\sim 2000^{\circ}\text{C}$  [76].

The hard carbons do not undergo significant rearrangement of the layers even when the temperature exceeds 3000 K. Such rearrangements are prevented by the crosslinks between the layers. There are some subtleties during carbonization of hard carbons in terms of changes in porosity that will be discussed later in this chapter.



### 4.1.2 Carbon Structure Analysis

Chapters 2 and 3 provided an introduction to some of the most useful methods for analysing carbon materials. Through use of gas adsorption, the amount and distribution of porosity that is available to gas molecules can be determined. Small-angle scattering can also be used to assess porosity in the carbon where it provides additional information on the porosity as it measures both open and closed porosity. Additionally it will be shown in this thesis that *in situ* small-angle x-ray scattering studies on operating electrochemical cells can be used to show pores being filled. Wide-angle scattering measurements, as indicated in the introduction to this chapter, can be used to gain an understanding of the atomic micro-structure of the carbon. For the remainder of this chapter, the structure of the carbons used in this study will be discussed.

## 4.2 Carbon Preparation

Four different carbon precursors were used for this work, together with commercially available graphite from Fluka. The materials used were:

- poly-vinyl chloride (*PVC*) from Aldrich fine chemicals,
- coal tar pitch from Crowley Tar Company Ltd. (*Pitch*),
- glucose from Aldrich fine chemicals (*Glucose*), and
- a phenolic resin from Chemplex (Australia) Ltd. (*Resin*).

The first two precursors were selected to represent the soft carbons whilst the last two were chosen to produce hard carbons. These precursors were chosen in order to demonstrate that the mechanisms proposed for sodium and lithium insertion into soft carbons apply to materials that nominally start out with vastly different chemical structures.

Both the PVC and pitch were heat-treated as received. For the glucose and resin, a pre-treatment process was required before they could be heat-treated further.

### **Glucose Pre-treatment**

A dehydration process was used in order to produce a useable precursor powder. When glucose is heated in air to temperatures between 150-200°C, it melts or caramelises to form a viscous fluid. During this melting, water vapour is evolved through condensation reactions, causing the melt to foam dramatically. Thus the glucose was first heated in air in an oven at 180°C for 24 hours to drive off most of the moisture. The overall yield from this dehydration stage was ~ 80 wt%. The foam was then crushed in an auto-grinder until it passed through a 300 µm screen. The resultant brown powder was then used as the precursor for all subsequent heat treatment processes.

### **Resin Pre-treatment**

Phenolic resins require a hardener in order to promote reaction and cross linking through a curing process. For this resin, hexamethylene tetramine (HMTA –  $(\text{H}_2\text{N})_2 - (\text{CH}_2)_6 - (\text{NH}_2)_2$ ) was used as the hardener. Powdered resin was mixed with ~ 16 wt% HMTA and then heated in air to a final temperature of 205°C. The resultant solid mass of cured resin was then crushed in the auto-grinder, again to pass through a 300 µm screen to give the resin precursor.

## **4.2.1 Sample Heat Treatment**

All samples except for those heated to 1700°C were heat treated in the same manner. A sample of powder (5 - 10 g) was weighed into an alumina boat. The boat was then placed in a Lindberg tube furnace equipped with a mullite ceramic tube. The samples were held at 110°C for one hour under an argon (UHP – Praxair) flow of 150 cm<sup>3</sup>/min. They were then heated at 1 °C/min to the final pyrolysis temperature where they were held for 1 hour. Throughout the heating process, the argon flow was maintained in order to remove any volatile species that were generated by the samples. This is critical as the gases released during pyrolysis can further react with the carbon. The 1700°C samples were loaded into a graphite tube and heated in an induction furnace

under vacuum with the final heat-treatment temperature measured with an infra-red pyrometer.

After pyrolysis, all samples were crushed in the auto-grinder until they passed through a 75  $\mu\text{m}$  screen. The resultant fine powder was suitable for gas adsorption, SAXS, WAXS and electrochemical testing. Table 4.1 shows the samples produced for this study.

*Table 4.1: Carbon Samples Prepared for this Study.*

Final Temperature	PVC	Pitch	Glucose	Resin
600 °C	✓	✓	✓	✓
700 °C	✓		✓	
800 °C	✓	✓	✓	✓
900 °C	✓		✓	
1000 °C	✓	✓	✓	✓
1100 °C	✓		✓	
1200 °C	✓	✓	✓	✓
1300 °C	✓		✓	
1400 °C	✓		✓	
1700 °C	✓		✓	

### 4.3 Carbon Analysis

#### 4.3.1 Gas adsorption

$\text{N}_2$  gas adsorption measurements were completed as outlined in Chapter 2 on all PVC and glucose samples. The PVC samples produced Type II isotherms (Figure 4.2) with gas molecules being adsorbed over the whole pressure range. This implies a multilayer adsorption process within mesopores and hence, as expected, these materials contained minimal nanoporosity. The adsorption and desorption branches follow each other very closely, showing that the mesopores were quite open to gas molecules. This is

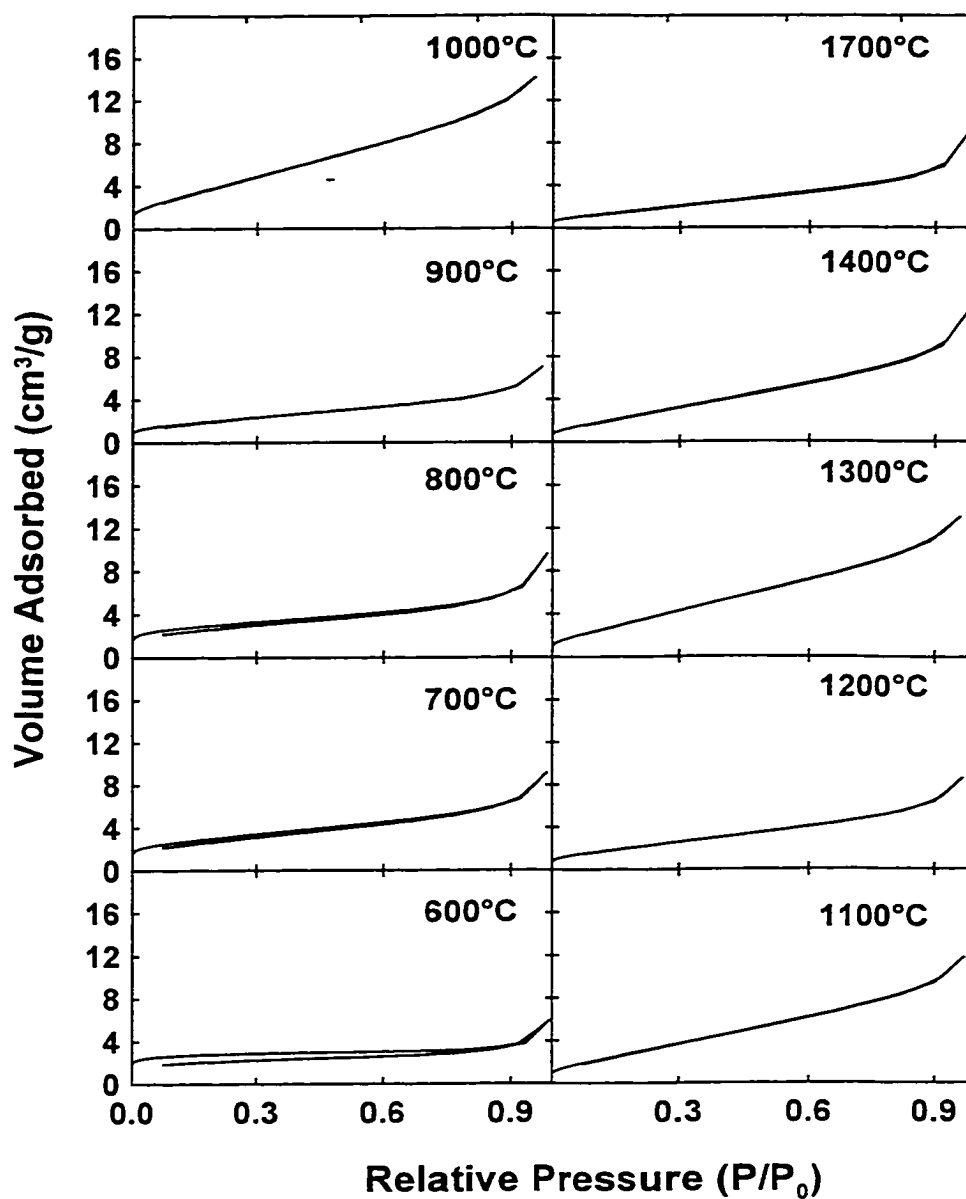


Figure 4.2:  $N_2$  Gas adsorption isotherms for PVC samples as a function of heat treatment temperature. For data sets where two curves can be resolved, the lower curve shows the adsorption data whilst the upper curve shows the desorption data.

not surprising given that the dimensions of the pores are large relative to the gas molecule dimensions. The amount of porosity increases with heat treatment temperature and then decreases. This implies that the amount of open porosity changes slightly during pyrolysis. Comparison with the glucose data presented later in the chapter shows however that the magnitude of the changes observed is quite low. The important point for these samples is that the volume of gas adsorbed is quite low, especially at low relative pressures, implying that the amount of  $N_2$  accessible open nanoporosity in these materials is low.

This behaviour is shown more clearly in Figure 4.3, which presents the DFT fit pore size distributions extracted from the isotherms (in all cases, the agreement between the calculated and experimental isotherms was excellent). These data show the changes in pore volume with temperature. It can be seen that, despite the differences in pore volumes, the pore size distribution remains reasonably constant, containing a wide range of pore sizes from 2 nm upwards, as expected for a meso/macroporous material. Close examination suggests that the major changes in pore structure occur around 2 - 4 nm. The amount of larger porosity ( $\sim 20$  nm) remains essentially constant from 700°C onwards – this is not unreasonable given that the majority of pyrolysis has occurred by this temperature, leaving a fixed macrostructure. Subsequent changes in structure occur on a much smaller level once developed – for example the 2 – 3 nm porosity level increases to 1000°C then decreases for higher temperatures.

It can be seen in Figure 4.4 that the glucose samples show dramatically different behaviour. The low temperature isotherms were Type I isotherms, with large volumes of gas adsorbed at low pressures [37]. The graphs show that the glucose samples contained significant quantities of nanoporosity (as expected for hard carbons), that was already well developed by 600°C, suggesting that the initial pore structure is controlled largely by crosslinking in the precursor material. As the heat treatment temperature increased above 900°C, the total volume adsorbed dropped dramatically and hysteresis began to occur between adsorption and desorption. The volume changes showed that the volume of nanopores accessible to  $N_2$  dropped rapidly whilst the hysteresis implied that the carbon also developed restricted pore openings, which prevent the pore from emptying until the external pressure is low enough to cause the pore neck to empty. At even higher

temperatures, the extent of hysteresis was reduced, implying that any partially blocked pores became completely blocked.

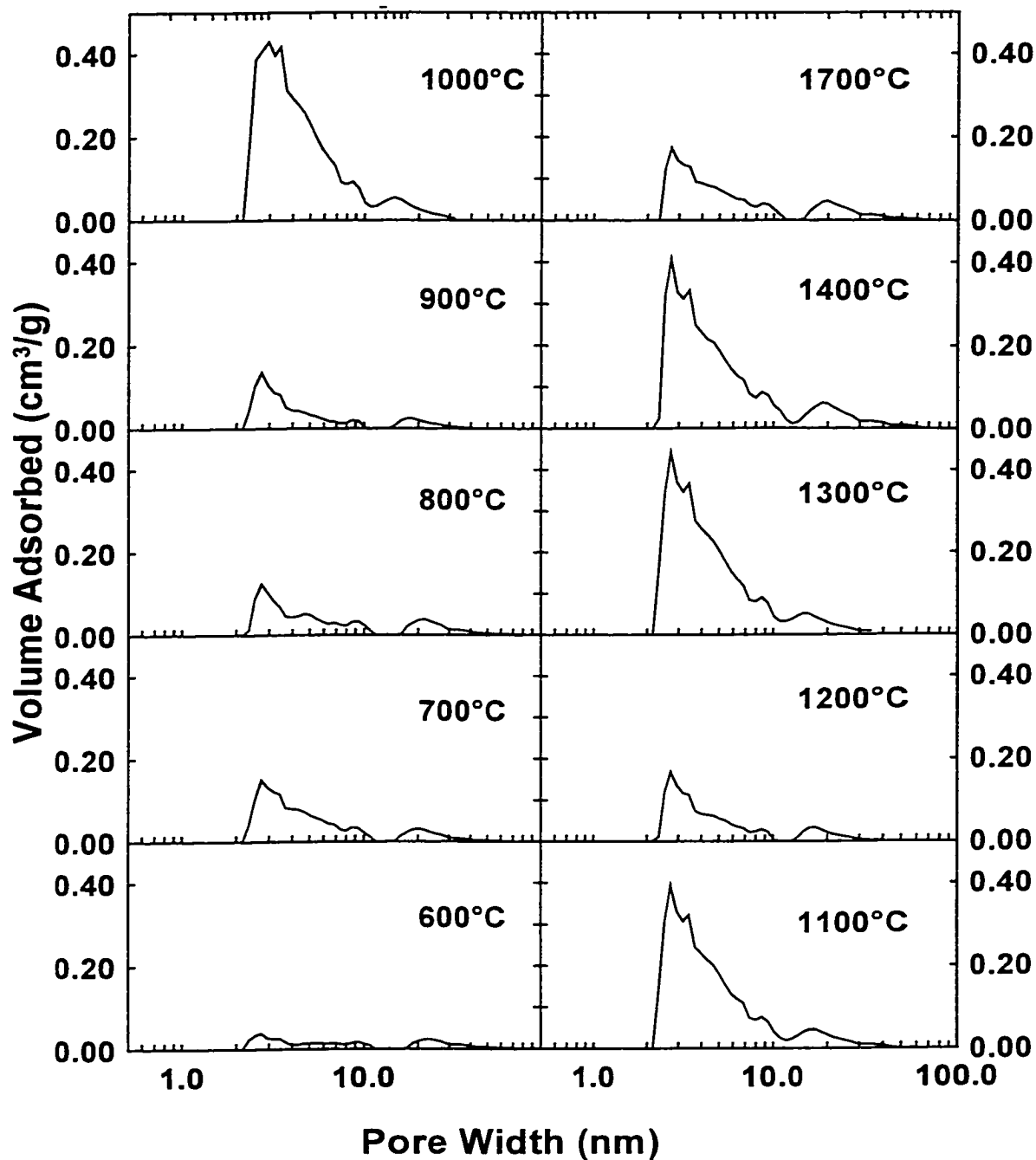


Figure 4.3: Pore size distributions for PVC carbon samples as a function of heat treatment temperature. These data were calculated with a carbon slit DFT pore model from the adsorption branch of the  $\text{N}_2$  gas adsorption isotherms presented in Figure 4.2.

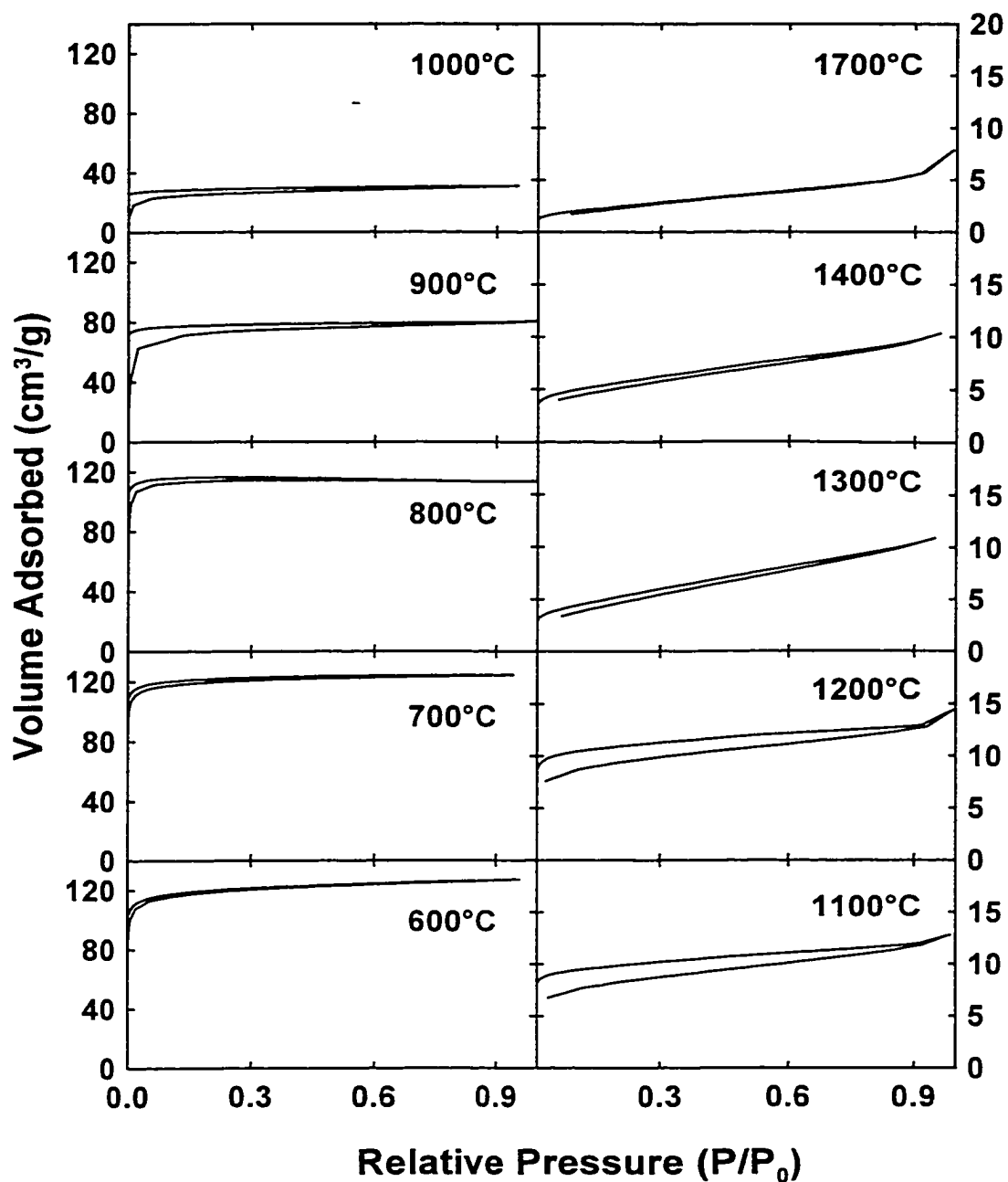


Figure 4.4:  $N_2$  Gas adsorption isotherms for glucose samples as a function of heat treatment temperature. For data sets where two curves can be resolved, the lower curve shows the adsorption data whilst the upper curve shows the desorption data. Note the different vertical scales for the panels on the right compared to those on the left.

The reduction in capacity and development of hysteresis in the gas adsorption behaviour of sugar carbons as a function of heat treatment temperature have been seen before and have been attributed to pore closure resulting from rotations of graphene sheets into a position where they block pore entrances [77]. This will be discussed in more detail in the next section on SAXS measurements.

The DFT pore size distributions for the glucose samples (Figure 4.5) clearly show the presence of nanopores of  $\sim 1$  nm in width. In fact for the samples up to 900°C, essentially all the porosity appears to be in this region. For higher heat treatment temperatures, it appears that mesoporosity develops at the expense of the nanopores and that the nanopore volume rapidly disappears. However, given that there is hysteresis between the adsorption and desorption branches of the isotherms, this is not necessarily the case – where pores have restricted openings, diffusion of gas molecules into the pores can become a major constraint for measuring the true volume adsorbed. For a material with equilibration determined as a rate of change of pressure over a fixed time interval, if molecules diffuse into pores slowly, then equilibration criteria may be met even though the adsorbate has not reached the true equilibrium state. This would result in the small pores filling at pressures higher than the true equilibrium pressure, causing the pore size distribution to appear to shift to larger dimensions. If the time interval over which the equilibration criteria are evaluated is increased then, especially for low pressure measurements, there is a good chance that instrument drift, outgassing and leaks will also effect the pressure.

Table 4.2 presents the BET and Langmuir surface area values together with the total volume of gas adsorbed for each of the PVC and glucose samples. The Langmuir equation was used for the glucose samples up to and including 900°C. After this temperature, the Langmuir plots lost linearity and hence the BET equation was used for the higher temperature glucose samples together with all the PVC samples. These data show that, as expected for materials containing a large volume of small pores, the surface area of the low temperature glucose samples was significantly higher than that for the PVC samples.



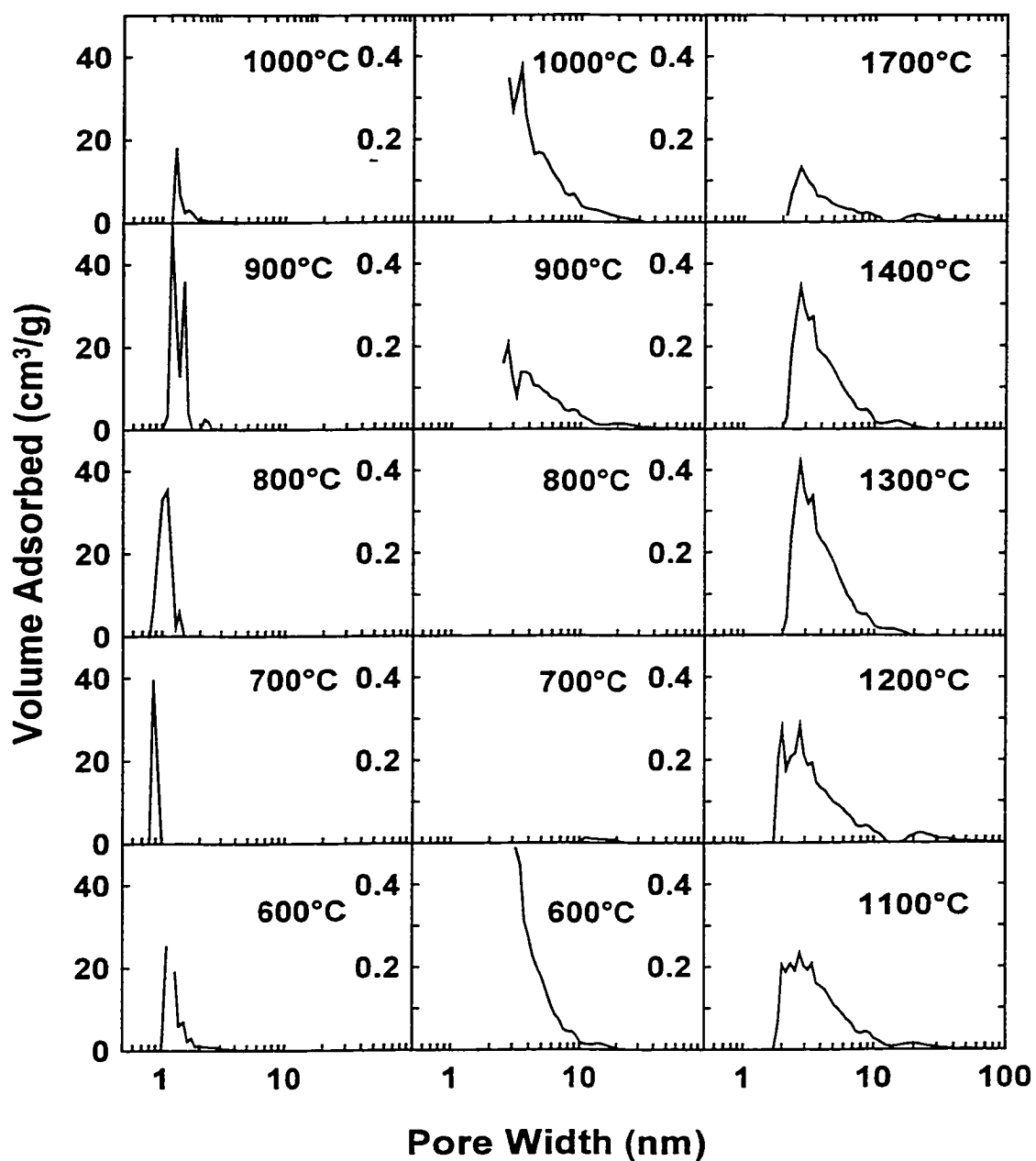


Figure 4.5: Pore size distributions for glucose derived carbon samples as a function of heat treatment temperature. These data were calculated with a carbon slit DFT pore model from the adsorption branch of the  $N_2$  gas adsorption isotherms presented in Figure 4.4. The centre panels show an expanded view of the low temperature samples for direct comparison with the results for the high temperature samples on the right.

*Table 4.2: BET and Langmuir surface areas for carbon samples as a function of heat treatment temperature. The error in these values is estimated to be less than  $\pm 10\%$ .*

Sample Temp. (°C)	PVC		GLUCOSE	
	Total Volume Adsorbed (cm <sup>3</sup> /g)	BET Surface Area (m <sup>2</sup> /g)	Total Volume Adsorbed (cm <sup>3</sup> /g)	BET/Langmuir Surface Area (m <sup>2</sup> /g)
600	6	7	127	550
700	9	10	124	540
800	10	9	114	500
900	7	7	81	350
1000	14	17	31	94
1100	9	7	13	27
1200	9	8	14	33
1300	13	15	11	16
1400	12	11	10	18
1700	9	7	8	9

### 4.3.2 SAXS Analysis

The SAXS data provide additional information on the nature of the porosity in the carbon samples. The set of SAXS curves obtained with the PVC samples is shown in Figure 4.6. The peak that is present at around  $q = 0.4 \text{ \AA}^{-1}$  is an artifact of the kapton film in the sample holder. Initially the PVC appears to have some nano-structure indicated by a hump in the SAXS profiles at  $\sim q = 0.3 \text{ \AA}^{-1}$ . As the pyrolysis temperature increases this feature disappears until, by 1700°C, the sample essentially shows only Porod's Law behaviour, implying the presence of macroporosity. Although the low temperature hump may result from the presence of nanopores in the structure, it is possible that it is actually scattering from mesophase spheres. If the feature results from nanopores, it probably comes from small disordered regions in the samples. These disordered regions become more ordered during heat treatment and hence their contribution to small-angle scattering

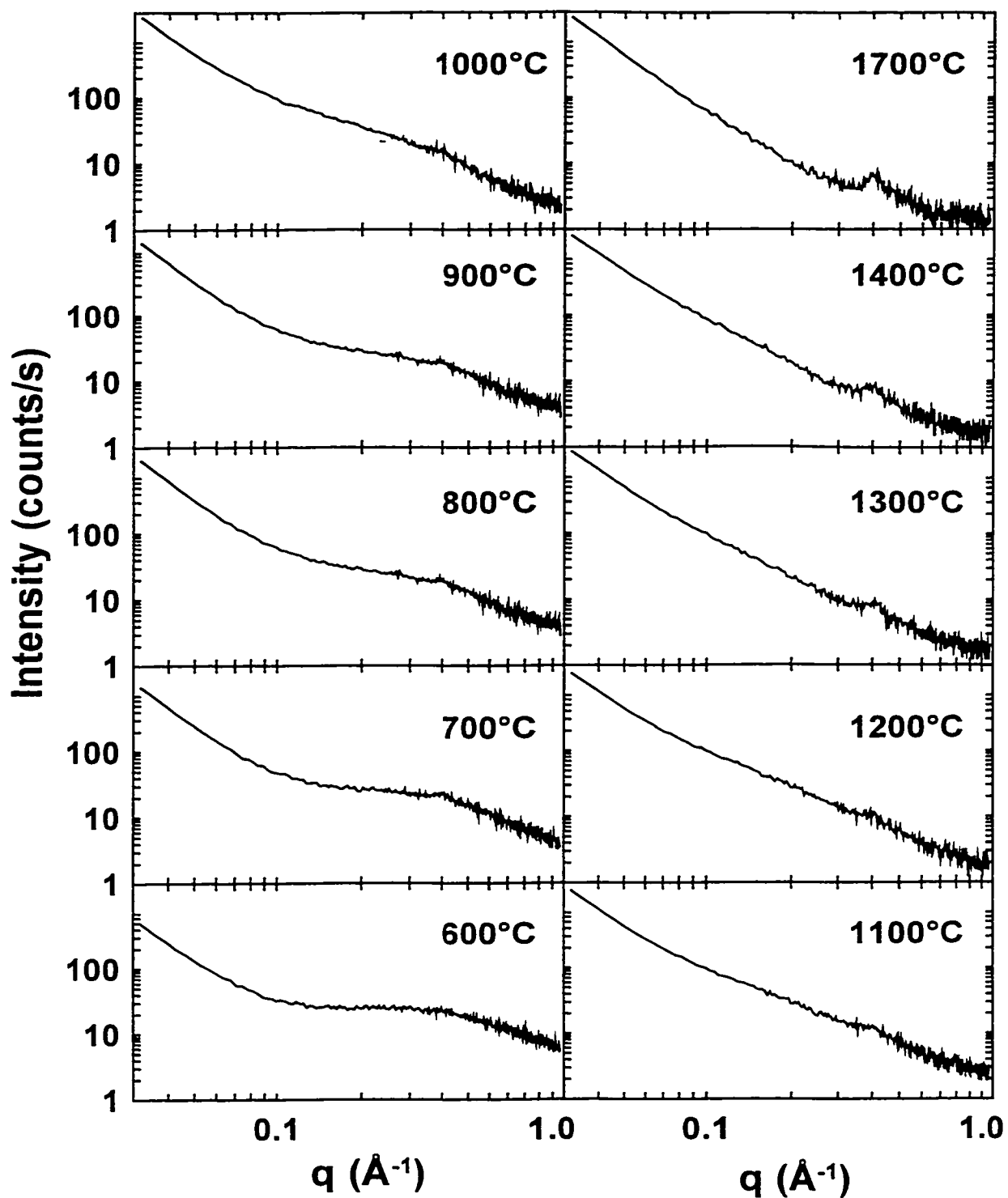


Figure 4.6: SAXS curves obtained for PVC carbon as a function of heat treatment temperature. The peak around  $q = 0.4 \text{ \AA}^{-1}$  is an artifact of the kapton film used to retain the sample in the holder.

decreases as the heat treatment temperature increases. If the feature results from mesophase then, as the spheres coalesce with increasing heat treatment temperature, their size would increase dramatically and they would therefore no longer contribute significantly to small-angle scattering.

Each small-angle curve was modeled using equation 3.41 to obtain structural fit parameters. The results obtained are listed in Table 4.3.

*Table 4.3: SAXS fit parameters for PVC samples modeled using equation 3.41 .*

<b>PVC</b>	<b>A</b>	<b>B</b>	<b>Rg(1)</b>	<b>C</b>	<b>Rg(2)</b>	<b>D</b>	<b>GOF</b>
<b>600 °C</b>	0.006	28.8	3.1	0.00000		0.0	0.18
<b>700 °C</b>	0.011	7.2	4.0	0.00000		0.0	0.18
<b>800 °C</b>	0.015	1.7	5.1	0.00000		1.6	0.17
<b>900 °C</b>	0.013	0.3	7.0	0.00000		1.5	0.15
<b>1000 °C</b>	0.017	0.1	7.9	0.00012	32	1.9	0.13
<b>1100 °C</b>	0.017	0.1	7.9	0.00012	32	1.9	0.10
<b>1200 °C</b>	0.016	0.1	8.3	0.00015	32	1.3	0.12
<b>1300 °C</b>	0.019	0.2	6.4	0.00018	32	1.1	0.11
<b>1400 °C</b>	0.017	0.3	5.5	0.00017	32	1.0	0.13
<b>1700 °C</b>	0.019	0.3	4.9	0.00007	32	1.0	0.18

The SAXS fit parameters for the PVC samples quantify the changes summarized earlier. It can be seen that the contribution from the nanosized scatterers disappears rapidly (drop in B parameter). Although a larger scatterer size is required to obtain a good quality fit for scans on higher temperature samples, the amount of this factor required is low (C parameter). These data are consistent with the gas adsorption results – both methods indicate that the amount of nanoporosity is negligible for most PVC samples.

The SAXS patterns for the glucose samples, shown in Figure 4.7, differ significantly from those obtained for the PVC samples. All samples show an increase in scattering relative to a Porod's law background over the intermediate  $q$  range. Unlike the PVC samples, this nano-size contribution increases in intensity as the heat treatment temperature increases. Close examination also suggests that this increased intensity results to some extent from a shift of the knee in the scattering curve to lower  $q$  (lower angles). As the nanopore intensity is superimposed on top of a sloping background, it is difficult to resolve the relative contributions to the total scattered intensity of the scattering from the nanopore and that from the background when the nanopore changes size. Therefore, the best way to analyse these data is to examine the fit parameters for each of the scans. These parameters are presented in Table 4.4. Only one pore size was required for this analysis.

*Table 4.4: SAXS fit parameters for glucose carbons as a function of heat treatment temperature.*

<b>Glucose</b>	<b>A</b>	<b>B</b>	<b>Rg(1)</b>	<b>D</b>	<b>GOF</b>	<b>BR<sub>g</sub><sup>3</sup></b>
<b>600 °C</b>	0.004	5.0	4.4	1.0	0.13	434
<b>700 °C</b>	0.007	1.5	6.1	1.5	0.09	329
<b>800 °C</b>	0.007	1.1	6.9	2.4	0.12	360
<b>900 °C</b>	0.005	0.6	7.8	2.2	0.12	285
<b>1000 °C</b>	0.004	0.8	7.6	1.5	0.17	380
<b>1100 °C</b>	0.003	0.8	8.0	1.6	0.21	386
<b>1200 °C</b>	0.003	0.9	7.9	2.6	0.24	444
<b>1300 °C</b>	0.004	0.5	9.0	2.0	0.32	353
<b>1400 °C</b>	0.005	0.4	9.3	0.9	0.32	317
<b>1700 °C</b>	0.003	0.2	12.1	2.0	1.03	390

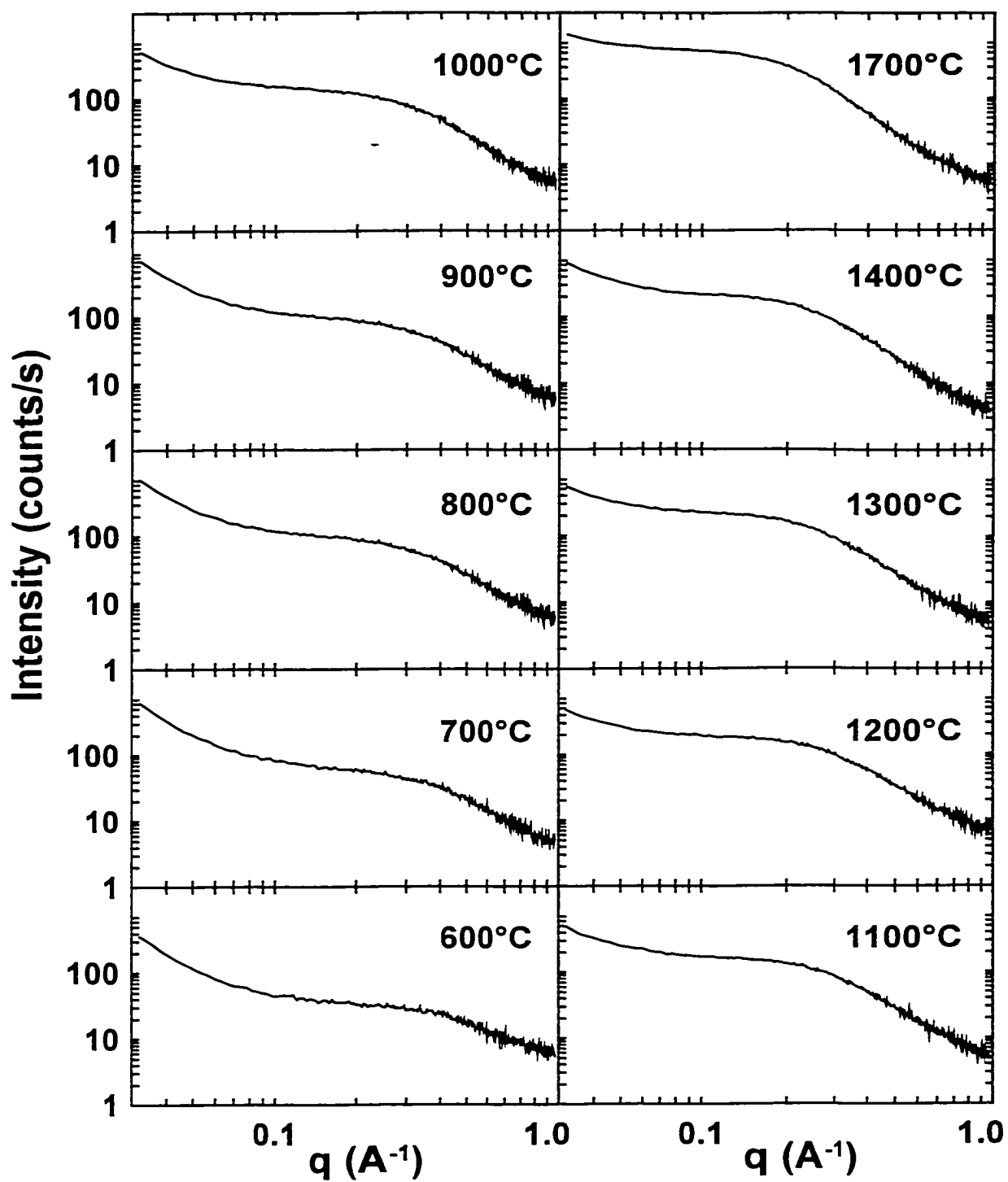
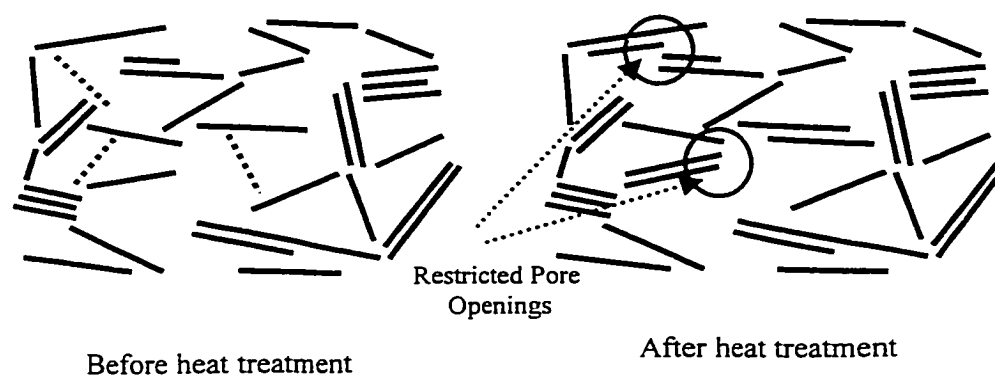


Figure 4.7: SAXS curves obtained for glucose carbon as a function of heat treatment temperature.

The fit parameters show that the pore size increases with heat treatment temperature, whilst the number of pores (as measured by the B parameter) decreases with temperature. As the B parameter is a measure of the number of pores, then the product of B and  $R_g^3$  indicates the total pore volume in the sample. This parameter is shown as the last column in Table 4.4. The values obtained for pore volume remain reasonably constant as the heat treatment temperature increases. This, together with the pore size changes, shows that as the heat treatment temperature increases, the pore volume remains fixed whilst the pore size increases, suggesting that pore walls between adjacent pores may be moving. This has been seen before and has been attributed to the rotation of graphene layers between two void volumes [77]. An example of such a process is shown in Figure 4.8. These data may appear to contradict the data obtained from gas adsorption analysis. These data showed the pore volume decreasing as the heat treatment temperature increased. However these data also showed that hysteresis developed in the isotherms, attributed to pore restrictions. Thus it is feasible that the sheets rotating to create larger pores also block off or partially restrict pore openings. Also at higher temperatures, some carbon moieties may be sufficiently mobile to diffuse from one location to another. This may also contribute to pore blockage as the carbons would tend to diffuse to the edges of sheets where more bonding sites are available.



*Figure 4.8: Schematic diagram to show how rotating graphene sheets create larger pores but may also block off pore openings. The left diagram on the left shows a low temperature sample, whilst that on the right shows the same sample after heating to a higher temperature. The rotating sheets are indicated on the left panel by dotted lines.*

### 4.3.3 WAXS Measurements

The WAXS patterns for the PVC samples (Figure 4.9) show a quite well developed 002 peak (around 25°) that increases in intensity and becomes narrower as the heat treatment temperature increases. This is consistent with the idea that these samples (and soft carbons in general) contain graphite-like domains that show an increase in layer stacking as the heat treatment temperature increases. The 100 peak (around 44°) also develops with heat treatment temperature consistent with an increase in size of the layers, as coalescence of domains occurs.

The WAXS patterns in Figure 4.10 show that the structure of the carbons derived from glucose change only slowly with increasing heat treatment temperature. There is some development of the 002 peak, although it still remains quite low in intensity relative to the background. This implies that layered stacking only occurs to a small extent in these materials, consistent with a structure where the layers are pinned relative to each other and require large energies (i.e. high temperatures) in order to break the interlayer crosslinking bonds. The slow development of the 002 peak is consistent with the pore closure mechanism proposed in the previous section – as some layers rotate into parallel alignment with other layers, the average number of layers per stack will increase. Given that it is unlikely that more than one layer within a pore will rotate, it is probable that the maximum extent of stacking extends only a few layers. There also appears to be some development of the 100 peak, implying that there is lateral growth of layers, although, as with the 002 peak, intensity over this angular range also only develops slowly.

In order to quantify the changes, layer stacking ratios ( $R$ ) for these samples together with the 002 average interlayer spacing ( $d_{002}$  – determined from the position of the peak maximum),  $L_c$  crystallite height values and  $L_a$  values calculated from the width and position of the 100 peaks are presented in Table 4.5. The layer stacking ratio,  $R$ , is simply the ratio of peak height to the height of the background, and provides an indication of the average number of stacked layers. The 002 peak position cannot be readily extracted from the data measured by the diffractometer, especially for the glucose



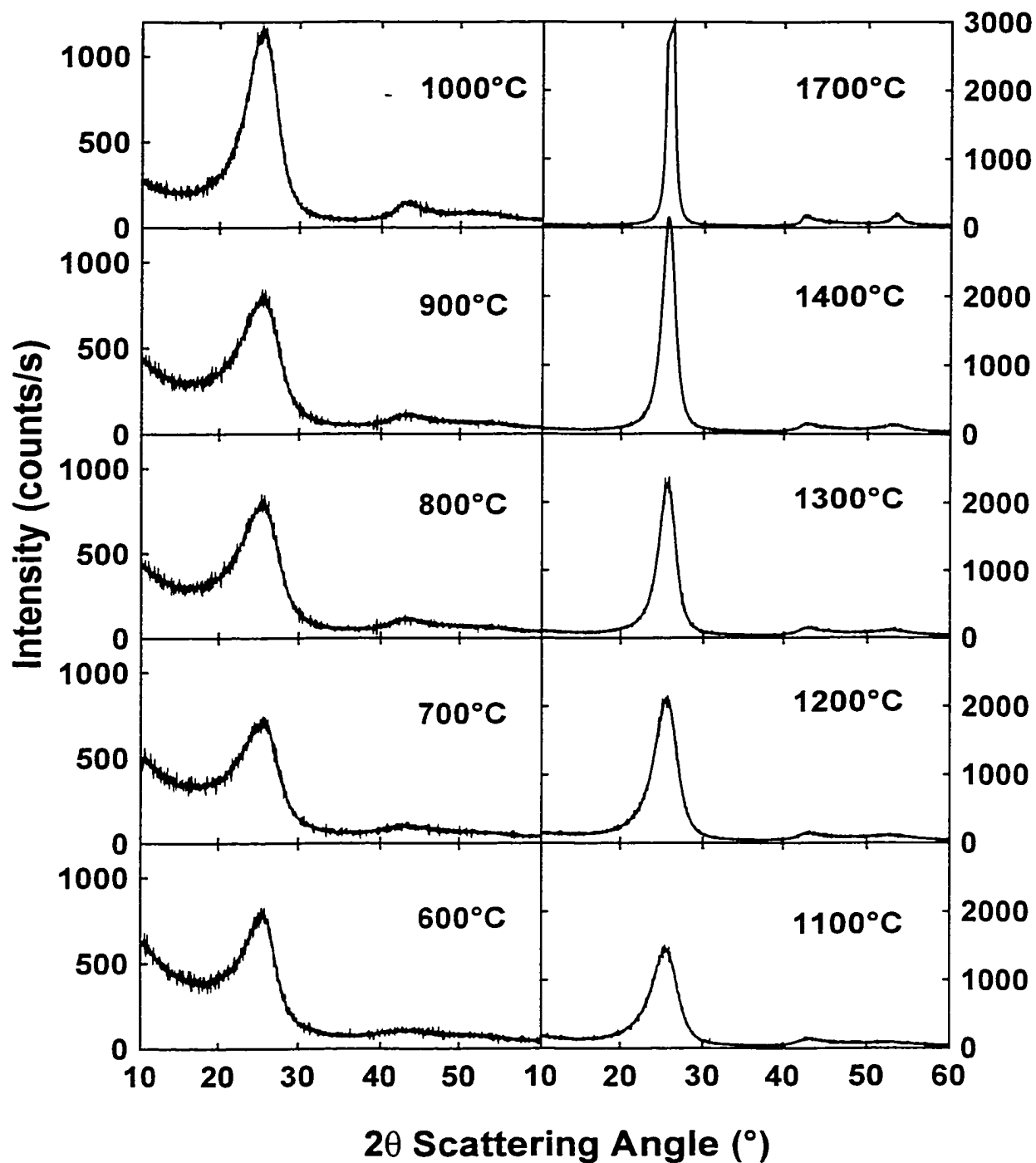


Figure 4.9: WAXS patterns measured on carbons derived from PVC as a function of heat treatment temperature. Note the difference in scale between the panels on the left and those on the right.

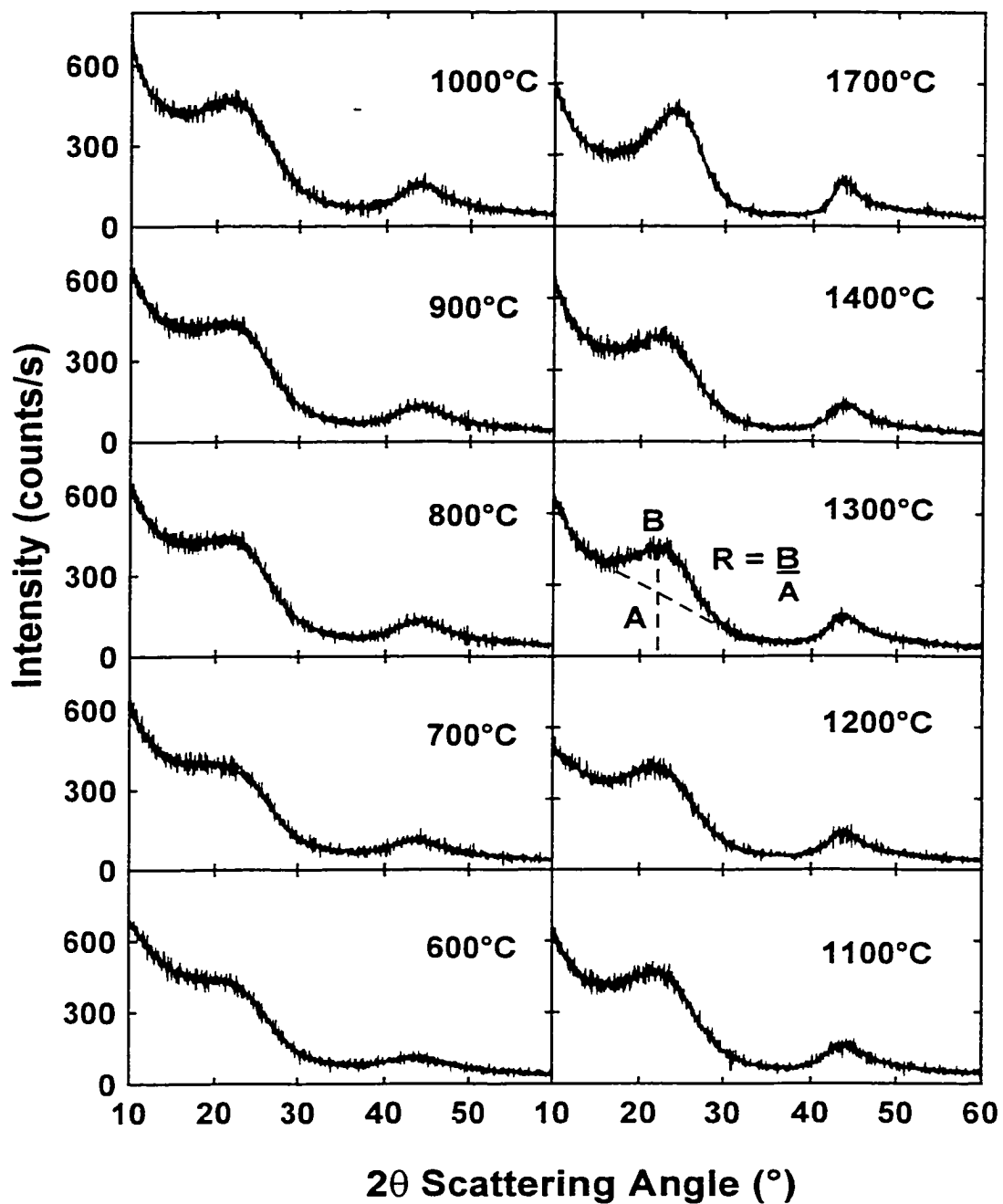


Figure 4.10: WAXS patterns measured on carbons derived from glucose as a function of heat treatment temperature. The method used to calculate the layer stacking ratio,  $R$ , is indicated on the 1300°C sample.

glucose samples. In order to determine the true peak position, the data need to be corrected for the change in atomic scattering factor with scattering angle together with the Lorentz and polarization factors. Figure 4.11 presents the WAXS data for the PVC samples whilst Figure 4.12 presents the WAXS data for the glucose samples after the corrections have been applied. This set of graphs shows that there is very little shift in the position of the 002 peaks in the PVC samples because they are already quite narrow, minimising the impact of the corrections. For the glucose carbons on the other hand, the correction causes the peaks to shift to higher angles, much closer to those seen for the PVC carbons.

*Table 4.5: Parameters calculated from WAXS patterns for both PVC and glucose.*

Temp.	PVC				GLUCOSE			
	R	$d_{002} \pm 0.2 \text{ \AA}$	$L_c (\text{\AA})$	$L_a (\text{\AA})$	R	$d_{002} \pm 0.5 \text{ \AA}$	$L_c (\text{\AA})$	$L_a (\text{\AA})$
600 °C	4	3.4(1)	11	24	1.4	3.6	9	20
700 °C	4	3.3(8)	10	31	1.4	3.5	8	23
800 °C	5	3.4(1)	13	33	1.5	3.5	8	25
900 °C	5	3.4(0)	12	36	1.6	3.5	9	27
1000 °C	11	3.4(2)	15	41	1.7	3.5	9	36
1100 °C	17	3.4(3)	21	52	1.6	3.5	9	36
1200 °C	24	3.4(3)	21	59	1.7	3.5	9	36
1300 °C	35	3.4(3)	29	61	1.7	3.5	9	36
1400 °C	73	3.4(3)	37	66	1.7	3.5	9	36
1700 °C	147	3.4(3)	102	81	2.7	3.5	11	45

The R values for the two materials clearly show the difference in layer stacking as a function of heat treatment temperature. The PVC samples show a rapid increase in R with increasing heat treatment temperature. The glucose samples on the other hand show only slight changes in R. The  $L_c$  values show the same trends as these R values, which is to be expected as they are measures of the same property. The interlayer spacing for the glucose samples is slightly higher than that for the PVC samples, although this may in

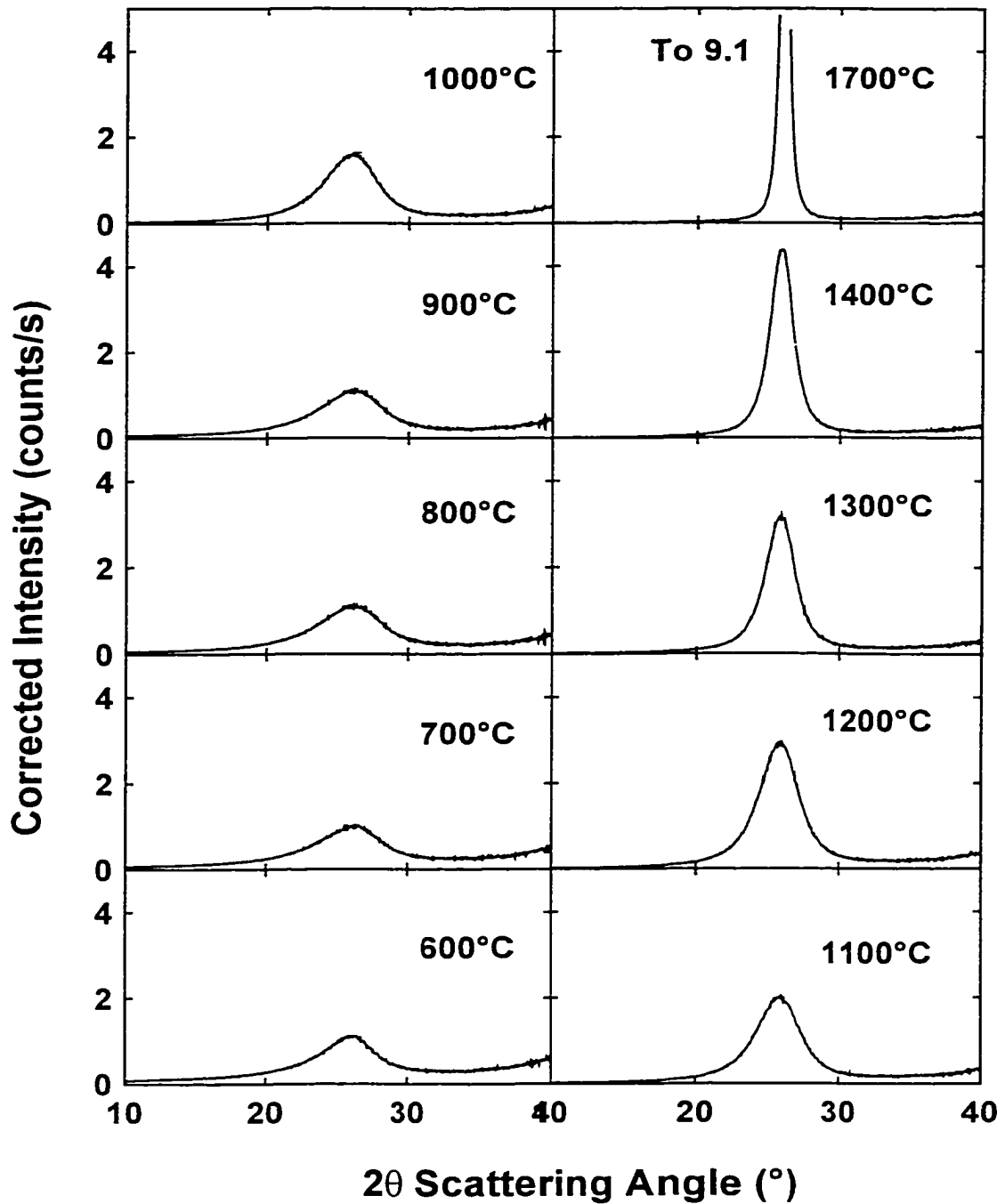


*Figure 4.11: WAXS patterns measured on carbons derived from PVC as a function of heat treatment temperature after correcting for the effects of the atomic scattering factor and applying the Lorentz-Polarization correction .*

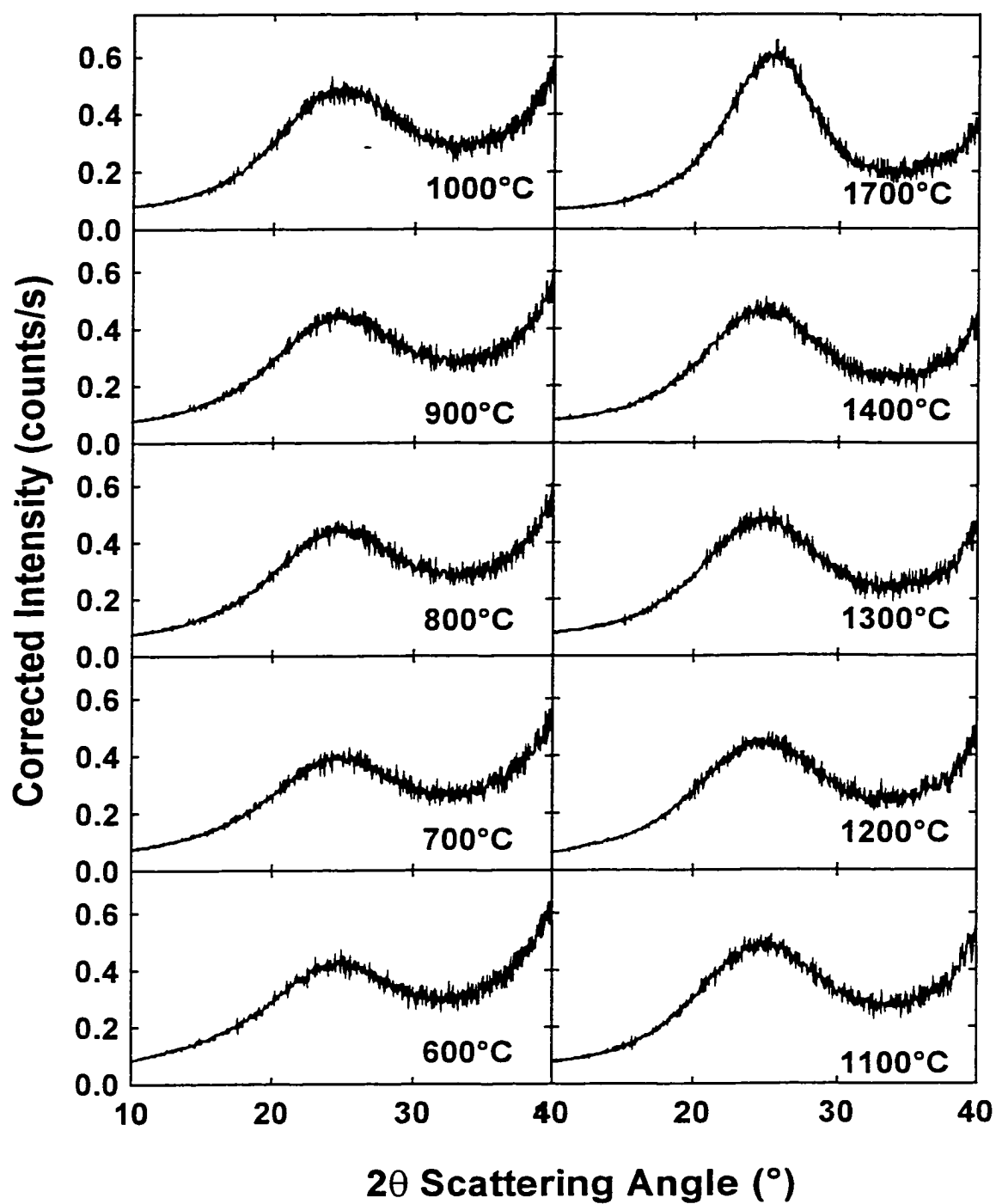


*Figure 4.12: WAXS patterns measured on carbons derived from glucose as a function of heat treatment temperature after correcting for the effects of the atomic scattering factor and applying the Lorentz-Polarization correction .*

part be due to the difficulties of finding the peak maximum in the WAXS patterns. For both the PVC and glucose samples, the interlayer distance is larger than the distance found in 2H graphite. This increased distance most likely results from turbostratic disorder within the material preventing layers from aligning in an ordered ABAB... type stacking sequence. For both materials the average sheet size increases with increasing temperature although it appears that the PVC samples increase in this dimension more than the glucose samples.

## **4.4 Carbon Models**

Based on the data presented in this chapter, the following models can be proposed to explain structural development in hard and soft carbons respectively.

### **4.4.1 Soft Carbon Model**

Soft carbons contain very little nanoporosity even during early stages of heat treatment, primarily because of significant layer stacking. As the heat treatment temperature increases, the number of stacked layers in small crystallite domains increases rapidly, whilst the lateral dimension of the sheets increases more slowly. These carbons can contain meso and macroporosity, allowing for multilayer gas adsorption, probably arising from a random arrangement of small crystallite domains. Even up to high temperatures ( $\sim 1700^{\circ}\text{C}$ ), the carbons contain turbostratic disorder which prevents all the layers stacking in a regular arrangement.

### **4.4.2 Hard Carbon Model**

Hard carbon materials tend to develop large volumes of nanoporosity at low temperatures. There is little change in the volume of porosity in these carbons as they are heat treated to higher temperatures, although the average pore size appears to increase. This increase in average pore size may occur through rotation of pore walls between adjacent pores into parallel alignment with other graphene sheets. This rotation has three

effects: it increases the pore size as required, it leads to a small increase in the average number of layers in a stack and it can result in pore openings being partially blocked if it rotates into the opening. This blockage causes the volume of open porosity measured by gas adsorption techniques to decrease, both through increased diffusion times and by creating a bottleneck in the adsorption process. It is also likely that many of the pore openings become small enough to prevent gas molecules entering.

The validity of these models is demonstrated in Figures 4.13 and 4.14, where the SAXS and WAXS patterns for the Pitch (soft carbon) and Resin (hard carbon) samples are presented. Values calculated from the SAXS and WAXS patterns in accordance with the methods used to quantify the changes in the PVC and glucose carbons are summarised in Tables 4.6 and 4.7.

The SAXS patterns show the presence of nanoporosity in the hard carbon that remains even after heat treatment to high temperature. As with the glucose samples, an increase in the average pore size shifts the contribution from the nanopores to the scattered intensity to lower angles, whilst the total pore volume remains approximately constant. The pitch carbons show some initial nanoporosity that rapidly disappears as the heat treatment temperature increases, leaving a material with primarily meso and macropores (Porod's law slope in SAXS curves).

The WAXS patterns show only slow development of carbon layering in the resin samples, with much of this probably resulting from graphene sheet rotations to create larger pores. The pitch samples show rapid growth of layered crystallites with increasing heat treatment temperature, consistent with a material that is highly mobile. Again, the interlayer spacing is large, implying the presence of significant turbostratic disorder.

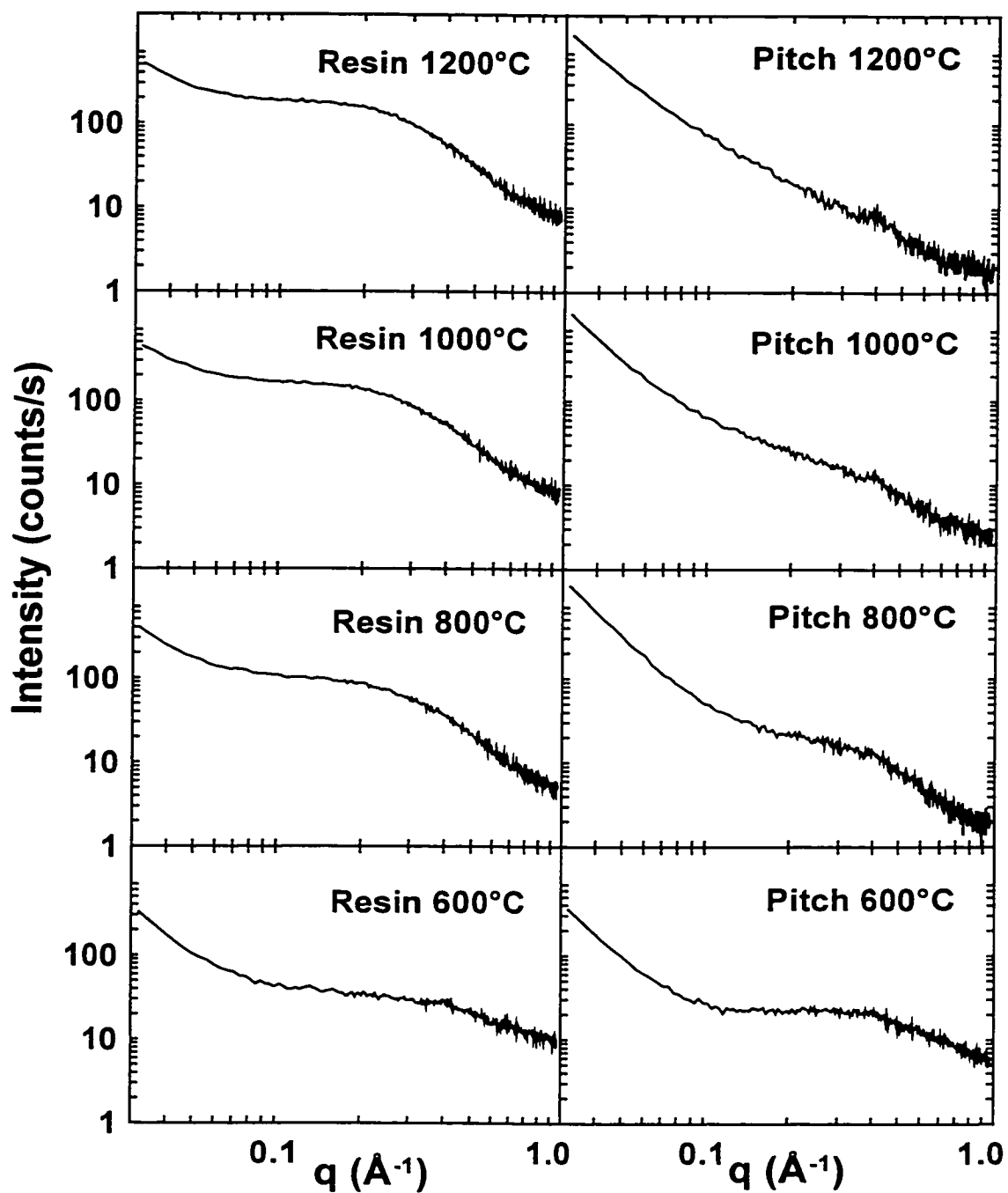


Figure 4.13: SAXS patterns for resin carbons (left panels) and pitch carbons (right hand panels). As with previous SAXS curves, the peak at around  $0.4 \text{ \AA}^{-1}$  comes from the kapton windows in the sample holder.



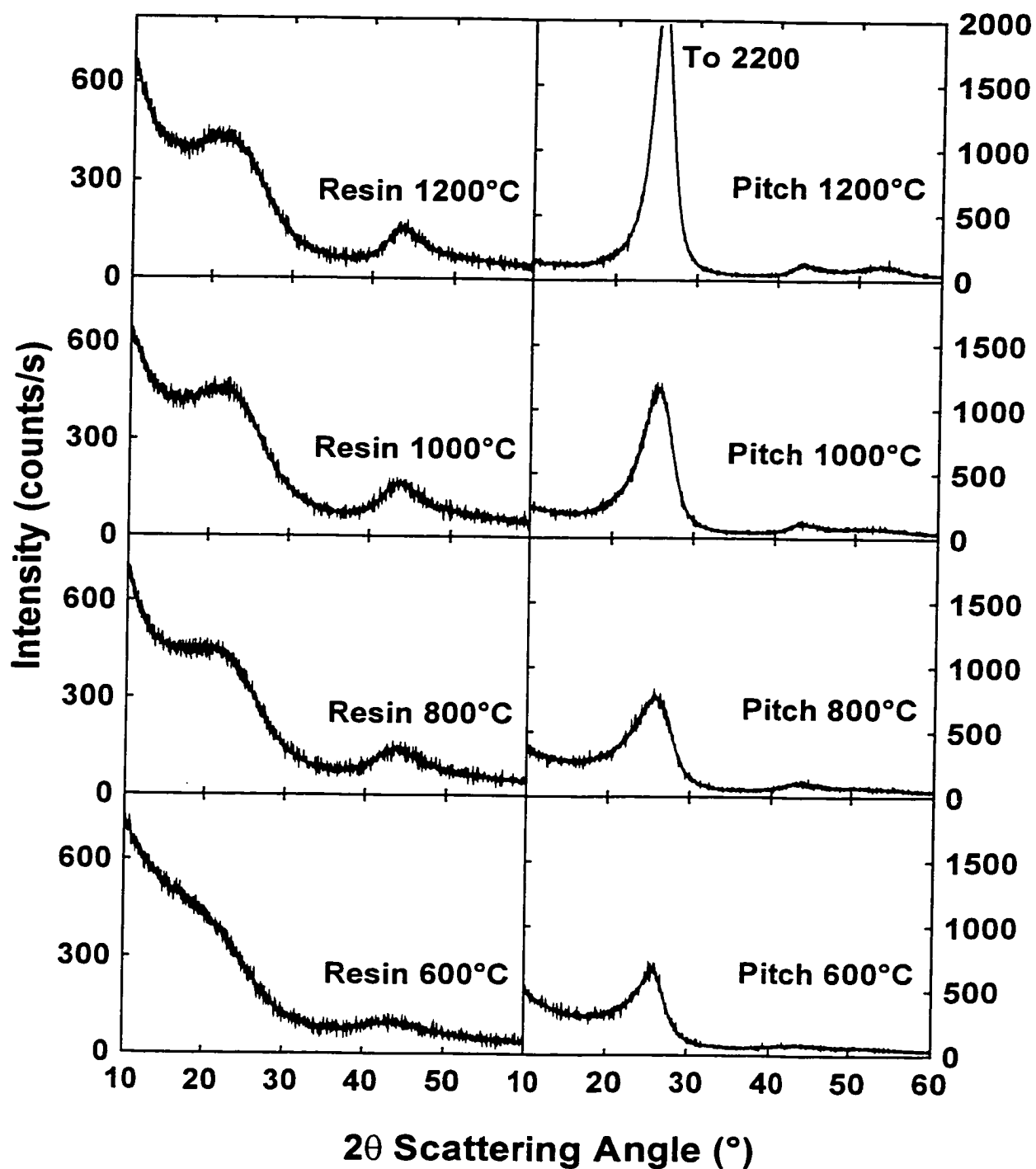


Figure 4.14: WAXS patterns for resin carbons (left panels) and pitch carbons (right hand panels).

*Table 4.6: Calculated SAXS Parameters for Pitch and Resin samples.*

<b>PITCH</b>	<b>A</b>	<b>B</b>	<b>Rg(1)</b>	<b>BR<sup>3</sup></b>	<b>D</b>	<b>GOF</b>
<b>600 °C</b>	0.004	24.12	3.15	757	0.0	0.20
<b>800 °C</b>	0.015	0.80	5.56	137	0.3	0.19
<b>1000 °C</b>	0.013	0.10	8.50	61	2.2	0.16
<b>1200 °C</b>	0.013	0.00	15.57	18	2.2	0.31

<b>RESIN</b>	<b>A</b>	<b>B</b>	<b>Rg(1)</b>	<b>BR<sup>3</sup></b>	<b>D</b>	<b>GOF</b>
<b>600 °C</b>	0.0035	3.58	4.56	339	6.7	0.09
<b>800 °C</b>	0.0034	0.73	7.35	290	2.0	0.16
<b>1000 °C</b>	0.0031	0.78	7.88	383	3.8	0.29
<b>1200 °C</b>	0.0036	0.81	8.01	416	3.3	0.49

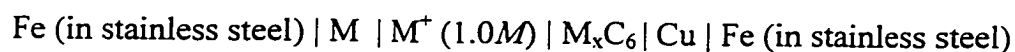
*Table 4.7: Calculated WAXS Parameters for Pitch and Resin samples.*

<b>Temp.</b>	<b>Pitch</b>				<b>Resin</b>			
	<b>R</b>	<b>d<sub>002</sub>(Å)</b>	<b>L<sub>c</sub>(Å)</b>	<b>L<sub>a</sub>(Å)</b>	<b>R</b>	<b>d<sub>002</sub>(Å)</b>	<b>L<sub>c</sub>(Å)</b>	<b>L<sub>a</sub>(Å)</b>
<b>600 °C</b>	4.1	3.43	18	22	1.1	3.6	7	18
<b>800 °C</b>	5.2	3.41	15	32	1.4	3.5	8	26
<b>1000 °C</b>	11	3.43	16	36	1.6	3.5	8	29
<b>1200 °C</b>	31	3.45	25	63	1.6	3.5	8	28

## Chapter 5

### Electrochemical Testing

The electrochemical cells used for this project are conceptually simple. A slurry of carbon powder coated onto a copper foil acts as one electrode whilst either lithium or sodium metal acts as the counter electrode. The electrodes are immersed in an electrolyte solution containing the hexafluorophosphate salt of the metal dissolved in an organic solvent. In traditional electrochemical notation, the cell can be written as:



A schematic diagram of such a cell is presented in Figure 5.1, where the carbon is

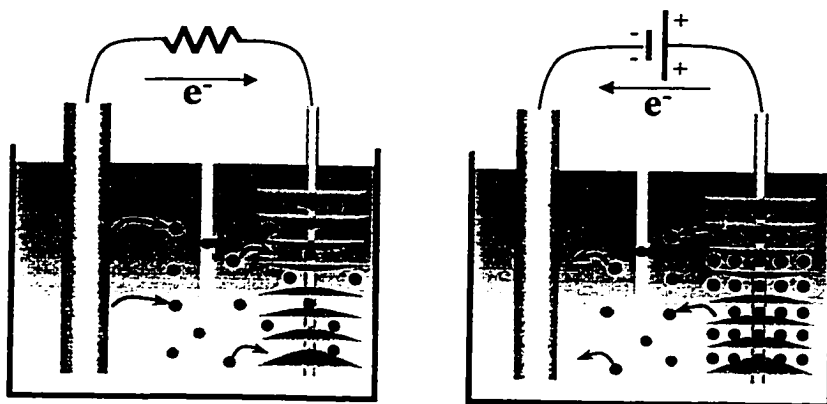


*Figure 5.1: Schematic diagram of electrochemical cells used in this study. The electrode on the left is the metal whilst that on the right is the test material. The left and right hand panels show the movement of ions and electrons during discharge and charge.*

represented by an ideal layered structure such as would be found in graphite. The first panel shows the spontaneous direction of operation of the cell – ions from solution enter the carbon matrix to combine with an electron from the external circuit. The metal electrode ionises, providing charge balance through release of both a metal ion and an electron. When the current flows in this direction, the cell is said to be discharging.

If an external potential is applied such that the current direction is reversed, then the reverse process occurs, as shown in the right hand panel. The metal is released from the carbon matrix whilst metal ions plate onto the metal electrode. When the current flows in this direction, the cell is said to be charging. Performing one discharge and one charge constitutes a cycle for the cell. The capacity for a given discharge or charge stage is the amount of charge (in mAh) passed during that stage per gram of active material.

The capacity is directly proportional to the amount of metal ions inserted into or removed from the carbon electrode.

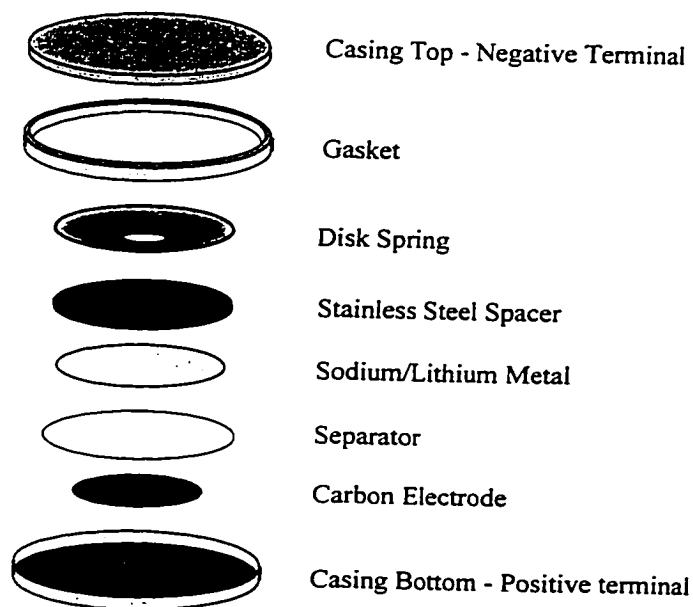


*Figure 5.2: Expanded view of cell components*

Figure 5.2 presents a schematic diagram of the actual coin cell design used. The separator material is a porous polypropylene film that prevents direct electrical contact

between the carbon and alkali metal electrodes whilst allowing solvated ions to flow. The disk spring is included to maintain constant pressure between the two electrodes. All coin cells were assembled and then hermetically sealed in a glove box under argon to prevent air exposure.

## 5.1 Thermodynamics of Operating Cells

If the chemical potentials of metal atoms in the two electrodes are  $\mu_{\text{metal}}$  and  $\mu_{\text{carbon}}$  respectively (in conventional electrochemical notation, the anode is the metal electrode during discharge and the carbon electrode during charge), then the free energy change that occurs when a metal “atom” moves from the metal electrode into the carbon is:

$$\Delta G = \mu_{\text{carbon}} - \mu_{\text{metal}} \quad (5.1)$$

The amount of electrical work ( $W$ ) done when  $n$  moles of electrons flow across a potential difference  $\varepsilon$  is:

$$W = nF\varepsilon, \quad (5.2)$$

where  $F$  is Faraday’s number, the charge on one mole of electrons.

If it is assumed that the amount of PV work occurring as the electrodes expand and contract is negligible [19], then the change in free energy of the alkali species is equal in magnitude to the amount of electrical work performed, i.e.

$$\Delta G = -nF\varepsilon. \quad (5.3)$$

Combining equation 5.1 with equation 5.3 when one electron flows gives:

$$-\varepsilon = \mu_{\text{carbon}} - \mu_{\text{metal}}, \quad (5.4)$$

(where  $e$  is the magnitude of the charge on an electron) which can be rearranged to:

$$\varepsilon = \frac{-(\mu_{\text{carbon}} - \mu_{\text{metal}})}{e}. \quad (5.5)$$

This equation shows that the open circuit voltage of a cell depends on the difference in chemical potential of alkali species in the two electrodes. As the chemical potential of metal atoms in the metal electrode is constant, the open-circuit voltage is effectively a measure of the chemical potential of metal atoms in the carbon electrode. Hence a graph of potential difference versus metal content in the carbon is, in essence, a graph of the chemical potential of the alkali species in the insertion sites in the carbon electrode (relative to the chemical potential of the metal).

Although the open circuit potential difference of the cells made in this study is a measure of the chemical potential of lithium/sodium species in the carbon electrodes, there are a number of other factors that will contribute to the measured cell potential when current is flowing. The materials in the cell provide an internal resistance, which manifests itself as an IR drop. This internal resistance arises primarily from the relatively low conductivity of the electrolyte solution. The presence of this IR drop is shown in Figure 5.3. This figure contains discharge-charge profiles for carbon electrodes where the current flow has been halted at regular intervals. The upper panel shows the measured sodium behavior, whilst the lower panel shows the lithium behavior. The IR drop for the lithium cell is larger than that for the sodium cell presumably because the lithium cell was operated at twice the current used in the sodium cell. Also there are most likely differences in ionic conductivity between the two electrolyte solutions. Although the calculated resistance is quite high ( $\sim 400 \Omega$ ), because the cells are operated at such low currents ( $\sim$  microamps), the resultant IR drop is low enough that it does not change the position of the electrode potential significantly ( $< 0.05 \text{ V}$ ). It certainly does not change the shape of the voltage profiles, which is the most important part of these data.

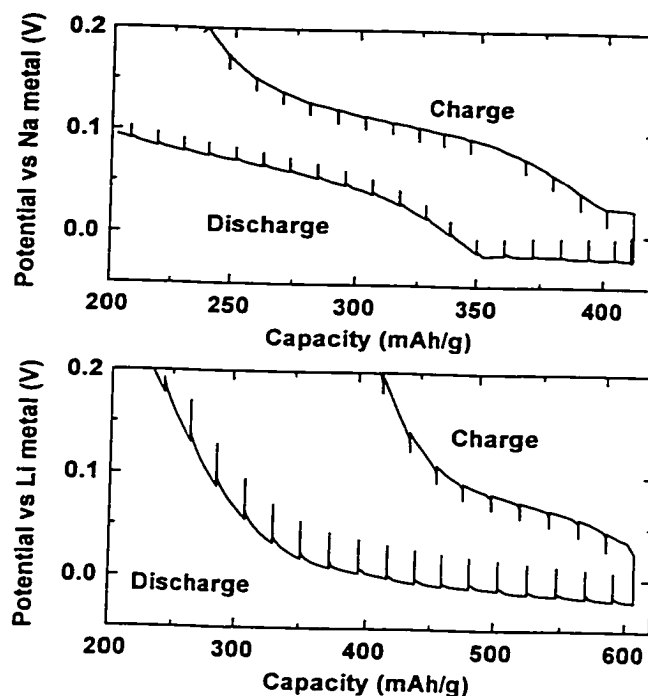


Figure 5.3: Measurement of IR drop within operating cells. Upper panel – sodium cell, lower panel – lithium cell.

## 5.2 Kinetics within operating cells

There are two factors that can impose a kinetic limitation on cell potential. The first is diffusion of species through the electrodes, the second is limitations imposed by kinetic barriers to insertion of lithium/sodium species into some sites within the carbon host. Diffusion effects can be minimised by operating at low currents. Activation effects are inherent to the materials being examined and cannot be eliminated in these cells. If there is an activation barrier to some insertion process that is large relative to the thermal energy,  $k_B T$ , then insertion of species into these sites will only occur slowly (if at all) once the cell potential is lower than the chemical potential of the alkali species in those sites. As more alkali species insert into alternative sites, it is reasonable to expect that the magnitude of the activation barrier may be reduced by changes in the local chemical environment. Thus if the cell potential is low enough, the sites “protected” by an activation barrier can be filled, although they will fill at a potential lower than the

chemical potential of the alkali species in those sites. This will produce hysteresis in the voltage profiles, with insertion occurring at a significantly lower cell potential than removal. Such behaviour has been seen with hydrogen containing carbons [78] and will be discussed in more detail in section 5.5.2.

### 5.3 Interpretation of Electrochemical Data

Figure 5.4 shows the different terminology used in discussing the electrochemical data. The upper panel shows the data after converting run time into capacity. As the cell discharges, the potential drops. Once the potential drops below 0 V relative to the metal, the cell is allowed to continue discharging until the metal plating is detected. This is shown in the inset in the upper panel where there is an obvious change in gradient of the potential curve. Once plating is seen, the current direction is reversed and the cell potential increased again. The lower panel shows the same data in an alternative format. In this case, the capacity during charge is folded back on top of the discharge. This format makes it easy to resolve the irreversible capacity (capacity loss between first discharge and first charge) and the reversible capacity (the amount of metal that can be inserted into and then removed from the carbon). This format also makes it easy to see hysteresis between discharge and charge and to see the capacity in regions such as the low voltage plateau. This format will be used to present the electrochemical data obtained on all carbon samples.

## 5.4 Experimental

### 5.4.1 Construction of thin film cells

Electrodes were prepared by dissolving ~ 200 mg of the carbon powder together with ~ 10 mg of super S carbon black (MMM Carbon) in ~ 140 mg of N-methyl pyrrolidinone (NMP) containing ~ 10 wt% poly(vinylidene fluoride) (PVDF) in NMP (NRC,Ottawa). Additional NMP was added to produce an appropriate slurry consistency.



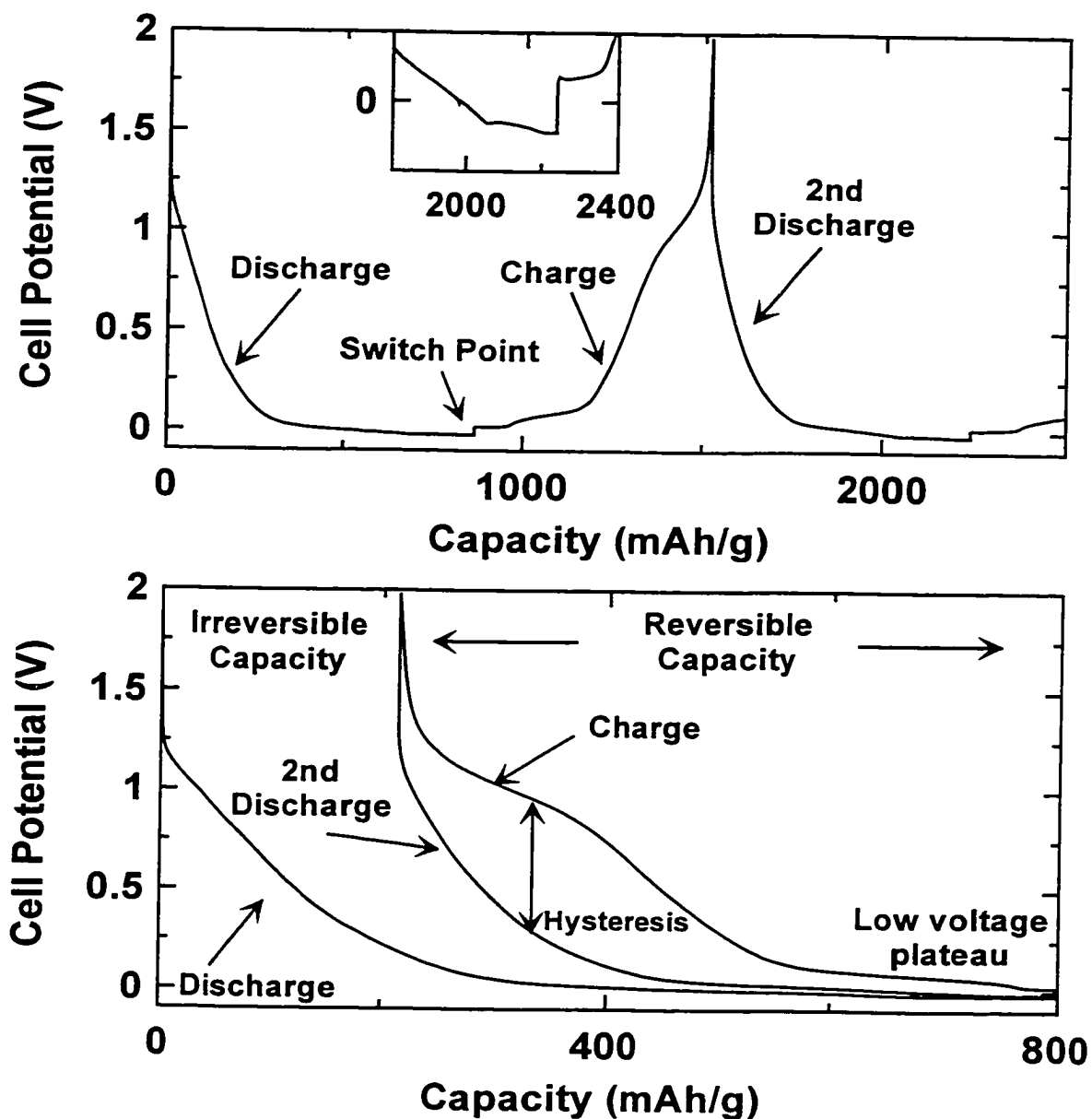


Figure 5.4: Interpretation of electrochemical test results. The upper panel is a potential vs capacity curve. The lower panel shows the same data with the charge folded back over the discharge data.

The slurry was mixed well and then poured out onto a piece of copper foil. The slurry was spread evenly onto the copper foil with a doctor blade and dried for ~ 2 hours in an

oven held at 110°C. A 12.5 mm diameter circular electrode containing ~ 8 mg of active material (i.e. the carbon), was then punched from this foil and taken into an argon filled glovebox and placed in the stainless steel cell can. Enough electrolyte solution (1M LiPF<sub>6</sub> or NaPF<sub>6</sub> dissolved in a 33:67 vol% blend of ethylene carbonate/diethyl carbonate – EC:DEC) was added to moisten the electrode. A Celgard 2400 microporous polyethylene film separator was added followed by more electrolyte. For the sodium cells, two polypropylene mesh spacers and a second separator were also added to enable the cells to run without shorting. Metal foils (commercially available for lithium, pressed by hand for sodium) were then added followed by the stainless steel spacer and disk spring combination. The cell top was added (isolated from the can by the polypropylene gasket) and the cell was hermetically sealed with a crimper. Stainless steel tabs were welded to the outside to allow for electrical contact to the charger bank. A current of 40 μA was used for the sodium cells whilst 80 μA was used for the lithium cells. These currents were low enough so that the cells were close to equilibrium at all times but also high enough to complete the required measurements in a reasonable period of time.

#### 5.4.2 Construction of *in situ* x-ray cells

For *in situ* x-ray measurements, more material was required than present on the copper foil in order to enhance the x-ray scattering. Pellet stock was prepared by mixing 6 g of carbon powder with ~ 0.3 g super S and 6 g of a binder solution containing ~ 2.5 wt% ethylene propylene diene terpolymer (EPDM) dissolved in cyclohexane. Excess cyclohexane was added and the resultant slurry was mixed with zirconia media beads in a shaker bottle for five minutes. The cyclohexane was then allowed to evaporate in a fumehood, giving a friable powder. Circular pellets containing ~ 0.1 g of active material were then pressed from this powder under 15,000 kPa with a hydraulic press.

For the *in situ* WAXS cells, a circular hole 17 mm in diameter was cut into the stainless steel can. Roscobond (Rosco, Port Chester, N.Y) pressure sensitive adhesive was applied to the inner rim of the can and a 0.01” thick beryllium window (Brush-Wellman, Grade PF-60) was pressed into the can against the rim. For the *in situ* SAXS

cells a hole was also cut in the cell cap. A 0.02" thick window was used in the can and a second window, 0.03" thick was pressed into the cell cap, again using Roscobond for adhesion. This window was required in the cap to allow the cell to be operated in transmission mode.

The *in situ* cells were assembled in the glovebox. The pellet was placed on the Be window in the cell can and saturated with electrolyte. Two separators were then added followed by the metal foil. A thin spacer and spring combination was used in the WAXS cells. As the spring and spacer absorbed x-rays strongly, they could not be used in the SAXS cells. The thicker Be windows in these cells provided the pressure required to provide good contact between the electrodes. After crimping, the cells were removed from the glovebox and beads of Torr-Seal epoxy resin (Varian) were placed around the edges of the holes in the can and cap in order to seal the joint completely (if no Torr-seal is added, the cell started leaking electrolyte after some time, suggesting that the electrolyte solution slowly dissolved the Roscobond).

The *in situ* WAXS cells were installed into a cell holder as shown in Figure 5.5. This holder maintained the cell in the correct location and orientation in the diffractometer whilst also providing electrical contact to both sides of the cell. The *in situ* SAXS cells were installed vertically in a delrin holder mounted in the diffractometer. This holder also provided electrical contact to the cell. A SAXS cell in the holder is shown in Figure 5.5.

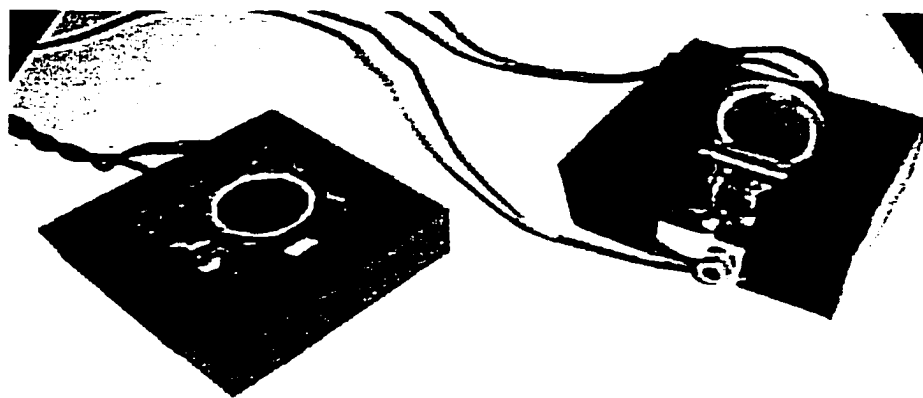


*Figure 5.5: Sample holders used for in situ WAXS (left) and SAXS (right) measurements.*

## 5.5 Electrochemical Test Results

### 5.5.1 Graphitic Carbon

The electrochemical curve for the graphitic carbon against lithium (Figure 5.6a) shows that such materials can accommodate a large amount of lithium ( $\sim 1$  lithium for every 6 carbons) with this capacity occurring along a set of plateaus in the potential curve. These plateaus correspond to the development of staged intercalation compounds, where the  $n$ th stage is  $n$  carbon layers separating each layer of lithium atoms. As the capacity increases, the stage number decreases, implying that the lithium layers become closer together.

The potential-capacity curve of the graphite against sodium (Figure 5.6b) shows that very little sodium can be incorporated into the carbon host (with no evidence for staging). In fact much of the capacity observed corresponds to insertion of sodium into the carbon black in the electrode together with some plating on the electrode surface, seen in the inset of Figure 5.6b. Normally the carbon black capacity is small relative to the capacity of the electrode and can be ignored to a first approximation. For example, in these electrodes, the small amount of super S contributes  $\sim 9$  mAh/g to the lithium capacity [79] and  $\sim 5$  mAh/g to the sodium capacity (measured during this project). In this case, because the sodium capacity is so low, the contribution from the carbon black to the reversible capacity cannot be ignored.

The observation that very little sodium intercalates into graphitic carbon under normal pressures is consistent with observations from other authors [11], [80]. Theoretical calculations suggest that this behaviour occurs because the attractive interaction between intercalated sodium and the carbon layers is extremely weak [81]. Thus there is no strong energetic driving force to encourage the sodium to intercalate rather than deposit as metal on the electrode surface.

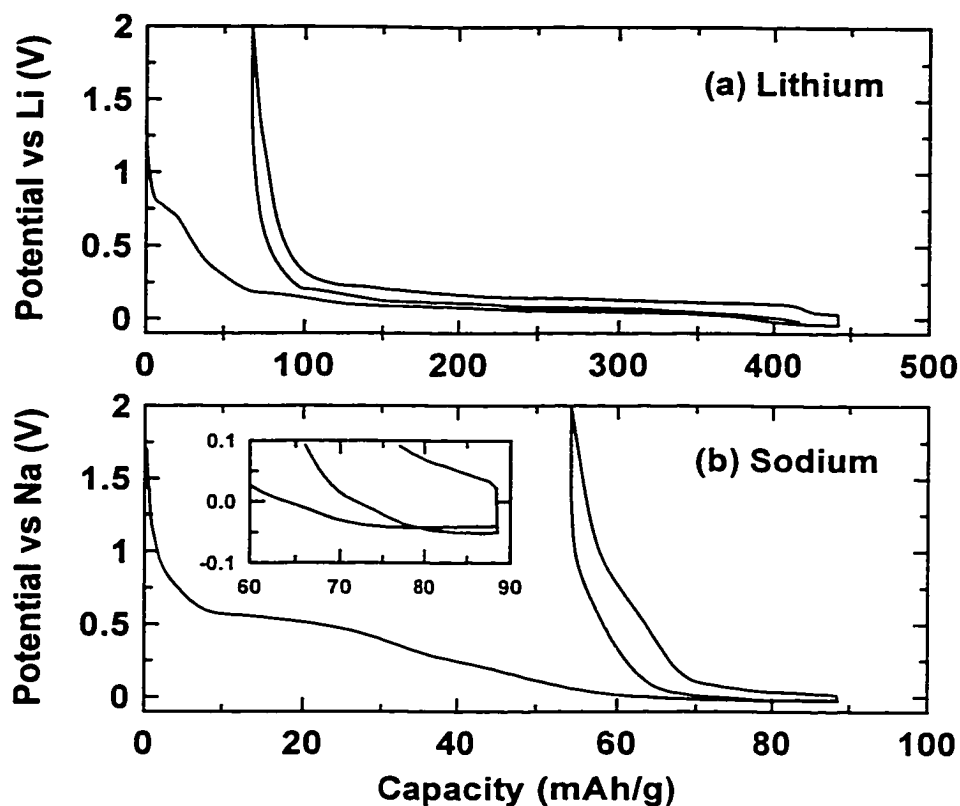


Figure 5.6: (a) Lithium and (b) sodium insertion into graphitic carbon. The inset in (b) shows evidence of metal plating at 80 mAh/g during the first discharge and 87 mAh/g during the second discharge.

### 5.5.2 Soft Carbon

The lithium and sodium electrochemical profiles obtained for carbons derived from PVC from 600°C to 1000°C are shown in Figure 5.7. The two most notable features for lithium insertion into the 600°C sample are the extremely high capacity and the large hysteresis in the voltage profile between charge and discharge. As the heat treatment temperature increases, the capacity drops rapidly (requiring a change of scale for the 800°C sample) and the extent of hysteresis also seems to be reduced. For sodium insertion, there also appears to be some hysteresis in the voltage profiles in the lower temperature samples, however there is no large drop in capacity as the temperature increases. The other feature of these profiles is that both sodium and lithium insert into

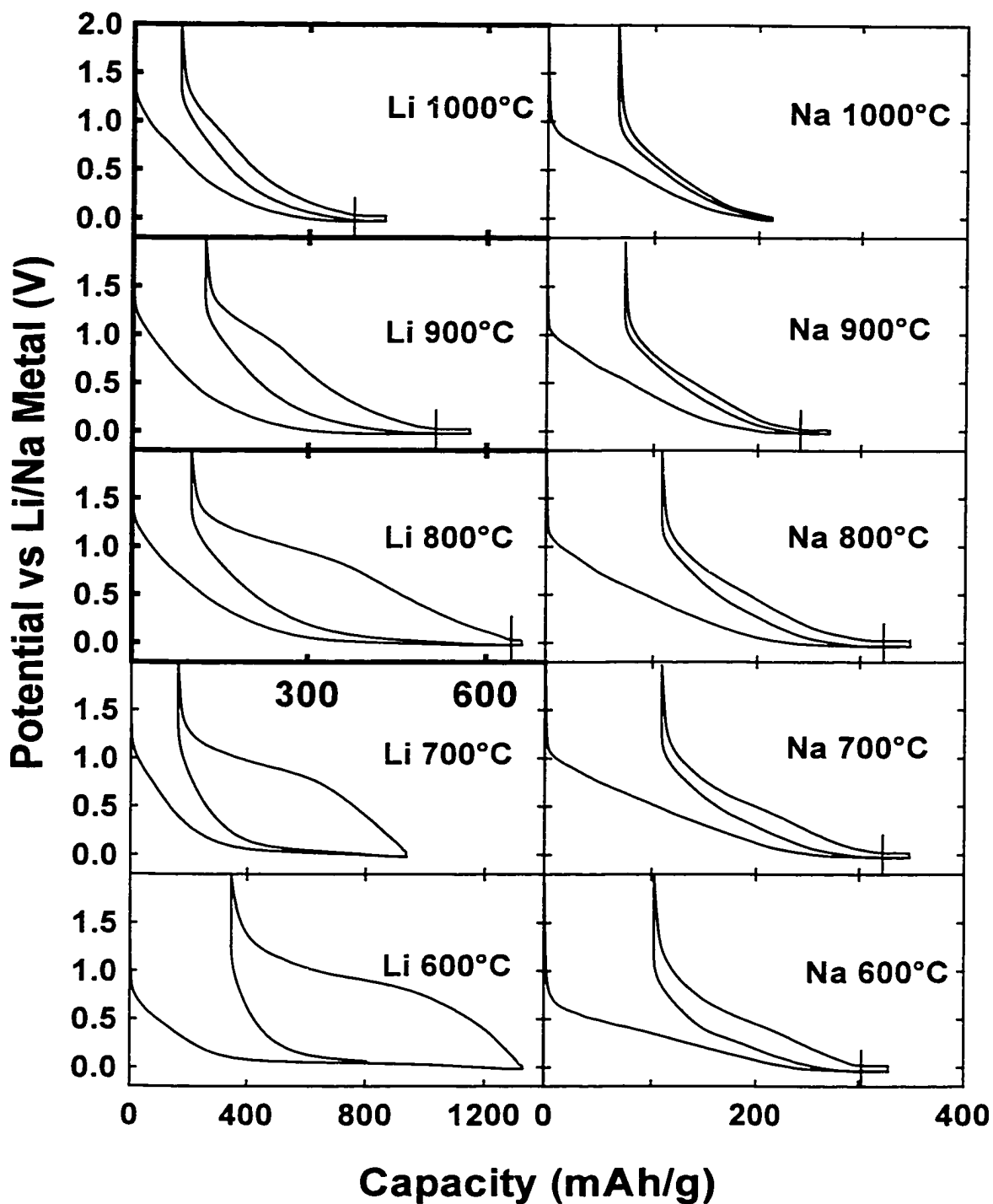


Figure 5.7: Electrochemical profiles for lithium (left panels) and sodium (right hand panels) insertion into PVC carbons. Note the change of scale for the 800 – 1000°C lithium samples. The vertical lines at the bottom of the curves in some panels indicate the onset of metal plating.

the carbon host at a range of potentials – as evidenced by the negative slope in the capacity curves. For the remainder of this thesis this behaviour will be referred to as insertion along the sloping voltage region.

In order to understand the changes occurring in these potential profiles it is worth examining the derivative curves. These curves can be generated by taking the derivatives,  $dQ/dV$ , of the capacity data and plotting these values against the cell potential. A plateau in the voltage profiles appears as a peak in the derivative curve, making such features much easier to resolve. This is important because alkali species entering sites with a uniform chemical environment will do so at constant chemical potential producing a plateau in the voltage profile. The derivative curves for the PVC cells are shown in Figure 5.8. The positive portion corresponds to removal of lithium/sodium from the carbon (charge), whilst the negative portion shows lithium/sodium insertion into the carbon (discharge). The most obvious feature of these derivative curves, particularly in the lower temperature lithium samples, is a peak centred around 0 V for lithium (not resolved for sodium) during discharge that shifts to  $\sim 1$  V for lithium and 0.5 V for sodium during charge. As the temperature increases, the size of these peaks decrease, whilst their positions remain reasonably constant, implying that there are sites within the carbon of approximately constant chemical potential and that the number of these sites available decreases with increasing temperature. The large difference in potential between discharge and charge for the lithium samples is the cause of the hysteresis in the voltage profiles and, as discussed earlier, indicates that insertion into these sites is hindered by a large activation barrier.

The primary compositional change that occurs to carbon materials from 600-1000°C is loss of hydrogen [82]. Work by Zheng [78] showed that there was a strong correlation between the hydrogen content of the carbon and the capacity of the 1V plateau on charge. Based on this evidence together with kinetic studies, it was proposed that lithium reacts with hydrogen-terminated aromatic carbon centres to form a species analogous to organo-lithium species ( $-C_2H_2Li_2$ ), as shown in Figure 5.9. This model was supported by theoretical calculations completed by Papenak [83].

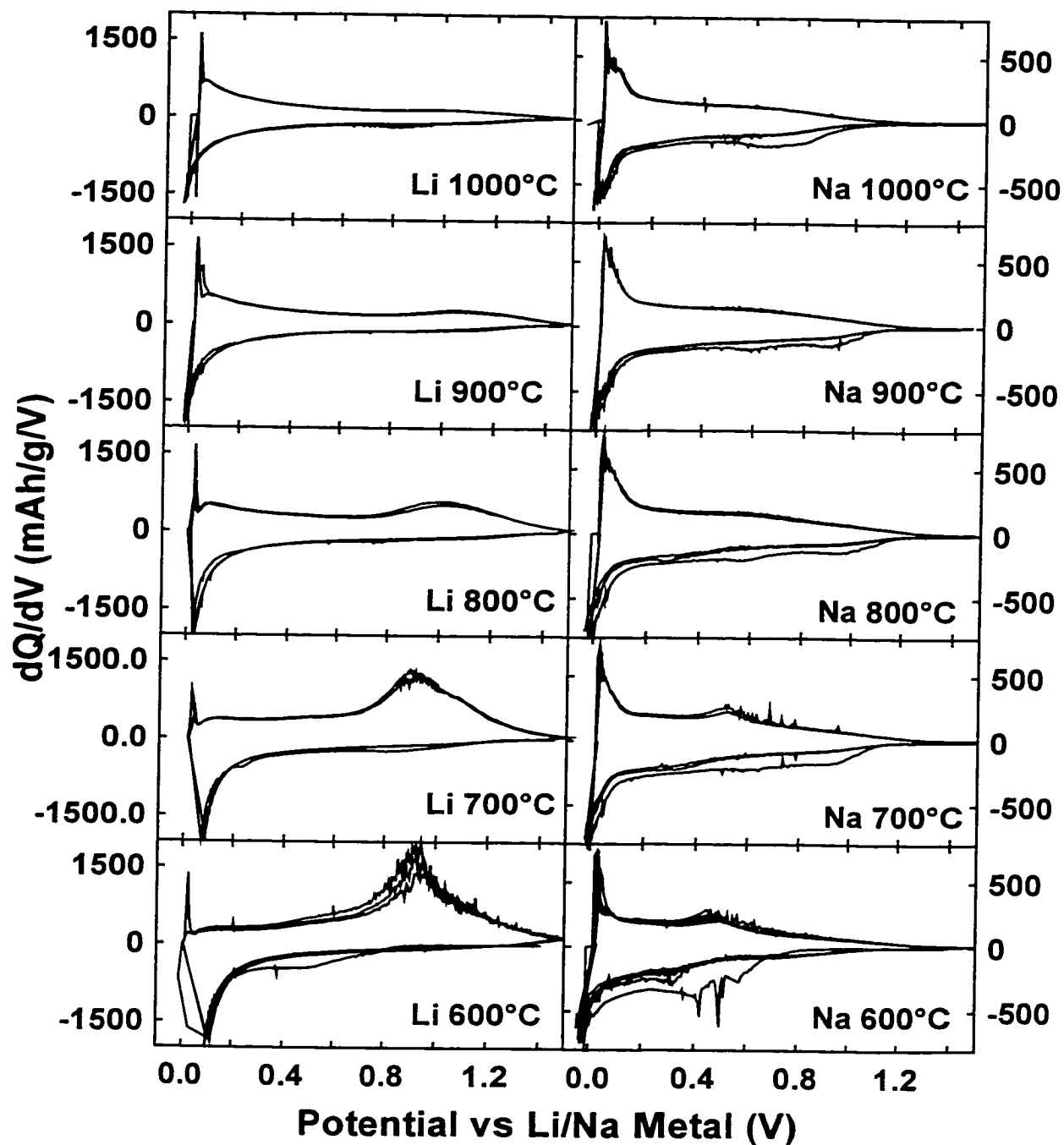
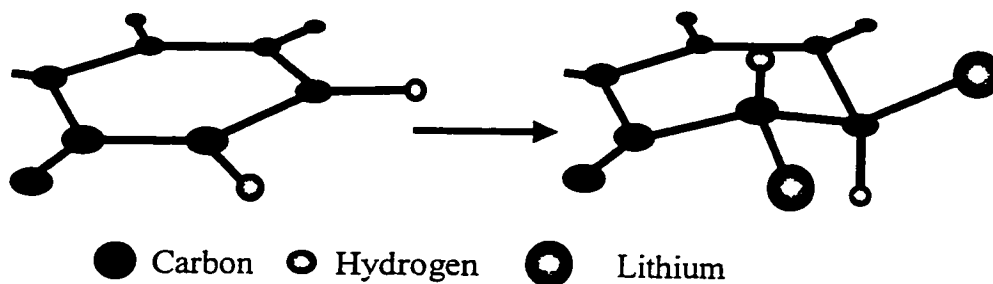


Figure 5.8: Differential capacity ( $dQ/dV$ ) curves for carbons prepared from PVC in the range 600-1000°C. The lower curves represent discharge whilst the upper curves represent charge.





*Figure 5.9: Reaction between lithium and hydrogen terminated aromatic carbons.*

For this reaction to occur, the carbon centres need to rehybridise from  $sp^2$  to  $sp^3$  and new bonds need to form to the lithium. It is likely that a relatively large activation barrier exists for the process of moving the carbon centres from the plane to tetrahedral positions. Assuming that this mechanism occurs for sodium insertion, then the hysteresis in the low temperature sodium profiles can also be explained through a similar process with different energetics. The obvious differences in energetics are that the sodium capacity through this mechanism is small compared to the lithium capacity and that the magnitude of the hysteresis introduced is significantly lower. This implies that the sodium bonds in a different manner that has a lower activation barrier and fewer sodium species can be accommodated in a given number of insertion sites.

As the heat treatment temperature increases, the differential capacity curves become smooth and featureless. This is consistent with the observed sloping voltage profiles and occurs for electrode materials containing sites with a distribution of chemical environments. To understand this behaviour, it is useful to examine the voltage profiles for the higher temperature samples presented in Figure 5.10. Examining these data in conjunction with the data for the lower temperature samples shows that, after accounting for interactions between lithium/sodium and hydrogen terminated carbon centres, both the lithium and sodium capacities along the sloping voltage profiles decrease with increasing temperature as shown in Figure 5.11.

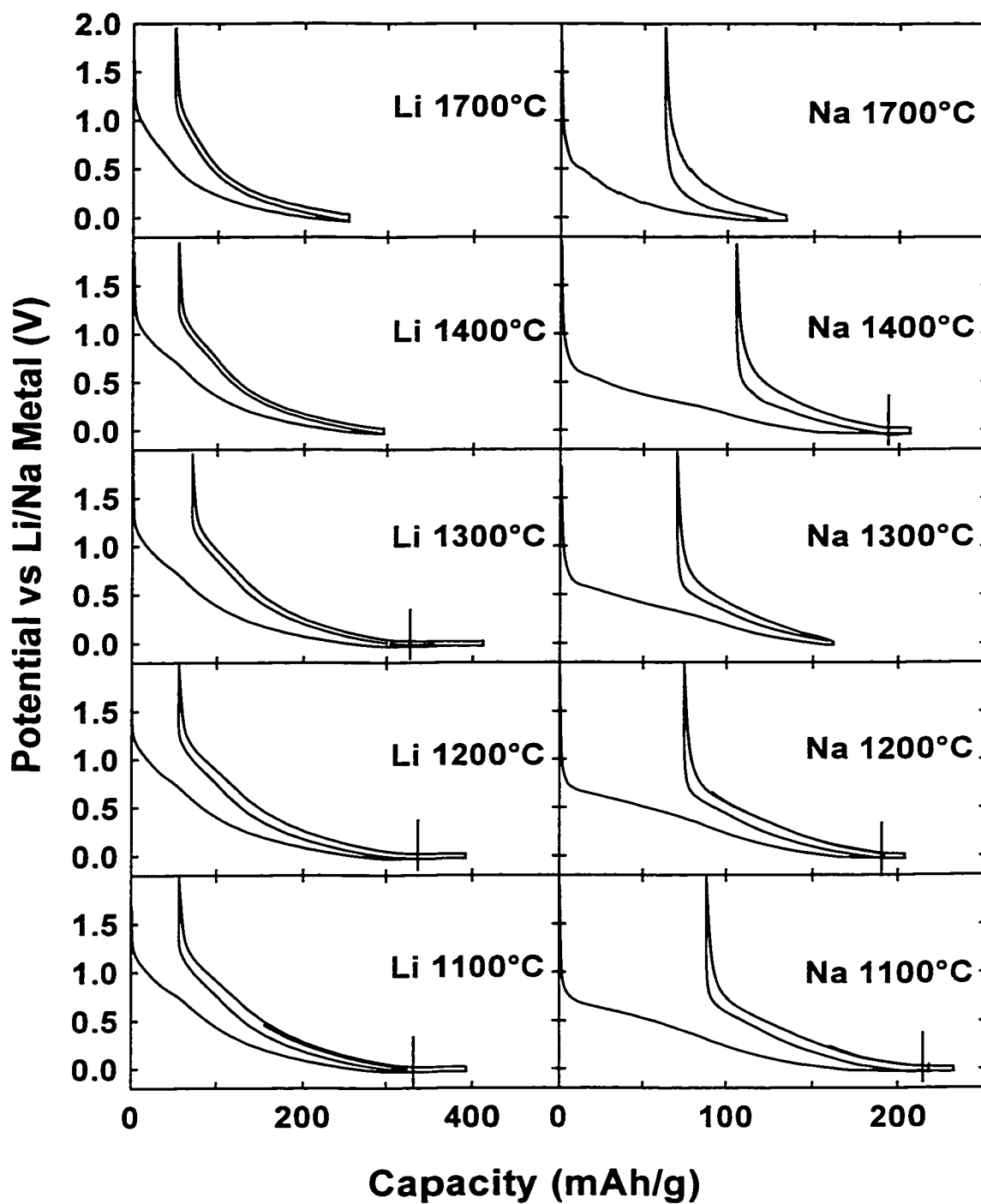
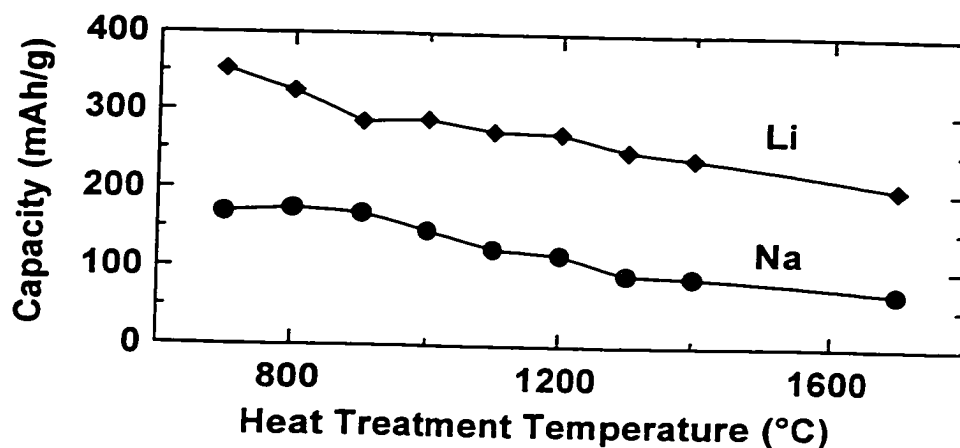


Figure 5.10: Lithium and sodium capacities for PVC carbons heat-treated to temperatures between 1100°C and 1700°C. The vertical lines at the bottom of the cycles indicate the start of metal plating.



*Figure 5.11: Change in reversible capacity with temperature for PVC carbons.*

It can be seen that the lithium and sodium capacities decrease at the same rate with the sodium capacity consistently lower than the lithium capacity. In the previous chapter, it was shown that as the heat treatment temperature increased, the average number of layers in a stack increased dramatically for the PVC carbons. This shows that the layers are quite mobile at elevated temperatures, being able to rotate into approximately parallel alignment with adjacent layers. However, even at quite high temperatures, the layers are not arranged in the regular ABAB stacking found in graphite, because crosslinks between layers prevent the necessary small scale rotations and translations required to form such an arrangement. It has been shown [84] that during lithium insertion into graphitic carbons, the graphene layers need to shift into an AA type stacking arrangement. Thus in the turbostratically disordered carbons it is likely that many of the layers are unable to shift because of edge pinning. This effectively makes some of the interlayer insertion sites inaccessible to lithium. As more layers move into parallel alignment, the number of layers pinned with inappropriate stacking increases. This causes the observed decrease in capacity. For higher temperatures, (eg > 2000°C) the turbostratic disorder starts to be relieved, allowing for an increase in capacity again, until the relatively high capacity of graphitic carbons is reached.

It was shown earlier that, unlike lithium, only small quantities of sodium could be inserted into graphitic carbons. Thus, even with layer shifting to AA stacking, the sites in graphite are not suitable for sodium insertion. This implies that some sites suitable for lithium insertion are not suitable for sodium insertion. This could explain the difference in capacity seen for the PVC carbons – many of the sites that can accommodate lithium in the low temperature samples are not suitable for sodium. If these sites are still present in the high temperature samples then the change in capacity for the two metals should follow the same trend but with a different “background”. This would manifest itself as a constant offset between the sodium and lithium capacities. This behaviour is evident in Figure 5.11. It is possible that this effect is caused in part by size differences – the atomic radius of sodium being 186 pm compared to 152 pm for lithium.

The electrochemical curves presented in Figure 5.12 for carbons prepared from the pitch precursor show that the behaviour seen for PVC is also seen for soft carbons prepared from a vastly different precursor. Chapter 4 showed that the structures of PVC and pitch derived carbon as a function of heat treatment temperature were similar. This, combined with the electrochemical data shows that, for materials with increasing layer stacking, the sodium and lithium capacity decreases with increasing heat treatment temperature. In addition, the hydrogen content in the low temperature samples produces a large lithium capacity together with hysteresis in the voltage profiles for both sodium and lithium insertion. As the temperature increases, the amount of residual hydrogen in the carbons decreases and the capacity attributed to interactions with hydrogen terminated carbon centres also decreases. This gives confidence that the mechanisms proposed for lithium and sodium insertion into PVC derived soft carbon will be valid for a wide range of soft carbon materials.

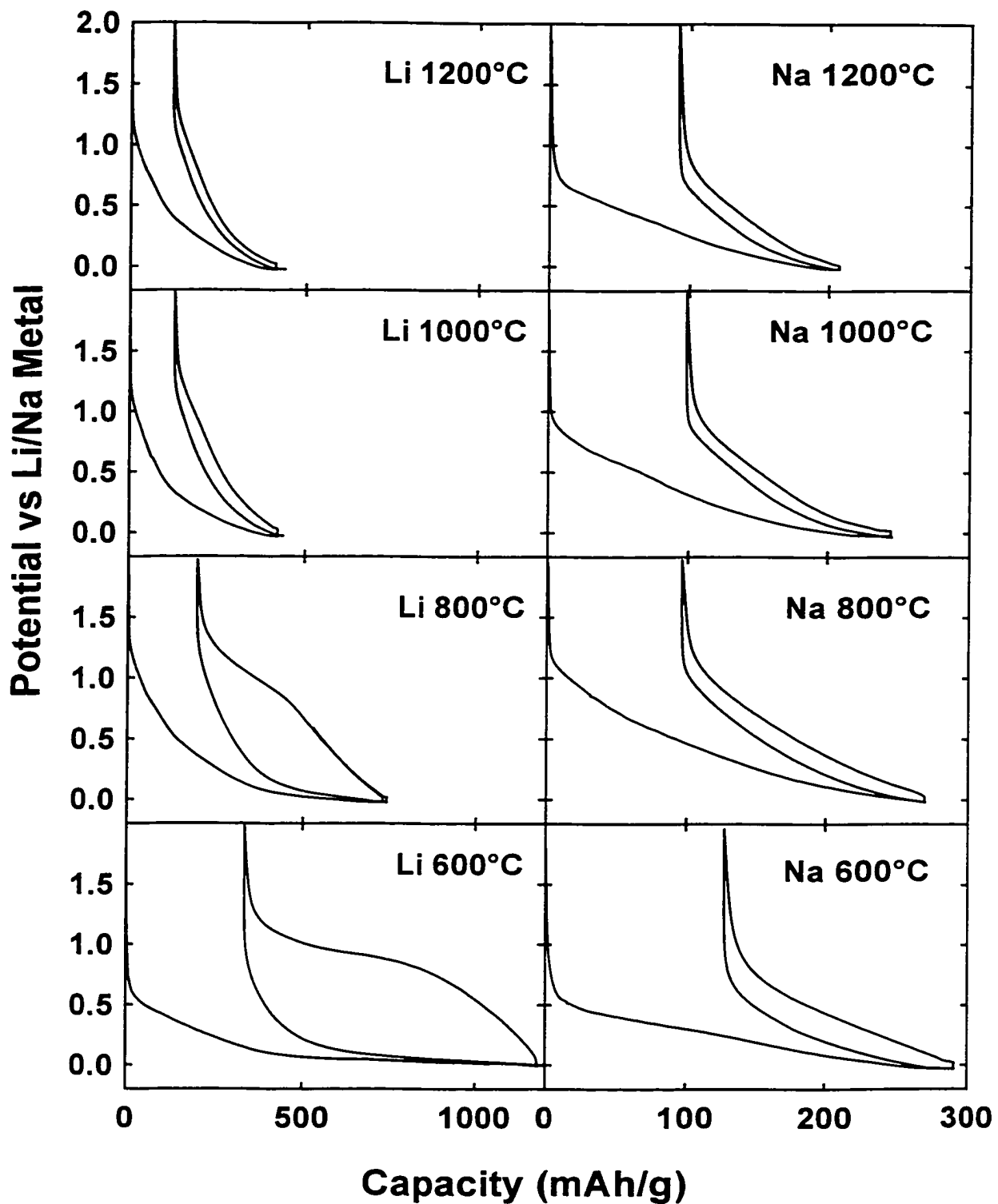


Figure 5.12: Electrochemical lithium and sodium insertion into soft carbons prepared from a pitch precursor.

### 5.5.3 Electrochemical Performance of Hard Carbons

The 600°C carbon (Figure 5.13) prepared from glucose showed similar behaviour to the 600°C carbon prepared from PVC (Figure 5.7). The lithium capacity was very high and the voltage profile exhibited hysteresis of  $\sim 1V$ . In order to show this behaviour, a much larger scale is used in Figure 5.13 for the 600 and 700°C samples than for the 800 – 1000°C samples. As for the PVC sample, the sodium cell also produced hysteresis but the capacity was low relative to the lithium cell. This would imply that both the lithium and sodium were interacting with hydrogen terminated aromatic centres, forcing the carbons to rehybridise. As the heat treatment temperature increased, the extent of hysteresis was reduced and the capacity attributable to hydrogen decreased, as expected for these hard carbons that also see loss of hydrogen as the primary compositional change occurring during carbonization to  $\sim 900^\circ\text{C}$  [82]. These samples also exhibited a sloping voltage region, implying that some interlayer insertion occurs. The x-ray studies of the structures of these carbons suggested that the graphene layer stacks on average extend for 1, 2 or 3 approximately parallel layers. It is therefore likely that much of the capacity along the sloping voltage region, particularly at low voltages, actually results from adsorption of lithium/sodium atoms onto the external surfaces of these layer stacks, rather than insertion between layers.

The most notable feature of these carbons for both sodium and lithium insertion is the presence of significant capacity at a potential close to that of the metal itself. This capacity has been referred to as capacity along the low voltage plateau [85]. For the sodium samples, this low voltage plateau is already well developed in the sample heat treated to 700°C. For lithium insertion, it only starts to contribute significant capacity for samples heat-treated to 900°C or higher.

Figure 5.14 presents the electrochemical data for the samples heated to higher temperatures. These curves show surprising differences between sodium and lithium insertion into these materials. As the heat treatment temperature increases above 1300°C, the lithium capacity along the low voltage plateau drops rapidly, until, by 1700°C,

essentially all the capacity (which is quite low for lithium insertion) occurs along the sloping voltage region. For the sodium cells, the capacity along the sloping voltage

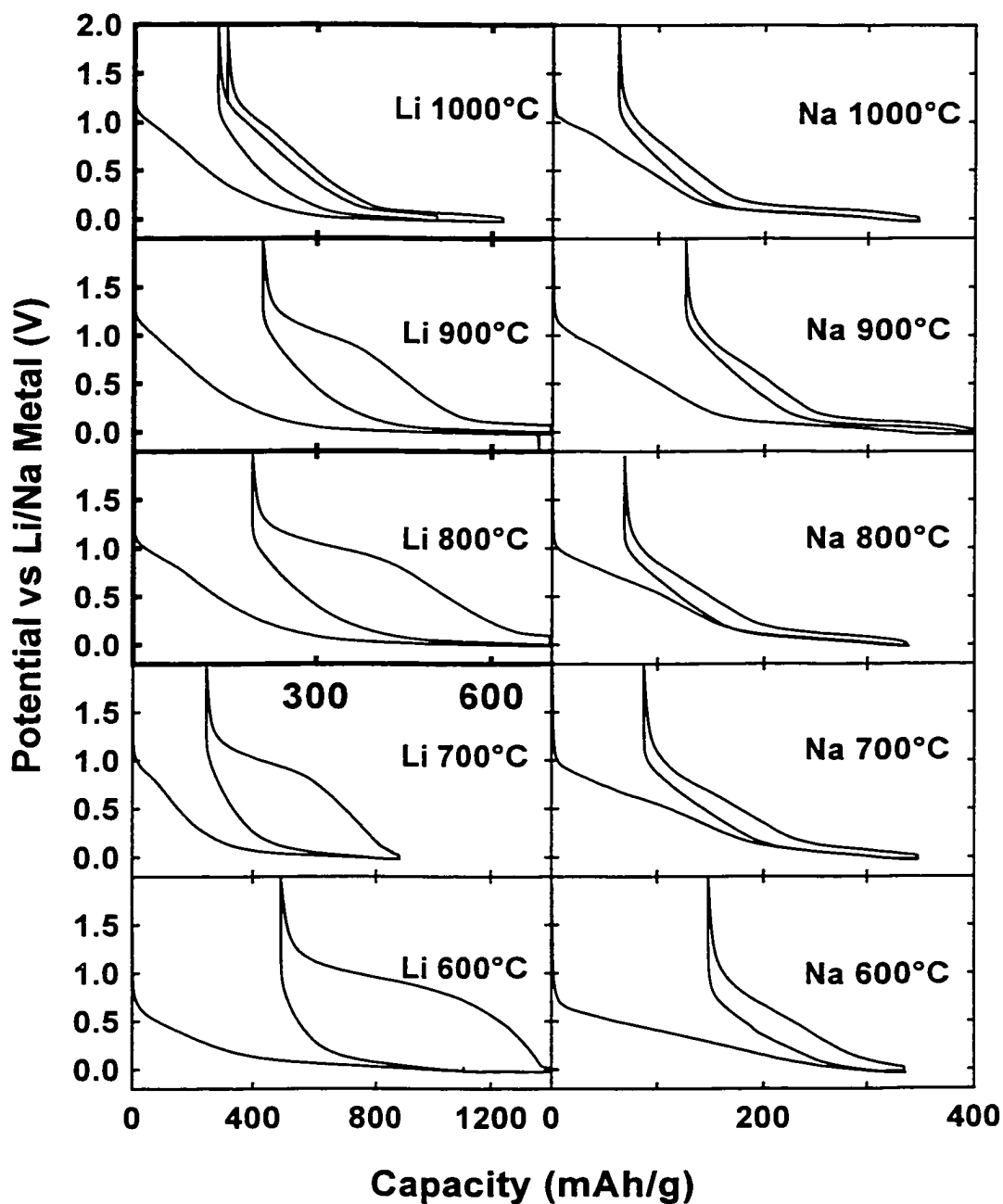


*Figure 5.13: Electrochemical profiles for lithium (left hand side) and sodium (right hand side) insertion into glucose derived carbons heat treated in the range 600 – 1000°C. Note that the scale for the lithium cells is different for the 600 and 700°C samples.*

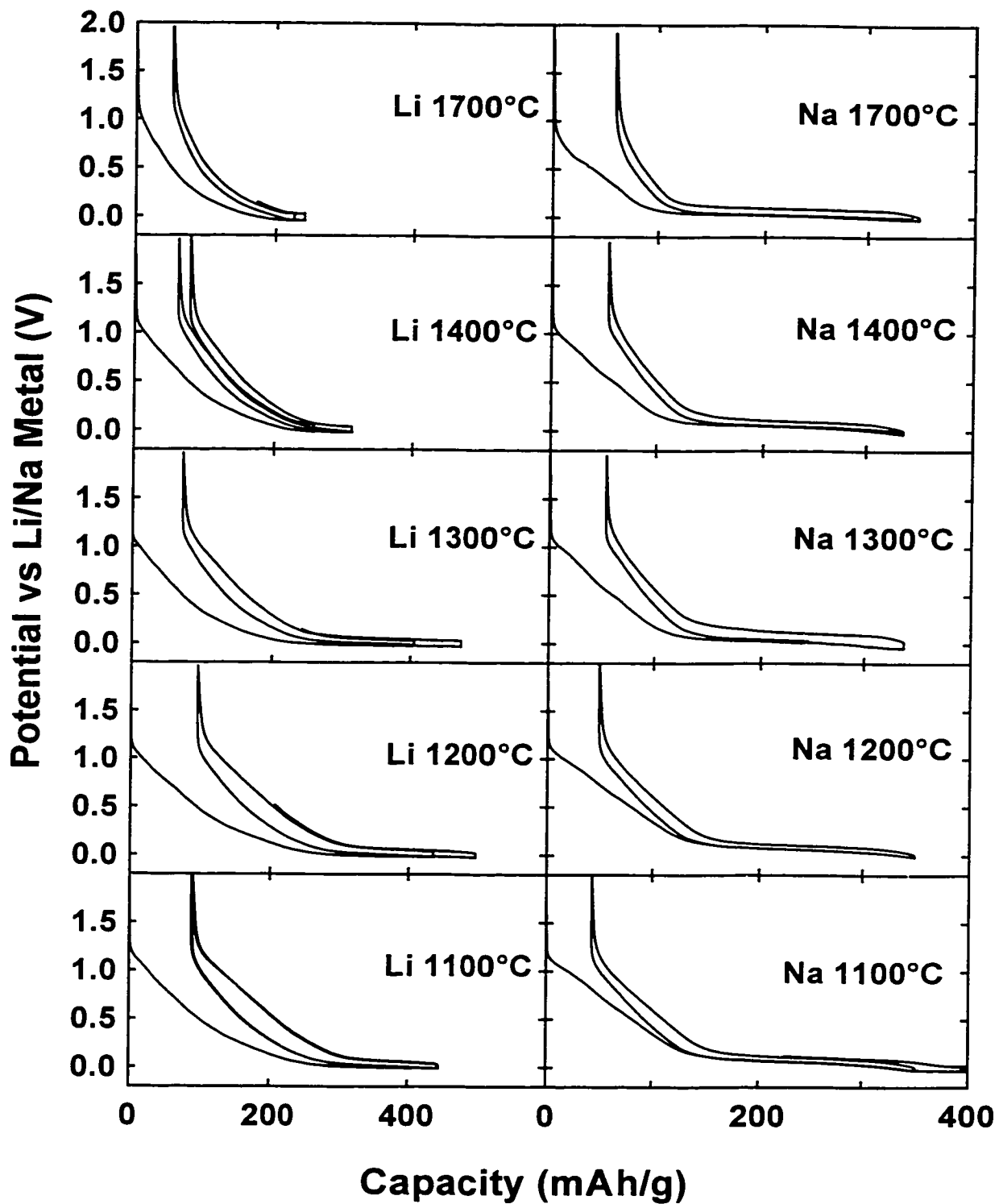


Figure 5.14: Electrochemical profiles for lithium (left hand side) and sodium (right hand side) insertion into glucose derived carbons heat treated in the range 1100 – 1700°C.



region decreases whilst the capacity along the low voltage plateau appears to remain essentially constant. The capacity changes seen are summarised in Table 5.1.

*Table 5.1: Capacity changes (mAh/g) for carbons derived from glucose as a function of heat treatment temperature*

	Lithium ( $\pm 10$ mAh/g)		Sodium ( $\pm 10$ mAh/g)	
	Sloping Voltage Region	Low Voltage Plateau	Sloping Voltage Region	Low Voltage Plateau
700°C	N/A	N/A	105	106 (50 %)
800°C	249	41 (14 %)	97	130 (57 %)
900°C	242	114 (32 %)	107	132 (55 %)
1000°C	211	214 (50 %)	104	163 (61 %)
1100°C	173	184 (52 %)	98	209 (68 %)
1200°C	206	190 (48 %)	105	189 (64 %)
1300°C	168	204 (55 %)	81	188 (70 %)
1400°C	184	55 (23 %)	75	201 (73 %)
1700°C	148	29 (16 %)	50	236 (83 %)

Although there is some scatter in these data, they clearly show the loss in capacity along the low voltage plateau of the lithium cells at higher temperatures. They also show the decrease in sloping voltage capacity for the sodium cells coupled with the retention of low voltage plateau capacity.

The differential capacity curves for the glucose samples are presented in Figure 5.15 and Figure 5.16 to help explain the nature of the insertion process along the low voltage plateau. These curves show only the low voltage region. The low voltage plateau appears as a narrow peak close to 0 V. For the sodium samples, it is apparent that the peak develops in size (i.e. increases capacity) between 700 and 1100°C and then remains at constant magnitude and position. However, for the higher temperature lithium samples, the peak shifts to lower voltages. As it shifts, part of the capacity is effectively lost because it is more energetically favourable to plate metal onto the electrode surface

than to insert into the sites at low cell potential. It appears that by 1700°C, the position of the peak is effectively too low to contribute to lithium capacity.

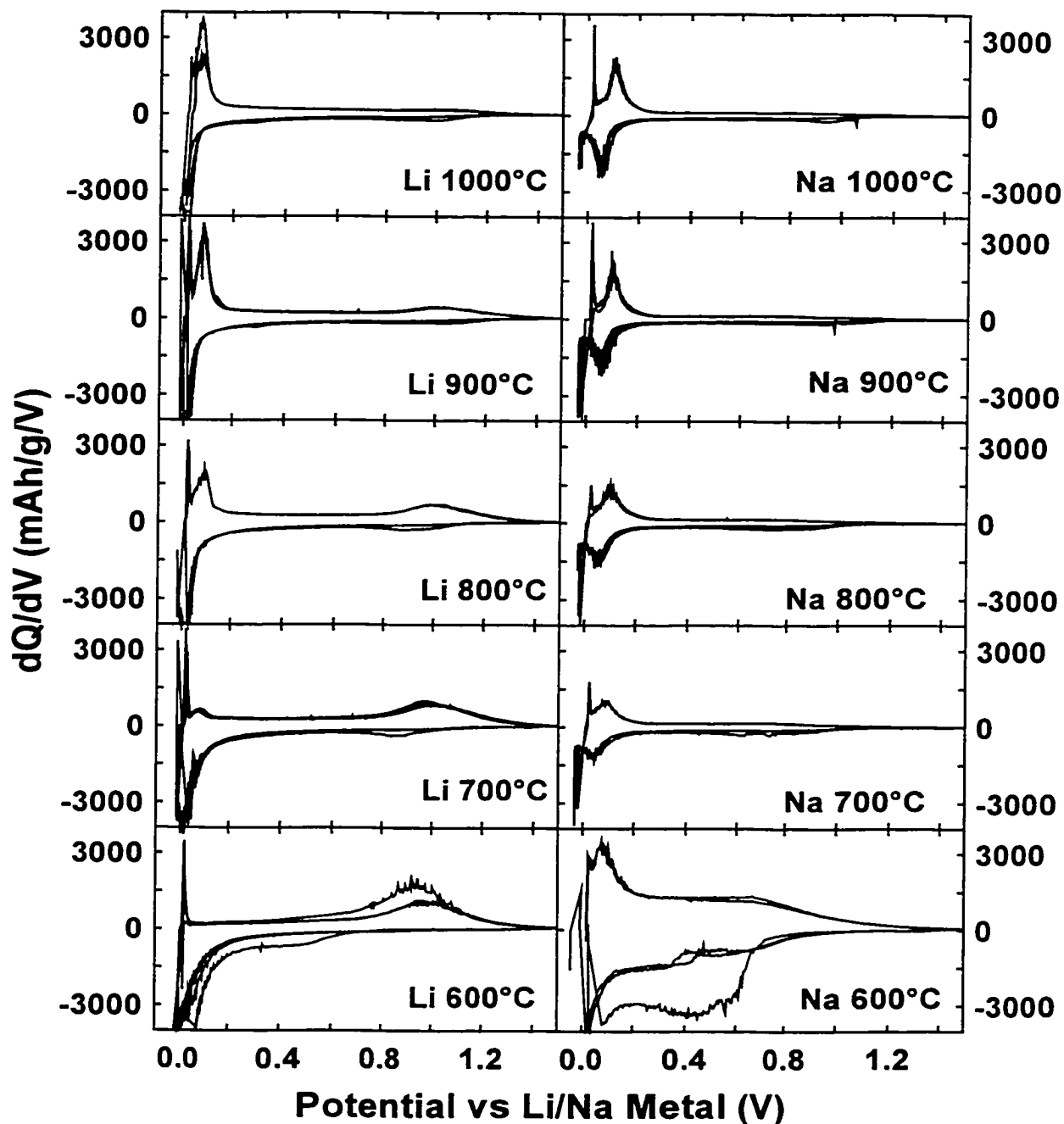


Figure 5.15: Differential capacity ( $dQ/dV$ ) as a function of heat treatment temperature in the range 600-1000°C for carbon samples derived from glucose.

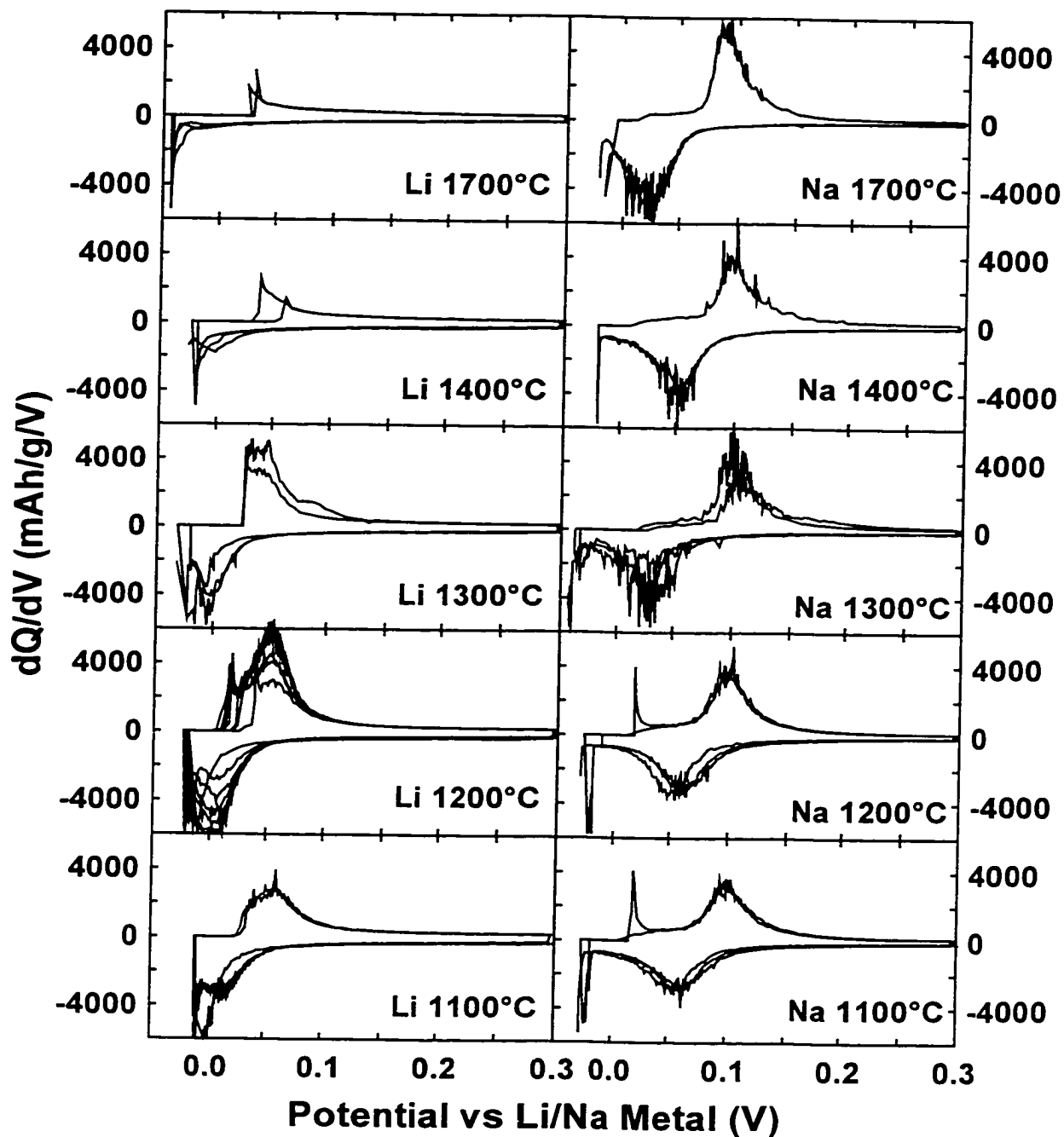


Figure 5.16: Differential capacity ( $dQ/dV$ ) as a function of heat treatment temperature in the range 1100-1700°C for carbon samples derived from glucose.

Table 5.2 shows the position of the low voltage plateau as a function of heat treatment temperature. The values quoted are the averages of the peak position in the derivative curve during charge and discharge. The shift of the low voltage plateau peak for the lithium cells with increasing temperature can be clearly seen. The data also show that there is very little change in the position of the sodium peak and that it is located at a higher potential than the equivalent lithium peak.

*Table 5.2: Average potential of the low voltage plateau (V) for glucose carbons as a function of heat treatment temperature.*

	700°C	800°C	900°C	1000°C	1100°C	1200°C	1300°C	1400°C	1700°C
<b>Li</b>	N/A	0.05	0.05	0.04	0.04	0.03	0.02	0.01	-0.01
<b>Na</b>	0.07	0.08	0.08	0.08	0.08	0.08	0.06	0.08	0.06

As the low voltage plateau occurs at a potential close to that of the metal and the inserted alkali species are removed with effectively no hysteresis, the sites into which sodium and lithium are inserting must have a chemical environment similar to that of the metal itself. Thus there is very little charge transfer between the inserted atoms and the carbon matrix along the low voltage plateau. The sloping voltage profile capacity at low voltage has been attributed to a combination of interlayer insertion and adsorption of a monolayer of alkali atoms onto the surfaces of graphene domains. These surfaces also form the walls of the pores and thus the pores can be thought of as a carbon surface with adsorbed lithium/sodium atoms. The energetics of multilayer adsorption of lithium and sodium are such that there would be very little charge transfer between the multi-layers and the first layer. Thus the low voltage plateau capacity can be attributed to adsorption of lithium/sodium into nanopores within the carbon. No low voltage plateau was seen in the soft carbons because such carbons contain negligible amounts of nanoporosity.

The explanation provided above still does not explain why the lithium capacity along the low voltage plateau decreases with increasing heat treatment temperature whilst

the sodium capacity remains essentially constant. This behaviour cannot be explained at this time.

The electrochemical profiles for the carbons prepared from the resin precursor are shown in Figure 5.17. These data show that other nano-porous hard carbons also contain significant capacity along the low voltage plateau together with some capacity along the sloping voltage region for both sodium and lithium insertion. The 600°C sample shows less capacity attributable to hydrogen content than the 600°C glucose sample. This implies that this carbon contains less hydrogen than the glucose carbon. This would explain the lack of hysteresis in the sodium profile and the presence of a large low voltage plateau for sodium insertion. Thus the 700°C glucose sample provides a more appropriate comparison than the 600°C glucose sample. Even though overall similar mechanisms operate for the two different hard carbons, there are some subtle structural and chemical differences, particularly in the low temperature samples, that modify the relative contributions from each of the mechanisms to capacity.

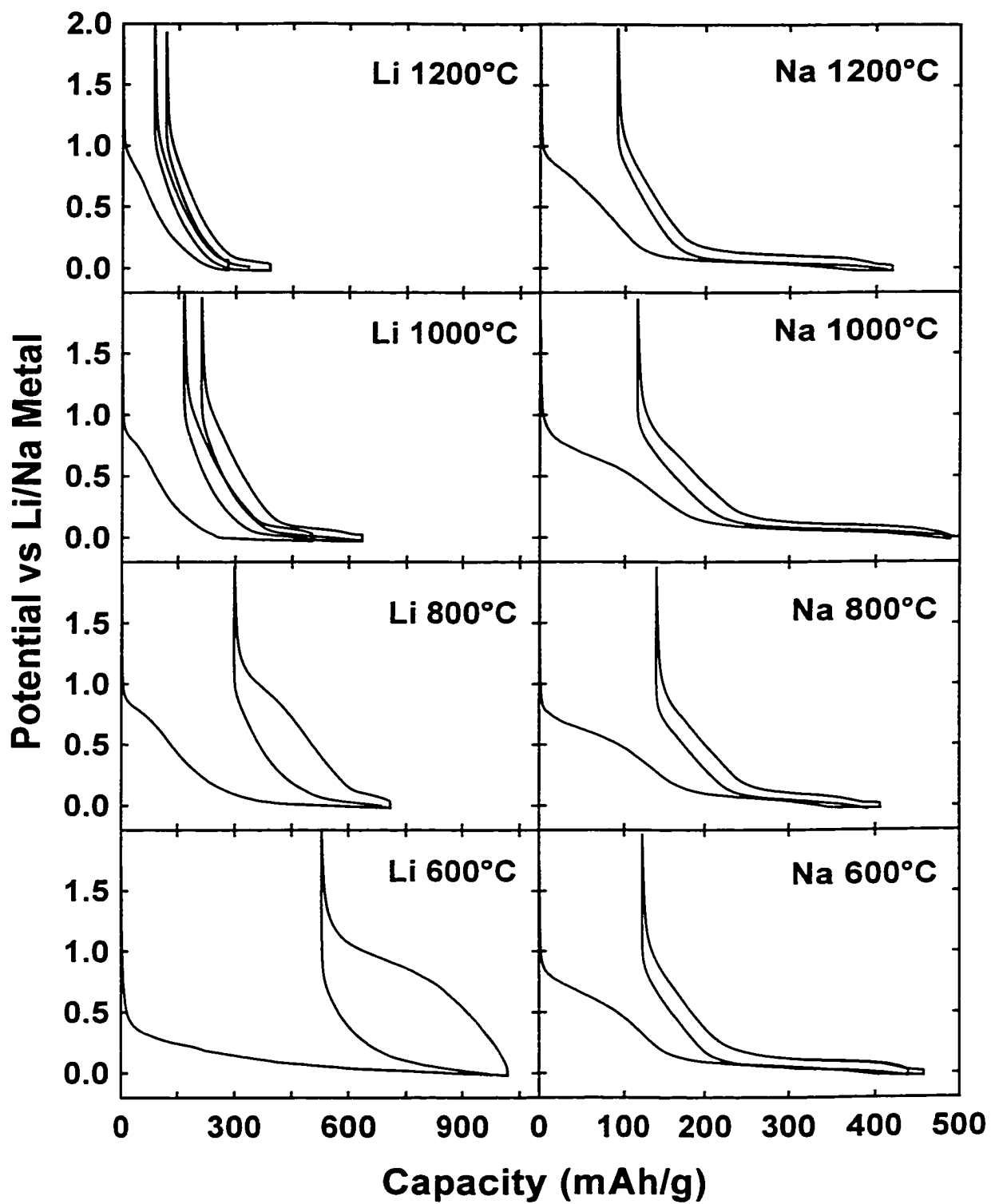


Figure 5.17: Capacity curves for heat-treated resin samples.

## Chapter 6

### *In situ* X-Ray Scattering

This chapter presents conclusive evidence to support both the interlayer and nanopore insertion mechanisms. *In situ* WAXS results will be used to prove that sodium and lithium insert between carbon layers along the sloping voltage profile, whilst *in situ* SAXS results will show that lithium and sodium enter nanoporosity along the low voltage plateau.

#### 6.1 *In situ* WAXS

It was shown in Chapter 4 that both soft and hard carbons heat-treated to intermediate temperatures (eg 1000°C) exhibit broad 002 peaks in WAXS measurements, indicative of some graphene layer stacking. The soft carbons have a greater number of layers stacked approximately parallel to each other than the hard carbons, although these layers are turbostratically disordered, and hence only approximate to a graphitic domain. In Chapter 5 it was proposed that the disorder between layers created a distribution of sites into which sodium and lithium species could be inserted at a range of chemical potentials. This distribution of chemical potentials generates a sloping voltage profile for both sodium and lithium insertion. In fact it was apparent that the turbostratic disorder was necessary for sodium insertion, as the sodium capacity of a carbon without such disorder was extremely low (eg graphite).

So far no direct evidence has been presented to support the hypothesis that sodium and lithium insert into sites created by disorder between graphene sheets. The

evidence presented in Chapter 5 was based on the shape of the electrochemical profiles and an understanding of how the carbon structures evolve. The ideal tool for showing the insertion of sodium and lithium between carbon layers is *in situ* WAXS because this technique is sensitive to the arrangement of the layers and the location of the alkali species in the layered structure.

### 6.1.1 Experimental

For these measurements, *in situ* WAXS cells were prepared as described in Chapter 5. The cells were then installed in the diffractometer and connected to the charger. An initial reference scan was collected between 15 and 60° 2 $\theta$  scattering angle. The cells were then discharged (500  $\mu$ A for Na, 750  $\mu$ A for Li) to a trip point of 0.2 V with respect to the metal. The current was then reduced to minimise premature plating (300  $\mu$ A Na, 500  $\mu$ A Li). After metal plating on the electrode surface was observed, the current direction was reversed and the cells were charged to 2 V. The diffractometer repeatedly scanned the electrode over the range shown above for one full cycle, with the time for one scan being small (3 hours) relative to the time for the cycle (1 week). Plating was deemed to have occurred when sharp peaks corresponding to the 110 peaks in BCC Na or Li (29° and 36° respectively) appeared in the x-ray profiles.

### 6.1.2 Soft Carbon at Low Scattering Angles with Na

Figure 6.1 shows the changes in the 002 peak for the soft carbon pitch sample (1000°C heat-treatment temperature) during sodium insertion and removal. Each scan has been offset from the previous scan by 20 counts/s in order to show the trends as clearly as possible. Figure 6.2 presents a selection of scans across the 002 peak from the cell, with the initial scan shown on each panel for reference. The sharp peaks at 27 and 28° come from the cell components.



From these data, it is apparent that the 002 peak intensity dropped and its position shifted to lower angles during discharge along the sloping voltage region (sodium insertion). The shift to lower angle resulted from an increase in the interlayer spacing. This would occur if the introduction of sodium into the lattice caused swelling. The drop in intensity is consistent with sodium inserting between the carbon layers. As shown in Chapter 3, the 002 peak results from constructive interference of x-rays scattered by adjacent layers. If a scattering species is introduced into the interlayer space, the scattered waves from this species will be out of phase with those from the layers over the range of angles corresponding to the 002 peak. The interlayer species therefore reduce the amplitude of the scattered beam and hence lower the intensity of the scattered beam over the 002 region. The combination of the drop in intensity and the increase in layer spacing clearly shows that sodium species insert between the carbon layers along the sloping potential region during discharge.

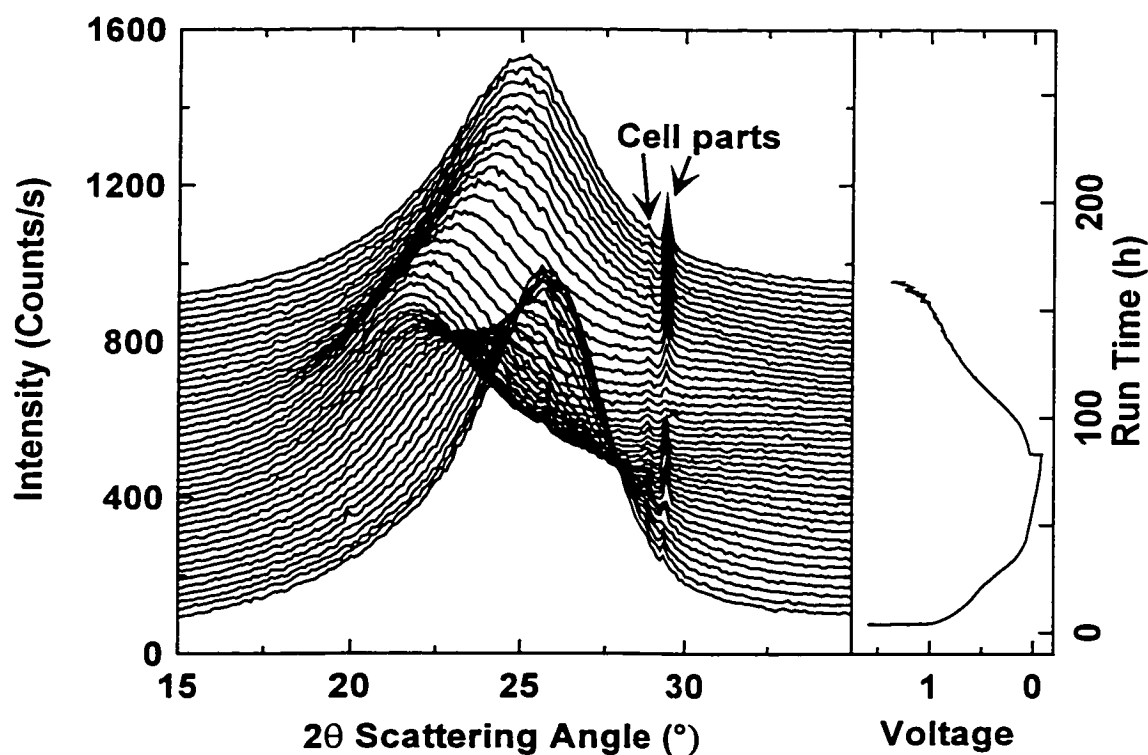


*Figure 6.1: In situ WAXS study of sodium insertion into soft carbon. Each scan is offset from the last by 20 counts/s to show changes.*

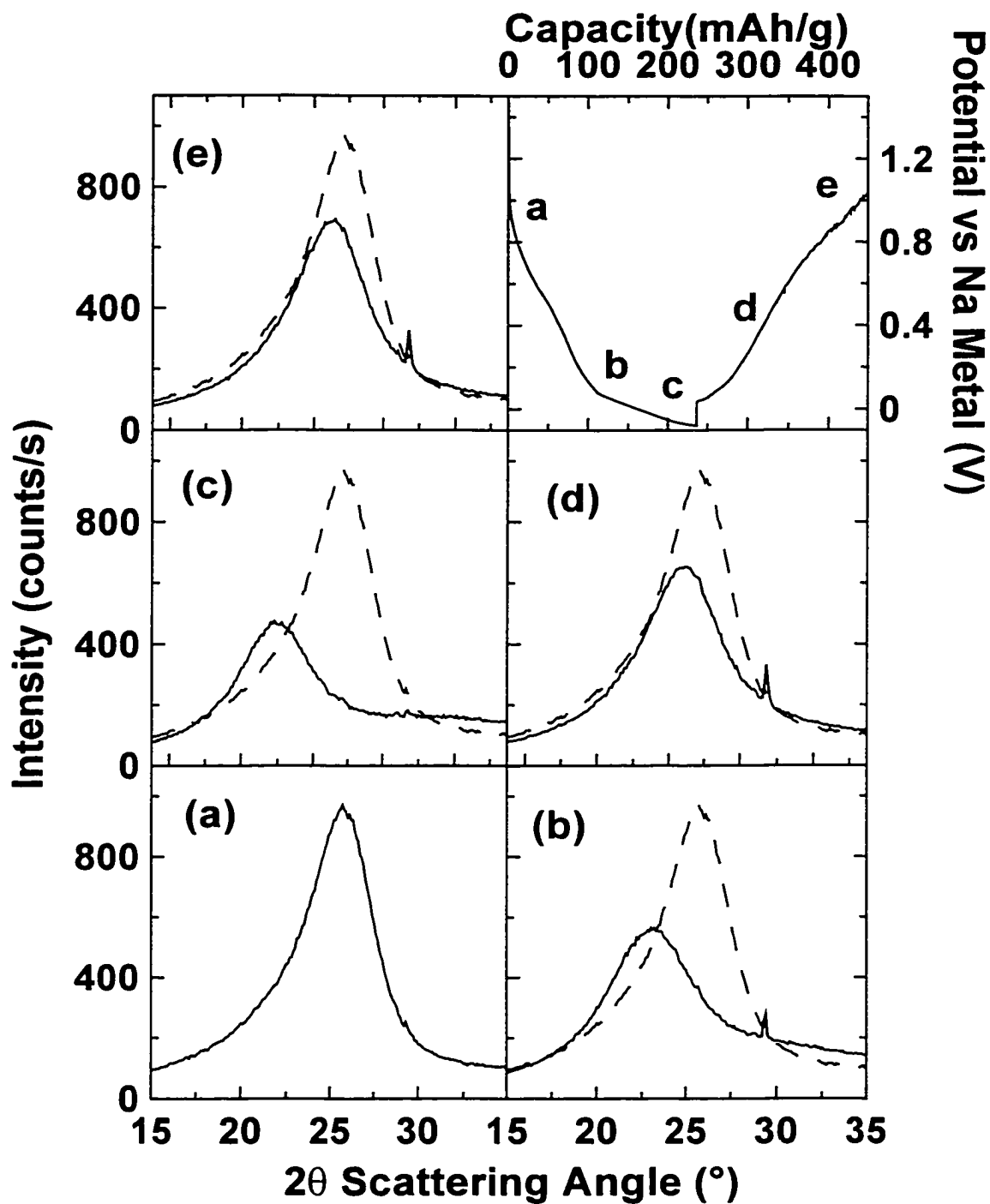
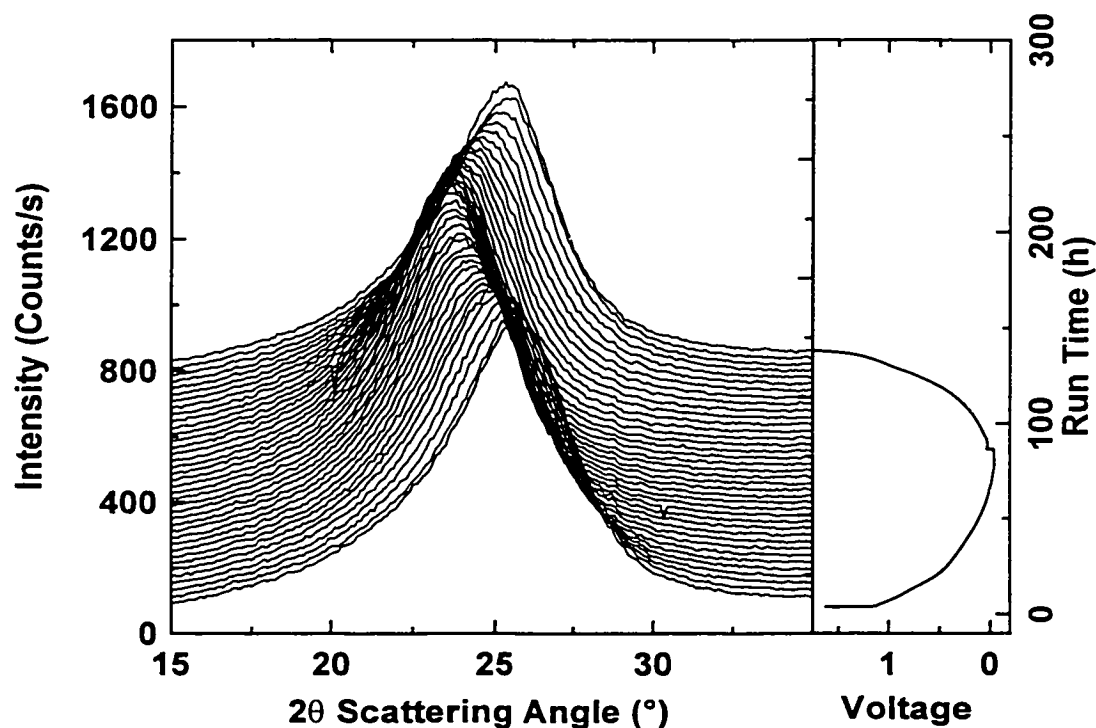


Figure 6.2: Selected scans for sodium insertion into soft carbon. The dashed line is the scan obtained before the current was switched on (as shown in (a)).

During charge, the reverse process occurred – the peak shifted back to higher angles and its intensity increased. This shows that the interlayer insertion process is reversible. The peak did not return to its original position, probably due in part to some sodium remaining trapped between the layers. This behaviour is specific to these pellet cells – the standard thin film electrode cells do not suffer from this incomplete sodium removal. The increase in intensity seen around  $32^\circ$  will be discussed briefly at the end of section 6.1.5.

### 6.1.3 Soft Carbon at Low Scattering Angles with Li

Figure 6.3 presents the set of 002 peak scans obtained for lithium into the same soft carbon, again with each scan offset by 20 from the previous scan. Figure 6.4 presents a selection of scans during the cycle, with the first scan included for reference.



*Figure 6.3: In situ WAXS study of lithium insertion into soft carbon. Each scan is offset from the last by 20 counts/s to show changes.*

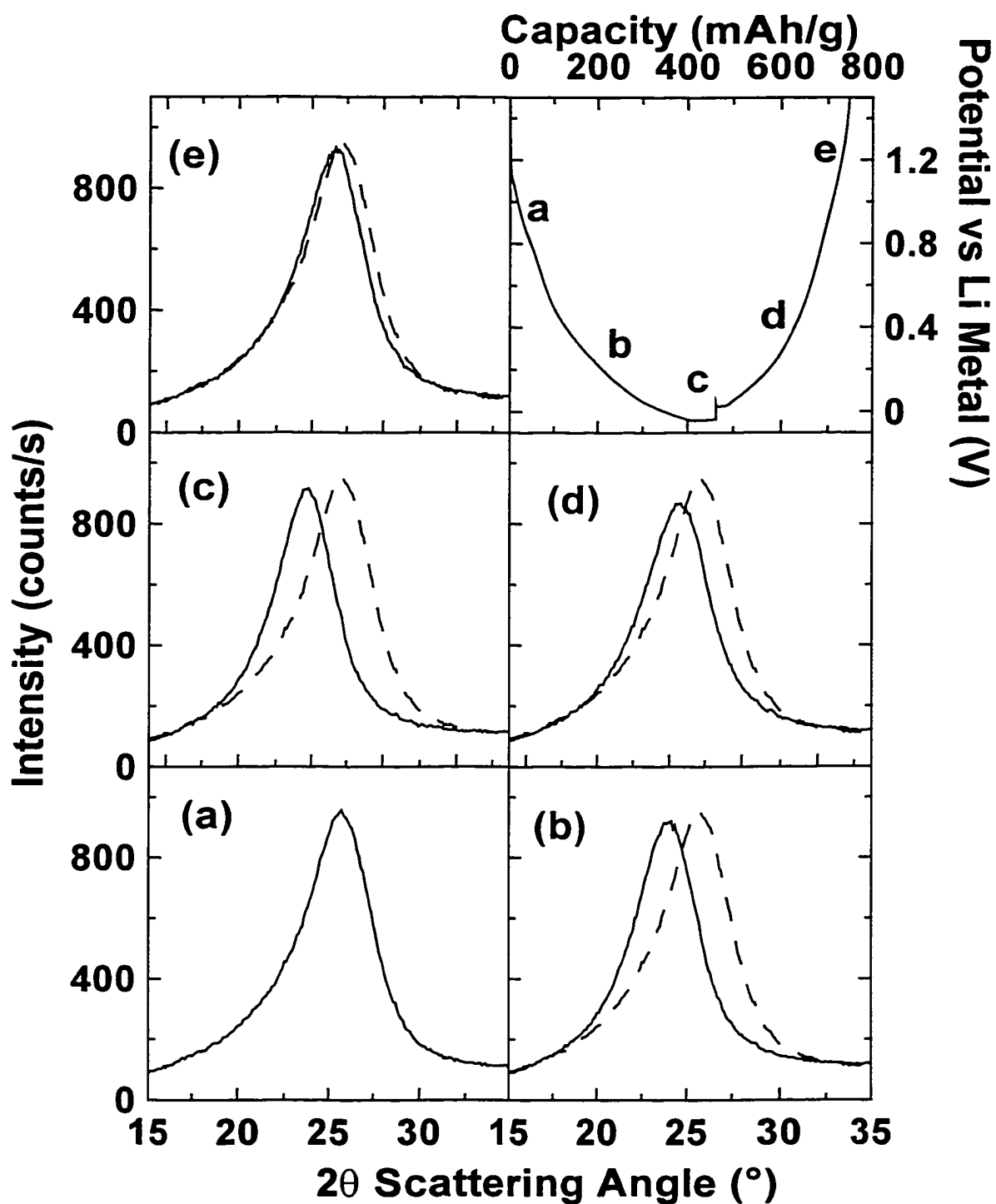


Figure 6.4: Selected scans for lithium insertion into soft carbon. The dashed line is the scan obtained before the current was switched on (as shown in (a)).

As for the sodium cell, the 002 peak shifted to lower angles and the intensity dropped during discharge along the sloping voltage portion of discharge. In going from panel b to panel c, it appears that the intensity remained constant as more Li inserted into the carbon. This is not the case, rather it is an artifact of Lorentz, atomic scattering factor and polarization effects that cause low angle peaks to increase in intensity. Like the results obtained for sodium insertion, these data show that lithium inserts between carbon layers (forcing them apart at the same time) along the sloping region of the voltage curve. When the cell was switched to charge, the peak shifted back to higher angles and the intensity increased, showing that the insertion process is reversible. In this case, the peak almost returned to the original position.

The magnitude of the intensity changes is much lower for the lithium cell than for the sodium cell. This is not surprising given that, for the same quantity of charge passed, the number of electrons inserted between the layers is much lower when lithium inserts than when sodium inserts. This reduction in electron insertion results in a lower magnitude of destructive interference, thereby reducing the magnitude of the intensity changes.

#### **6.1.4 Soft Carbon at High Scattering Angles with Na and Li**

Figure 6.5 and Figure 6.6 show a selection of scans during discharge and charge for sodium and lithium interacting with the soft carbon. There are a number of features of interest in these plots. Figure 6.5 shows the development of intensity around  $32^\circ$  during sodium insertion. This feature is reversible and will be discussed at the end of section 6.1.5. Figure 6.5 also shows that the intensity around  $53^\circ$  decreases during sodium insertion and increases again during sodium removal. Similar behaviour was also seen for the lithium cell. It is important to note that for lithium insertion (Figure 6.6) the intensity around  $47^\circ$  increased as the intensity around  $53^\circ$  decreased. This is consistent with the 004 peak shifting to lower angles as the carbon layers expand. A similar process would also be expected to occur for the sodium cell, with the intensity increasing at lower angles than for the lithium cell ( $\sim 43^\circ$ ) because of the larger expansion of the carbon layers (as indicated by the larger shift of the 002 peak).

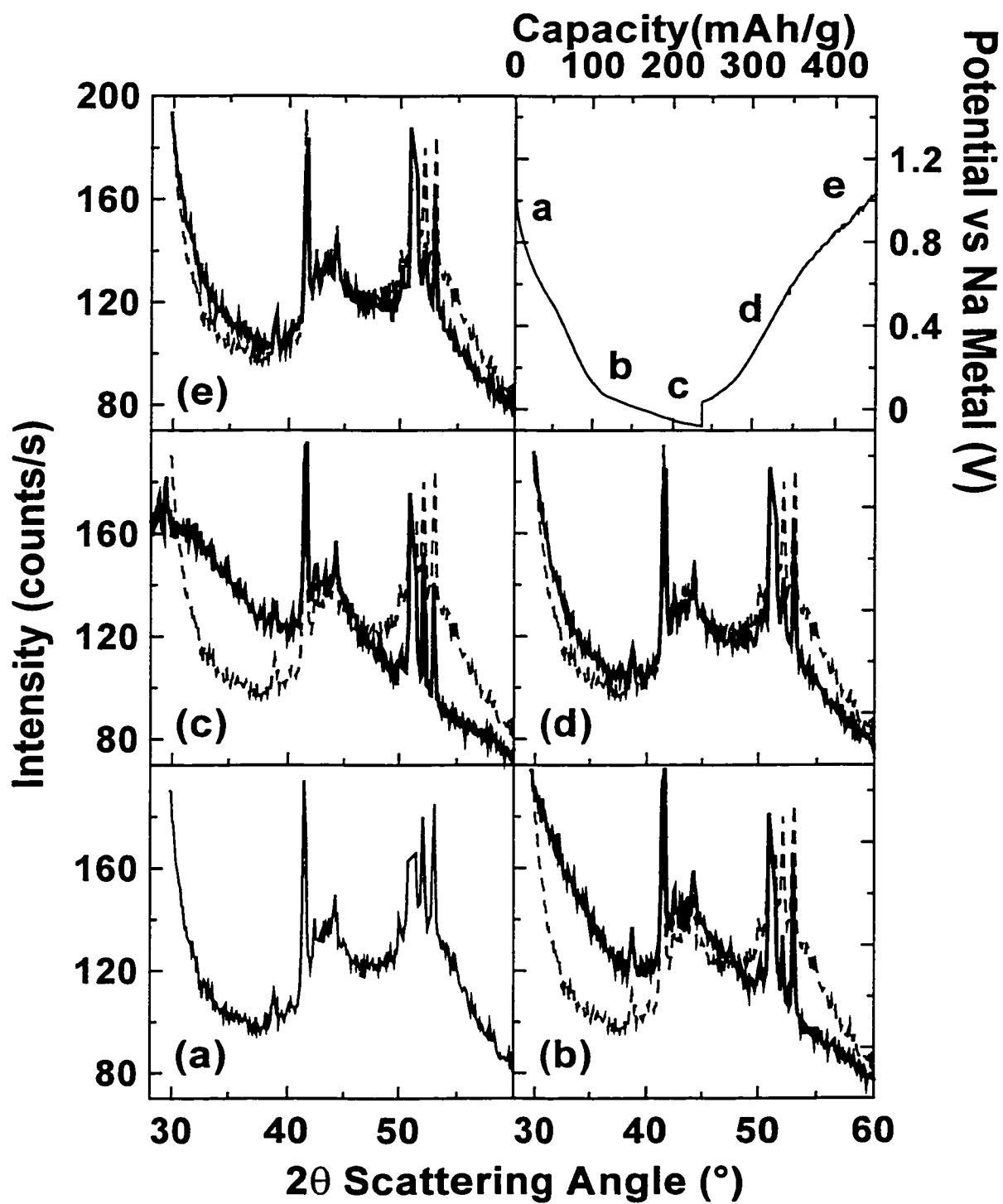


Figure 6.5: High angle WAXS patterns for sodium insertion into soft carbon. The initial scan has been included as a dashed line on panels (b) to (e) for reference. The sharp peaks are Bragg reflections from cell components.

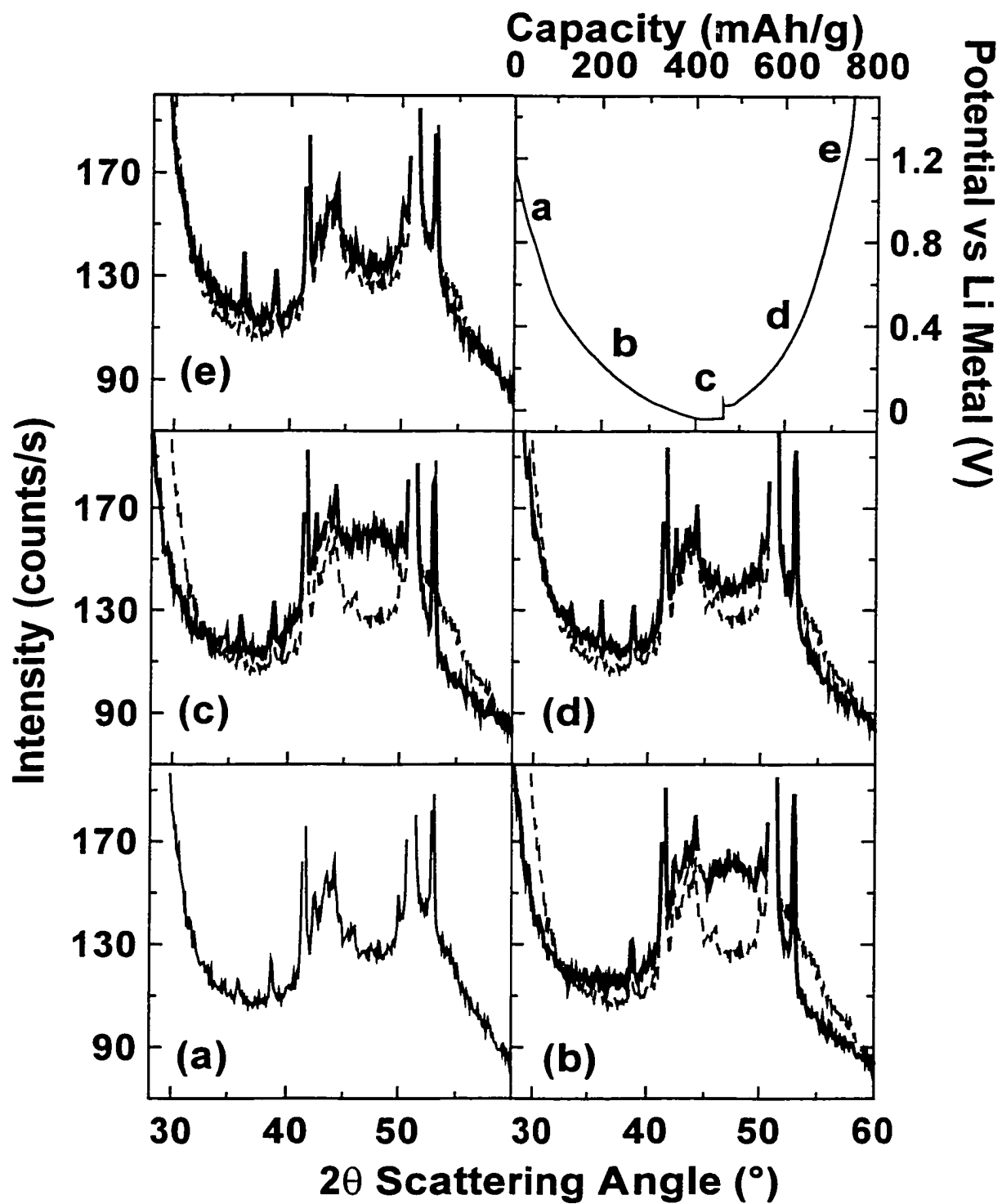


Figure 6.6: High angle WAXS patterns for lithium insertion into soft carbon. The initial scan has been included as a dashed line on panels (b) to (e) for reference.

As stated above the intensity around  $53^\circ$  dropped as expected, however there was no corresponding increase in intensity at lower angles. As a result of the higher scattering cross-section of sodium relative to lithium, the intensity increase should be much larger for the sodium cell than for the lithium cell and hence should be obvious in the scan patterns unless the carbon is highly strained. If more strain develops in the sodium cell than in the lithium cell during discharge then much of the 004 peak intensity would be eliminated. In order to examine this hypothesis, the layer stack model developed in Chapter 3 was used to try to replicate the observed intensity changes.

### **6.1.5 Model Calculations for Na and Li Insertion in Soft Carbon**

The layer model was used to calculate the intensity changes expected for a given amount of sodium/lithium between graphene sheets. In order to be able to compare the results from the calculations with those measured experimentally, there was a need to correct the experimental data for instrumental effects before determining the true position and intensity of the 002 peak. This data correction process is complicated by a number of factors. Attenuation of the incident and scattered beams by the beryllium window decreases with increasing scattering angle. Also, at low angles, it is probable that part of the beam hits the rim of the stainless steel can. As stainless steel has such a large absorption coefficient, it is likely that any part of the beam contacting the can would be absorbed to a large extent. The calculations are further complicated because the cell can is circular whilst the beam footprint is rectangular and because the can rim is raised above the beryllium window. This creates a shadow region where part of the beam footprint that would ordinarily impact the Be window, contacts the can before it gets to the level of the window. Although this combined can/rim attenuation can be calculated analytically, the resultant correction factor will be potentially inaccurate because of only partial absorption by the edge of the rim and by the presence of the torr-seal bead. There is also a need to account for the Lorentz and polarization factors in order to extract accurate intensities when the scattering angle of the peak maximum changes and to deal with the enhanced background scattering from the sample in the cell caused by the presence of electrolyte species in the electrode.



A combination of empirical and analytical corrections was used to overcome this rather complicated situation. The scattering pattern for a pellet of the carbon was measured in air. A constant background term was then subtracted from the first scan measured on the cell. These background corrected data were multiplied by a constant and a constant background term was added so that the in-cell and out of cell curves coincided at intermediate angles. An empirical can attenuation correction was then applied below  $22^\circ$ , in order to have the two scans overlap in this region. The resultant fit between the in and out of cell scans was excellent, as shown in Figure 6.7.

The corrections outlined above were also applied to all other scans from the *in situ* runs, together with corrections for polarization and powder averaging, in order to determine the 002 peak position and magnitude of the intensity changes. The peak position was converted to an average interlayer spacing using the Bragg equation,  $d_{002} = \lambda / 2 \sin \theta$ , whilst the intensity values were converted to fractional intensities, relative to the maximum intensity for the 002 peak of the first scan. The results obtained for both the sodium and lithium cells are shown in Figure 6.8. This graph clearly shows the drop in intensity occurring in conjunction with the increase in interlayer spacing for both sodium and lithium insertion.

A number of calculations were completed for layer stacks of different average size and different amounts of strain. The results obtained were compared by eye (after scaling with appropriate multiplicative factors) to the data for the corrected first scan in order to determine the best fit to the 002 peak. The main factor that controlled the fit was the strain level. This meant that stacks with different numbers of layers could fit the 002 peak reasonably well, with only subtle differences between the resultant fits. Overall, after taking into consideration the fit to the 002 peak at the bottom of discharge together with the predicted intensities for the 004 peak, a stack of average 6 layers was selected to show that a significant amount of strain was required to model the sodium data. Similar trends to those outlined below were observed for different stack sizes.

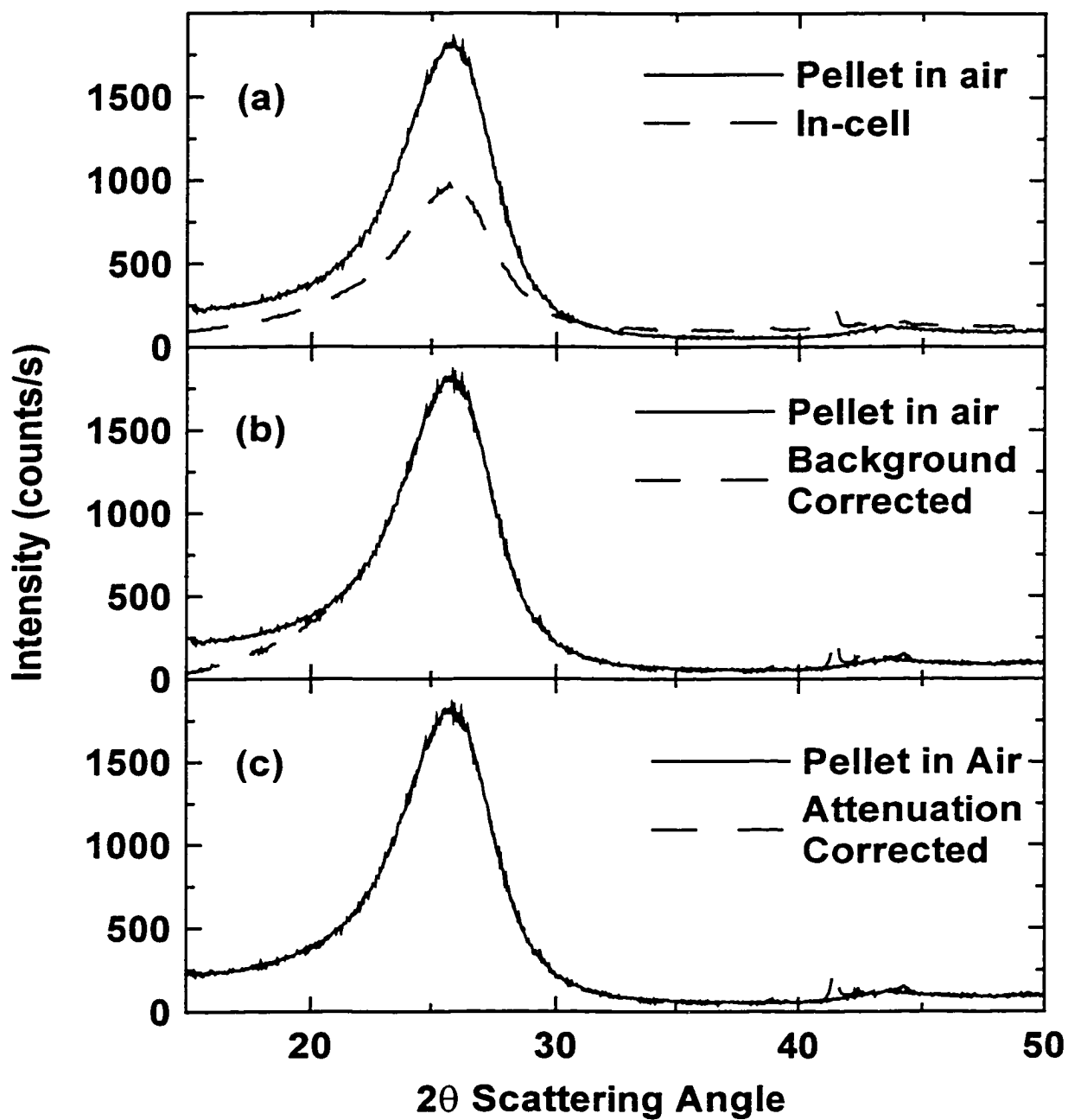


Figure 6.7: In-cell vs out of cell scans (a), together with the results for corrections (b), (c) to the in-cell data.

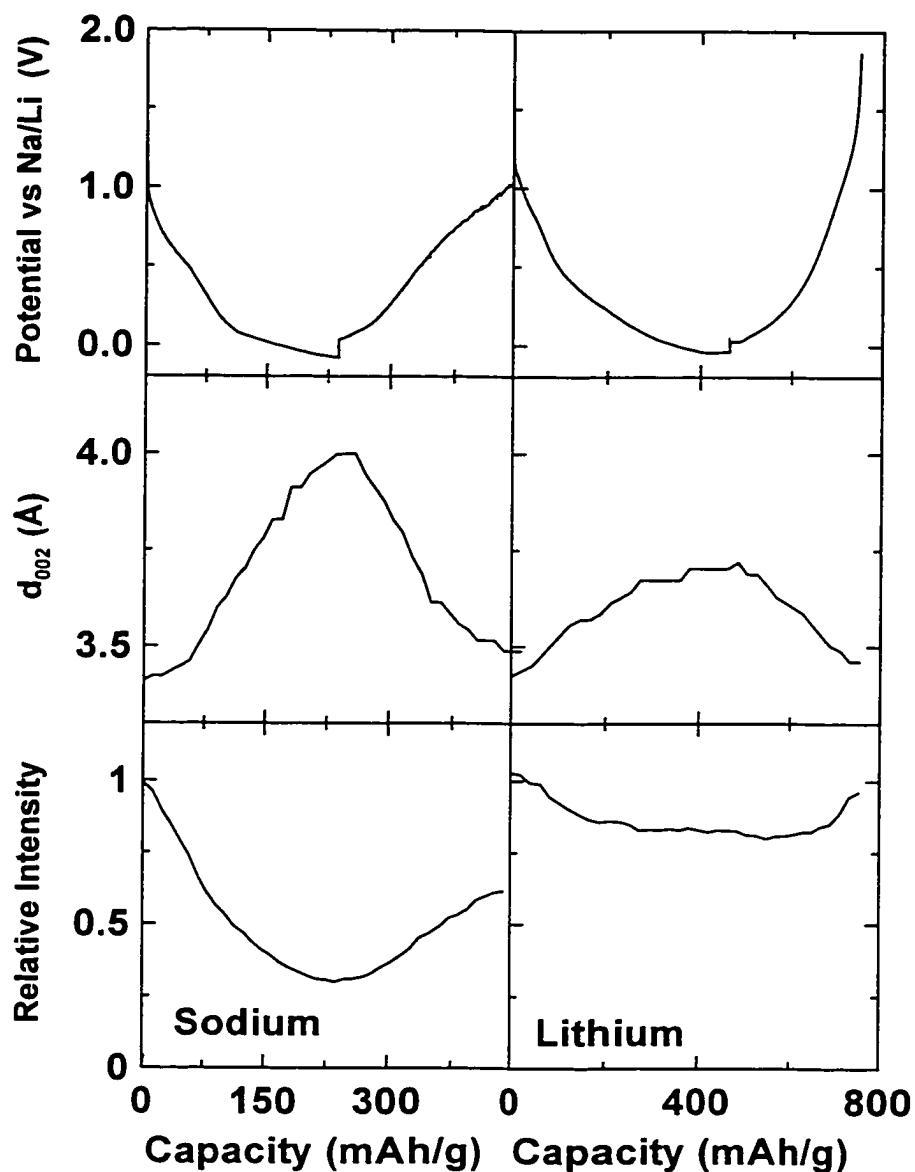


Figure 6.8: Intensity changes and 002 peak positions for sodium and lithium insertion into pitch-derived soft carbon.

The corrected experimental data together with the calculated fit to the first scans are shown in Figure 6.9a. It can be seen that the 002 peak fit is reasonable, whilst the model appears to underestimate the intensity for the 004 peak. However, the 100 peak is asymmetrical and hence has a slowly decaying tail that artificially increases the intensity of the experimental 004 peak. Thus the true 004 peak intensity is lower than that seen in the experimental data and the model fit is considered to be reasonable.

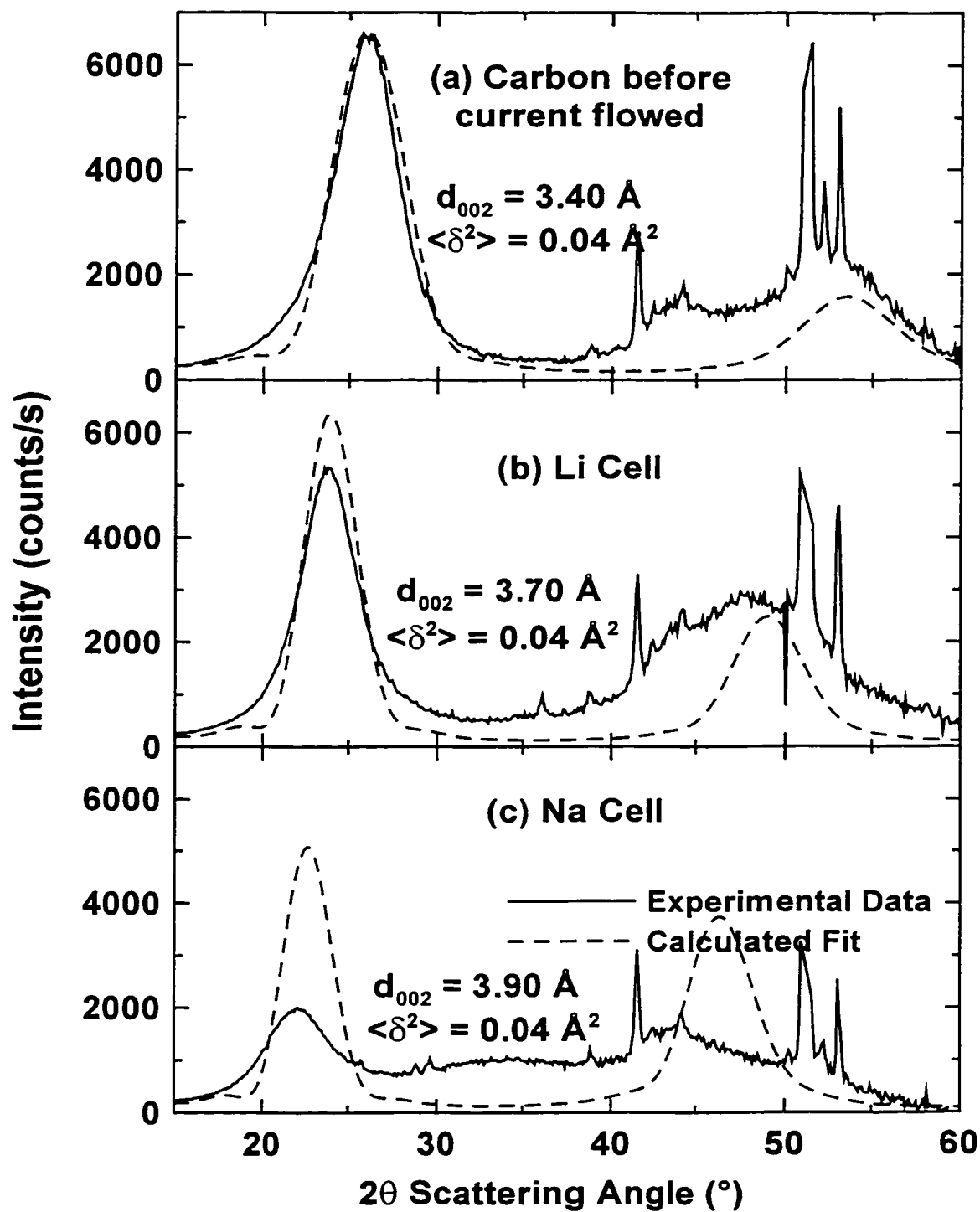


Figure 6.9: Experimental vs calculated intensity profiles for soft carbon with no change in strain – (a) scan before current was switched on; (b) bottom of discharge for lithium insertion; (c) bottom of discharge for sodium insertion.

Once the stack size was selected, the multiplicative factor was fixed, the sodium/lithium content was increased to that present at the end of discharge and the interlayer spacing was increased. The model calculation was then repeated with the new parameters over a range of strain values for the lithium and sodium loaded samples. The resultant calculated curves for the same strain level used to fit the first scan are shown in Figures 6.9b and c, together with the experimental curves for the sodium and lithium *in situ* cells at the bottom of discharge. It can be seen that without changing the strain level, the model calculation predicted a higher intensity for the 002 and 004 peaks of the sodium/lithium loaded carbons than was observed experimentally (after allowing for the contribution from the 100 peak to the experimental data). The effect of increasing the strain level is shown in Figure 6.10. It can be seen that the model fits the lithium data reasonably well. With the inclusion of strain, the fit is better for the sodium cell than the model without strain (particularly for the 004 peak) but is still not good. This highlights the limitations of the simple model used, particularly the assumption that the carbon can be approximated by a series of isolated crystallite domains that scatter independently.

Further work would be required to develop a more complex model, however this would not change the overall trends, namely that sodium and lithium insert between approximately parallel carbon layers, forcing them apart.

As seen earlier (Figures 6.2 and 6.5) the intensity around  $32^\circ$  increased during discharge of the *in situ* sodium cell through formation of a broad hump, and then decreased again during charge. One possible explanation for this behaviour is that this intensity may result from localised sodium clustering as shown in the upper panel of Figure 6.11. A small cluster of sodium atoms arranged with BCC packing would generate intensity around  $32^\circ$ . Such behaviour is shown in the lower panel of Figure 6.11, where the Debye powder pattern for  $2 \times 2 \times 2$  unit cells of BCC Na has been calculated using equation 3.53. The increase in strain required to more effectively model the magnitude of the intensity changes may in part result from this sort of uneven expansion of the layers.

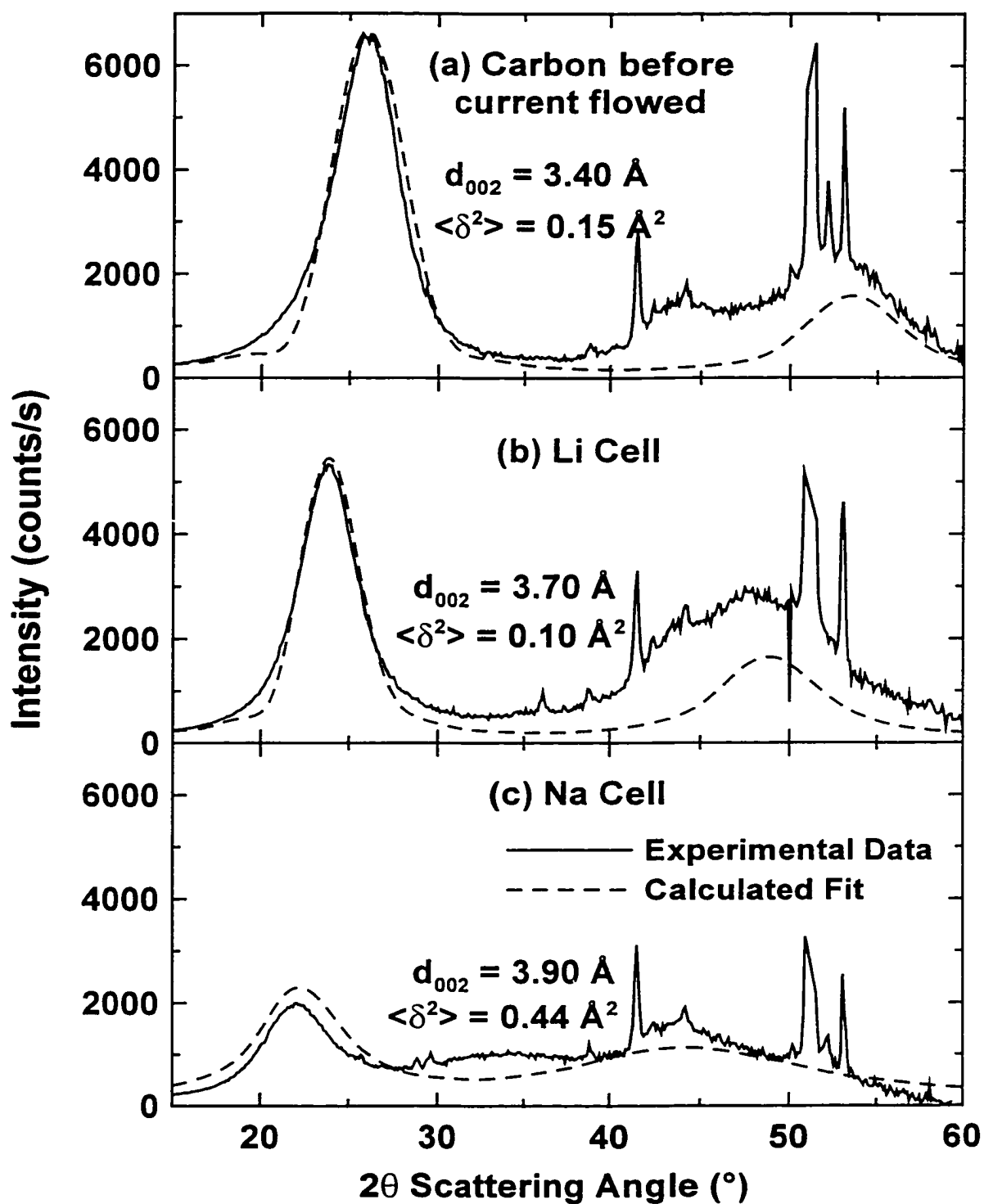


Figure 6.10: Experimental vs calculated intensity profiles for soft carbon after increasing strain – (a) scan before current was switched on; (b) bottom of discharge for lithium insertion; (c) bottom of discharge for sodium insertion.

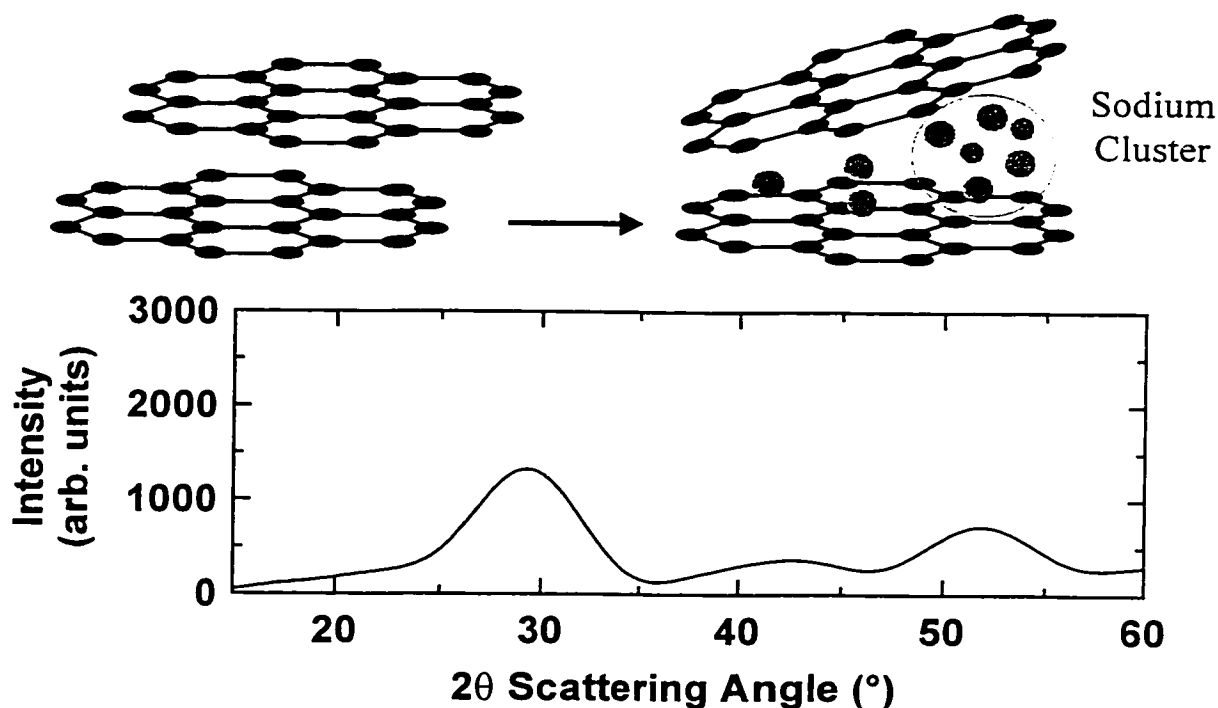


Figure 6.11: Upper panel - exaggerated schematic of sodium cluster formation between graphene layers that were originally parallel. This would reduce the intensity across the 002 peak. Lower Panel - Calculated Debye pattern for 2 x 2 x 2 unit cells of BCC Na.

### 6.1.6 Hard carbon with sodium and lithium at low angles

The hard carbon materials also exhibit a sloping voltage region, although the much lower intensity of the 002 peak in these materials relative to the soft carbons makes the changes occurring during discharge or charge along this region of the voltage curve difficult to resolve. This is a significant problem for lithium insertion where the changes are small already because of the low x-ray scattering cross-section of lithium. Despite these difficulties, a set of scans during sodium and lithium (Figure 6.12 and Figure 6.13, with each scan offset by 10 from the previous scan) insertion and removal were measured on hard carbon prepared by heat-treating glucose to 1000°C.

Although it is difficult to see from Figure 6.12, some of the same trends seen for sodium insertion into soft carbon along the sloping voltage regions were also seen for the glucose-derived sample. This is easier to observe in Figure 6.14, where each panel shows

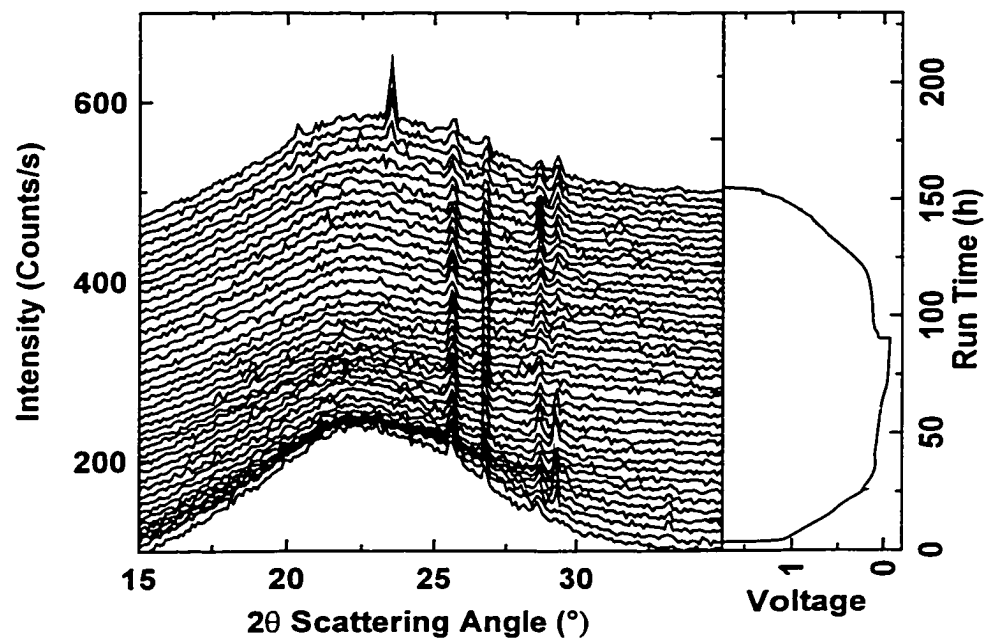


Figure 6.12: WAXS measurements of sodium insertion into hard carbon. Each scan has been offset from the last by 10 counts/s for clarity.

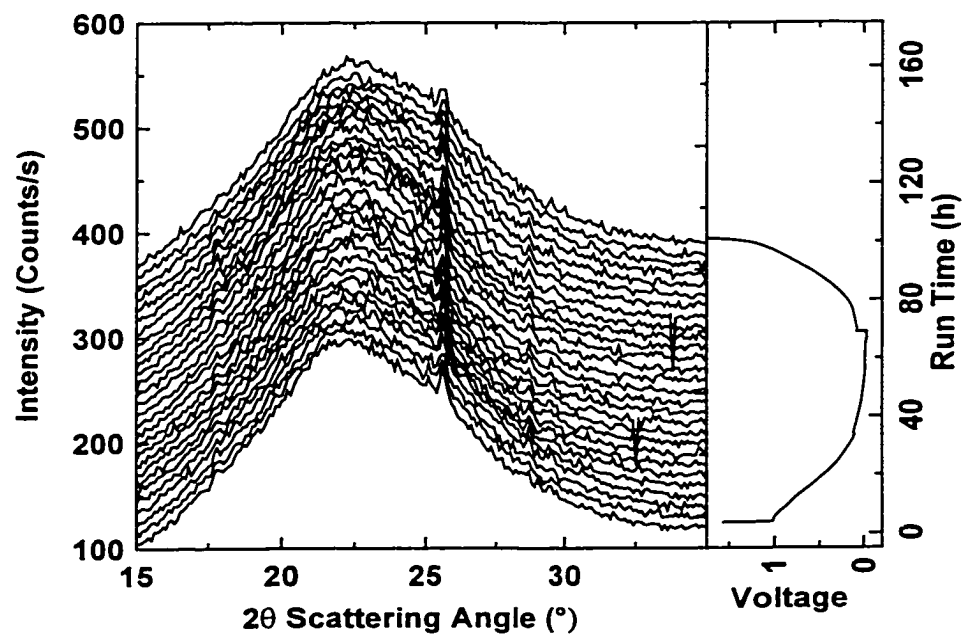


Figure 6.13: WAXS measurements of lithium insertion into hard carbon. Each scan has been offset from the last by 10 counts/s for clarity.



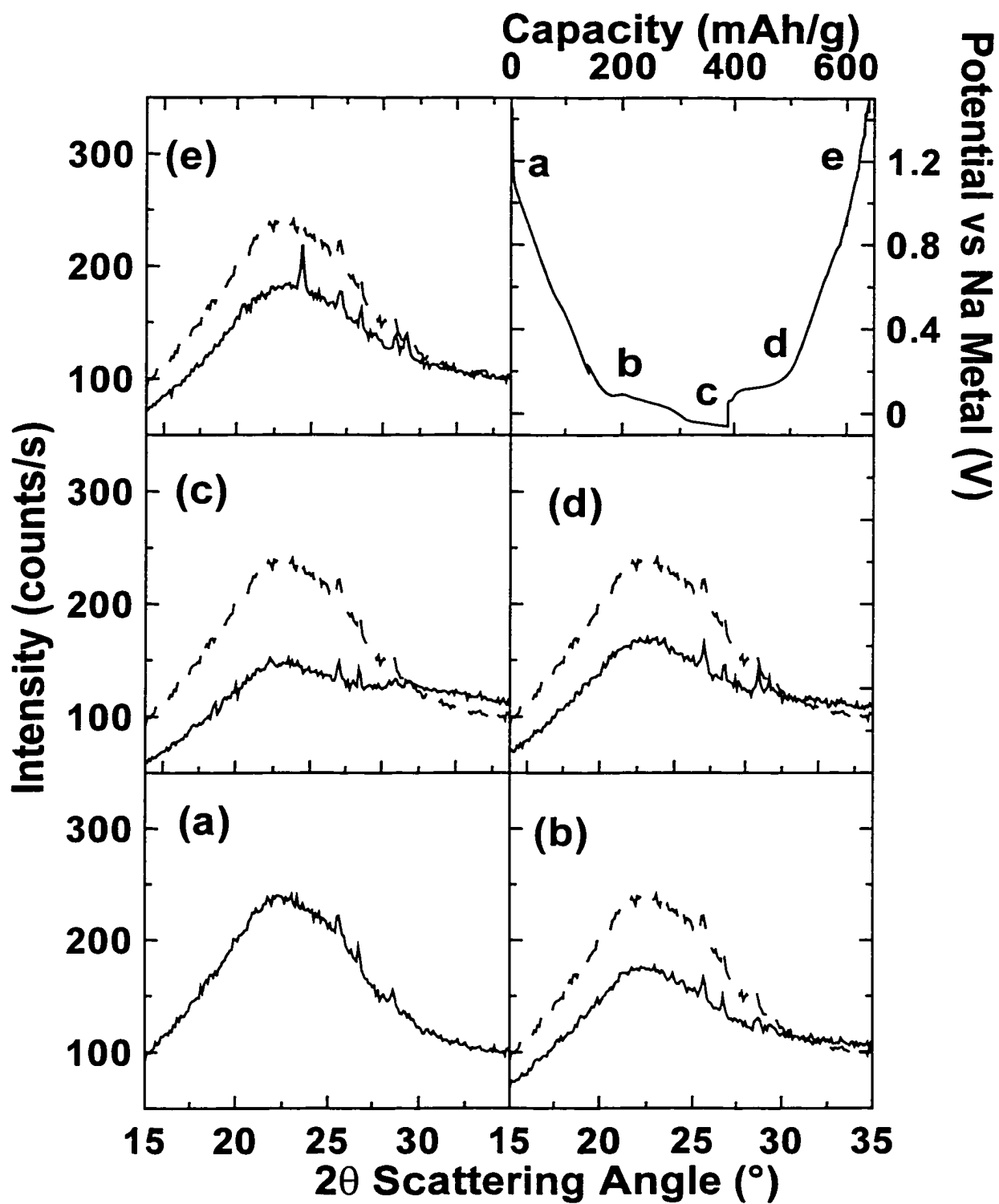


Figure 6.14: Selected WAXS scans for sodium insertion into hard carbon.

the first scan as a reference. As the cell was discharged along the sloping voltage region (panel a to b) the intensity of the 002 peak dropped and there was a slight shift to higher scattering angles.

A small hump appeared, centred around  $32^\circ 2\theta$ , along the low voltage plateau (panel b to c). It is possible that this is caused by the presence of small sodium clusters within the nanopores of the carbon (the shape and location of this peak correspond well with the pattern for BCC Na nano-domains shown in Figure 6.11). There is an obvious similarity between this nanopore mechanism and that proposed for Na insertion into soft carbon, making the two processes difficult to separate. It is possible that the size of the clusters formed in the hard carbons is larger than those formed in the soft carbons. It is also likely that some of this intensity comes from sodium atoms bonded to the surface of the crystallites, although in the case of the hard carbons, the surfaces of the crystallites correspond to the walls of the pores. Hence it is very difficult to separate the surface layers from the sodium atoms adsorbed in the nanopores. The *in situ* SAXS studies presented in section 6.3 are more useful for examining pore structure changes.

The data for the lithium cell show very little change in intensity (Figure 6.15) throughout the scan. This results from the low scattering cross-section of lithium and highlights the potential limitations of x-ray scattering measurements on light elements.

### **6.1.7 Hard carbon with sodium and lithium at high angles**

The high angle results for the sodium and lithium cells are presented in Figure 6.16 and Figure 6.17 respectively. The sodium cell scans show the development of intensity around  $32^\circ$  occurring along the low voltage plateau. They also show that the intensity around  $45^\circ$  decreases during discharge then increases during charge. This behaviour cannot be explained at this time. As with the low angle scans, the lithium cell showed very little change in intensity during discharge and charge primarily due to the low x-ray scattering cross-section of lithium.

Overall the results from the *in situ* WAXS measurements of the glucose carbon are consistent with those obtained from the soft carbon, showing that alkali atoms insert between carbon layers along the sloping voltage profile of the electrochemical curves.

The sodium results also suggest that sodium may form small clusters during insertion along the low voltage plateau.

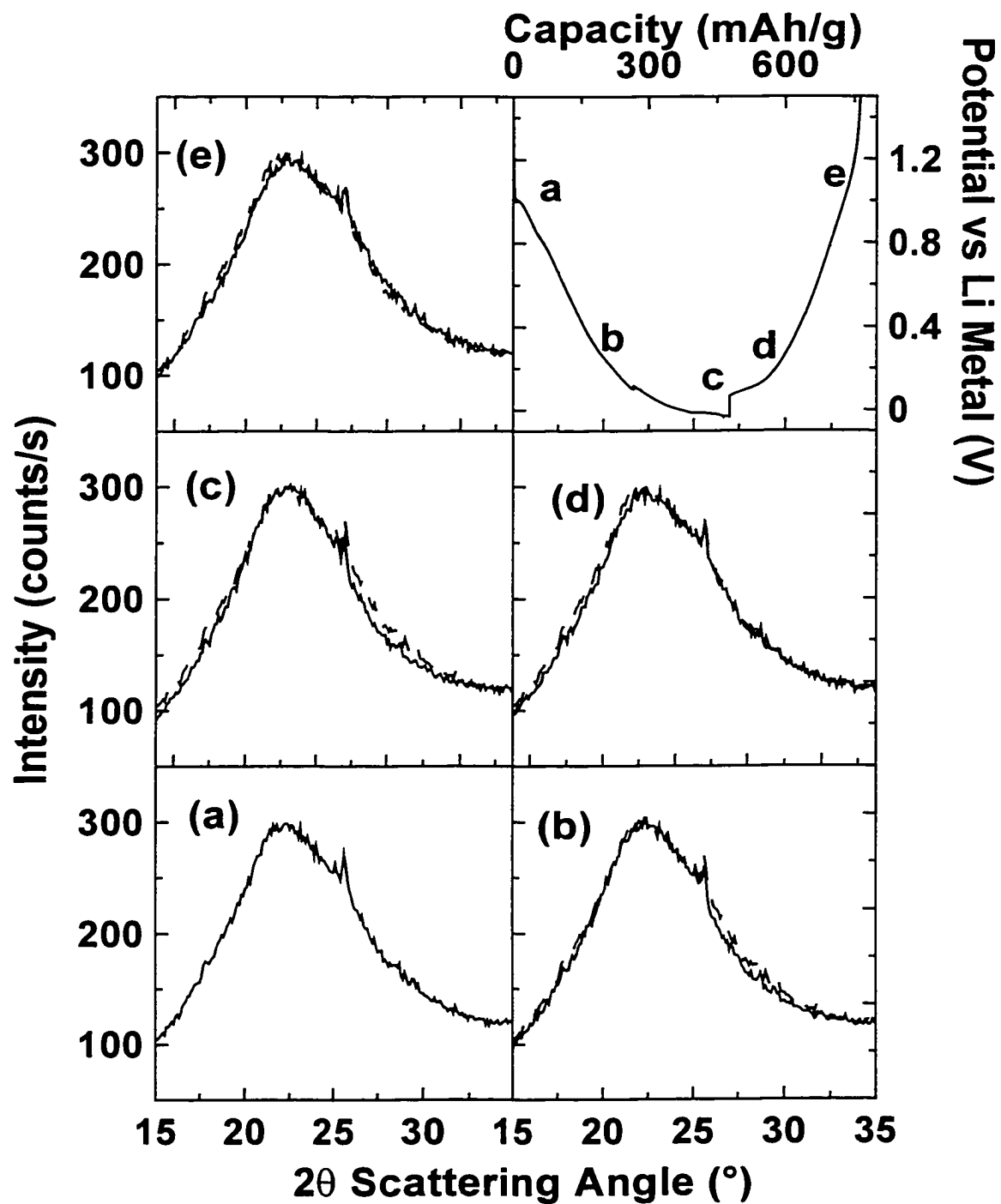


Figure 6.15: Selected WAXS scans for lithium insertion into hard carbon.

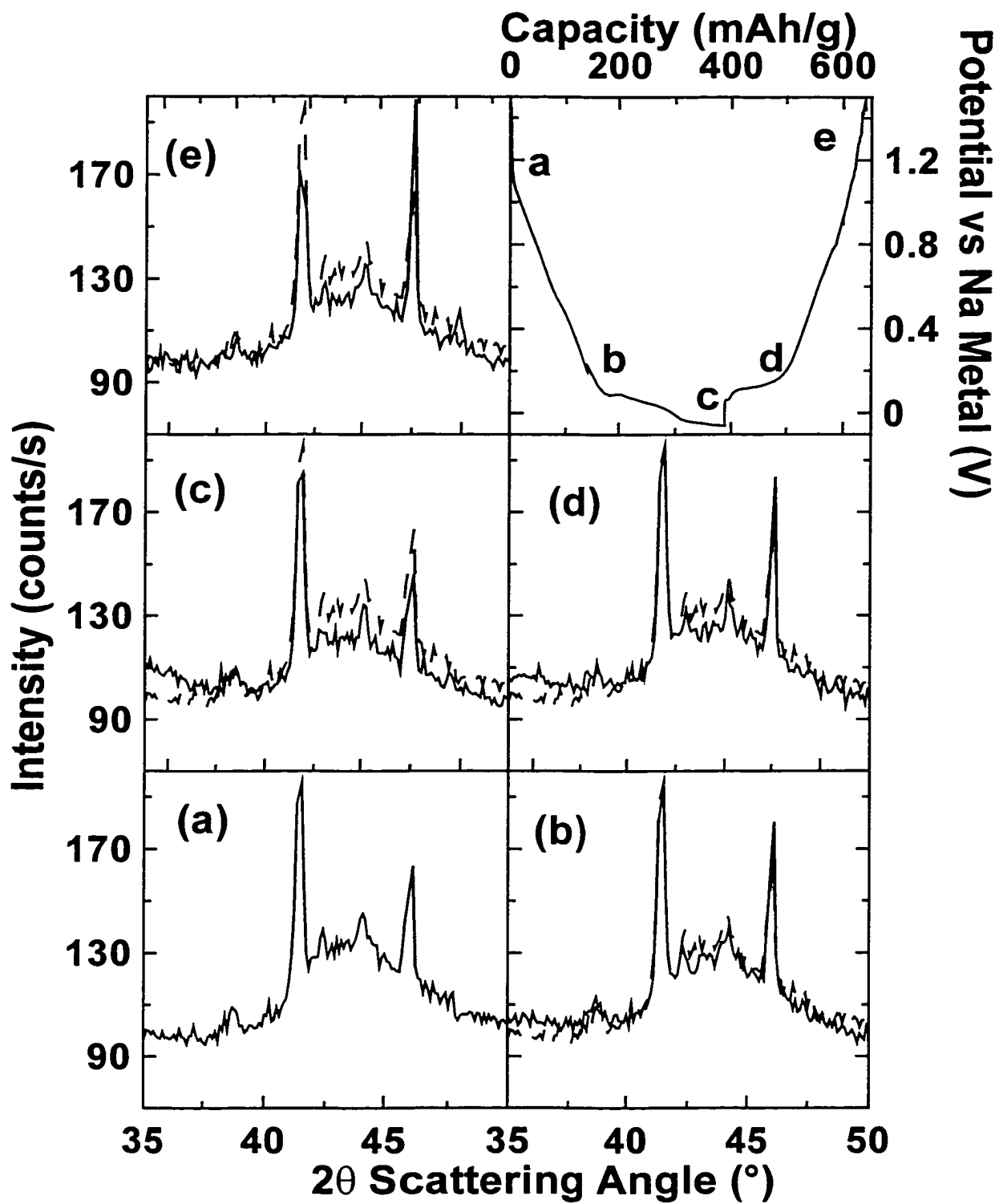


Figure 6.16: Selected high angle WAXS scans for sodium insertion into hard carbon.

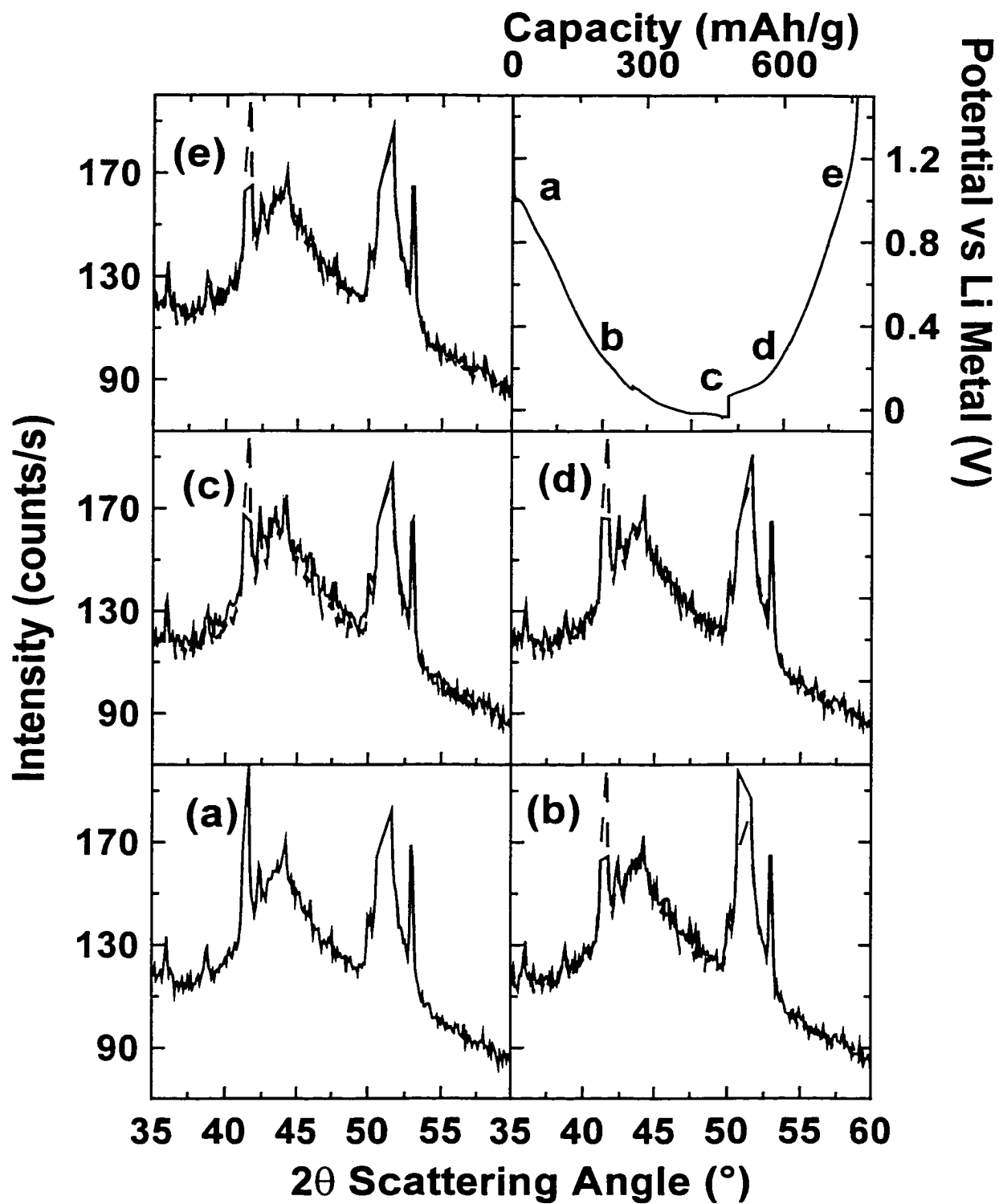


Figure 6.17: Selected high angle WAXS scans for lithium insertion into hard carbon.

## 6.2 SAXS Studies

In the previous chapter it was proposed that sodium and lithium insert into hard carbon materials through a combination of interlayer insertion and insertion into nanopores in the carbon. It has already been shown that the interlayer insertion mechanism does occur, as predicted. This section presents conclusive evidence to support the proposed nanopore insertion mechanism, through interpretation of *in situ* small-angle x-ray scattering data.

The pore insertion mechanism was proposed based on two observations. First, SAXS measurements completed on the hard carbons clearly showed the presence of scattering regions of only a few nanometres in size. This scattering was created by an electron density contrast between graphene sheets and the void space between the sheets, caused by a combination of defects within the sheets and crosslinks between adjacent sheets. Gas adsorption measurements on the same materials have shown that, especially for the lower temperature samples, a large fraction of this void space is accessible to gas molecules. Fitting the adsorption isotherms with model isotherms calculated through DFT methods for a range of slit widths between graphene layers also showed that most of the open porosity in these materials is of only a few nanometres in size. Thus the SAXS and gas adsorption data are entirely consistent with each other and are measuring the same features in the materials. These two techniques also showed that soft carbons contain very little of this nanoporosity. Most of the pore volume in these materials is much larger in size and can be attributed to void space between crystallite domains and macroporosity within particles.

The second observation used to support the nanopore insertion mechanism was that the electrochemical profiles of the hard carbons contain low voltage plateaus for both lithium and sodium. There are two parts to this observation. First, this plateau was only seen for hard carbon samples that contained high volumes of nanoporosity (as measured by SAXS). Second, the plateau occurred at a potential close to that of the metal itself. This implies that the extent of charge transfer from the metal to the carbon was quite

small. This would most likely occur only if the metal species was at a reasonable distance from the carbon and hence did not experience a large attractive force from the pore walls. Such a situation exists within void space, especially if the pore already has alkali species adsorbed onto the walls.

Despite this consistent, reasonable and logical interpretation of the data, it could be argued that the evidence outlined above is largely circumstantial. There is no direct observation of filling of the pores by the alkali species. To conclusively show that the proposed mechanism occurs in reality, an alternative test was required - one that was sensitive to such changes. Gas adsorption measurements of carbon samples at different points along the electrochemical profile may appear to be a reasonable option. This was tried but the results were unable to support this mechanism as gas adsorption requires gas molecules to interact physically with the filled carbons and there needs to be a pathway through which the gas molecules can access the nanoporosity. It must be remembered however that, during discharge of an electrochemical cell, reactions occur at the electrode surface to form what is known as the solid electrolyte interphase (SEI) layer. This layer is a continuous film that is ionically conductive [86]. However it does present a physical barrier on the particle surfaces preventing passage of gas molecules. Thus, when gas adsorption profiles of a hard carbon sample after discharging for only a short time were measured, the adsorbed volume dropped to a fraction of its initial volume.

Small-angle x-ray scattering studies are ideally suited to probe such problems. A physical barrier that is essentially continuous is transparent to x-rays at small-angles (although some absorption will occur, dependent on the thickness and composition of the layer). Thus SAXS can be used to probe the interior of particles. It is sensitive to changes in electron density and thus, if pores in the material are filled with another species, the contrast will change causing the scattering to change. *In situ* studies of operating electrodes provide an opportunity to observe such a pore filling process dynamically.

An electrochemical cell set-up was therefore developed to allow for transmission measurements of operating electrodes. The cells were assembled with carbon pellets as detailed in Chapter 5 and placed in the diffractometer. An initial scan was collected between 0.3 and 15° scattering angle to act as a reference for all subsequent scans. The

cells were then discharged at a relatively high current (750  $\mu\text{A}$  for Li cells and 500  $\mu\text{A}$  for Na cells) until a trip point of 0.2 V with respect to the metal was reached (close to the point at which the low voltage plateau starts to appear). During this time a series of x-ray scans were collected, with the time interval for each scan ( $\sim 2 \frac{1}{2}$  hours) being small relative to the discharge time (days). After the trip point was reached, the current was reduced (500  $\mu\text{A}$  for Li cells, 300  $\mu\text{A}$  for Na cells) and the x-ray scans continued. Once plating was seen in the voltage profile, the current direction was reversed and the cells were charged (500  $\mu\text{A}$  for Li cells, 300  $\mu\text{A}$  for Na cells) to a trip point of 2 V, again with the diffractometer scanning continuously.

Before analysing the *in situ* data, there was a need to ensure that the SAXS curves obtained were representative of the carbon itself. This was achieved by measuring the SAXS profile for a pellet of material in air and comparing the resultant scan with that obtained before current was applied to the cell. Glucose-derived hard carbon was used for this work as it produced a significant amount of small-angle scattering and hence any changes in scattering in and out of the cell would be more obvious. The scans obtained are presented in Figure 6.18. The shapes of the two scans are similar although the pellet in the cell scatters with decreased intensity. This is not surprising given that the x-ray beam has to pass through all the cell components in addition to the carbon pellet (eg Be windows, electrolyte, separator, metal foil) before reaching the detector and hence will be absorbed to a larger extent. The *in situ* SAXS data from this cell were modeled using equation 3.41, repeated here as equation 6.1 to aid the discussion below:

$$I(q) = \frac{A}{q^n} + \frac{B a_1^6 (\eta_{\text{nanopore}})^2}{(1 + a_1^6 q^2)^2} + \frac{C a_2^6}{(1 + a_2^6 q^2)^2} + D, \quad (6.1)$$

By allowing the background parameter, D, to vary for each pellet, and by only allowing A and B to change by a constant factor (fixing C at zero) the data for both curves could be fit well with a value of 2.82  $\text{\AA}$  for  $a_1$ . This implies that the cell components serve only to attenuate the beam and do not, on their own, contribute significantly to small-angle scattering. The fit parameters were obtained by minimising the value of the goodness of fit parameter, GOF (equation 3.42), using Microsoft Excel<sup>®</sup>.



The fits obtained are also shown on Figure 6.18, together with a scan for graphite containing no nanoporosity. This scan was used to determine the exponent of  $q$  in the first term of equation 6.1. This parameter optimised to 3.3.

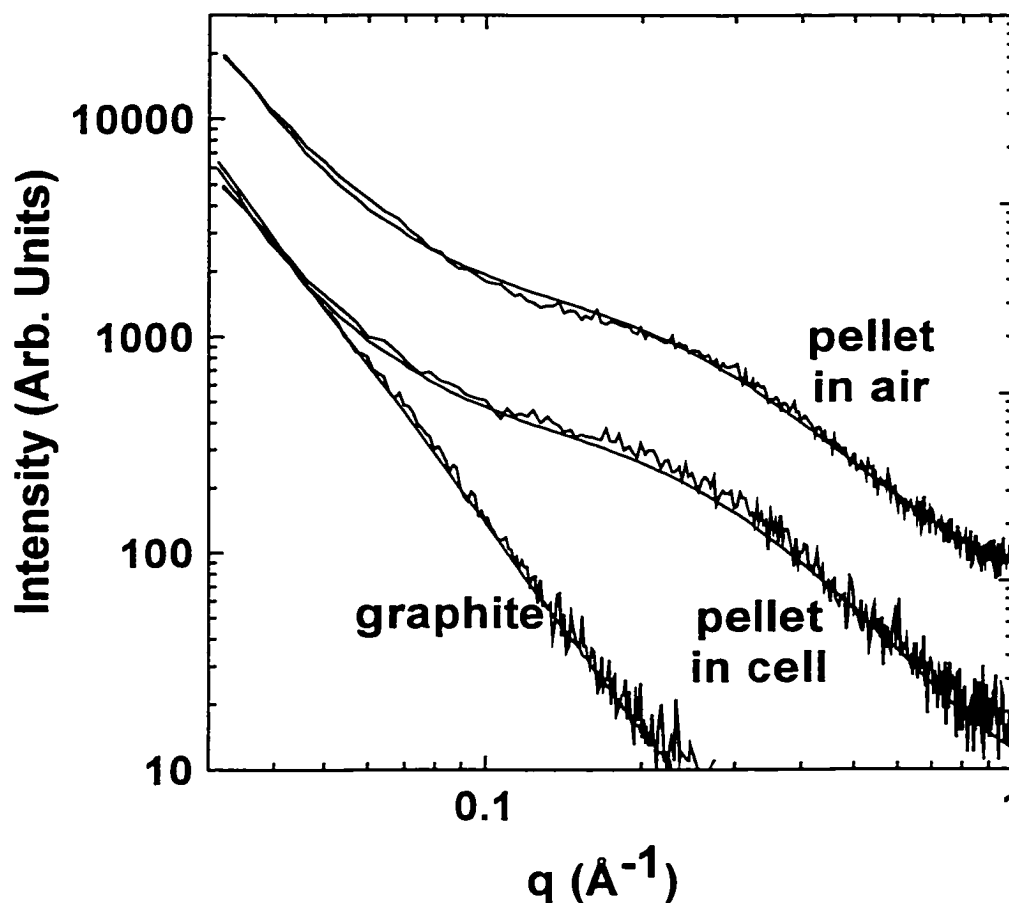


*Figure 6.18: A comparison of intensity curves for hard carbon pellets in and out of an electrochemical transmission cell. The scan obtained for graphite showing Porod's law behaviour with a slope of  $-3.3$  is also included, as are fits to each of the scans.*

Although better fits could be obtained by allowing  $A$ ,  $B$  and  $a_1$  to vary independently for each pellet, the changes in these parameters relative to those obtained through restricted fitting were small. This demonstrates that the in-cell scans provide a reliable fingerprint of the carbon structure. The restricted and best-fit parameters are shown in Table 6.1.

Table 6.1: Comparison of fits for glucose derived hard carbons in air and within an *in situ* SAXS cell.

Sample	A ( $\text{\AA}^3$ )	B	$a_1$ ( $\text{\AA}$ )	D	GOF
Pellet in Air ( $a_1$ fixed at 2.82 $\text{\AA}$ )	0.21	3.32	2.82	71	3.5
Pellet in Cell ( $a_1$ fixed at 2.82 $\text{\AA}$ )	$0.25 \times 0.21$ = 0.052	$0.25 \times 3.32$ = 0.83	2.82	10	3.3
Pellet in Air (best fit)	0.21	4.12	2.70	64	3.3
Pellet in Cell (best Fit)	0.048	0.76	2.94	9	1.9

In addition to demonstrating that the cell components acted only to attenuate the beam, there was a need to verify that changes observed in the x-ray scans resulted predominantly from changes in the nanopores in the carbon and not through contributions from these other components. It was quite fortuitous that this assessment could be performed by measuring a set of SAXS scans on an operating cell containing one of the materials of interest. As soft carbons contain negligible nanoporosity, if there is no measurable change introduced by the other cell components then the *in situ* scattering profiles for this material should show no changes in scattered intensity during the discharge-charge process.

### 6.2.1 *In situ* SAXS study of Soft Carbon

An *in situ* SAXS cell containing a pellet of pitch-derived carbon heat-treated to 1000°C was prepared and run against sodium metal. Unfortunately this cell shorted out during charge and thus only the discharge and part of the charge data were obtained. The procedure outline below was used to obtain the best-fit model parameters for each scan. Again the model of Kelliat et al. (equation 6.1) was used, although for this work, as the

electron density between the pores and the surrounding matrix was expected to change, it needed to be explicitly included as a variable (hereafter referred to as  $\Delta\rho$ ).

As the first scan was used as a reference scan for all subsequent scans, it was important to fit this scan well. A good fit was obtained with C set at zero and  $\Delta\rho$  set equal to 1. The selection of this particular starting value for  $\Delta\rho$  will be explained in conjunction with the analysis of the *in situ* SAXS scans for the hard carbon. A reasonable value for  $a_2$  was selected based on the trends observed for the *in situ* scans. For this material,  $a_2$  was set at 15 Å. All subsequent scans were then fit to the above model, with only  $\Delta\rho$  and C allowed to vary.  $\Delta\rho$  was allowed to vary to identify any changes in electron density contrast as a result of sodium/lithium insertion into pores, whilst C was allowed to vary to incorporate any matrix cracking effects that may have resulted from insertion of sodium/lithium between the graphene layers. The fitting process was automated through use of a macro in Excel<sup>®</sup>. The resultant fit quality was excellent for all scans, implying that the simple model used was a reliable assessment tool.

Sample curves at different positions along the electrochemical profile are shown in Figure 6.19, together with the results obtained from the fitting procedure detailed above. Two features are apparent: the fits lines are difficult to resolve from the scans themselves, showing the excellent quality of the fits obtained and there was very little change in the SAXS profile of the cell throughout the cycle. This shows that the other components in the cell do not contribute significantly to any changes in the scattering behaviour and that there is no evidence of nanopore insertion into soft carbon (not surprising given that these carbons contain negligible amounts of nanoporosity).

Figure 6.20 shows the fit parameters obtained for each scan (remembering that only C and  $\Delta\rho$  were allowed to vary). The quality and consistency of the fits is apparent from the plot of GOF. Although the cell shorted out during charge, it is apparent that there is only a small decrease in the electron density contrast during discharge that increases again during charge. It is likely that this corresponds to sodium insertion into residual nanoporosity – as the B parameter for this material optimised to 0.065, this carbon contains only a small number of such pores.

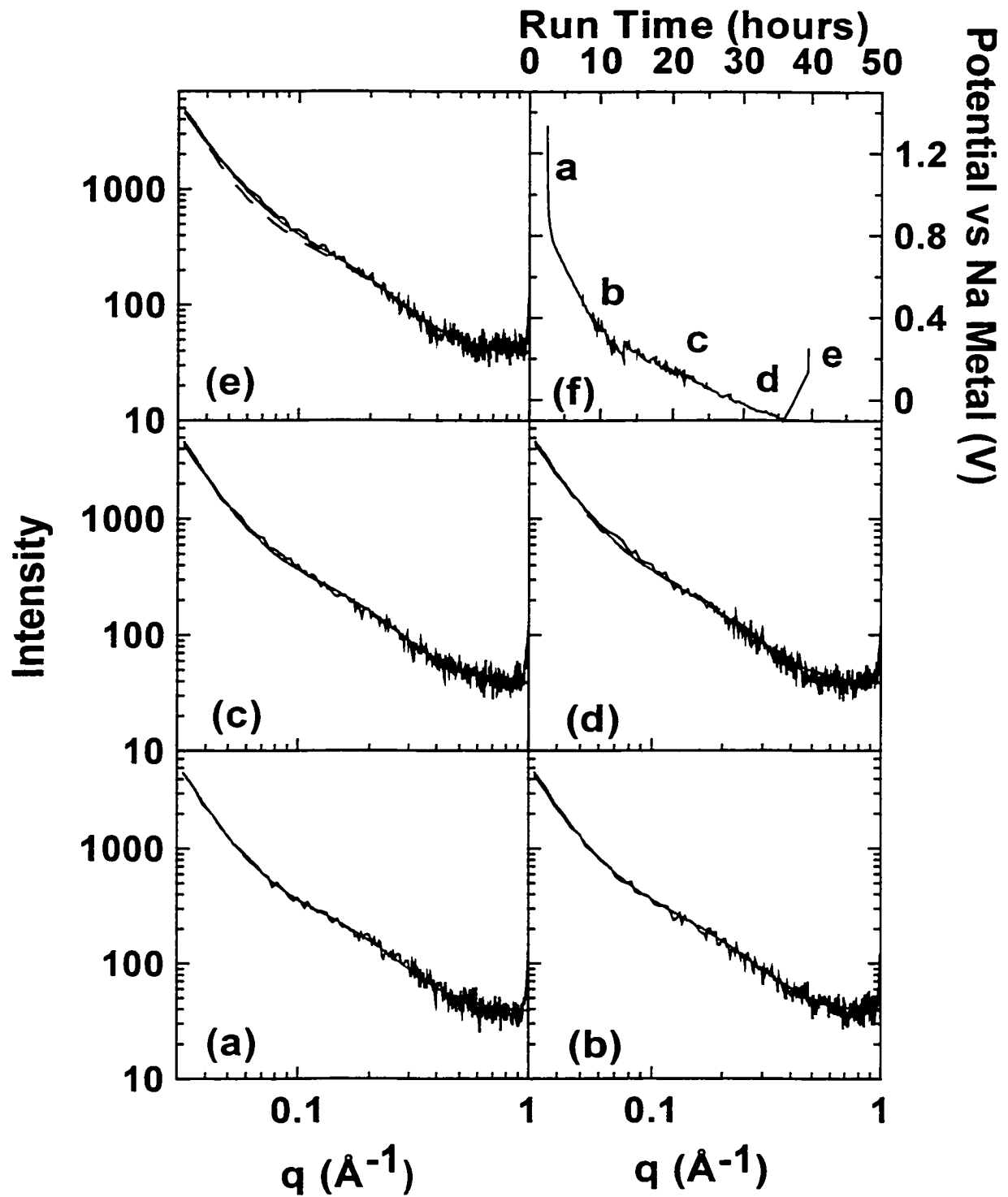


Figure 6.19: Sample SAXS curves during discharge and charge of a soft carbon cell. The fit obtained for the first scan is shown on subsequent scans for reference.

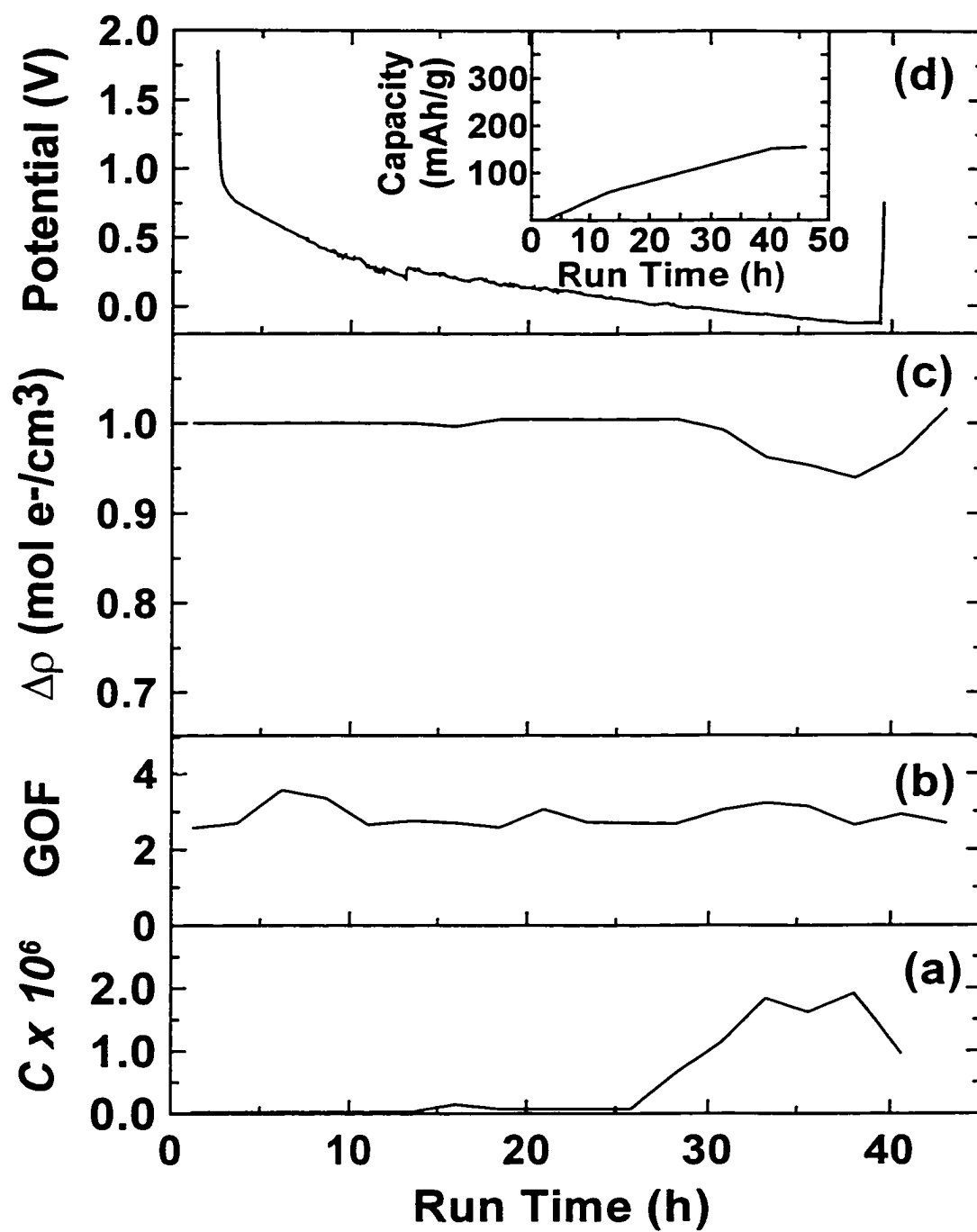


Figure 6.20: SAXS fit parameters for sodium insertion into and removal from soft carbon.

The results obtained for the pitch sample show that the only significant changes that occur in the SAXS pattern arise from changes in the pores in the carbon material and not from other cell components.

### 6.2.2 Sodium and Lithium SAXS Studies of Hard Carbon

The set of SAXS scans obtained for sodium insertion into a pellet pressed from the glucose carbon heat-treated to 1000°C is more interesting. The same fitting routine used to analyse the pitch scans was used for this material. The results obtained are presented in Figure 6.21. Again each scan panel contains the fit to the first scan as a reference shown with a dashed line. The scattering from the nanoporosity appears as the broad hump on the sloping background.

As the cell discharged along the sloping voltage region (a to b), there was no change in this hump, although an increase in intensity occurred at lower  $q$  values. This was accounted for in the fits by an increase in  $C$ , (with  $a_2$  set at 10Å). This change may have resulted from the development of micro-cracks in the material. As the cell discharged along the low voltage plateau (b to c), the nanopore intensity steadily decreased, until, at the bottom of discharge (c) it was difficult to resolve from the sloping background of the scattering curve. This provides very clear evidence that the contrast between the pores and the surrounding matrix decreased along the low voltage plateau. For this to occur, the electron density in the pores must have increased. This would occur as sodium entered the pores (to the x-ray beam, this is equivalent to electrons entering the pores). After the cell was switched to charge, the nanopore scattering reappeared (c to d) along the low voltage plateau, consistent with an increase in contrast, again caused by sodium leaving the pores. For sodium removal along the sloping potential region, there was no change in the scattering from the nanopores. It appears that the cracking process occurring during discharge (increasing the  $C$  parameter), increasing the intensity at low  $q$ , was not a reversible process. This is to be expected for something that can be classified as mechanical failure.

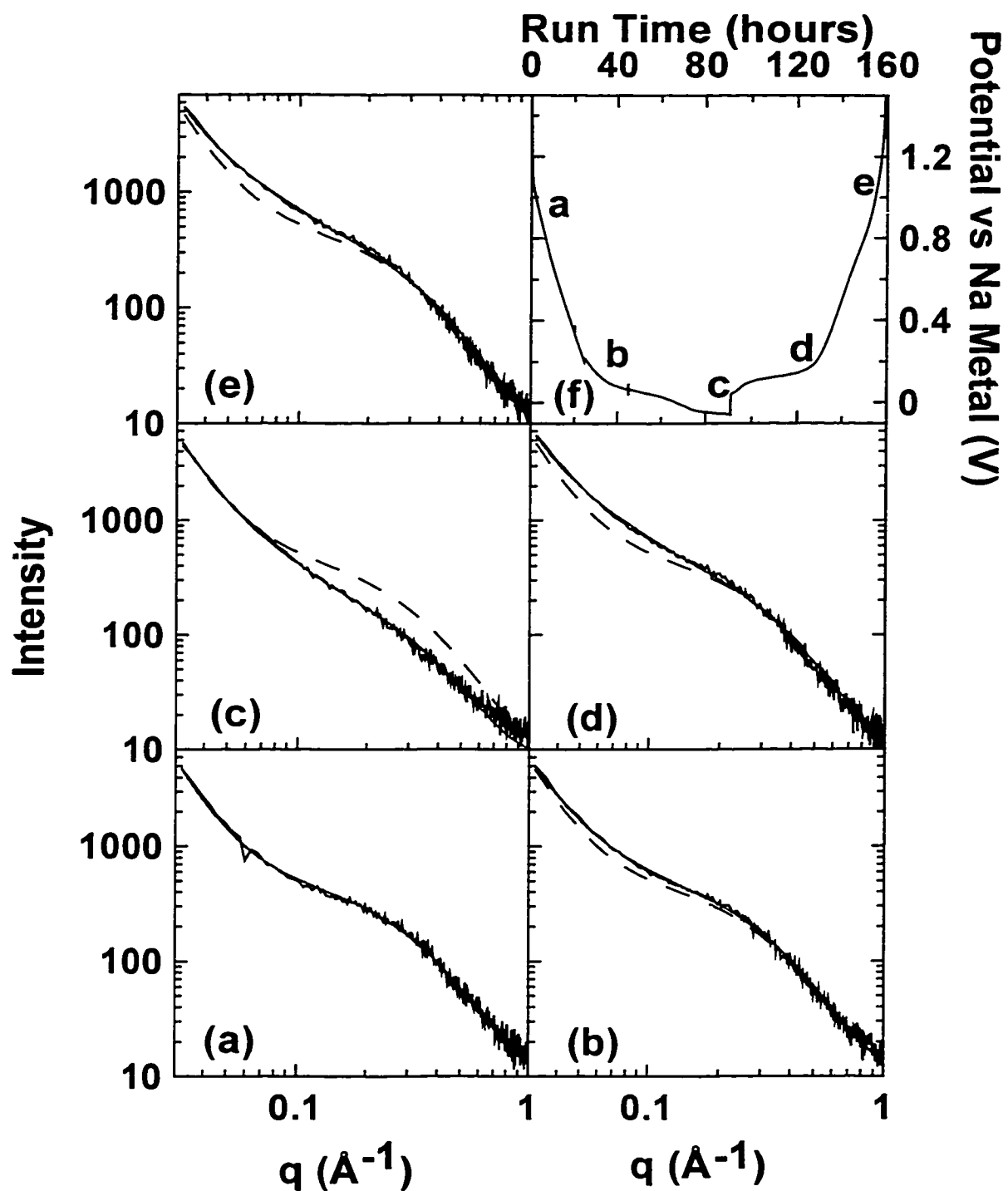


Figure 6.21: Sample SAXS scans for sodium insertion into glucose-derived hard carbon. The fit obtained for the first scan is included as a dashed line reference on subsequent scans. Each panel also includes the fit obtained.

It is the fit parameters that provide the best evidence in support of the nanopore insertion model. The values for  $\Delta\rho$  and C, together with the goodness of fit are presented in Figure 6.22. Again the quality of the fits obtained was excellent and uniform for all scans. The C parameter shows a steady increase, consistent with the development of micro-cracks. Close inspection of the voltage profile showed that after  $\sim 80$  hrs of discharge, the metal was plating on the electrode surface. Plating of metal would not decrease the contrast between the pores and the matrix and hence, during plating, the contrast remained constant. In order to determine whether the electron density contrast changes observed were realistic, a very simple pore filling model was used. The initial contrast was determined by calculating the contrast expected for a carbon of bulk density  $1.5 \text{ g/cm}^3$  (a reasonable value for a hard carbon where the contribution of macropores has been removed) with 25 % nanoporosity (again a reasonable value for a hard carbon). This gives a true density value of  $2.0 \text{ g/cm}^3$  for the carbon matrix surrounding the pores, and a density of  $0.0 \text{ g/cm}^3$  in the pores. As carbon has an atomic mass of 12 but only six electrons, the magnitude of the electron density of the matrix is half that of the true density. This therefore gives carbon with an electron density of  $1.0 \text{ mol e}^-/\text{cm}^3$ . The pores contain  $0.0 \text{ mol e}^-/\text{cm}^3$  hence the initial electron density contrast,  $(\rho_{\text{carbon}} - \rho_{\text{pore}})$ , is simply  $1.0 \text{ mol e}^-/\text{cm}^3$ . Nanopore insertion was then modeled by assuming that no sodium enters the pores until the start of the low voltage plateau. After this point, all the current passing through the cell was assumed to result from sodium entering nanoporosity. The amount of sodium entering the pores,  $n(\text{Na})$ , could be calculated from the amount of charge passed and the resultant electron density within the pores could then be calculated from the assumed pore volume of the carbon. Thus the electron density contrast was given by:

$$\Delta\rho = 1 - \frac{n(\text{Na}) \times 11}{\phi}, \quad (6.2)$$



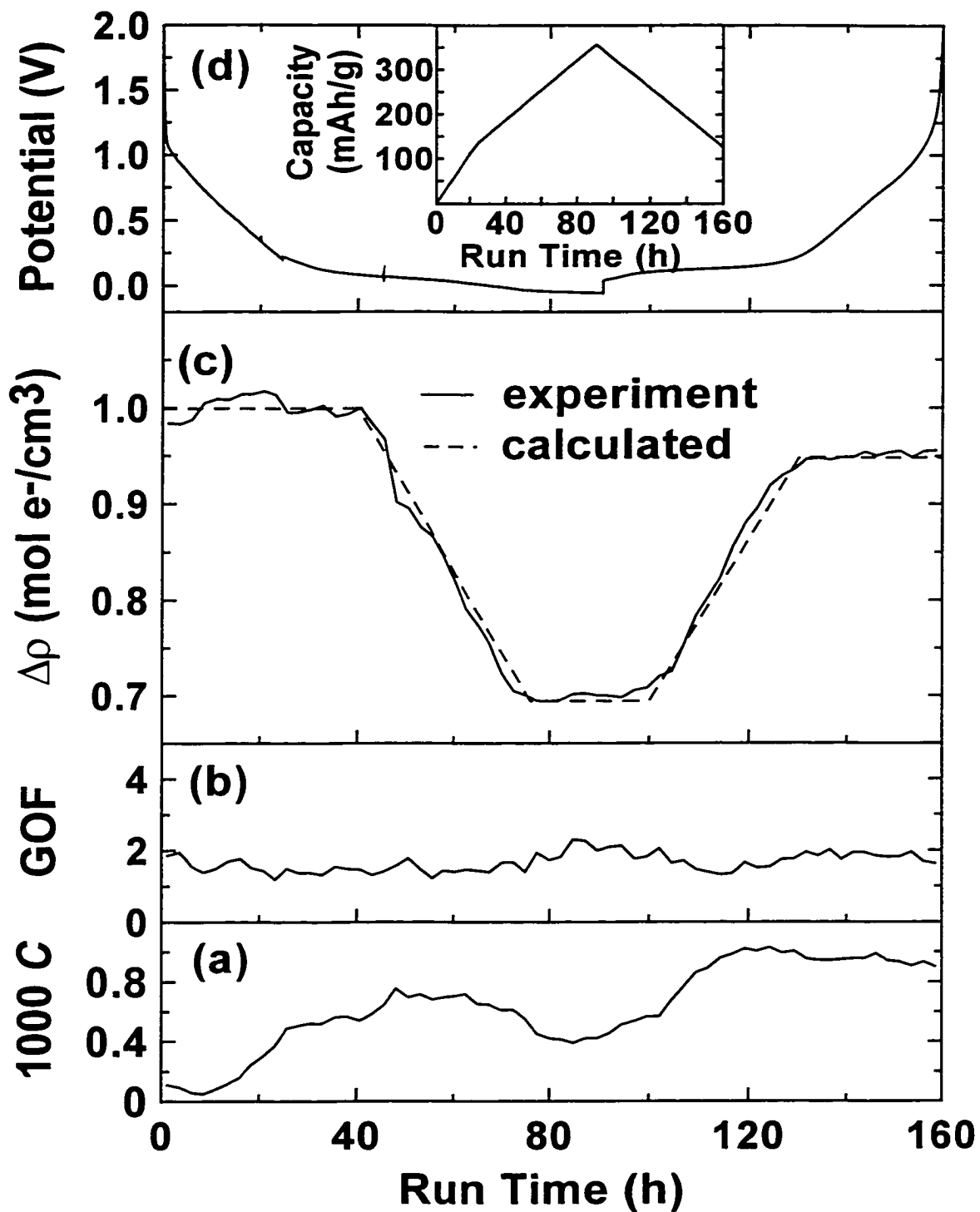


Figure 6.22: Fit parameters obtained for sodium insertion into hard carbon. The dashed line in (c) shows the electron density calculated from equation 6.1.

where  $\phi$  is the void fraction of the carbon (0.25) and the factor of 11 is the number of moles of electrons per mole of sodium. No further sodium was allowed to enter the pores in the model during the plating process. During charge it was assumed that the amount of sodium in the pores was decreasing, with all charge removed along the low voltage plateau, after allowing for stripping of plated metal from the electrode surface, being assigned to removal of sodium from the pores.

The results from this calculation are shown as the dashed line in panel c of Figure 6.22. The agreement between the calculated and experimentally determined values is remarkable during both discharge and charge. The calculation even shows that the amount of sodium removed from the pores during charge is less than the amount originally inserted. This may have resulted from diffusion limitations introduced by the high current used.

The same experiment was completed for lithium insertion into the glucose-derived carbon. The sample fits obtained along the voltage profile are shown in Figure 6.23. Again these results show a decrease in nanopore intensity along the low voltage plateau, although the intensity changes seen are much lower than for sodium insertion. The fit quality obtained although acceptable was not as good as for the sodium samples.

The same simple pore-filling model was used to predict the expected contrast changes for lithium insertion into this carbon. The only change required was to change the number of electrons per mole from 11 for sodium to 3 for lithium. Thus the electron density contrast changes and hence the intensity changes for a given amount of charge flow during discharge along the low voltage plateau is expected to be much lower. The fit parameters together with the model fit are shown in Figure 6.24. The poorer quality of the fits obtained is apparent from the GOF plot. Despite this fit limitation, it can be seen that the agreement between the calculated and experimental fit contrasts is good in terms of the magnitude of the change in contrast and the removal of lithium during charge. The experimental contrast decreases over a longer time scale than predicted during discharge – in addition to irreversible capacity losses resulting from surface reactions this may result from some of the experimental capacity during this low voltage plateau actually occurring as interlayer insertion – it is more difficult to separate the two

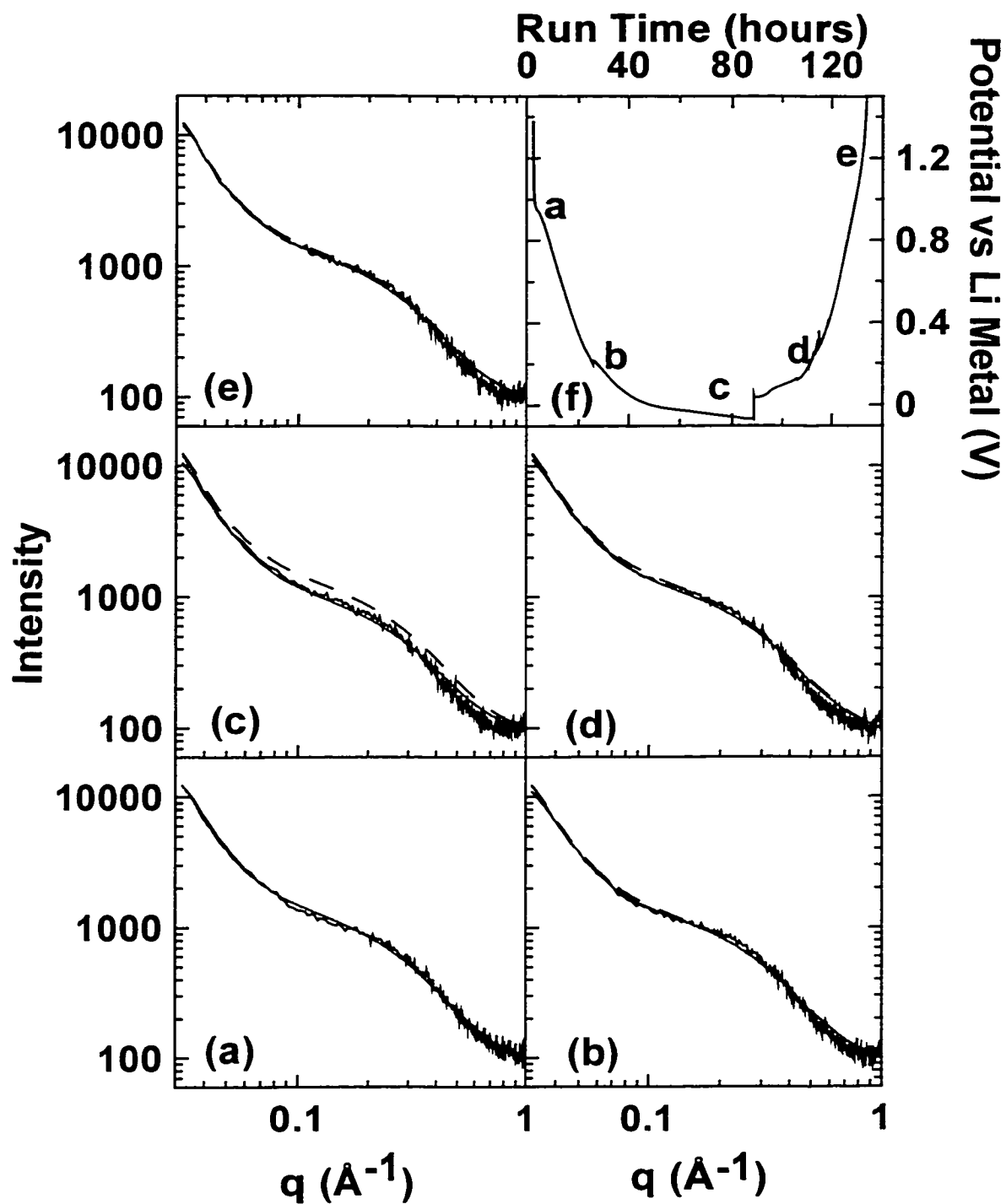


Figure 6.23: Sample SAXS scans for lithium insertion into glucose-derived hard carbon. The fit obtained for the first scan is included as a dashed line reference on subsequent scans. Each panel also includes the fit obtained.

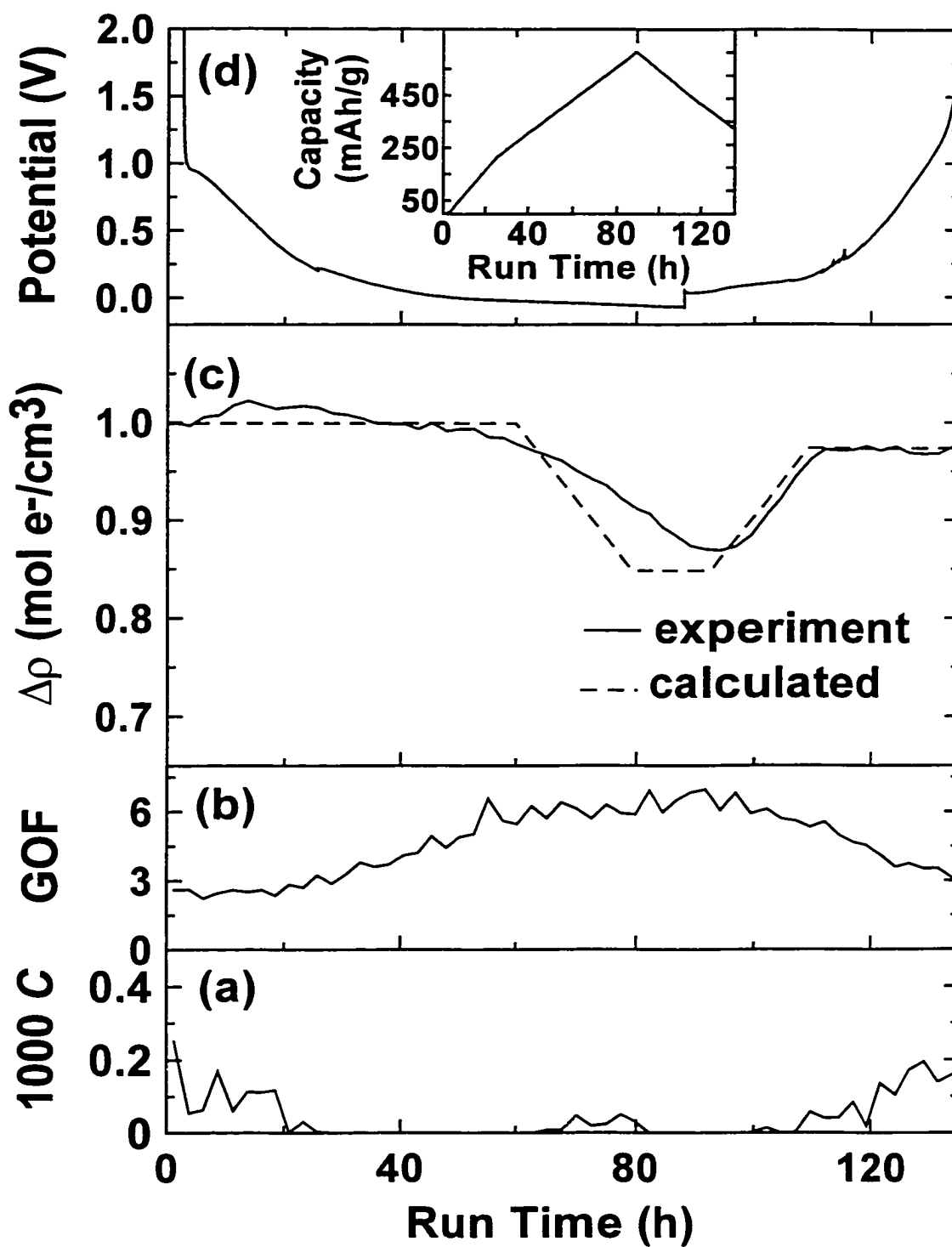


Figure 6.24: Fit parameters obtained for lithium insertion into hard carbon. The dashed line in (c) shows the electron density calculated from equation 6.1.

processes for the lithium cells than for the sodium cells around the transition region in the voltage profile. The better fit during charge may also result from the same situation - if the interlayer insertion process is kinetically controlled then lithium will insert slowly during discharge, overlapping with nanopore insertion along the low voltage plateau. The nanopore inserted lithium will then be removed first during charge, giving better agreement with the calculated value. Such behaviour would be enhanced in a cell operated at a relatively high current in order to complete the experiment in a reasonable period of time. Although it would have been interesting to study sodium insertion into the 1700°C glucose carbon, because of its low capacity along the sloping voltage region, the high temperature samples were prepared as the thesis was being written and hence there was not enough time.

## **Chapter 7**

### **High Temperature Studies**

So far in this thesis, results have been presented for tests completed at room temperature. In order to show that the results obtained are valid for carbons held at high temperatures in an operating aluminium reduction cell, a sodium vapour test, designed to expose carbon samples to sodium vapour at elevated temperature, was developed. The sodium loaded carbons produced from this test could then be analysed by x-ray scattering.

Before describing the test used, it is worth discussing how sodium performance in an aluminium reduction cell is quantified by the industry. There are three standard test methods used: sodium expansion, sodium penetration and sodium vapour testing.

#### **7.1 Sodium Expansion Testing**

The sodium expansion test is an industry standardised test used to compare the extent of expansion of different cathode carbons in a simulated reduction cell environment. A schematic diagram of the test is shown in Figure 7.1a. For this test, the sample is immersed to a set depth in the bath solution and has a set of rods for measuring changes in the length of the immersed sample depth. This can then give a direct measure of the expansion caused by sodium uptake. For carbons operated at constant current, sodium expansion increases rapidly during the initial passage of current flow then the rate of expansion decreases until what appears to be a limiting value is reached [15]. This is

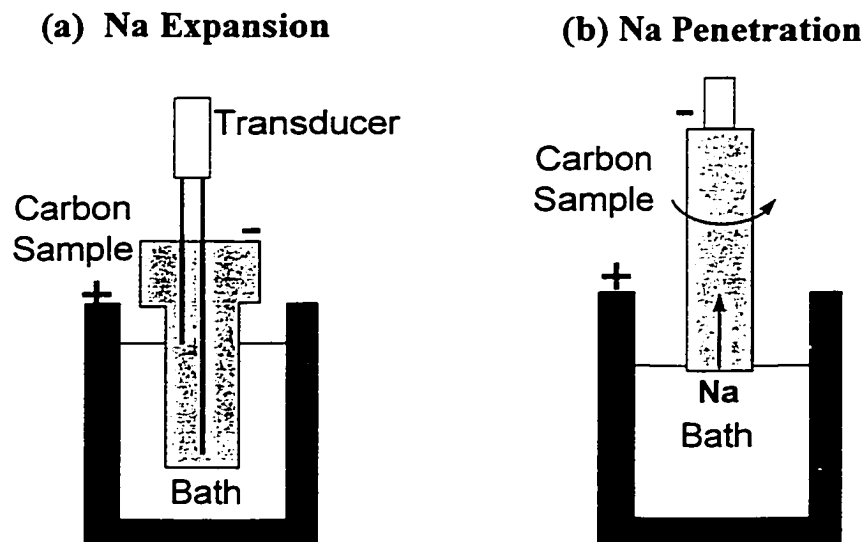


Figure 7.1: Schematic diagrams of sodium (a) expansion and (b) penetration tests.

generally attributed to saturation of the carbon with sodium, however, depending on the test set-up, it can also be caused by depletion of sodium from the bath. The maximum linear expansion measured by this technique for most commercial cathode materials is less than 2% of the initial length. This may appear to be a small number, however cathode carbons are classified as brittle materials and hence will suffer brittle failure with only small length changes.

Table 7.1 presents approximate ranges for sodium expansion of different grades of cathode carbon [87].

Table 7.1: Sodium Expansion Values for Commercial Cathode Carbons

Carbon Type	Approximate Heat Treatment Temperature	Sodium Expansion $\Delta L/L$ (%)
Anthracite aggregate with coal tar pitch binder	1200°C	0.6 – 1.5 %
Semi-Graphitic - graphitic aggregate with coal tar pitch binder	1200°C	0.3 – 0.5 %
Graphitized – semi-graphitic blocks pyrolysed to higher temperatures	> 2700°C	0.05 – 0.15 %

These three different cathode carbon classes show one clear trend - as the cathode carbon becomes more graphitic in nature, the amount of sodium expansion decreases. This is consistent with the reduction in room temperature electrochemical sodium capacity seen for soft carbons as the heat treatment temperature increases.

## **7.2 Sodium Penetration Test**

This test, shown schematically in Figure 7.1b, can be run in the same equipment used for the sodium expansion test. In this case however, the sample is only immersed to a very small depth into the bath. When current is applied, sodium migrates up through the cathode carbon. After testing, the sample is removed, sectioned and analysed chemically, primarily to determine sodium content as a function of position. This test is used to study the rate of sodium penetration into the carbon (by comparing the sodium depth profiles for samples immersed for different periods of time) and the amount of sodium that the carbon can accommodate.

## **7.3 Sodium Vapour Testing**

Interpreting the results from the sodium expansion and penetration tests to extract sodium insertion mechanisms is difficult, primarily because of “contamination” from other bath species. For example, bath material can migrate through the macroporosity increasing local sodium concentrations. In order to overcome this limitation, sodium vapour testing can be used. The traditional test involves placing a sample of carbon in a crucible or retort together with sodium metal in a furnace. The furnace is then heated up to generate sodium vapour. This vapour penetrates the carbon matrix, and in extreme cases can cause the carbons to shatter. This test normally uses large amounts of material. An alternative sodium vapour test was developed for this thesis that could be used to assess sodium performance of small quantities of carbon.



### 7.3.1 Experimental

For this test, ~ 0.5 g of carbon powder was loaded into a thin walled stainless steel tube welded closed at one end. Sodium metal was then added and the tube was welded shut. This sample tube preparation was all carried out in an argon-filled glovebox. Several sample tubes were prepared for each carbon with different quantities of sodium in each tube. The tubes were then placed in a Lindberg tube furnace and heated at  $1^{\circ}\text{C min}^{-1}$  to  $890^{\circ}\text{C}$  under flowing argon to prevent rusting. The furnace was held at  $890^{\circ}\text{C}$  for 1 hour and then switched off. The tubes were weighed before and after heating to check for any leaks. After cooling, the tubes were taken into a helium-filled glovebox and opened. Samples from each tube were loaded into air sensitive sample holders for measurement of WAXS patterns.

### 7.3.2 Interactions of Sodium Vapour with Soft Carbon

Figure 7.2 shows the WAXS patterns obtained for a sample of pitch derived carbon heat treated to  $1000^{\circ}\text{C}$  after exposure to sodium at high temperature. The potential vs capacity curve for an electrochemical sodium cell made with this carbon is also shown. The approximate equivalent locations of each vapour sample (assuming all the sodium present in the tube enters the carbon) are indicated on the upper panel. Similar behaviour to that seen in the *in situ* WAXS study (Figure 6.2) was also seen for the vapour sample – the intensity dropped with increasing sodium content and the 002 peak shifted to lower angles. This implies that sodium vapour inserts between the layers (reducing the scattered intensity through destructive interference) and forces the layers apart, presumably generating the bulk expansion seen in tests such as the sodium expansion test. These data also show the development of intensity around  $30^{\circ}$ , possibly attributable to adsorption of sodium onto the external surfaces of the graphene domains and to the creation of small sodium clusters through uneven layer expansion. The sample with high sodium loading (Figure 7.2d) exhibits a narrower 002 peak than the other samples, implying that there was less strain in this sample. In Chapter 6 (Figure 6.11) it

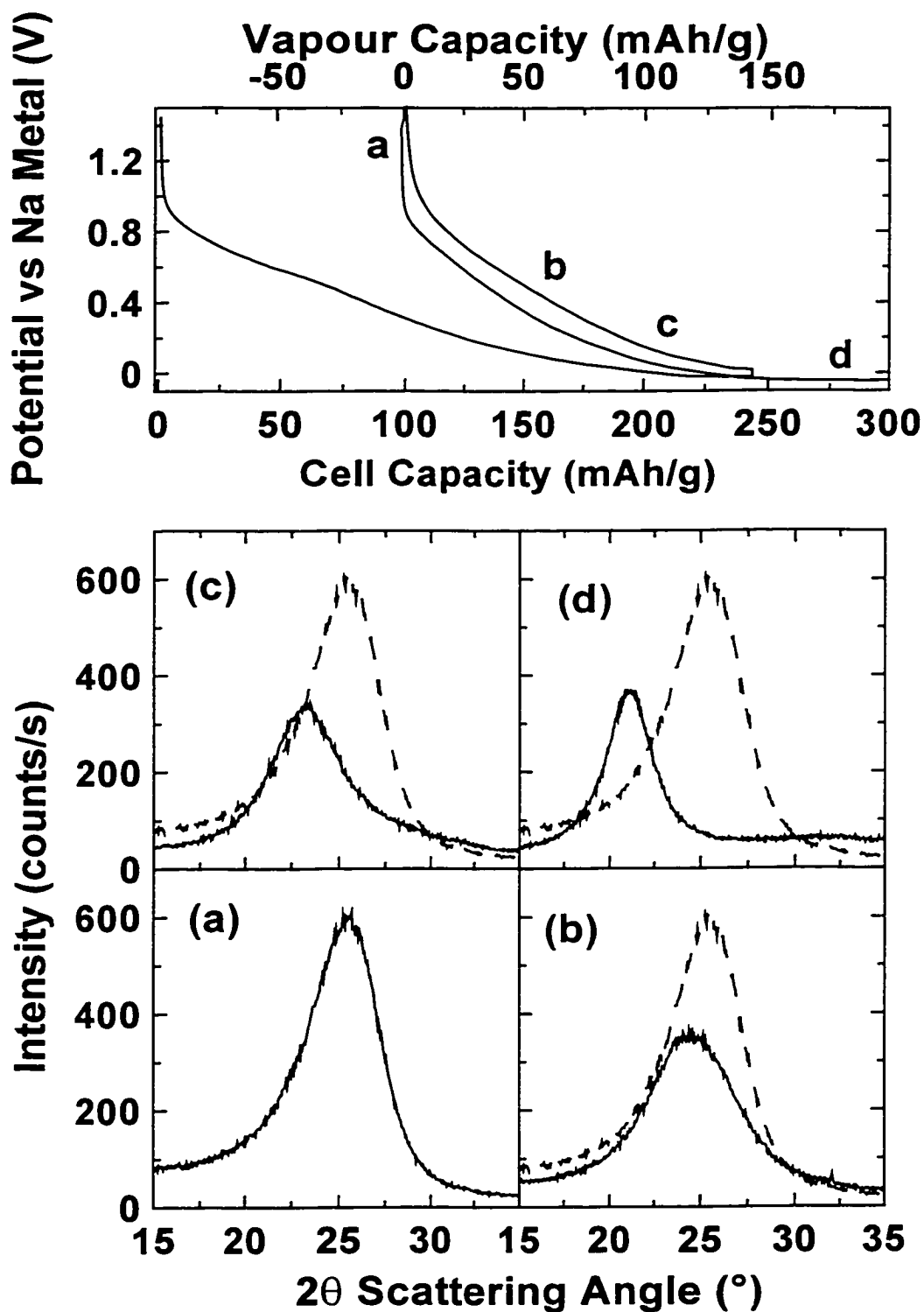


*Figure 7.2: Pitch carbon samples exposed to sodium vapour at 890°C. The equivalent capacity in a room temperature electrochemical cell for each scan is shown in the upper panel. The scan for the unexposed carbon itself is included as the dashed line on all subsequent panels.*

was proposed that uneven expansion of the graphene layers and the formation of small sodium clusters may have generated the high strain seen for the sodium filled carbons. The increased sodium content of sample d in Figure 7.2 may actually help to even out the expansion, effectively reducing the strain.

### 7.3.3 Interactions of Sodium Vapour with Hard Carbon

Figure 7.3 presents the WAXS scans for glucose derived carbon heat treated to 1100°C after exposure to different amounts of sodium vapour. The scan measured on the unexposed carbon is included for reference on each subsequent scan. The top panel presents the electrochemical sodium data obtained for this material at room temperature. The approximate capacity of each vapour sample was determined by the mass ratio of sodium and carbon in the vapour tube. As for the soft carbon sample, similar trends to those seen for the *in situ* room-temperature electrochemical tests (Figure 6.2) were also seen for the vapour-exposed samples. The intensity drops as the sodium content increases, implying sodium insertion between graphene layers. Also a broad hump, possibly corresponding to insertion of sodium into nanopores, appears around 32° scattering angle. This intensity seems to develop along the low voltage plateau for this material, consistent with the proposed pore filling mechanism.

These results show that the interlayer insertion mechanism identified from room temperature electrochemical studies also occur for sodium insertion at high temperature. They also suggest that nanopore insertion may also be occurring at high temperatures, consistent with the mechanism identified for insertion along the low voltage plateau in the hard carbon.

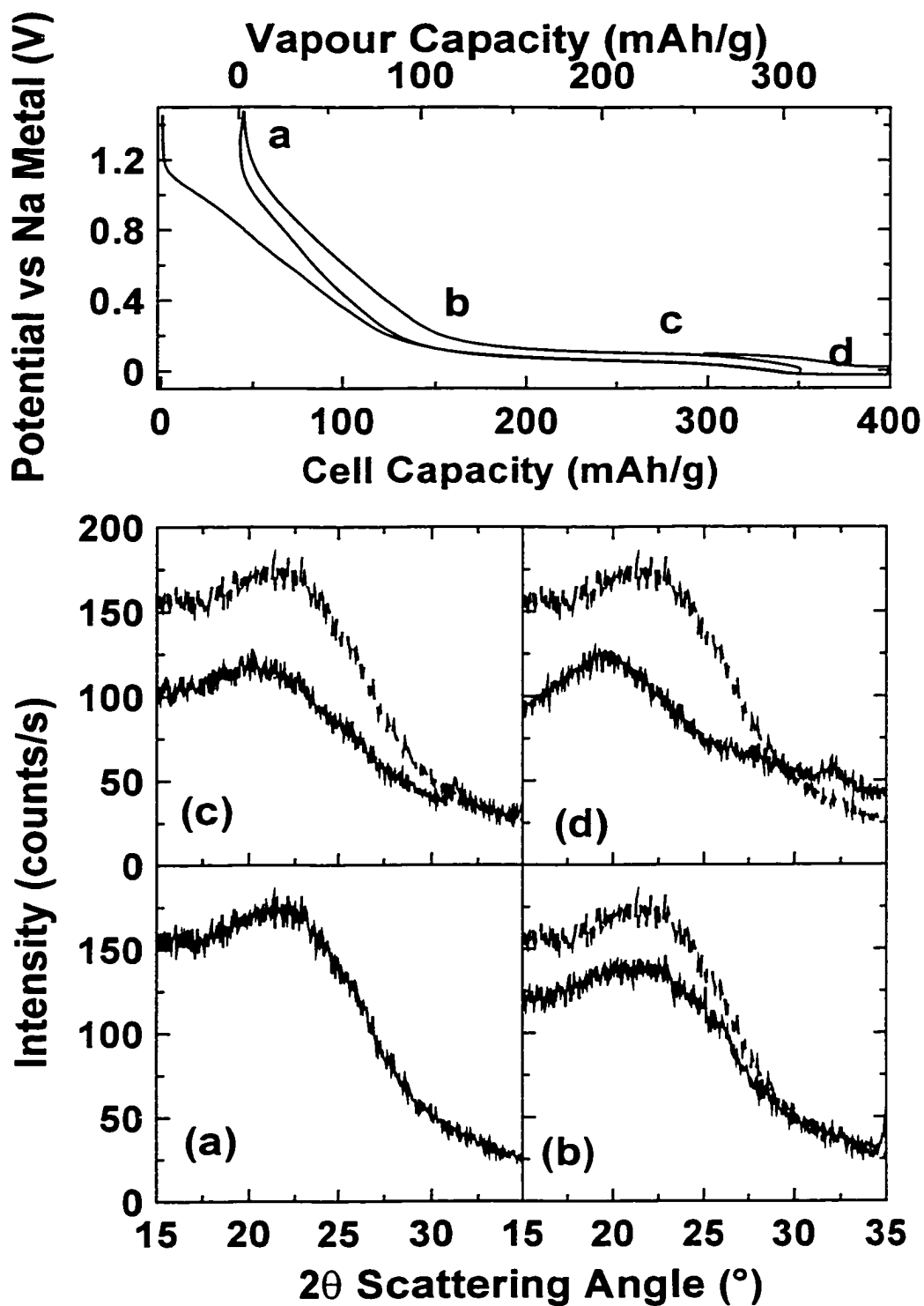


Figure 7.3: Glucose carbon samples exposed to sodium vapour at 890°C. The equivalent capacity in a room temperature electrochemical cell for each scan is shown in the upper panel. The scan for the unexposed carbon itself is included as the dashed line on all subsequent panels.

## Chapter 8

### Conclusions

When this project was started, the primary techniques used to assess sodium insertion in carbon materials were high temperature tests such as the sodium expansion and sodium penetration tests designed to understand the physical process of cathode carbon expansion in aluminium reduction cells. Lithium insertion into carbon materials was studied using room temperature electrochemical techniques, designed to understand the mechanism for lithium insertion in order to develop anode materials for rechargeable lithium-ion batteries with high lithium capacities. Literature studies showed that a few researchers were starting to apply room temperature electrochemical methods to studies of sodium insertion into cathode carbons, although the results obtained were of limited use.

This thesis has shown that a combination of room temperature electrochemical studies and high temperature vapour studies can bridge the gap between these different research fields. From this work the mechanisms for sodium insertion into carbons prepared from different precursors and heat treated to different temperatures have been identified, whilst the high temperature studies have shown that the mechanisms in operation at room temperature also occur at much higher temperatures. It has been shown that there are three predominant mechanisms that can occur.

Previous research [78] showed that lithium interacts with hydrogen terminated aromatic carbon centres, forcing the carbons to rehybridise in low temperature carbons containing significant quantities of residual hydrogen. The results from this thesis suggest that, although some sodium capacity in low temperature carbons can be attributed

to a similar mechanism, this process is much more important for lithium insertion than for sodium insertion. This implies that the interaction between sodium and the hydrogen-terminated carbons is much weaker than the interaction between lithium and the hydrogen terminated carbons. For lithium insertion, this process was proposed based on the extent and magnitude of the hysteresis seen in the room temperature electrochemical profiles together with the strong correlation between residual hydrogen content and lithium capacity. The work presented in this thesis has shown that sodium produces similar effects – hysteresis in the voltage profile that decreases as the hydrogen content decreases. The magnitude of the hysteresis was much lower for sodium than for lithium, suggesting a lower activation barrier and hence, most likely, less rehybridisation of the carbon centres. A combination of electrochemical measurements and *in situ* wide-angle x-ray scattering studies was used to demonstrate that sodium/lithium insert between parallel or approximately parallel carbon layers at a range of potentials. This interlayer insertion forces the layers apart in the soft carbons. In the hard carbons, it appears that the increased disorder and reduced layer stacking means that the extent of matrix expansion is quite low. As the carbon heat treatment temperature increases, the capacity from this mechanism decreases, particularly for soft carbons. This was attributed to the gradual alignment of layers with increasing temperature and the pinning of these layers by interlayer crosslinks. As the materials become highly graphitized, the lithium inserts between layers forming a series of staged intercalation compounds. This occurs because the interlayer pinning is relieved at high temperatures, creating a structure with carbon layers free to slide relative to each other in order to create the necessary space for the lithium atoms. This behaviour was not seen for sodium insertion, consistent with modeling work [81] that suggested that the attractive forces between intercalated sodium atoms and the carbon layers was weak.

In hard carbon materials, in addition to the interlayer insertion, a significant quantity of both sodium and lithium could be accommodated in nanopores, producing low voltage plateaus. This was clearly demonstrated with *in situ* small-angle scattering studies of operating electrochemical cells. Although these nanopores close off to gas molecules such as N<sub>2</sub> with increasing heat treatment temperature, they still remain accessible to sodium and, until high temperatures are used, to lithium.

One of the dangers of relying only on room temperature electrochemical studies was that the proposed mechanism might not be valid for the same carbons when placed in a high temperature environment. The x-ray scattering measurements of carbons exposed to sodium vapour showed that the same behaviour was in fact observed at high temperatures. Thus it is believed that the results presented in this thesis can be used semi-quantitatively to explain sodium uptake in cathode carbons in operating aluminium reduction cells.

One obvious question still remains – how is sodium uptake linked to sodium expansion? This has not been answered here directly. Indirectly, the *in situ* WAXS results suggest that certainly for the soft carbons, sodium insertion forces the graphene layers apart. With increasing heat treatment temperature, the amount of sodium that can be inserted through this mechanism decreases, correlating well with the decrease in sodium expansion for carbons heat treated to higher temperatures. The hard carbons show only minimal changes in sodium insertion with increasing temperature and therefore it is reasonable to assume that the expansion characteristics of these materials will not change dramatically with increased heat treatment temperature.

Based on the work presented here, the following general advice can be provided: if the absolute magnitude of sodium expansion is critical, then soft carbons heat treated to high temperatures provide the best solution. If prevention of mechanical failure is more important then both the expansion characteristics and the mechanical properties of the carbon need to be considered. Thus, hard carbons (that may also have other operational benefits) may be suitable as cathode carbon materials, provided the expansion does not exceed the mechanical capabilities of the carbon.

# **Appendix A**

## **Repeatability**

This thesis was written to show how carbon structural and electrochemical properties varied with carbon type and heat treatment temperature, with the assumption that the measurements made were reliable. In order to support this assumption, this appendix therefore briefly presents data for measurements performed on samples prepared in the same way but at different times to provide an indication of the expected level of sample to sample variability. Overall, the repeatability of the techniques is good, although there are small differences between samples that can only partly be attributed to random noise. Despite these minor variations, the magnitude of the changes observed between different materials is much larger than the within-sample variability, giving confidence in the conclusions drawn from the data. The repeatability of the individual measurements also show that the carbon samples can be prepared with the same structure each time, and thus indirectly, the results presented in this appendix show that the heat-treatment process used was also reliable. The repeat measurements quoted in this chapter were made on two samples heat treated on different days.

### **A1. Gas Adsorption**

Figure A1 shows repeat gas adsorption measurements for low and high porosity carbons. It can be seen that the technique is quite reliable, particularly for differentiating between nanoporous and non-porous carbons, which was the primary reason for completing gas adsorption measurements.



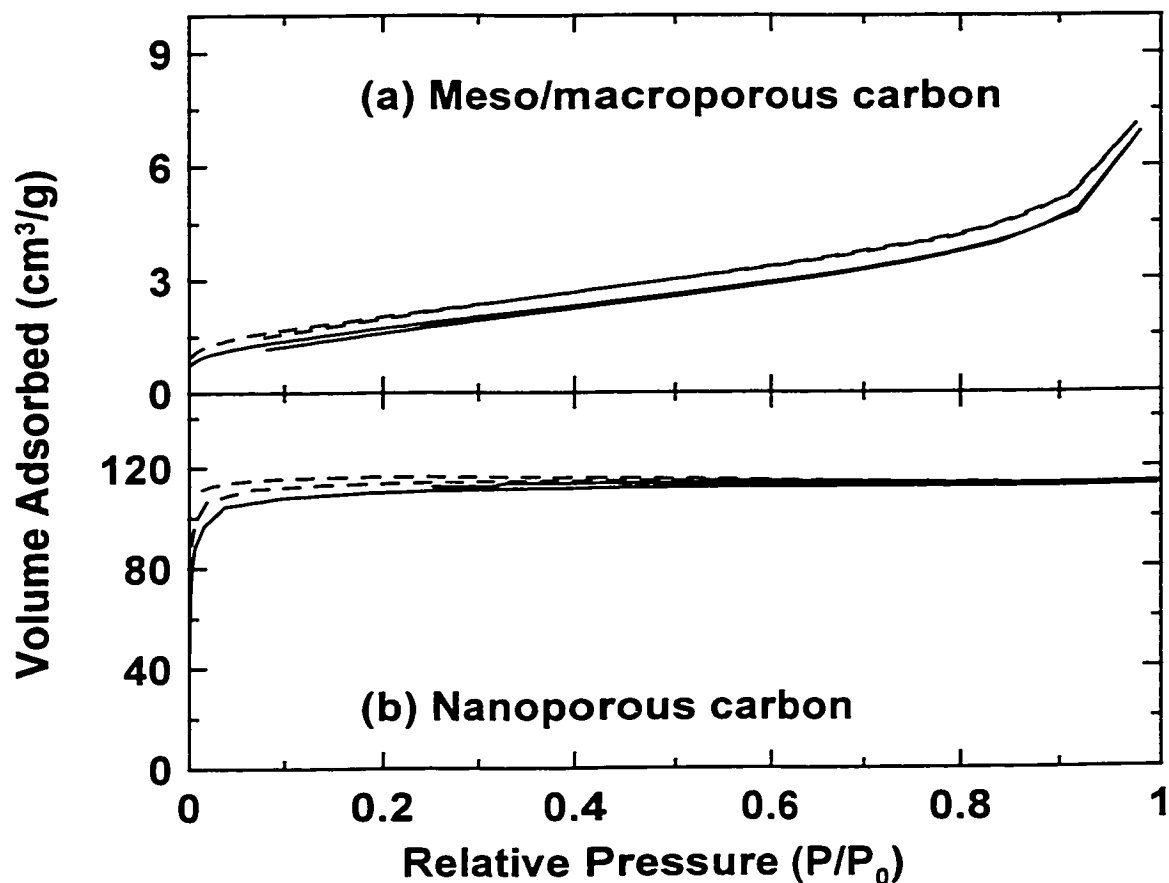


Figure A1: Repeat  $N_2$  gas adsorption measurements for (a) mesoporous carbon and (b) nanoporous carbon.

## A2. WAXS Measurements

Figure A2 shows repeat WAXS measurements on typical soft and hard carbons. It can be seen that this technique is highly reproducible making it difficult to separate the two scans. This technique is expected to be reproducible, primarily because it is sensitive to changes in atomic arrangements, which should be essentially the same in samples prepared by heat treatment from the same precursor. Any differences between repeat samples can be primarily attributed to random noise.

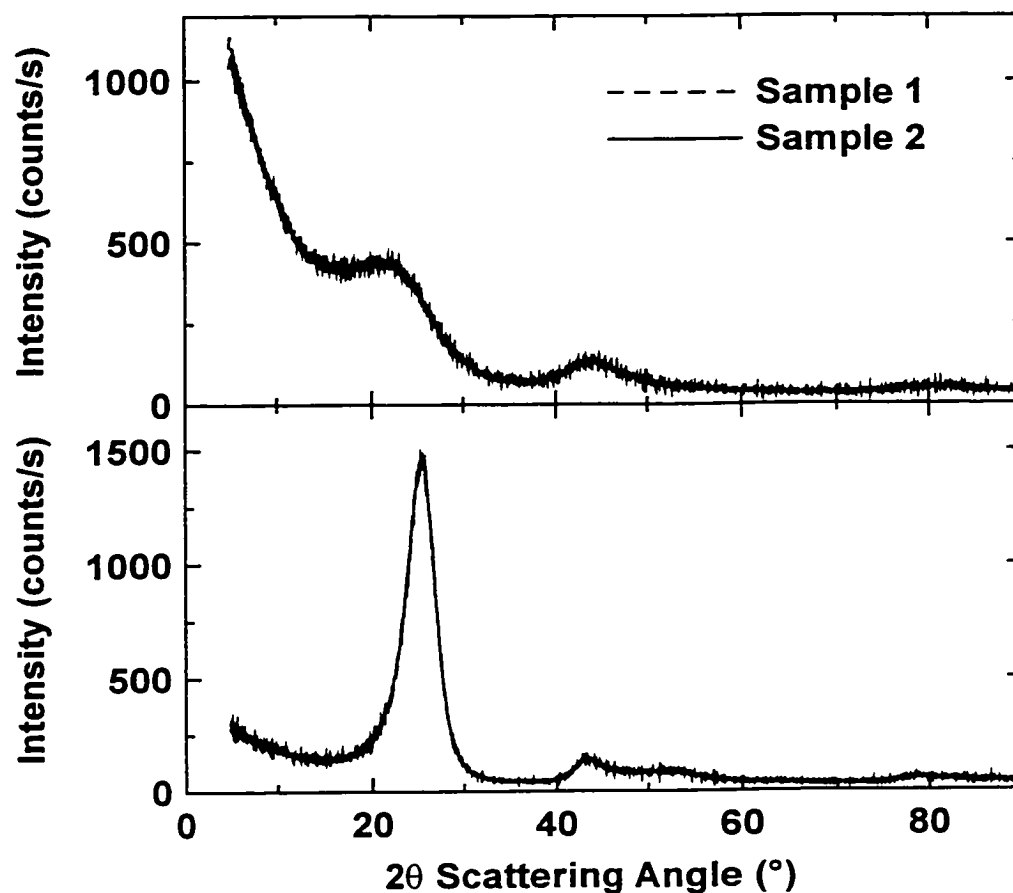


Figure A2: Repeat WAXS measurements completed on a typical hard carbon (upper panel) and a typical soft carbon (lower panel)

### A3. SAXS Measurements

Repeat SAXS measurements were completed on both a nano-porous carbon and a meso/macro-porous soft carbon are presented in Figure A3. Again the technique is highly reproducible.

### A4. Electrochemical cell performance

The cell construction and operating procedure was able to produce the same results for samples heat-treated on different days and cells made on different days for

both sodium and lithium insertion as shown in Figure A4, although there are some subtle differences in irreversible capacity.

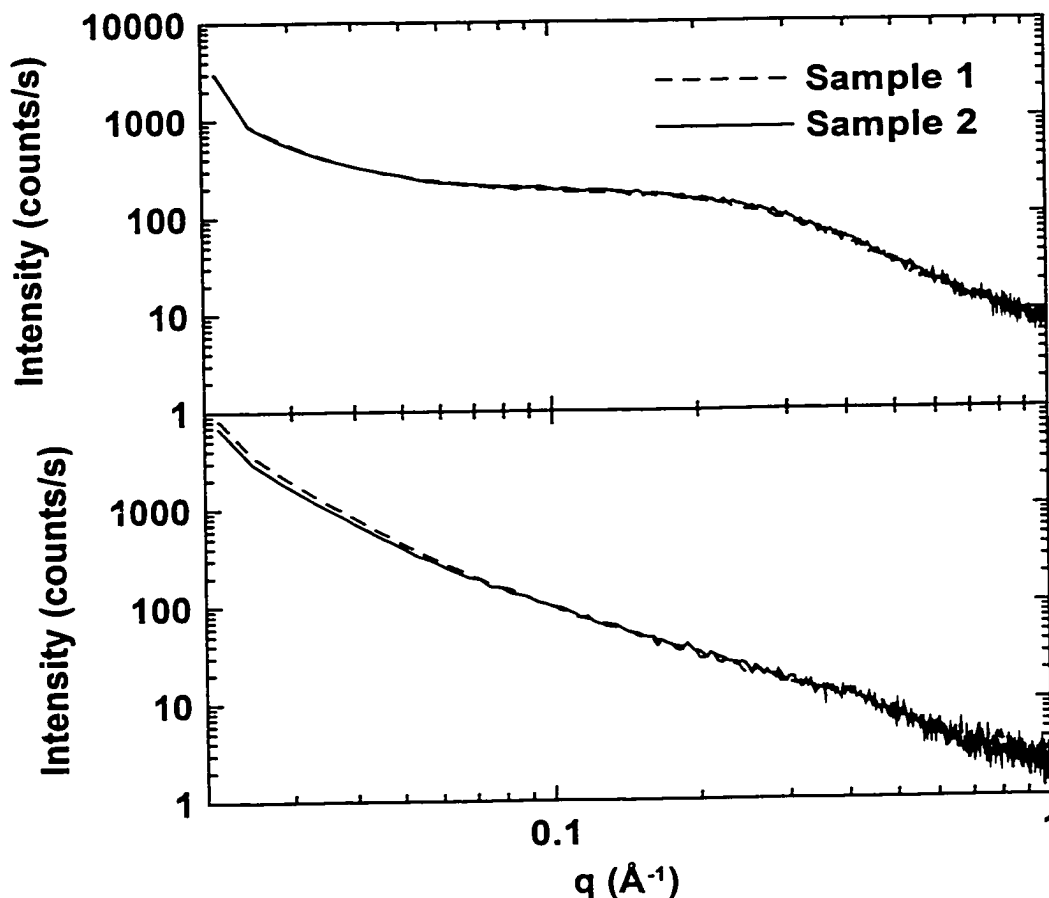


Figure A3: Repeat SAXS measurements completed on a typical nano-porous hard carbon (upper panel) and a typical meso/macro-porous soft carbon (lower panel).

The irreversible capacity is at least partly controlled by the amount and type of species adsorbed by the carbon of interest from the air prior to installation into the cell [88]. Although the time the carbon and electrodes are exposed to air is minimised, the irreversible capacity is expected to show some day to day variation. However it can be seen that the amount of variation is reasonably low. Some of the irreversible capacity, particularly for the sodium samples is also partly due to incomplete stripping of metal from the electrode surface during charge. The amount of plated metal varies as sometimes the plating trip point occurred outside of normal working hours. Incomplete stripping does not interfere significantly with cell performance but will contribute excess irreversible capacity.

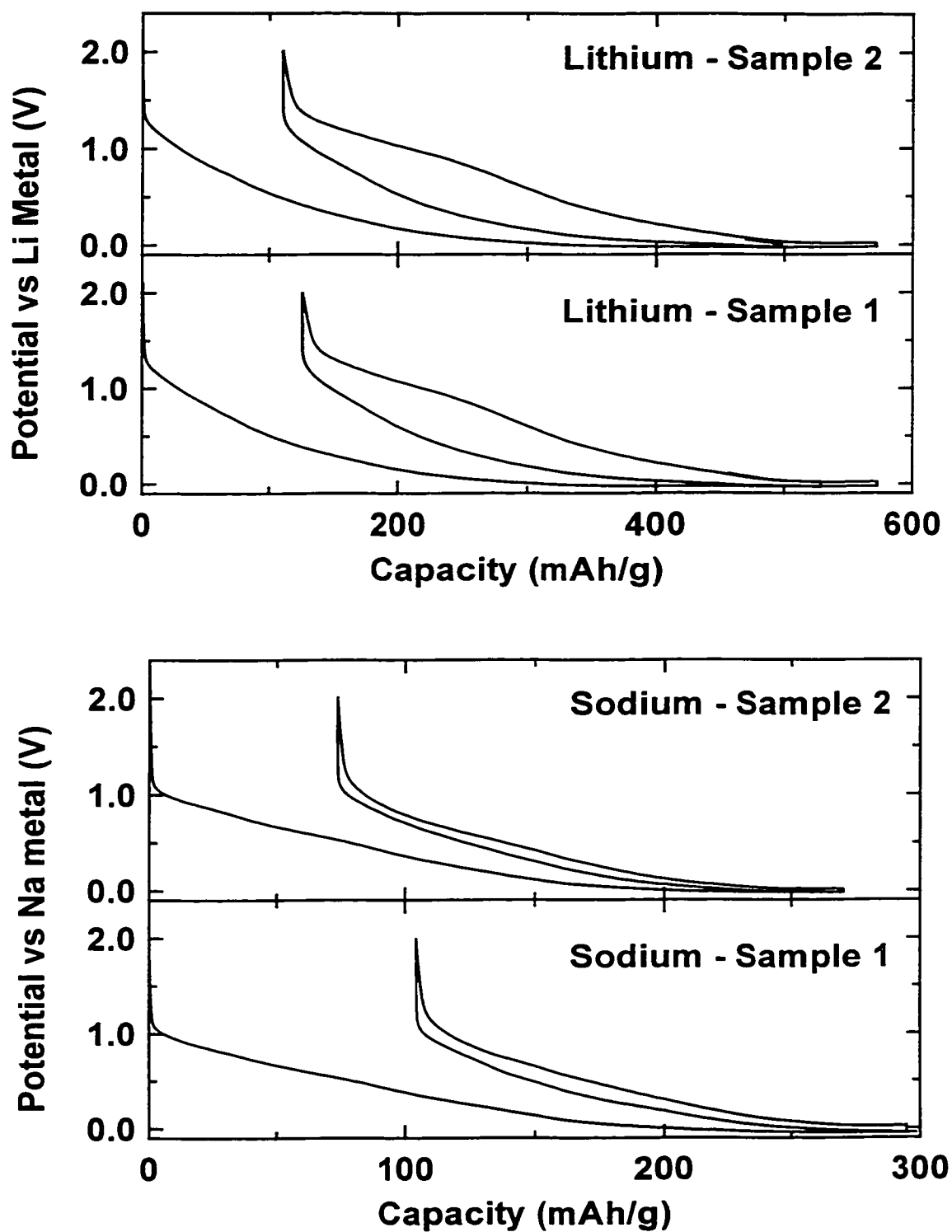


Figure A4: Repeat sodium and lithium cells for carbon electrodes prepared from samples heat-treated on different days.

Overall the variation in irreversible capacity is acceptable, especially as this property is not of great significance for the work presented in this thesis. The more important point is that the shape and capacity of the reversible portion of the potential profile is consistent between samples for both sodium and lithium. A similar level of repeatability has been seen for other samples, allowing the error in reversible capacity to be estimated at  $\pm 10$  mAh/g for both sodium and lithium insertion.

#### **A5. *In situ* cell data**

A number of repeat in-situ SAXS and WAXS cells were constructed and operated. The trends presented in Chapter 6 for a given material were also seen in the repeat measurements. As with the other measurements therefore, the in-situ results are considered to be reliable.

# Appendix B

## Mathematical Derivations

### B1. Derivation of the Langmuir model

It was shown that, under the Langmuir model assumptions, that:

$$\theta_1 = K_1 P \theta_0, \text{ where:} \tag{B1.1}$$

- $\theta_1$  represents the fraction of occupied sites and  $\theta_0$  represents the fraction of unoccupied sites.
- $P$  is the equilibrium gas pressure
- $P_0$  is the saturation pressure of the gas.
- $K_1$  is the ratio of the two rate constants:  $K_1 = k_{\text{ads}(1)} / k_{\text{des}(1)}$
- $V_M$  is the gas volume required to form a mono-layer of gas molecules on the surface.
- $V_P$  is the volume of gas adsorbed at equilibrium pressure  $P$ .

From these definitions, we have:

$$\theta_0 = 1 - \theta_1 \text{ and,} \tag{B1.2}$$

$$\theta_1 = V_P / V_M . \tag{B1.3}$$

Substituting these back into equation B1.1 gives:

$$\frac{V_P}{V_M} = K_1 P \left( 1 - \frac{V_P}{V_M} \right), \quad (\text{B1.4})$$

$$V_P = K_1 P (V_M - V_P), \quad (\text{B1.5})$$

$$V_P = \frac{V_M K_1 P}{(1 + K_1 P)}, \quad (\text{B1.6})$$

$$\frac{1}{V_P} = \frac{(1 + K_1 P)}{V_M K_1 P}, \quad (\text{B1.7})$$

$$\frac{P}{V_P} = \frac{1}{K_1 V_M} + \frac{P}{V_M}. \quad (\text{B1.8})$$

Dividing through by the saturation pressure and letting  $c = K_1 P_0$  gives the Langmuir equation:

$$\boxed{\frac{P}{P_0 V_P} = \frac{1}{c V_M} + \frac{1}{V_M} \left( \frac{P}{P_0} \right)} \quad (\text{B1.9})$$

## B2. Derivation of the BET equation.

For the BET equation, the set of equations to describe each  $\theta_n$  term, where  $\theta_n$  is the fraction of sites covered with a stack of  $n$  molecules, are:

$$\begin{aligned}
 \theta_1 &= K_1 P \theta_0, \\
 \theta_2 &= K P \theta_1, \\
 \theta_3 &= K P \theta_2, \\
 \theta_4 &= K P \theta_3, \\
 \theta_n &= K P \theta_{n-1}.
 \end{aligned}
 \tag{B2.1}$$

This is a set of recursive equations that can be rewritten as:

$$\begin{aligned}
 \theta_2 &= K P \theta_1, \\
 \theta_3 &= (K P)^2 \theta_1, \\
 \theta_4 &= (K P)^3 \theta_1, \\
 \theta_n &= (K P)^{n-1} \theta_1.
 \end{aligned}
 \tag{B2.2}$$

It was also shown that:

$$\frac{V_p}{V_m} = \frac{\sum_{n=0}^{n=L} n \theta_n}{\sum_{n=0}^{n=L} \theta_n}.
 \tag{B2.3}$$

Substituting each of the modified expressions for  $\theta_n$  into the numerator gives:



$$\sum_{n=0}^{n=L} n \theta_n = \theta_1 + 2(KP)\theta_1 + 3(KP)^2 \theta_1 + \dots + L(KP)^{L-1} \theta_1, \quad (\text{B2.4})$$

which can be rearranged to give:

$$\sum_{n=0}^{n=L} n \theta_n = \theta_1 (1 + 2(KP) + 3(KP)^2 + \dots + L(KP)^{L-1}). \quad (\text{B2.5})$$

As the fraction of sites filled with  $n$  layers decreases as  $n$  increases,  $KP < 1$  and, as  $L$  is large (i.e. multi-layer adsorption extends for many layers), the series converges to:

$$\sum_{n=0}^{n=L} n \theta_n = \frac{\theta_1}{(1-KP)^2}. \quad (\text{B2.6})$$

Similarly, the denominator in equation B2.3 becomes:

$$\sum_{n=0}^{n=L} \theta_n = \theta_0 + \theta_1 (1 + KP + (KP)^2 + \dots + (KP)^{L-1}), \text{ which converges to:} \quad (\text{B2.7})$$

$$\sum_{n=0}^{n=L} \theta_n = \theta_0 + \frac{\theta_1}{(1-KP)} \quad (\text{B2.8})$$

Substituting for  $\theta_0$  gives:

$$\sum_{n=0}^{n=L} \theta_n = \frac{\theta_1}{K_1 P} + \frac{\theta_1}{(1-KP)}. \quad (\text{B2.9})$$

Equations B2.6 and B2.9 can be substituted into equation B2.3 to give:

$$\frac{V_p}{V_m} = \frac{\frac{\theta_1}{(1-KP)^2}}{\frac{\theta_1}{K_1P} + \frac{\theta_1}{(1-KP)}} \quad (\text{B2.10})$$

After rearranging, this becomes:

$$\frac{V_p}{V_m} = \frac{K_1P}{(1-KP)(1-KP+K_1P)} \quad (\text{B2.11})$$

When the equilibrium pressure equals the saturation pressure,  $P_0$ , the gas condenses to a liquid and the volume adsorbed approaches infinity. For this to occur,  $(1-KP) \rightarrow 0$  and hence  $K=1/P_0$ . Also, letting  $c=K_1P_0$ , as for the Langmuir derivation, allows for equation B2.11 to be written as:

$$\frac{V_p}{V_m} = \frac{cP/P_0}{(1-P/P_0)(1-P/P_0+cP/P_0)}, \text{ which rearranges to:} \quad (\text{B2.12})$$

$$\frac{(1-P/P_0+cP/P_0)}{V_m c} = \frac{P/P_0}{(1-P/P_0)V_p} \quad (\text{B2.13})$$

This then gives the BET equation:

$$\boxed{\frac{1}{(P_0/P-1)V_p} = \frac{1}{V_m c} + \frac{(c-1)}{V_m c} \left( \frac{P}{P_0} \right)} \quad (\text{B2.14})$$

### B3. Evaluation of the Integral $\int_V e^{-i \mathbf{q} \cdot \mathbf{r}} dV$

$$\int_V e^{-i \mathbf{q} \cdot \mathbf{r}} dV = \int e^{-i |q| r \cos \phi} r^2 \sin \phi dr d\theta d\phi \quad (\text{B3.1})$$

$$= \int_{\theta=0}^{\theta=2\pi} d\theta \int_{\phi=0}^{\phi=\pi} r^2 dr \int_{r=0}^{r=R} e^{-iqr \cos \phi} \sin \phi d\phi \quad (\text{B3.2})$$

$$= 2\pi \int_{r=0}^{r=R} r^2 dr \left[ \frac{1}{iqr} e^{-iqr \cos \phi} \right]_{\phi=0}^{\phi=\pi} \quad (\text{B3.3})$$

$$= 2\pi \int_{r=0}^{r=R} r^2 dr \left[ \frac{e^{iqr} - e^{-iqr}}{iqr} \right] \quad (\text{B3.4})$$

$$= 2\pi \int_{r=0}^{r=R} r^2 \frac{2 \sin(qr)}{qr} dr \quad (\text{B3.5})$$

$$= \frac{4\pi}{q^2} \int_{r=0}^{r=R} q r \sin(qr) dr \quad (\text{B3.6})$$

Letting  $a = qr$  gives:  $da = q dr$ . This allows the above integral to be rewritten as:

$$= \frac{4\pi}{q^2} \int_{r=0}^{r=R} \frac{a}{q} \sin(a) da \quad (\text{B3.7})$$

$$= \frac{4\pi}{q^3} [\sin(a) - a \cos(a)]_{r=0}^{r=R} \quad (\text{B3.8})$$

$$= \frac{4\pi}{q^3} [\sin(qr) - qr \cos(qr)]_{r=0}^{r=R} \quad (\text{B3.9})$$

$$\int e^{-i \mathbf{q} \cdot \mathbf{r}} dV = \frac{4\pi [\sin(qR) - qR \cos(qR)]}{q^3}. \quad (\text{B3.10})$$

Using the volume of a sphere,  $V$ , this can be rewritten as:

$$\int e^{-i \mathbf{q} \cdot \mathbf{r}} dV = \frac{3V [\sin(qR) - qR \cos(qR)]}{(qR)^3}. \quad (\text{B3.11})$$

**B4. Average value of  $e^{i\mathbf{q}\cdot\mathbf{r}_{12}}$  for an isotropic distribution with fixed  $r_{12}$ .**

$$\overline{e^{i\mathbf{q}\cdot\mathbf{r}_{12}}} = \frac{\int_V e^{i\mathbf{q}\cdot\mathbf{r}_{12} \cos\phi} dV}{4\pi r_{12}^2}, \quad (\text{B4.1})$$

where  $\phi$  is the angle between  $\mathbf{q}$  and  $\mathbf{r}$ .

$$\overline{e^{i\mathbf{q}\cdot\mathbf{r}_{12}}} = \frac{\int_{\phi=0}^{\phi=\pi} \int_{\theta=0}^{\theta=2\pi} e^{i\mathbf{q}\cdot\mathbf{r}_{12} \cos\phi} r_{12}^2 \sin\phi d\phi d\theta}{4\pi r_{12}^2} \quad (\text{B4.2})$$

$$\overline{e^{i\mathbf{q}\cdot\mathbf{r}_{12}}} = \frac{1}{2} \int_{\phi=0}^{\phi=\pi} e^{i\mathbf{q}\cdot\mathbf{r}_{12} \cos\phi} \sin\phi d\phi. \quad (\text{B4.3})$$

letting  $u = \cos\phi$  gives:

$$\int_{\phi=0}^{\phi=\pi} e^{i\mathbf{q}\cdot\mathbf{r}_{12} \cos\phi} \sin\phi d\phi = \int_{u=1}^{u=-1} -e^{i\mathbf{q}\cdot\mathbf{r}_{12} u} du. \quad (\text{B4.4})$$

The solution to this integral is:

$$\int_{u=1}^{u=-1} -e^{i\mathbf{q}\cdot\mathbf{r}_{12} u} du = \left[ \frac{-e^{i\mathbf{q}\cdot\mathbf{r}_{12} u}}{i\mathbf{q}\cdot\mathbf{r}_{12}} \right]_{u=1}^{u=-1} = \frac{e^{i\mathbf{q}\cdot\mathbf{r}_{12}} - e^{-i\mathbf{q}\cdot\mathbf{r}_{12}}}{i\mathbf{q}\cdot\mathbf{r}_{12}} = \frac{2\sin(\mathbf{q}\cdot\mathbf{r}_{12})}{\mathbf{q}\cdot\mathbf{r}_{12}} \quad (\text{B4.5})$$

Thus the average value is:

$$\overline{e^{i\mathbf{q}\cdot\mathbf{r}_{12}}} = \frac{\sin(\mathbf{q}\cdot\mathbf{r}_{12})}{\mathbf{q}\cdot\mathbf{r}_{12}}. \quad (\text{B4.6})$$

## Bibliography

- 1 CRC Handbook of Chemistry and Physics, 76<sup>th</sup> edition; Lide, D. R., Ed; CRC Press: Boca Raton, 1995.
- 2 Greenwood, N. N.; Earnshaw, A. *Chemistry of the Elements*; Pergamon Press: Oxford, 1984, pp. 243-247.
- 3 Haupin, W. E. *Light Metals* **1995**, 195.
- 4 Nixon, J. C. *Bull. Proc. Australas. Inst. Min. Metall.* **1987**, 292, 85.
- 5 Bratland, D.; Grojtheim, K.; Krohn, C. *Light Metals* **1976**, 3.
- 6 Sorlie, M.; Oye, H. A. *Cathodes in Aluminium Electrolysis, 2<sup>nd</sup> edition*; Aluminium Verlag: Dusseldorf, 1994.
- 7 Naas T.; Oye, H. A. *Light Metals* **1999**, 193.
- 8 *Aluminium Electrolysis, 2<sup>nd</sup> edition*; Grojtheim, K.; Kvande, H., Eds.; Aluminium Verlag: Dusseldorf, 1982.
- 9 Brilloit, P.; Lossius, L. P.; Oye, H. A. *Metall. Trans. B* **1993**, 24B, 75.
- 10 Sorlie, M.; Oye, H. A. *Light Metals* **1989**, 625.
- 11 Asher, R. C. *J. Inorg. Nucl. Chem.* **1959**, 10, 238.
- 12 Berger, D.; Carton, B.; Metrot, A.; Herold, A. In *Chemistry of Physics and Carbon*; Walker Jr., P. L.; Thrower, P. A., Eds.; Marcel Dekker: New York, 1975; Vol. 12, pp 1-36.
- 13 Wilkening, S.; Busse, G. *Light Metals* **1981**, 653.
- 14 Sorlie, M.; Oye, H. A. *J. App. Electrochem.* **1989**, 19, 580.
- 15 Schreiner, H.; Oye, H. A. *Light Metals* **1995**, 463.
- 16 Mikhalev, Y.; Oye, H. A. *Carbon* **1996**, 34, 37.

- 17 Sechet, C.; Sarneo, D.; Mermoux, M.; Touzain, Ph.; Bonnetain, L.; Dumas, D.; Allard, B.; Paulus, R. *Mol. Cryst. Liq. Cryst.* **1994**, *245*, 153.
- 18 Flandrois, S.; Simon, B. *Carbon* **2000**, *37*, 165.
- 19 Dahn, J. R.; Tao Zheng; Yinghu Liu; Xue, J. S. *Science* **1995**, *270*, 590.
- 20 Billaud, D.; Lemont, S.; Yazami, R. *Electrochimica. Acta.* **1992**, *37*, 1675.
- 21 Doeff, M. M.; Ma, Y.; Visco, S. J.; De Jonghe, L. C. *J. Electrochem. Soc.* **1993**, *140*, L169.
- 22 Vondrak, J. *Collect. Czech. Chem. Commun.* **1995**, *60*, 1158.
- 23 Joncourt, L.; Mermoux, M.; Touzain, Ph.; Bonnetain, L.; Dumas, D.; Allard, B. *J. Phys. Chem. Solids* **1996**, *57*, 877.
- 24 Alcantara, R.; Fernandez Madrigal, F. J.; Lavela, P.; Tirado, J. L.; Jimenez Mateos, J. M.; Gomez de Salazar, C.; Stoyanova, R.; Zhecheva, E. *Carbon* **2000**, *38*, 1031.
- 25 German, R. M. *Metall. Trans. A* **1992**, *23A*, 1455.
- 26 Presz, A.; Skibska, M.; Pilecki, M. *Powder Handling & Processing* **1995**, *7*, 321.
- 27 Byrne, J. F.; Marsh, H. In *Porosity in Carbons*; Patrick, J. W., Ed.; Edward Arnold: London, 1995; pp 1-48.
- 28 Fritz Stoeckli, H. *Carbon* **1990**, *28*, 1.
- 29 Kobayashi, M.; Ishikawa, E.; Toda, Y. *Carbon* **1993**, *31*, 990.
- 30 Ismail, I. M. K. *Carbon*, **1990**, *28*, 423.
- 31 Mitropoulos, A. Ch.; Haynes, J. M.; Richardson, R. M.; Steriotis, T. A.; Stubos, A. K.; Kanellopoulos, N. K. *Carbon* **1996**, *34*, 775.
- 32 Adamson, A. W. *Physical Chemistry of Surfaces*, 5<sup>th</sup> edition, John Wiley & Sons, Inc.: New York, 1990.
- 33 Langmuir, I. *J. Am. Chem. Soc.* **1916**, *38*, 2221.
- 34 Brunauer, S.; Emmett, P. H.; Teller, E. *J. Am. Chem. Soc.* **1938**, *Feb.*, 309.
- 35 McClellan, A. L.; Harnsberger, H. F. *J. Coll. Int. Sci.* **1967**, *23*, 577.

- 36 Brunauer, S.; Copeland, L. E.; Kantro, D. L. In *The Solid-Gas Interface, Volume 1*; Flood, E. A., Ed.; Marcel Dekker, Inc.: New York, 1967.
- 37 Sing, K. S. W. In *Porosity in Carbons*; Patrick, J. W., Ed.; Edward Arnold: London, 1995; pp 49-66.
- 38 Dubinin, M. M. In *Chemistry of Physics and Carbon*; Walker Jr., P. L., Ed.; Marcel Dekker: New York, 1966; Vol. 2, pp 51-118.
- 39 Adamson, A. W. *Physical Chemistry of Surfaces, 5<sup>th</sup> edition*, John Wiley & Sons, Inc.: New York, 1990.
- 40 Dubinin, M. M. *Carbon* **1985**, *23*, 373.
- 41 Dubinin, M. M.; Polyakov, N. S.; Kataeva, L. I. *Carbon* **1991**, *29*, 481.
- 42 Marsh, H.; Rand, B. *J. Coll. Int. Sci.* **1970**, *33*, 101.
- 43 Stoeckli, H. F. *Carbon* **1989**, *27*, 962.
- 44 Olivier, J. P.; Conklin, W. B. Determination of Pore Size Distribution from Density Functional Theoretic Models of Adsorption and Condensation within Porous Solids. International Symposium on the Effects of Surface Heterogeneity in Adsorption and Catalysis on Solids, Kazimierz Dolny, Poland; 1992.
- 45 Olivier, J. P. *J. Porous Mat.* **1995**, *2*, 9.
- 46 Seaton, N. A.; Walton, J. P. R. B.; Quirke, N. *Carbon* **1989**, *27*, 853.
- 47 Cullity, B. D. *Elements of x-ray diffraction*; Addison-Wesley Pub. Co.: Reading MA, 1967; Chapter 4.
- 48 Hickl, P.; Ballauff, M.; Jada, A. *Macromolecules* **1996**, *29*, 4006.
- 49 Bu, Zimei; Koide, Shohei; Engleman, D. M. *Protein Science* **1998**, *7*, 2681.
- 50 Guinier, A.; Fournet, G. *Small-Angle Scattering of X-rays*; John Wiley & Sons, Inc.: New York, 1955.
- 51 Li, X. K.; Liu, L.; Li, Zh. H.; Wu, D.; Shen, Sh. D. *Carbon* **2000**, *38*, 623.
- 52 Gardner, M. A. PhD Thesis, University of Kent at Canterbury, UK, 1995.
- 53 Hall, P. J.; Antxustegi, Mirai M.; Ruiz, W. *Fuel* **1998**, *77*, 1663.

- 54 Maslen, E. N.; Fox, A. G.; O'Keefe, M. A. In *International Tables for Crystallography Vol. C*; Wilson, A. J. C. Ed.; Kluwer Academic Publishers: London, 1992; pp 476-511.
- 55 Debye, P.; Anderson Jr., H. R.; Brumberger, H. *J. App. Phys.* **1957**, *28*, 679.
- 56 Kalliat, M.; Kwak, C. Y.; Schmidt, P. W. In *New Approaches in Coal Chemistry*; Blaustein, D.; Bockrath, B. C.; Friedman, S., Eds.; American Coal Society: Washington, 1981.
- 57 Porod, G. In *Small Angle X-ray Scattering*; Glatter, O.; Kratky, O., Eds.; Academic Press Inc. Ltd.: London, 1982; pp 17-51.
- 58 Maire, J.; Mering, J. In *Chemistry of Physics and Carbon*; Walker Jr., P. L.; Thrower, P. A., Eds.; Marcel Dekker: New York, 1970; Vol. 6, pp 125-190.
- 59 Hang Shi. Ph.D. thesis, Simon Fraser University, BC, 1993.
- 60 Zheng, T.; Xing, W.; Dahn, J. R. *Carbon* **1996**, *34*, 1501.
- 61 Wang Yinghua. *J. Appl. Cryst.* **1987**, *20*, 258.
- 62 Guinier, A. In *X-Ray Diffraction in Crystals, Imperfect Crystals, and Amorphous Bodies*; Dover Publications Inc.: New York, 1994.
- 63 Marcilla-Gomis, A.; Garcia-Cortes, A. N.; Martin-Martinez, J. M. *Carbon* **1996**, *34*, 1531.
- 64 Quirke, N.; Tennison, S. R. R. *Carbon* **1996**, *34*, 1281.
- 65 Foley, N. J.; Thomas, K. M.; Forshaw, P. L.; Stanton, D.; Norman, P. R. *Langmuir* **1997**, *13*, 2083.
- 66 Seron, A.; Benaddi, H.; Beguin, F.; Frackowiak, E.; Bretelle, J. L.; Thiry, M. C.; Bandosz, T. J.; Jagiello, J.; Schwarz, J. A. *Carbon* **1996**, *34*, 481.
- 67 Rozwadowski, M.; Wojsz, R. *Carbon* **1988**, *26*, 111.
- 68 Harris, P. J. F. *International Materials Reviews*, **1997**, *42*, 206.
- 69 Franklin, R. E. *Proc. Royal Soc. A* **1951**, *209*, 196.
- 70 Yinghu Liu; Xue, J. S.; Tao Zheng; Dahn, J. R. *Carbon* **1996**, *34*, 193.
- 71 Wyckoff, R. W. G. In *Crystal Structures, Volume 1*; Robert E. Kreiger Publishing Company: Malabar, FL, 1982; Chapter 1.



- 72 Ruland, W. In *Chemistry of Physics and Carbon*; Walker Jr., P. L., Ed.; Marcel Dekker: New York, 1968; Vol. 4, pp 1-84.
- 73 Biscoe, J.; Warren, B. E. *J. Appl. Phys.* **1942**, *13*, 364.
- 74 Rand, B.; McEnaney, B. *Br. Ceram. Trans. J.* **1985**, *84*, 157.
- 75 Marsh, H. A.; Walker Jr, P. L., In *Chemistry of Physics and Carbon*; Walker Jr., P. L.; Thrower, P. A. Eds.; Marcel Dekker: New York, 1979; Vol. 15, pp 230-286.
- 76 Tao Zheng; Reimers, J. N.; Dahn, J. R. *Phys. Rev. B* **1995**, *51*, 734.
- 77 Dahn, J. R.; Weibing Xing; Yuan Gao *Carbon* **1997**, *35*, 825.
- 78 Zheng Tao; McKinnon, W. R.; Dahn, J. R. *J. Electrochem. Soc.* **1996**, *143*, 2137.
- 79 Dahn, J. R. *Phys. Rev. B* **1991**, *44*, 9170.
- 80 Ge, P.; Fouletier, M. *Solid State Ionics* **1988**, *28-30*, 1172.
- 81 DiVincenzo, D. P.; Mele, E. J. *Phys. Rev. B* **1985**, *32*, 2538.
- 82 Zheng, Tao; Xue, J. S.; Dahn, J. R. *Chem. Mater.* **1996**, *8*, 389.
- 83 Papanek, P.; Radosavljevic, M.; Fischer, J.E. *Chem. Mater.* **1996**, *8*, 1519.
- 84 Dahn, J. R.; Fong, R.; Spoon, M. J. *Phys. Rev. B* **1990**, *42*, 6424.
- 85 Buiel, E.; George, A. E.; Dahn, J. R. *J. Electrochem. Soc.* **1998**, *145*, 2252.
- 86 Aurbach, D.; Zaban, A.; Ein-Eli, I. W.; Chusid, O.; Markovsky, B.; Levi, M.; Levi, E.; Schechter, A.; Granot, E. *J. Power Sources* **1997**, *68*, 91.
- 87 Grojtheim, K.; Welch, B. J. *Aluminium Smelter Technology, 2<sup>nd</sup> edition*; Aluminium Verlag: Dusseldorf, 1988.
- 88 Xing, Weibing; Dahn, J. R. *J. Electrochem. Soc.* **1997**, *144*, 1195.